

Battery Design for Battery-Electric Long-Haul Trucks

Olaf Teichert

Vollständiger Abdruck der von der TUM School of Engineering and Design der Technischen Universität München zur Erlangung eines
Doktors der Ingenieurwissenschaften (Dr.-Ing.)
genehmigten Dissertation.

Vorsitz: Prof. Dr.-Ing. Andreas Jossen

Prüfer der Dissertation:

1. Prof. Dr.-Ing. Markus Lienkamp
2. Prof. Gregory Offer, Ph.D.

Die Dissertation wurde am 18.04.2023 bei der Technischen Universität München eingereicht
und durch die TUM School of Engineering and Design am 23.11.2023 angenommen.

Für Chu.

Contents

List of Abbreviations	III
Formula Symbols	V
1 Introduction	1
2 State of the art	5
2.1 Long-haul truck electrification	5
2.2 Battery design	7
2.2.1 Cell technologies and selection methods	8
2.2.2 Battery modeling	10
2.2.3 Power profiles	16
2.2.4 Battery lifetime simulation	18
2.2.5 Battery thermal management system design	19
2.3 Research gap	19
3 Method & results	21
3.1 Step 1: cell selection	22
3.1.1 Summary of the published cell selection method	23
3.1.2 Contributions	24
3.1.3 Changes to the published method	40
3.1.4 Updated results	42
3.2 Step 2: battery model parametrization	43
3.2.1 Summary of the published battery model	43
3.2.2 Contributions	44
3.2.3 Changes to the published battery model	63
3.2.4 Electric model parametrization	65
3.2.5 Thermal model parametrization	67
3.2.6 Electric & thermal model validation	67
3.2.7 Aging model parametrization & validation	74
3.3 Step 3: power profile generation	75
3.3.1 Method	75
3.3.2 Results	82
3.4 Step 4: battery lifetime simulation	85
3.5 Step 5: battery thermal management system design	87
4 Discussion & Conclusion	91
List of Figures	i
List of Tables	iii
Bibliography	v
Prior Publications	xv
Supervised Student's Thesis	xvii
Appendix	xix

List of Abbreviations

AC	Alternating Current
BET	Battery-Electric Truck
BEV	Battery-Electric Vehicle
BTMS	Battery Thermal Management System
CCS	Combined Charging System
CFD	Computational Fluid Dynamics
COP	Coefficient Of Performance
DC	Direct Current
DOD	Depth Of Discharge
DT	Diesel Truck
ECM	Equivalent Circuit Model
EOL	End Of Life
FEC	Full Equivalent Cycles
FEM	Finite Element Model
GVW	Gross Vehicle Weight
HPPC	Hybrid Pulse Power Characterization
IEA	International Energy Agency
LCO	Lithium Cobalt Oxide
LFP	Lithium Iron Phosphate
LTO	Lithium Titanium Oxide
MCS	Megawatt Charging System
MPC	Model Predictive Control
NCA	Nickel Cobalt Aluminum
NMC	Nickel Manganese Cobalt
OCV	Open Circuit Voltage
RMS	Root Mean Square
SEI	Solid Electrolyte Interface
SOC	State Of Charge
SOP	Start of production
TCO	Total Cost of Ownership
WLTP	Worldwide harmonized Light vehicles Test Procedure

Formula Symbols

Formula Symbols	Unit	Description
c_c	JK^{-1}	Cell heat capacity
c_s	JK^{-1}	Sensor heat capacity
c_h	JK^{-1}	Housing heat capacity
C_1	F	Capacitance of first RC-element
COP_{heat}	-	Heating system Coefficient Of Performance (COP)
COP_{cool}	-	Cooling system COP
I_{cell}	A	Cell current
$I_{\text{ch,lim}}$	A	Maximum charging current
$I_{\text{dch,lim}}$	A	Maximum discharging current
$I_{\text{ch,cont}}$	A	Maximum continuous charging current
$I_{\text{dch,cont}}$	A	Maximum continuous discharging current
n	-	Full Equivalent Cycles (FEC)
n_{cyc}	-	Cycle life
n_{annual}	-	Annual FEC
n_{cells}	-	Number of cells in battery
P_{cell}	W	Cell power
P_{loss}	W	Ohmic losses
P_{heat}	W	Applied heating power
P_{cool}	W	Applied cooling power
Q	Ah	Cell capacity
Q_{loss}	Ah	Capacity loss
$Q_{\text{throughput}}$	Ah	Capacity throughput
$R_{0,c}$	Ω	Series charging resistance
$R_{0,d}$	Ω	Series discharging resistance
R_1	Ω	Resistance of first RC-element

R_{inc}	-	Resistance increase
R_{CS}	WK^{-1}	Thermal resistance between cell and sensor
R_{ch}	WK^{-1}	Thermal resistance between cell and housing
R_{hs}	WK^{-1}	Thermal resistance between housing and sensor
R_{out}	WK^{-1}	Thermal resistance between housing and ambient
SOC	-	State Of Charge (SOC)
SOC_{max}	-	Upper SOC limit
SOC_{min}	-	Lower SOC limit
t	years	Time
t_{eq}	years	Equivalent aging time
t_{RC}	s	Time constant of RC element
t_{cal}	years	Calendar life
T_c	$^{\circ}C$	Cell temperature
T_s	$^{\circ}C$	Sensor temperature
T_h	$^{\circ}C$	Housing temperature
U_k	V	Cell terminal voltage
U_{max}	V	Upper voltage limit
U_{min}	V	Lower voltage limit
U_{OCV}	V	Open Circuit Voltage (OCV)
U_1	V	Voltage across RC element
z	-	Aging exponent
α	-	Aging coefficient
Δt	s	Time step duration

Subscripts

cal	-	Calendar
cyc	-	Cyclic
end	-	At the end of life
j	-	Simulation time step index
Q	-	Capacity loss
R	-	Resistance increase

1 Introduction

Under the "Green Deal", the European Union aims to reduce greenhouse gas emissions to less than 55 % from 1990 levels by 2030, and become climate-neutral by 2050 [1]. One quarter of these greenhouse gas emissions is caused by the transport sector, where road transport is responsible for the largest share (72 % in 2019) [2, p. 7]. A rapid transition to zero-emission vehicles is therefore vital to meet the Green Deal targets.

The largest share of road transport emissions in the EU is caused by passenger vehicles (60.6 % in 2019 [2, p.18]), where one type of zero-emission vehicle, the Battery-Electric Vehicle (BEV), has seen promising growth in recent years. In Europe, BEV sales increased by 65 % from 2021 to 2022, reaching a car sales share of 9 % [3, p. 15]. The number of available BEV models has also seen a continuous increase from approximately 50 models in 2015 to almost 300 models in 2021 [3, p. 19].

The second largest share of road transport emissions within the EU is caused by heavy-duty vehicles (27.1 % in 2019 [2, p.18]), illustrated in Figure 1.1. This includes emissions from buses & coaches, construction & utility vehicles, service vehicles (≤ 7.5 t), and trucks operating on urban-delivery, regional-delivery and long-haul routes. While the sales share of electric buses has been continuously increasing in Europe, reaching 6 % in 2021, only 0.1 % of heavy-duty trucks sold in 2021 were electrified [3, p. 35]. In particular long-haul trucks, which are the largest emitters among heavy-duty vehicles in Europe (37.1 % of all heavy-duty vehicle fuel consumption [4, p. 181]), are challenging to decarbonize due to long travel distances and heavy loads. Yet, to reach the Green Deal targets, an effective zero-emission alternative is required.

Several decarbonization pathways for long-haul trucks are currently being explored, including synthetic fuels, hydrogen, catenary systems, and battery-powered vehicles. Each pathway has advantages and disadvantages.

Synthetic fuels, also known as e-fuels, are manufactured from hydrogen and CO₂. If the hydrogen is generated using renewable energy resources and the CO₂ is captured from the air, these fuels are climate-neutral. Synthetic fuels benefit from a high energy density and could be integrated in existing vehicle and fuel infrastructure [5]. However, the fuels have a low well-to-wheel efficiency, meaning that it would require about 5 times more renewable energy sources to decarbonize the mobility sector using synthetic fuels compared to a battery-electric option [6, p. 11]. Additionally, although carbon emissions are accounted for, burning synthetic fuels would still locally emit particulate matter and nitrogen oxides.

Hydrogen can be used for propulsion by converting it into electricity in a fuel cell and powering an electric machine, emitting only water. The energy density of compressed hydrogen on a system level is lower than that of fossil fuels, but higher than that of batteries. It is therefore often proposed as a zero-emission alternative for applications where volume and weight constraints might make a battery-electric option challenging to realize [7, p. 25]. Additionally, compared to BEV, hydrogen vehicles can be refueled faster, although BEV charging times have been

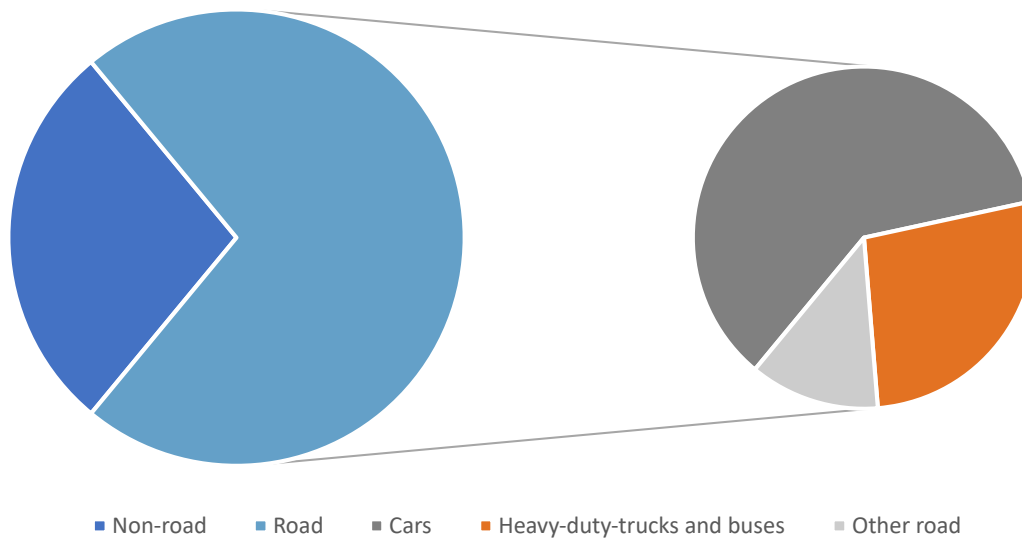


Figure 1.1: Share of heavy-duty truck emissions in the transport sector [2, p. 18].

continuously decreasing [8]. That said, a decarbonization pathway based on hydrogen faces two major challenges. First, the infrastructure is still sparse: In 2020 only 540 hydrogen refueling stations were in operation globally, compared to 1.3 million charging points for BEV [9]. Second, the conversion step from electricity to hydrogen and back causes efficiency losses, resulting in a decarbonization pathway that would require 2.5 times the amount of renewable energy sources compared to a battery-electric option [10, p. 20].

Alternatively, hydrogen may be used for propulsion by burning it in a combustion engine. This use of hydrogen benefits from synergies with fossil fuel combustion engine technology [11] and does not require expensive materials for the fuel cell catalyst [11]. However, although combusting hydrogen does not result in CO₂ emissions, the high combustion temperature does cause nitrogen oxide emissions. Additionally, the tank-to-wheel efficiency for combusting hydrogen is lower than the fuel cell option, resulting in a further increased need for renewable energy sources for this decarbonization pathway.

Catenary systems are a hybrid propulsion technique where the truck has a vehicle battery and a pantograph, which allows the vehicle to attach to overhead powerlines where these are available [12]. As a result, smaller batteries onboard the vehicle may suffice, reducing the vehicle cost and increasing payload capability. However, this concept would require large investments in overhead charging infrastructure estimated at $\text{€}2.44 \cdot 10^6 \text{ km}^{-1}$ [13].

Finally, climate-neutral long-haul trucks might be realized with a battery-electric powertrain. This option has a high well-to-wheel efficiency and could benefit from synergies with the passenger car market, where battery-electric drivetrains have dominated among zero-emission alternatives [9]. However, the required driving range and payload capacity might be challenging to realize, due to the low energy density of batteries compared to fossil fuels [14].

All decarbonization pathways have their own advantages and disadvantages. However, taking into account the low availability of renewable energy sources and the slow development of new infrastructure, Battery-Electric Truck (BET) may be our best bet for reaching the goals of the Green Deal. With this thesis, I hope to contribute to making battery-electric long-haul trucks feasible and cost-competitive with status-quo Diesel Truck (DT).

The most crucial component for realizing battery-electric long-haul trucks is the traction battery. The long travel distances and heavy payloads that are typical for this vehicle type result in a high energy demand. At the same time, the available volume onboard the vehicle is limited, and the battery mass should not result in payload losses compared to a DT. Additionally, fast-charging capability is required to allow recharging the vehicle during the driver's rest period and a high cycle life is needed to cover the high annual mileage. All these requirements need to be met at a competitive price point as the logistics market expects payback periods on investments of less than two years [15].

These requirements result in a conflict, because batteries that excel at cycle life typically offer a lower energy density, and cells that are capable of fast-charging might be more expensive [16, 17]. The system design needs to be considered too, because the battery life is influenced by the Battery Thermal Management System (BTMS). To find a good trade-off between these characteristics in the battery design, I developed a structured approach to design the battery of a battery-electric truck.

The structure of this thesis is illustrated in Figure 1.2. After this introduction, I will describe previous research on truck electrification and battery design, and define the research gap. Subsequently, I will present the developed method, which consists of five steps: cell selection, battery model parametrization, power profile generation, battery lifetime simulation, and BTMS design. The cell selection method and battery model have been published in previous work. Results will be presented after describing the method of each step. Finally, chapter 4 provides a discussion and conclusion.

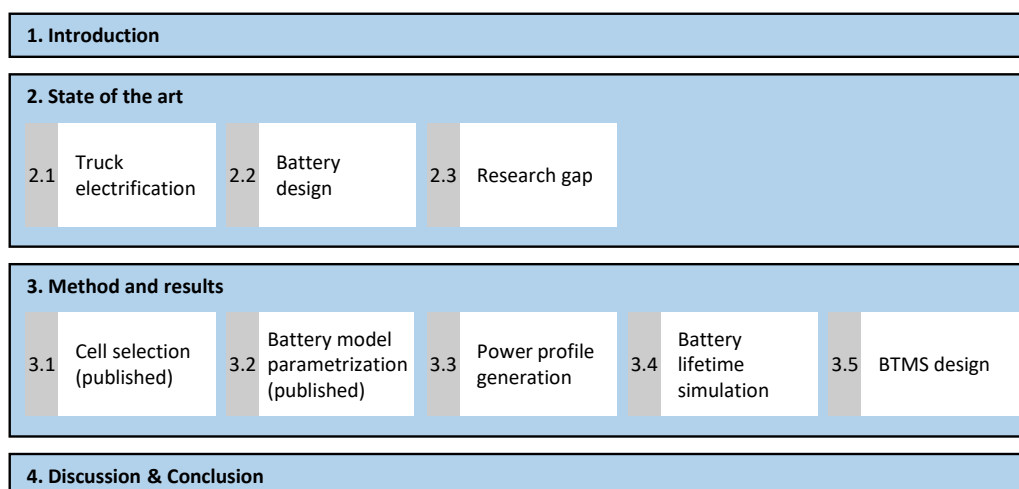


Figure 1.2: Thesis structure

2 State of the art

Related work can be clustered into two groups: studies investigating the feasibility and cost competitiveness of truck electrification, and studies focusing on battery design. In the following, I will give an overview of previous work in both groups and conclude with the research gap.

2.1 Long-haul truck electrification

The first study investigating zero-emission alternatives for long-haul transport was published in 2013 by den Boer et al. [18]. The authors explored options for zero-emission road freight transport, concluding that battery-electric technology is a feasible option for short-distance transport, but not a viable mainstream option for long-haul applications without on-the-road charging technologies.

A 2016 study commissioned by Shell [19] agrees with this result, concluding that the restrictions on range and payload would be too severe for a battery-electric powertrain.

In 2017, Sripad et al. [14] reached a similar conclusion. The authors carried out Monte-Carlo simulations to determine the required battery capacity and resulting battery mass, battery cost and maximum payload capacity for status quo lithium-ion cells and beyond lithium-ion cells. Their results show that in order to achieve cost competitiveness with DT the improved performance of beyond lithium-ion cells is required.

The 2017 International Energy Agency (IEA) study on the future of trucks [15] excluded BET from their cost comparison among vehicle and fuel technologies for long-haul transport, instead focusing on diesel hybrids, trucks fueled with natural gas, hydrogen trucks, and electric trucks operating on electricity from catenary-based electric road systems.

Until 2017, battery-electric propulsion was not seen as a viable option for long-haul transport. However, two important aspects were not considered. First, battery technology has been improving rapidly. Energy density and specific energy have more than tripled since the initial introduction of lithium-ion batteries [20], while the cell price has been falling by 25 % every time the cumulative volume of deployed cells doubled [21]. Additionally, on pack-level, costs have come down due to improvements in the cell-to-pack cost ratio [22], while energy density has increased due to novel cell-to-pack integration concepts [21].

Second, the studies concluding that BET are not feasible assumed that a range between 965 km and 1100 km is required to mimic DT operation. However, current EU regulations prohibit a driver from driving more than 4.5 h without a rest period of 45 min . At the maximum speed for trucks of 80 km h^{-1} , this results in a range between rest periods of 360 km. If charging infrastructure is available during the rest periods, the required range of a BET operating with a single driver can therefore be reduced significantly.

More recent studies underline the feasibility of BET. Only a few months after Transport & Environment published a report concluding that battery electric vehicle technology is limited to small and medium trucks [23], the authors published an update [24] stating that long range BET not only have the potential to bring the EU close to zero emissions, but also that the transition would be cost effective for the trucking sector. In their 2021 report [25] they expect between 88 000 and 185 000 battery-electric long-haul trucks on the road in 2030.

In 2018 Sripad et al. [26] revisited the conclusion from their 2017 article, finding that economic competitiveness of electric semi-trucks for hauling ranges of up to 500 miles will be enabled if optimistic but feasible conditions for vehicle drag, charging infrastructure availability, cost of charging, battery cost and battery cycle life are met.

Phadke et al. [27] found that at the 2021 global average battery pack price of $\$135 \text{ kWh}^{-1}$ a BET with 600 km range operating 480 km per day offers about 13 % lower Total Cost of Ownership (TCO) than a DT with only a 3 % reduction in payload capacity.

This is in line with announcements from truck manufacturers. An overview of long-haul BET models, their characteristics and their Start of production (SOP) is shown in Table 2.1. Manufacturers expect a rapid uptake: MAN [28] announced that 40 % of their long-haul truck sales will be zero-emission in 2030; Scania [29] aims at 50 % of its sales to be electric in 2030; and Daimler, Iveco, Scania, Volvo Group, DAF and MAN all announced their commitment to sell 100 % fossil-free trucks by 2040 [30].

Table 2.1: Characteristics and SOP of announced long-haul trucks [31]

Truck	SOP	tractor mass	Installed energy	Battery chemistry	Range
Daimler eActros LongHaul	Q4 2024	11 t	600 kWh	LFP	500 km
Scania 45R	Q3 2023	10.7 t	624 kWh	NMC	350 km
Volvo FH electric	Q4 2022	10.55 t	540 kWh	NCA	300 km
Nikola TRE BEV	Q3 2023	12.3 t	738 kWh	NMC	530 km
DAF XFe FT	Q2 2023	9.8 t	525 kWh	LFP	500 km
MAN eTruck	2024	10.34 t	534 kWh	NMC	611 km

However, the point at which BET become cost competitive with DT depends on a wide range of factors. First, on the vehicle range and annual mileage. Wolff et al. [32] investigated the cost-effectiveness and well-to-wheel emissions of different powertrain concepts for different annual mileages and vehicle ranges. The authors considered different scenarios: a 2020 scenario, a realistic 2030 scenario, and an optimistic 2030 scenario. Their results for the realistic 2030 scenario show that BET are the most cost-competitive option up to a range of 600 km. At this range, BET have the lowest well-to-wheel emissions as well for a typical long-haul truck annual mileage.

Second, it depends on local policy and the divergence between diesel cost and the cost of charging. Basma et al. [33] analyzed the year in which BET and DT reach TCO parity in seven European countries, taking into account ownership taxes, electricity and diesel costs, maintenance costs, road tolls, battery replacement, and charging infrastructure costs. They conclude that TCO parity will be reached during this decade for all considered countries, but the year at which it will be reached varies from 2021 in Germany to 2027 in Italy. Noll et al. [34] compared the road-freight TCO for 5 drive-technologies in 3 applications and 10 countries. They find that cost competitiveness in the heavy-duty long-haul segment is exhibited already today in countries that have enacted targeted policy measures. Earl et al. [35] analyzed the potential of battery-electric heavy-duty trucks in the EU. Their analysis of the total cost of ownership shows that the biggest sensitivity to cost competitiveness is the electricity price.

Third, it depends on the available charging infrastructure. Forrest et al. [36] compared the trip share that can be covered by battery-powered trucks and hydrogen-powered trucks for different ranges and charging capacities. Their results show that the share of covered trips can be greatly increased by enabling fast charging during the day.

Finally, the characteristics of the BET battery are crucial for a cost-effective and feasible implementation. The battery of a BET must be: small, to fit into the available volume on board the vehicle; light, to avoid any reductions in payload; resistant to aging, to avoid battery replacement during the operating life; fast-charging capable, to enable recharging during driver rest periods; and low cost to minimize investment costs. Previous studies investigated the impact of the battery properties on the feasibility and cost-effectiveness of BET.

Mareev et al. [37] determined the required battery capacity for long-distance truck operation in Germany, taking into account battery charging during driver rest periods. They then performed a life cycle cost analysis for two different cell types, which showed that life cycle costs are strongly influenced by battery lifetime, justifying the use of more expensive but aging-resistant cells.

Nykvist and Olsson [38] modeled the feasibility of BET that use fast charging with high power. Their results show that battery characteristics strongly influence the cost competitiveness of BET and that battery lifetime may be more important than specific battery price.

Mauler et al. [39] compared the life-cycle costs of a BET with Lithium Iron Phosphate (LFP) cells, a BET with high-nickel cells, and a hydrogen truck in the united states, taking into account lost profits due to charging times and lower cargo capacity. The results show that LFP batteries excel in volume-constrained transport on short hauls, while high nickel batteries have an advantage in weight-constrained transport. Hydrogen trucks become competitive only on long and weight-constrained routes.

In conclusion, announcements from truck manufacturers and recent studies agree that long-haul trucks are primed for electrification now. However, the boundary conditions for widespread adoption are complex, requiring targeted policy measures and the implementation of a dense charging infrastructure network. Additionally, several studies address the importance of the battery characteristics. Although these studies compare the suitability of different battery cells, or battery sizes, a holistic battery design method is still missing.

2.2 Battery design

Battery technology is a vast research field. Between 2000 and 2019 more than 170 000 articles related to batteries have been published [40]. These articles cover a wide range of topics, including material development, battery diagnostics, operating strategies, and thermal management systems. However, only few researchers presented methodologies for a holistic battery system design.

Burda [41] developed a range of tools that support the battery design for a passenger vehicle: battery sizing and package definition during the concept phase, technology selection and packaging during the definition phase, simulation and detailed design during the realization phase, and finally validation and homologation during the construction phase. All tools were applied to the design and realization of the MUTE BEV prototype. As one of the limitations, the author states that costs were not included in this battery design method.

Hesse et al. [42] provide a guideline for the system design of lithium-ion based stationary storage systems. They first discuss the performance and aging characteristics of different electrode materials. Subsequently, they describe which additional components are needed in a stationary storage system, and discuss different stationary storage applications and the resulting load patterns. Finally, they present different simulation models that allow optimizing the sizing, position and energy dispatch control for different applications.

Naumann [43] optimized the size and installed photovoltaic peak power of a home energy storage system to maximize its profitability. The author took special consideration of the battery aging behavior by characterizing an LFP cell using extensive calendar and cycle aging studies. However, different cells or the impact of the battery thermal management system design are not considered.

Rothgang et al. [44] analyzed the design process for electric public buses. The authors qualitatively discuss the impact of different bus operating strategies, cell selection and the thermal management system. However, the trade-offs in individual design decisions are not quantified.

Reiter [45] presented a procedure for top-level thermal design of lithium-ion battery systems in electric passenger vehicles. The procedure compares different cell formats, taking the electrical connections and cell parameter variations into account. However, different cell chemistries were not considered.

Epp et al. [46] focused on the battery packaging. They presented a multi-physically coupled battery design tool that optimizes space allocation of the main system components for different cell geometries. For a passenger car use case, they optimized the design of the mechanical battery frame, the cooling plate topology, and the integration capability of the electronics, finding a Pareto-optimal result in terms of installation space and cost.

In addition to studies presenting holistic design methods, other studies cover individual aspects of the battery design process: cell selection, battery modeling, load profile generation, battery life simulation or BTMS design. The state-of-the-art in these domains will be discussed in the following.

Further battery-design aspects, including optimization of the battery size [47] and cell interconnections [45], are not covered in this thesis. I assume that the battery size will be minimized while enabling BET to mimic DT operation in worst-case conditions, thereby removing the need for battery size optimization; and I consider the optimization of cell interconnections and geometric positioning to be part of the detailed battery design, which will not be covered in this thesis.

2.2.1 Cell technologies and selection methods

Although a wide range of energy storage technologies exists, state-of-the-art BEV solely use lithium-ion batteries [48], due to their high energy density, high efficiency, low self discharge, and long cycle life [42]. Therefore, I will limit myself to lithium-ion cells here. Post Lithium-ion cell technologies, such as lithium-sulfur or sodium-ion batteries are not considered, because they are not commercially available yet. Despite these restrictions, lithium-ion cells are available with vastly different parameters.

Lithium-ion cells consist of a positive and a negative electrode, a separator, the electrolyte plus additives, and the cell housing. By changing the properties of these components, the cell characteristics can be modified [49].

The positive electrode typically consists of an aluminum current collector and the active material. Different active materials are used in lithium-ion cells. The first commercially available lithium-ion battery, presented by Sony, used Lithium Cobalt Oxide (LCO) as the active material on the positive electrode [50]. LCO has excellent cycling performance, low self-discharge, and an adequate gravimetric and volumetric energy density [51]. However, the high cost of cobalt disqualifies it for automotive applications [50].

Most widely used in automotive applications are batteries with a Nickel Manganese Cobalt (NMC) or Nickel Cobalt Aluminum (NCA) positive electrode [52]. Automotive companies are moving towards lower cobalt content in both materials to reduce costs [53]. These materials offer high energy densities and good cycling stability [54], but require additional safety measures on pack level [21].

Alternatively LFP is used, which shows excellent safety and aging characteristics [55]. Additionally, the cost and environmental impact of the material is low [56]. On the downside, LFP has a lower energy density than NMC or NCA cells, although this may be compensated on pack level by lower requirements of the cooling and safety systems [21]. Batteries with an LFP positive electrode are used in the China-built Tesla model 3 and in many Chinese vehicle models [57].

The negative electrode typically consists of a copper current collector and graphite as the active material. Graphite is low cost and achieves an adequate energy density. The energy density can be increased by adding silicon to the graphite anode, although high silicon contents might reduce the cell's cycle life [58].

Higher charging rates and a longer cycle life can be achieved with Lithium Titanium Oxide (LTO) as the negative electrode active material [59]. However, using LTO instead of graphite results in a lower energy density. Additionally, the use of titanium leads to a higher cost compared to graphite [58].

By combining different active materials for the positive and negative electrodes, cells with widely different properties can be created. Additionally, cell properties are affected by the active material thickness, cell tab design, electrolyte composition, separator material and cell form factor [60]. As a result, lithium-ion cells are available with vastly different properties, which led to the development of cell selection methods.

The most well known decision aid for energy storage device selection is the Ragone diagram presented by David Ragone in 1968 [61] and shown in Figure 2.1. The Ragone diagram visualizes the specific energy and specific power of an energy storage technology as a band representing different battery construction details and parameters, such as battery age, discharge rate, charge state and temperature. To assess the suitability of an energy storage technology for an automotive application, the specific power and specific energy that are required to propel a vehicle at a given speed for a given distance are superimposed in the figure. This enables a visual comparison of the range and vehicle speed that could be enabled by different energy storage technologies.

Since its initial publication, the Ragone plot has been extended to include further energy storage technologies, such as supercapacitors and lithium-ion batteries, and has been applied in a wider range of applications [50]. Other studies included additional cell characteristics in the Ragone plot. Catenaro et al. [62] developed an enhanced Ragone plot that takes the operating temperature of the cell into account, where the impact of the temperature on the relationship between energy and power is determined using pulse tests at different temperatures. Dechent et al. [63] proposed a further extension of the Ragone plot, called ENPOLITE, which visualizes

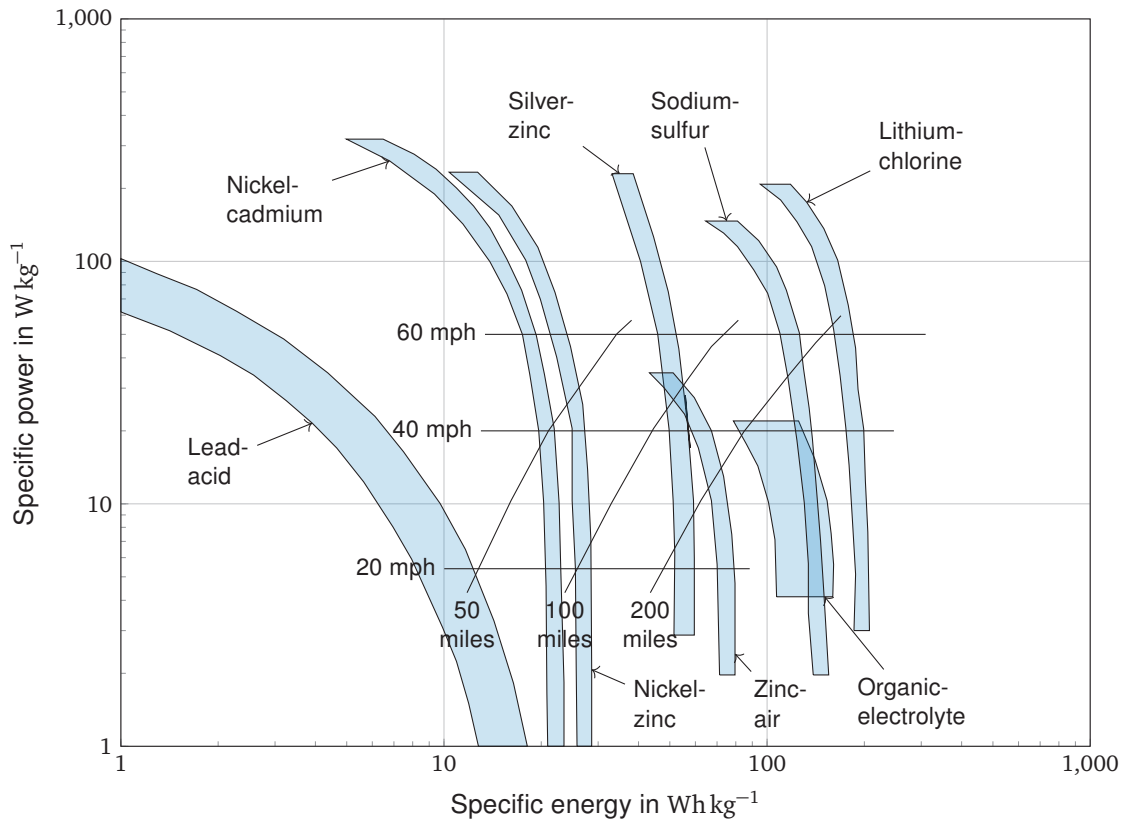


Figure 2.1: The original Ragone diagram [61]. Lithium-ion batteries and other energy storage devices were only included in later versions.

the energy, power, lifetime and temperature of energy storage technologies in a single figure, that contains the information from aging tests of several hundred cells with different chemistries, shape factors and load profiles.

Few studies describe cell selection methods unrelated to the Ragone plot. Panday and Bansal [64] proposed a multi-criteria decision making method that selects an energy storage device by comparing its characteristics to a target specification. The differences are then mapped in an Euclidean space and the energy storage device with the shortest distance from the ideal solution is selected. Loganathan et al. [65] presented a weighted-sum model for the selection of lithium-ion batteries in electric vehicles. The authors reviewed characteristics such as price, safety and energy density of various lithium-ion batteries, and ranked them on a five-point scale. Subsequently, weights were assigned to each characteristic and the performance of different lithium-ion batteries was compared.

Although different cell selection methods have been proposed in previous studies, they require knowledge about the required cell properties and don't consider the impact on system cost.

2.2.2 Battery modeling

After a cell is selected, battery models can be used for a detailed assessment of the cell's performance under different operating conditions. The battery model should cover the electric, thermal and aging behavior of the cell. In the following, I will describe different model types, the models I will use in this thesis, and their fundamentals. Subsequently, I will discuss previous work using combined electric, thermal, aging models.

Electric models

Electric models can be grouped into three categories: physics-based models, Equivalent Circuit Model (ECM), and black-box models. Physics-based models, e.g. PyBamm [66], aim to describe the battery structure and the physical and chemical processes that take place inside the battery in high detail [67]. For example, the porous structure of the electrode materials is simulated by a large number of spherical particles [68]. The simulation models resulting from this approach provide spatial concentration, potential and temperature distributions, and thus provide detailed insights into battery behavior. This type of model enables investigating design parameters of the battery structure, such as layer thickness or conductivity, and their influences in a targeted manner. However, solving these models is computationally expensive and parametrizing them requires detailed knowledge of the investigated battery cell.

ECM aim to simulate battery behavior with a small number of electrical components, such as voltage sources, resistors, capacitors and inductors, each of which is used to represent a specific physical effect [69]. These models allow fast computation times and are easier to parametrize than physics-based models. However, the possibilities for investigating the interaction between individual cell parameters is limited.

In contrast to the previous two types of battery models, black-box models regard the battery as a closed system whose input and output variables, such as current, voltage and SOC are linked by means of various methods [70]. Black-box models can be simple equations with low accuracy, such as the Peuckert equation [71], or complex artificial neural networks [72], that require vast amounts of measurement data to train.

In this thesis, I will use an ECM-based battery model, because battery designers typically have limited information about the internals of a cell, need higher accuracy than simple equations, and may not have enough operating data to train an artificial neural network.

ECM typically consist of a voltage source U_{OCV} , that models the cell's open circuit voltage, a series resistance R_0 , and a number of RC-elements. Figure 2.2 shows an ECM with a single RC-element, where R_1 and C_1 denote the RC-element components, U_1 denotes the voltage across the RC-element, U_k the voltage over the cell terminal and I_{cell} the cell current. Positive currents correspond to charging.

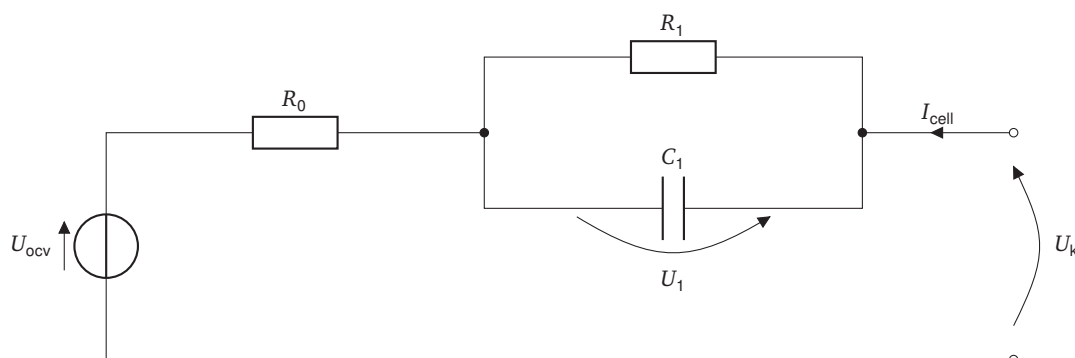


Figure 2.2: An ECM with a single RC-element.

The SOC dependency of the open circuit voltage can be parametrized using a pOCV measurement. In the pOCV measurement the cell voltage is measured while charging and discharging the cell with a low current. The OCV is approximated by taking the average of the cell voltage measured in a charging and discharging direction, as shown in Figure 2.3 [73].

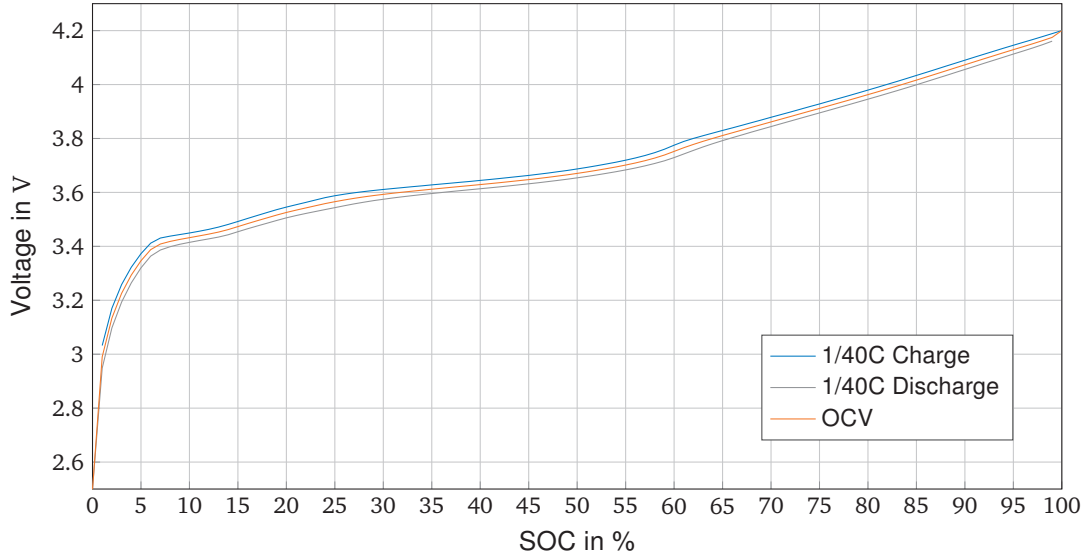


Figure 2.3: pOCV measurement and OCV-curve of the VW ID.3 cell [74]

The series resistance R_0 and RC-element components, R_1 and C_1 can be parametrized using a Hybrid Pulse Power Characterization (HPPC). In the HPPC, the cell voltage is measured in response to a current pulse, as shown in Figure 2.4. The measurement should be repeated at different SOC and temperature to include the impact of these factors.

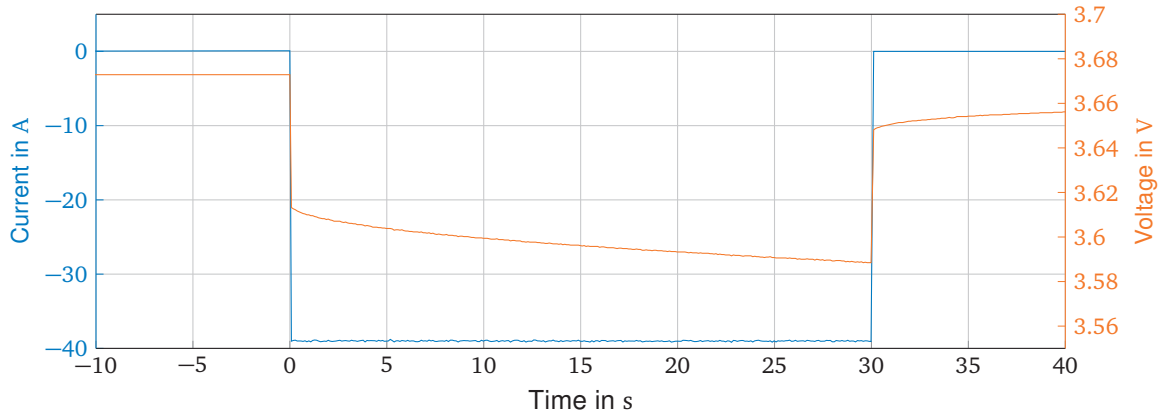


Figure 2.4: Voltage response to a 1/2C 30s current pulse for the VW ID.3 cell at 50% SOC and 20 °C [74]

The corresponding increase in cell resistance can be calculated using Equation (2.1), where R_j denotes the resistance and the subscript j the time step.

$$R_j = \frac{U_{k,j} - U_{k,j=0}}{I_{\text{cell},j} - I_{\text{cell},j=0}} \quad (2.1)$$

The cell's resistance increases with the pulse duration. This transient behavior is modeled by the ECM using Equation (2.2), where t denotes the pulse duration. The parameters R_0 , R_1 and C_1 can be found using a curve fitting algorithm, such as the "Trust-Region-Reflective Least Squares Algorithm" provided in the Matlab curve fitting toolbox. An example is shown in Figure 2.5. The quality of the fit is described by the coefficient of determination, R^2 .

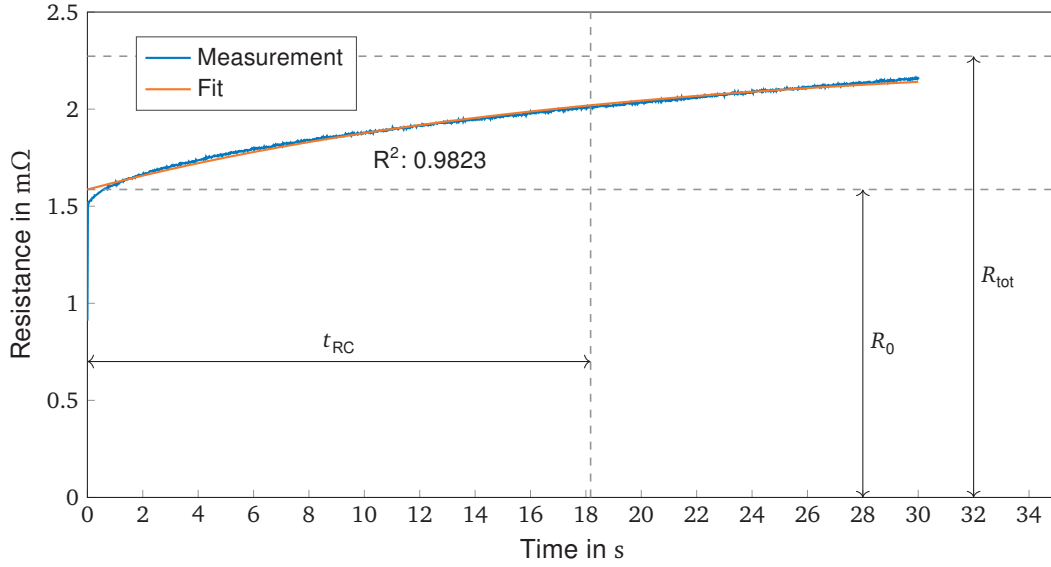


Figure 2.5: Exemplary curve fit for the VW ID.3 cell at 50% SOC and 20 °C. The curve fit achieves a coefficient of determination of 98.2%, where the biggest deviation occurs at the beginning of the pulse.

$$R_j = R_0 + R_1 \left(1 - \exp\left(\frac{-t}{R_1 C_1}\right) \right) \quad (2.2)$$

The series resistance, R_0 , corresponds to the internal resistance at the start of the pulse. As the pulse duration increases, the internal resistance increases, approaching an asymptotic value of R_{tot} , calculated by Equation (2.3). The speed at which this asymptotic value is reached is described by the RC-time, t_{RC} , given by Equation (2.4), which corresponds to the time until the RC-element resistance reaches 63% of its asymptotic value. Multiple RC-elements may be used to cover different physical effects and achieve a better curve fit, but lead to an increase in computation time.

$$\lim_{j \rightarrow \infty} R_j = R_{\text{tot}} = R_0 + R_1 \quad (2.3)$$

$$t_{\text{RC}} = R_1 C_1 \quad (2.4)$$

Thermal models

Thermal models model the thermal behavior of the cell and the interaction with the battery housing, cooling system and ambient temperature. Thermal models can be categorized as lumped-capacitance model or multi-dimensional models [75].

Multi-dimensional models include transient Finite Element Model (FEM) and Computational Fluid Dynamics (CFD) simulations. These models enable modeling the battery geometry and coolant flow in great detail, but require large computational resources and knowledge about the detailed battery design.

Lumped-capacitance models assume that the temperature of a solid object is uniform and can be represented by a single, lumped value. Although they are not as accurate as multi-dimensional models, they require less computational resources and are easier to parametrize.

In this thesis, I will use a lumped-capacitance thermal model, because the detailed battery design is not known yet and the model should require little computation power to allow simulating the battery life.

Using a lumped-capacitance model, the cell is modeled as a thermal mass with a given heat capacity and a connection to other thermal masses described by a thermal resistance. Heat generated in the cell is added to thermal mass, while heat exchange between the thermal masses is a function of the temperature difference and the thermal resistance. Additionally, heat may be added or removed by a heating or cooling system.

Aging models

Aging models model the capacity loss, Q_{loss} , and internal resistance increase, R_{inc} , caused by aging. Aging models can be grouped into two categories: physical models and semi-empirical models [76].

Physical models aim to model individual aging mechanisms such as Solid Electrolyte Interface (SEI) growth, particle cracking or lithium plating [77]. The models can achieve high accuracy and investigate the interaction between different battery design parameters, but require solving many partial differential equations and a thorough understanding of all physical and chemical mechanisms [76].

Semi-empirical aging models use curve-fits to capture the relationship of various stress factors in relatively simple analytical formula. They require large test matrices to parametrize, but do not require detailed knowledge about the cell internals and allow fast computation [76].

Because information about the cell internals is typically not known to a battery designer and fast computation times are required, I use semi-empirical aging models in this thesis.

Semi-empirical aging models calculate calendar and cyclic aging separately, using Equation (2.5) - (2.8), where α describes the impact of stress factors such as temperature or Depth Of Discharge (DOD), t denotes time, n FEC, and the exponent z describes the shape of the degradation curve. The subscripts Q , R , cal , and cyc denote capacity loss, resistance increase, calendar and cyclic aging respectively. The total capacity loss and internal resistance increase are the sum of the calendar and cyclic components as given in Equation (2.9) and (2.10).

$$Q_{\text{loss,cal}} = \alpha_{Q,\text{cal}} t^{z_{Q,\text{cal}}} \quad (2.5)$$

$$Q_{\text{loss,cyc}} = \alpha_{Q,\text{cyc}} n^{z_{Q,\text{cyc}}} \quad (2.6)$$

$$R_{\text{inc,cal}} = \alpha_{R,\text{cal}} t^{z_{R,\text{cal}}} \quad (2.7)$$

$$R_{\text{inc,cyc}} = \alpha_{R,\text{cyc}} n^{z_{R,\text{cyc}}} \quad (2.8)$$

$$Q_{\text{loss}} = Q_{\text{loss,cal}} + Q_{\text{loss,cyc}} \quad (2.9)$$

$$R_{\text{inc}} = R_{\text{inc,cal}} + R_{\text{inc,cyc}} \quad (2.10)$$

To model dynamic aging conditions, the incremental capacity loss and internal resistance increase need to be determined for the stress factors over a given time step. Unless the

exponent z is 1, these increments depend on the aging state of the battery at the beginning of the time step. The approach to update the aging state is illustrated at the example of calendar capacity loss.

An equivalent time, t_{eq} , is defined corresponding to the time that would have passed under the current aging coefficients to reach the capacity loss at the beginning of the time step, as given in Equation (2.11). The aging at the next time step can then be calculated using Equation (2.12). For cyclic aging, the same approach is used by calculating the equivalent FEC.

$$t_{\text{eq}} = \left(\frac{Q_{\text{loss,cal},j}}{\alpha_{\text{Q,cal}}} \right)^{1/z_{\text{Q,cal}}} \quad (2.11)$$

$$Q_{\text{loss,cal},j+1} = \alpha_{\text{Q,cal}}(t_{\text{eq}} + \Delta t)^{z_{\text{Q,cal}}} \quad (2.12)$$

The capacity loss and internal resistance increase caused by calendar aging can be updated at every time step. For cyclic aging this is not possible, because stress factors such as DOD or the average cycling voltage can only be determined once a cycle is completed. To determine if a cycle is completed, rainflow counting is used. Rainflow counting is a cycle counting scheme that has traditionally been employed to analyze cumulative damage fatigue in stress/strain hysteresis [78].

The rainflow counting algorithm determines the DOD and average cycling voltage based on SOC vertices that are detected by changes in the sign of the cell current, i.e. a change from charging to discharging or vice versa. The sequence of SOC vertices is stored and updated when a new SOC vertex is reached.

Figure 2.6 illustrates how the algorithm works, where the initial sequence of SOC vertices is shown on the panel on the left and subsequent sequences are shown on the panels to the right. Panel A shows the initial SOC vertices. When a new SOC vertex is detected, it is appended to the previous SOC vertices, as shown in panel B, and the DOD between the last and previous SOC vertices is calculated. If the last DOD is smaller than the previous DOD, the simulation continues, resulting in the SOC vertices in panel C. If the last DOD is larger than or equal to the previous DOD, the SOC vertices of the previous DOD are removed from the list, as shown in panel D, and cyclic degradation is calculated for the DOD and average cycling voltage of the removed SOC vertices. The algorithm continues until the last DOD is smaller than the previous DOD, or the list of SOC vertices has reduced to 2 or fewer points. The algorithm is executed every time a new SOC vertex is added to the list.

Combined electric, thermal, aging models

Combining ECM with thermal lumped capacitance models and semi-empirical aging models, the combined electric, thermal and aging behavior of a battery can be simulated, as demonstrated by the following studies.

Schmalstieg et al. [79] presented a coupled electric-thermal-aging model for a 2 Ah lithium-ion cell. The aging model is parametrized by conducting calendar and cycle aging tests for more than 60 cells. However, the model was only validated on cell level.

Neubauer [80] developed the Battery Lifetime Analysis and Simulation Tool (BLAST), which pairs a battery degradation model with an electrical and thermal model. The tool allows simulating

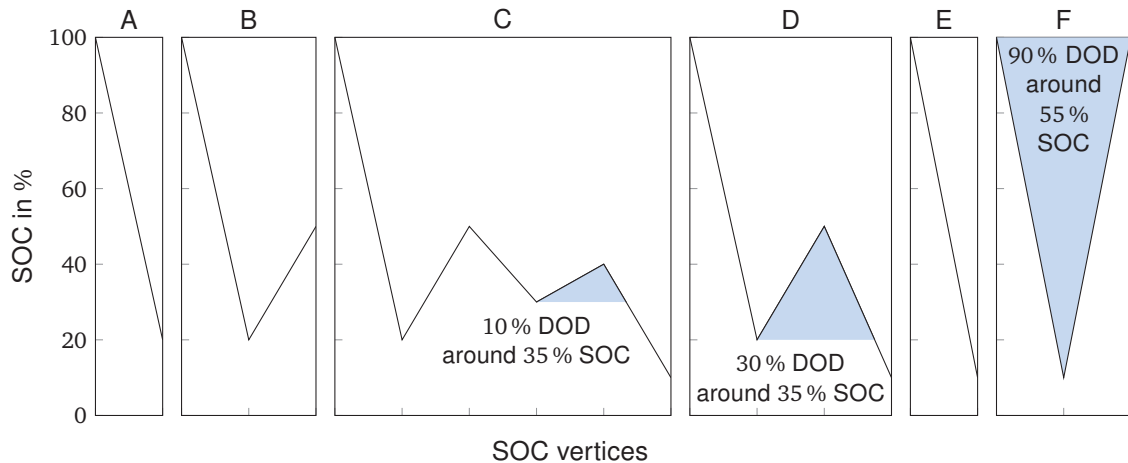


Figure 2.6: Illustration of the rainflow counting algorithm that is used to calculate cyclic aging.

vehicle, stationary storage and behind-the-meter applications, although only the electric model of the behind-the-meter model is available open-source. Additionally, no validation data was presented.

Naumann et al. [43] developed the SimSES software tool, which models the battery as an ECM and couples it with a thermal and degradation model. As of February 2023, the open-source version of the model contains parametrizations of eight different lithium-ion cells and one sodium-ion cell. However, none of the available cells are currently used in automotive applications or were validated on vehicle level.

Schimpe et al. [81] assessed the system efficiency of a stationary storage system using a detailed electric-thermal model of a 3 Ah lithium-ion cell. The cell model was scaled to system level and validated using experimental data of a prototype stationary battery system.

Yuksel et al. [82] combined an ECM with a vehicle model, thermal model and battery life model to assess the impact of driver behavior and different climates. However, no validation was presented.

Although previous studies presented combined electric, thermal, aging models, an open-source model for a state-of-the-art automotive grade battery cell that was validated on vehicle level is still missing.

2.2.3 Power profiles

To model battery behavior under typical operating conditions, the power demand under such conditions needs to be quantified. In automotive applications, power demand is typically derived based on standardized driving cycles, which are used for homologation purposes. One example of such a driving cycle is the Worldwide harmonized Light vehicles Test Procedure (WLTP), which is used to determine the fuel consumption of combustion, hybrid and fully electric cars [83].

Similarly, for heavy-duty vehicles, the European Union developed the VECTO driving cycles, including five different cycles for trucks and five for buses and coaches [84]. Since 1 January 2019, these cycles are used for determining CO₂ emissions and fuel consumption from heavy duty vehicles (trucks, buses and coaches) with a gross vehicle weight above 3500 kg [85, p. 3].

However, as the name suggests, these driving cycles are limited to a vehicle's driving phase, not taking into account the time spent charging or parked. Additionally, variations in trip distance and duration are not taken into account. To estimate the battery life for typical truck operation, these aspects need to be included. Previous studies generated load profiles for truck operation for longer time periods.

Walz et al. [86] presented a method to generate synthetic charging profiles of electric trucks for grid planning purposes. The authors used trip chain generation to obtain a charging profile based on historic mobility data of conventional vehicles and estimations of BET energy consumption during driving. The resulting power profile describes the charging power in 15-minute intervals for an entire year. Although this is sufficient for modeling the impact of charging on the grid, it does not capture the dynamic behavior of the power drawn from or supplied to the battery during driving and can therefore not be used to simulate battery aging. Additionally, the authors did not consider the impact of differences in driving behavior at different vehicle speeds, or the payload distribution on the vehicle energy consumption.

In a later work, Walz et al. [87] presented an implementation that includes a vehicle payload distribution and used it to model the cumulative energy demand of 300 trucks in different weight classes: up to 7.5 t, up to 18 t and above 18 t. However, the resolution of driving energy consumption is still too low to accurately model battery aging.

Tong et al. [88] estimated location-specific hourly charging powers for a national fleet of long-haul electric trucks based on bottom-up truck mass modeling, vehicle energy modeling, large-scale truck traffic data, and simulation of electric truck operation and charging behavior. However, vehicle energy consumption was calculated based on the average speed and the fraction of uphill driving, instead of a longitudinal transient simulation, and therefore does not capture the dynamic power profile of the battery during driving.

Borlaug et al. [89] developed synthetic depot charging load profiles for heavy-duty trucks from the real-world operating schedules of three different fleets. However, they used an average energy consumption rate during driving, independent of payload or trip speed variations.

The power profiles presented in previous studies show a lack of detail in the driving phase, due to their focus on the interaction between BET and the grid. This is also seen for BEV [90, 91] with one notable exception.

Gaete et al. [92] presented a method that combines both driving cycles and mobility data to generate power profiles for passenger vehicles. As a driving cycle, they used the WLTP profile and allow modeling different vehicles. For the mobility behavior they used data from the "Mobilität in Deutschland" study [93], which provides probability distributions for the amount of trips per day, trip destination, distance, duration, and trip departure times. By using stochastic sampling, trips can be assigned to each day and the power profile can be determined using a longitudinal vehicle simulation.

Although previous studies developed power profiles for BET, they were all generated to assess the impact on the electricity grid. To model battery aging, a power profile should capture both high dynamic driving behavior and high-level mobility patterns. The solution presented by Gaete et al. [92] enables this for passenger vehicles, but cannot be directly implemented to generate a power profile for trucks for the following reasons. First, truck drivers will aim to minimize the time spent away from the depot, rendering an individual sampling of the departure time of each trip unreasonable. Second, EU regulations regarding rest duration need to be enforced, and third,

the payload distribution must be included in the vehicle simulation, due to its large impact on energy consumption.

2.2.4 Battery lifetime simulation

By combining a load profile and an electric, thermal, aging model, the battery life under different operating conditions and ambient temperatures can be simulated, as demonstrated by the following studies.

Yuksel and Michalek [94] combined a thermal model with an aging model to investigate how much improvement in battery life can be obtained by implementing passive air cooling for an LFP battery in a plug-in hybrid vehicle. They investigated two climates: Miami, Florida, and Phoenix, Arizona. The authors assumed that the vehicle makes two trips per day followed by a slow-charging event. The simulation was performed for the duration of one week at the average ambient temperature of each season (spring, summer, fall, winter) for both climates and then extrapolated to estimate the battery life. In a later work [95], the authors used the same model to investigate the impact of driving behavior by implementing different driving cycles, and the impact of different temperature thresholds for activating the cooling system.

Neubauer and Wood [96] investigated the impact of driver aggression, climate, cabin thermal management, and battery thermal management on the utility of a BEV, taking battery degradation into account. Battery operation was simulated over lifetime, where the power drawn from the battery during driving was approximated using a Root Mean Square (RMS) value. This enabled using relatively large time steps for calculating the battery electric and thermal response: 1 min during driving, charging and preconditioning, and 10 min during resting.

Diorio et al. [97] presented a simulation framework to predict the performance and economic benefit of behind the meter energy storage. To include battery replacements in their financial analysis, the battery operation was simulated over lifetime, albeit with a one-hour time step.

Reiter [45] developed a detailed electric-thermal model that simulates multiple individual cells, taking temperature and current distributions within the pack into account. Due to the high computational load of the model, the authors simulated load cycles of several minutes or hours and subsequently used load-spectrum analysis to compare aging behavior of different cooling designs.

Naumann [43] presented a detailed electric-thermal-aging simulation in MATLAB and investigated the impact of simulation parameters on the computation time and quality of the results. They concluded that for their analysis of the aging behavior of a home energy storage system, the load profile can be downsampled to a time step of 5 min without causing a large model error, because the profiles show few dynamics below this sample time. Subsequently, they simulated the battery operating behavior over a simulation period of 20 years.

Previous studies presented simulations to estimate battery life under different operating conditions, taking into account variations in ambient temperature and operating conditions. Different approaches are presented to deal with the resulting computation load: load-spectrum analysis, extrapolating simulations results at representative temperatures for each season, or using large simulation time steps. However, taking both highly dynamic loads resulting from driving a BEV and ambient temperature changes into account requires a simulation over lifetime with a small time step.

2.2.5 Battery thermal management system design

Finally, battery simulations may be used to assess different BTMS designs. Temperatures above 25 °C cause accelerated capacity loss and internal resistance increase in lithium-ion cells, thereby shortening a battery's operating life [98]. Temperatures above 60 °C can lead to safety critical conditions that might result in a thermal runaway, and should thus be avoided at all times [98].

To prevent the negative effects of operating lithium-ion cells at high temperatures, a wide range of BTMS is used to cool the cells. The review papers by Xia et al. [75] and Jaguemont et al. [99] give a detailed overview of state-of-the-art BTMS and their advantages and disadvantages.

Two top-level design parameters of BTMS are the installed cooling power and the temperature threshold at which the cooling system is activated. High cooling powers enable withdrawing a large amount of heat from the battery, even during worst-case operating conditions. Lower cooling powers, on the other hand, might be sufficient if high thermal losses occur rarely and are dampened by the battery's thermal inertia, enabling smaller, lighter, less noisy and cheaper cooling systems.

The cooling threshold is the temperature threshold at which the cooling system is activated. Low cooling thresholds ensure the battery is operated in its ideal temperature window, but result in an increased energy consumption because the cooling system is activated more frequently. Few studies investigated the impact of different cooling strategies.

Xie et al. [100] developed an Model Predictive Control (MPC)-based control strategy for a refrigerant cooling system. Their results show that battery aging could be maintained, while the cooling system energy consumption is reduced by 24.5 % compared to an on-off controller. These results were extrapolated from a 2 hour operating profile.

Pham et al. [101] presented a control strategy for a refrigerant cooling system in a hybrid-electric heavy-duty truck, that reduces the total fuel consumption by 1.8 % while maintaining a favorable battery temperature.

Although the optimization of the BTMS control was addressed in previous studies, battery aging was not considered or extrapolated from a short driving cycle. Furthermore, the impact of the installed cooling power has not been investigated.

2.3 Research gap

Section 2.1 showed that long-haul trucks are primed for electrification, while the studies discussed in Section 2.2 highlight that a holistic battery design method can reduce the system cost. However, a holistic method for the battery design of BET is still missing. The resulting research gap is illustrated in Figure 2.7. To fill this gap and advance the adoption of BET, I developed a battery design method for battery-electric trucks. Additionally, the method contributes to the state-of-the-art of cell selection, battery modeling, power profile generation, battery life simulation and BTMS design.

Although different cell selection methods exist in literature, none of them quantifies the impact of cell characteristics on system properties, most notably on the system cost. To bridge this gap, I developed a novel cell selection method and applied it to a BET application.

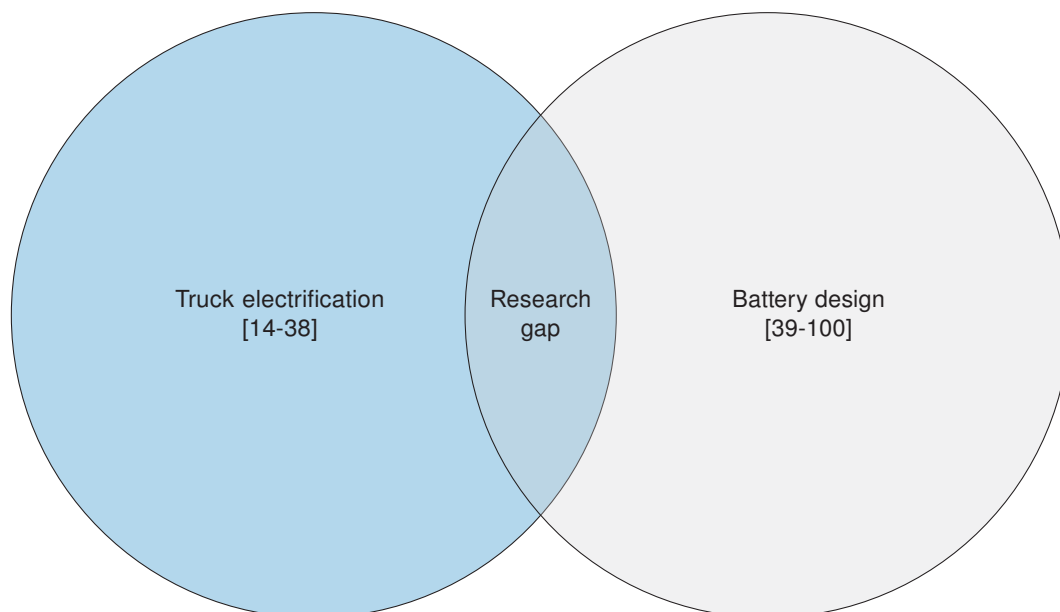


Figure 2.7: Research gap

Although previous studies presented parametrized and validated electric-thermal-aging models, they are not parametrized using a status-quo automotive grade cell, nor are they validated on vehicle level. Therefore, I conducted measurements and used the data that I co-published with Wassiliadis et al. [74] to parametrize an electric-thermal-aging model for the VW ID.3 cell and validated it on vehicle level.

Although previous studies developed power profiles for BET, they do not capture the dynamic behavior occurring during driving. To improve upon this, I extended the method presented by Gaete et al. [92] to generate a detailed power profile for BET.

Although previous studies presented battery life simulations under different operating conditions, all use simplifications to deal with the high computational load. To model the highly dynamic loads occurring during driving over the entire battery life without any simplifications, I implemented my battery simulation in a compiled programming language.

Finally, although previous studies presented optimization of the BTMS control strategy, they did not analyze battery aging for varying operating profiles and the impact of the installed cooling power has not been investigated. Therefore, I used my computationally efficient implementation of my validated electric-thermal-aging model to quantify the impact of different cooling thresholds and installed cooling powers on the battery life and safety.

3 Method & results

To design the battery for a long-haul BET, I developed the five-step method shown in Figure 3.1. The method can be used to define the top-level battery properties during the early-stage design phase.

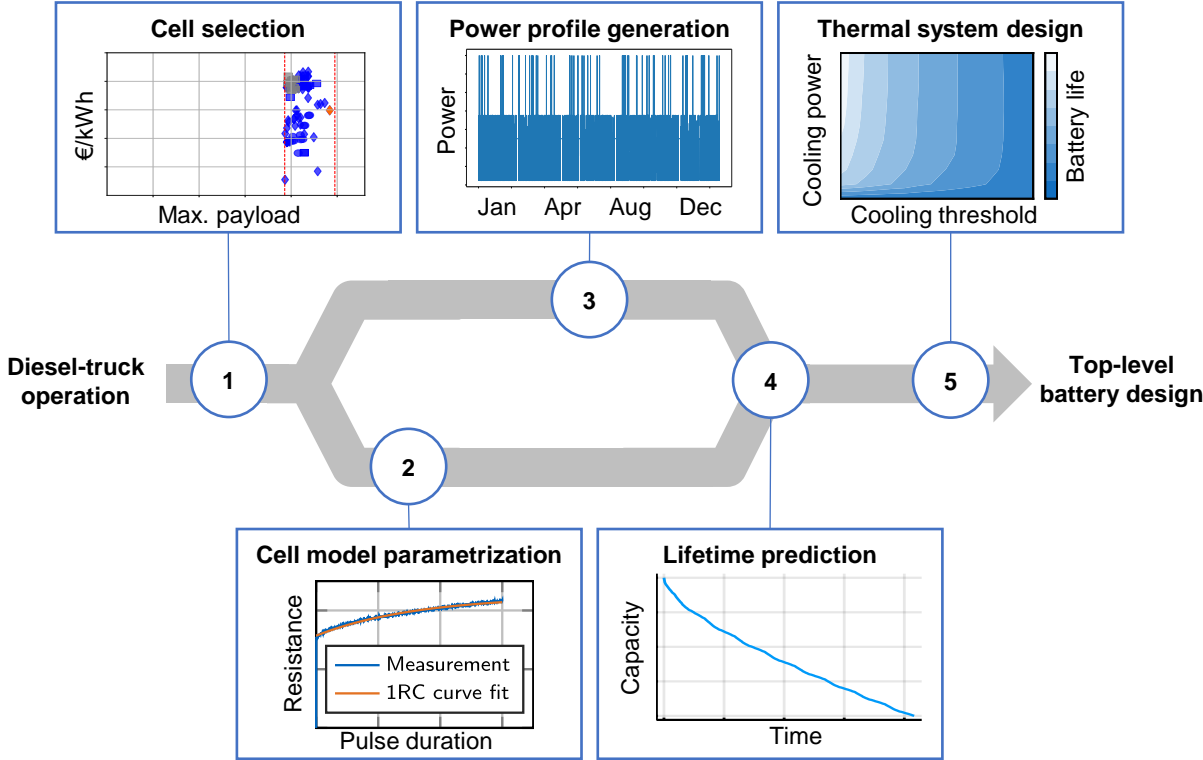


Figure 3.1: Overview of the battery design method. The results from the first step are used as an input to the second and third step, which then feed in to the fourth step. Finally, the fifth step uses the model from the fourth step to generate a top-level battery-design.

As an input, the method uses truck regulations, standardized truck driving cycles and real world DT operating data. The generated battery design is capable of mimicking DT operation, without any time loss.

In step 1, a battery cell is selected using the self-developed techno-economic cell selection method. Techno-economic cell selection uses datasheet values to determine the impact of cell characteristics on system properties. For a truck, these are the maximal payload that a BET would be able to transport, the volume that a battery would require onboard the vehicle, and the cell price that would result in cost parity with a DT. I implement the method to select a suitable cell from a database containing 160 unique cells.

Selecting a cell based on datasheet values enables the comparison of a wide range of cells, but leads to large simplifications in the estimation of the battery life. Therefore, in steps 2 to 5 of the method, a more detailed analysis is conducted for the selected cell.

In step 2, the selected cell is characterized to parametrize a combined electric, thermal, and aging model. Subsequently, the parametrized model is validated using over 100 hours of measurement data on vehicle level.

In step 3, a power profile is generated that describes the energy supply and demand resulting from driving and charging a BET. As an input, the battery size and mass that were determined in step 1 are combined with standardized truck driving cycles and truck mobility statistics, such as trip distance and trip duration. To obtain a representative power profile that includes both demanding long trips with high payload and days with multiple shorter trips, the power profile covers a long time period, in this case one year.

In step 4, the parametrized electric-thermal-aging model, including the thermal system design of the parametrized electric vehicle, is scaled to match the truck battery size and combined with the obtained power profile to predict the battery life under typical operating conditions. Additionally, safety is evaluated by analyzing the maximum cell temperature that is reached during operation.

Finally, in step 5, a parameter sensitivity analysis investigates the impact of the BTMS design on the battery life and battery safety. Specifically, the installed cooling power and the cooling threshold are analyzed.

The result of the five-step process is a top-level battery design for a battery-electric truck, defining:

- the battery cell,
- the price at which this cell must be purchased to reach cost parity with status quo DT,
- the required volume for the battery onboard the vehicle,
- the truck's payload capability,
- the battery life under typical truck operating conditions,
- and the impact of the cooling system design on the battery life and safety.

The method supports an iterative approach, where the price at which the selected cell must be purchased to reach cost parity can be updated based on the detailed simulation results. Additionally, an initial cell selection may be corrected based on discouraging results from the battery life simulation or safety assessment.

The full method including all models is made available open source and can be accessed at the following repository: <https://github.com/TUMFTM/TruckBatteryDesign>. In the following, each step of the method is presented in detail.

3.1 Step 1: cell selection

In the first step, a suitable cell for a long-haul BET is selected. I published the cell selection method as a first author in a previous publication [102]. In the following, I will summarize the previous publication, specify my contribution and provide the published manuscript. Subsequently,

additions to the publication are explained and the updated results are presented. Note that in the included previously published manuscript, the term "weight" is used instead of "mass", because it is more common in the truck industry.

3.1.1 Summary of the published cell selection method

The publication presents a method to find the most suitable cell for a battery-electric long-haul truck by quantifying the impact of cell characteristic on system level properties: the volume required for the battery onboard the vehicle, the maximum vehicle payload, and the price at which a cell must be purchased to reach cost parity with a status quo diesel truck, from hereon referred to as cost-parity price.

The method combines a vehicle simulation with a sizing algorithm and a cost model, as shown in Figure 3.2. First, a quasi-static longitudinal vehicle simulation is used to determine the vehicle's energy consumption at different vehicle masses. As inputs, the simulation uses vehicle characteristics of newly registered diesel trucks and the VECTO long-haul driving cycle [103], which is used by the European Union to simulate emissions of newly registered heavy-duty vehicles.

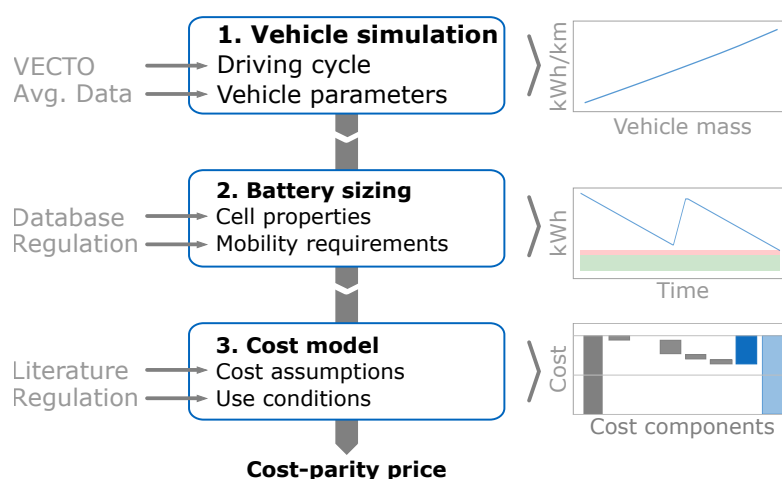


Figure 3.2: Schematic of the cell selection method [102]

Subsequently, a battery sizing algorithm determines the required battery size. The BET is required to cover the same operating pattern as a diesel truck. In Europe, truck drivers may drive up to 4.5 hours, after which they have to take a mandatory break of 45 minutes [104]. The 45-minute rest period may be replaced by a 15-minute break, followed by a 30-minute break, resulting in the same stop duration after 4.5 hours of driving [104]. The maximum daily driving time for a single driver is limited to ten hours [104]. Assuming that the stops can be used to recharge the BET, a nine-hour drive with a 45-minute stop duration is the most demanding scenario.

The required battery size is thus determined by the amount of energy that can be recharged during the rest period. This amount may be limited by the installed charging power or the maximum charging rate of a battery cell. The sizing algorithm oversizes the battery to account for the share of usable energy, and the End Of Life (EOL) condition of the battery. The resulting battery can power a fully loaded vehicle for the maximal legal driving duration during its entire operating life.

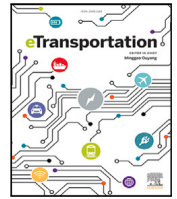
The battery sizing algorithm sizes the battery for all cells in a database containing 160 unique cells. The cell's are characterized based on the specification in their datasheet, such as energy density, specific energy, charging rate and cycle life. Based on each cell's characteristics, the sizing algorithm sizes the battery and determines the battery volume, battery mass, resulting maximum payload, and the battery lifetime.

Finally, the cost model determines the cost-parity price. For this purpose, the cost model considers all cost components that differ between a BET and DT: maintenance, taxes, tolls, energy costs, powertrain costs and the cost for the battery itself. The costs for maintenance, taxes, tolls, and the powertrain are independent of the selected cell. The energy costs are influenced by the battery size, which may depend on the cell's maximum charging rate, and its specific energy. The cost for the battery depends on the battery life, which is influenced by the determined battery size, the impact of the cell's specific energy on energy consumption, the cell's cycle life and the cell's calendar life. The cost-parity price for each cell is found using bisection.

The method was applied in two scenarios: trucks charged at 350 kW and trucks charged at 1 MW. The results showed that trucks charged at 350 kW require purchasing cells at a lower price ($\text{€ } 60 \text{ kWh}^{-1}$) to reach cost-parity with DT compared to trucks charged at 1 MW ($\text{€ } 100 \text{ kWh}^{-1}$). A parameter sensitivity analysis showed that the cell cycle life, cost of charging and vehicle energy consumption have the biggest impact on the cost-effectiveness of battery electric trucks. Note that the vehicle energy consumption can be reduced by optimizing the vehicle's drag area, rolling friction coefficient or powertrain efficiency.

3.1.2 Contributions

I initiated the idea of the paper, implemented the method, wrote the first draft of the manuscript and implemented all revisions. Steffen Link created the cell database and provided some of the cost-model parameters. Steffen Link, Jakob Schneider, Sebastian Wolff and Markus Lienkamp provided valuable feedback during the many iterations following the first draft.



Techno-economic cell selection for battery-electric long-haul trucks

Olaf Teichert^{a,*}, Steffen Link^b, Jakob Schneider^a, Sebastian Wolff^a, Markus Lienkamp^a

^a Technical University of Munich, School of Engineering & Design, Institute of Automotive Technology, 85748 Garching, Germany

^b Fraunhofer Institute for Systems and Innovation Research ISL, 76139 Karlsruhe, Germany

ARTICLE INFO

Keywords:

Techno-economic design
Battery cell selection
Lithium-ion
Battery-electric trucks

ABSTRACT

To reach cost-parity with diesel trucks, battery-electric trucks require fast-chargeable lithium-ion cells with a high energy density and cycle life, at a low specific cost. However, cells generally excel at only a fraction of these characteristics. To help select the optimal cell, we have developed the techno-economic cell selection method. The method determines the price per kilowatt-hour that is required to reach cost-parity with a diesel truck, based on the characteristics provided in a cell's datasheet. We demonstrate the method by selecting the optimal cell out of a database containing 160 cells for a long-haul truck operating with a single driver in Germany in two scenarios: charged at 350 kW and charged at 1 MW. The results show that for trucks charged at the current maximum charging power of 350 kW, the cell price needs to drop to ca. €60 kWh⁻¹ to reach cost-parity with a diesel truck. When 1 MW charging power is available, cost-parity can be reached at a cell price around €100 kWh⁻¹, which is within reach of optimistic cost estimates. However, the most cost-effective cells require more volume and result in a lower maximum payload than a diesel truck. A parameter sensitivity analysis shows that best-in-class cell energy density and packaging efficiency are required to match the payload capacity and powertrain volume of a diesel truck. The cell cycle life, cost of charging and vehicle energy consumption have the biggest impact on the cost-effectiveness of battery electric trucks.

1. Introduction

Heavy-duty vehicles generate a quarter of all green house gas emissions in the transport sector, meaning that they must be quickly decarbonized if climate targets are to be met [1]. One option for reducing emissions is the implementation of battery-electric trucks (BET), which has been the subject of a wide range of studies and reports [2]. Whether BETs become cost-competitive with diesel trucks (DT) depends on the vehicle-acquisition cost, fuel and electricity prices [3], available charging infrastructure [4], driving distance [5] and local policy [6]. Furthermore, the battery of a BET must be: light, to avoid any reductions in payload; small, to fit into the available volume on board the vehicle; fast-charging capable, to enable recharging during driver rest periods; resistant to aging, to avoid battery replacement during the service life; and low-cost to minimize investment costs. Previous studies have investigated the suitability of different cell technologies for BETs.

Sripad et al. [7] carried out Monte-Carlo simulations to determine the required battery capacity and resulting battery weight, battery cost, and maximum payload capacity, for status-quo lithium-ion cells and beyond-lithium-ion cells. Their results show that in order to achieve cost-competitiveness with DTs the improved performance of beyond-lithium-ion cells is required. However, these results might

be overly conservative because the authors did not consider en-route fast-charging.

Mareev et al. [8] determined the required battery capacity for long-haul truck operation in Germany incorporating battery charging during driver rest periods. Subsequently they conducted a life cycle cost analysis for a low-cost low-performance cell and a high-cost high-performance cell. Their results show that the life cycle costs are strongly influenced by the battery life, justifying the use of more expensive, but aging-resistant cells.

Çabukoglu et al. [9] investigated the feasibility of BETs in a case study in Switzerland, showing that the share of vehicle kilometers that can be electrified increases when the energy density of the batteries is increased.

Nykqvist and Olsson [10] modeled the feasibility of BETs that use high-power fast charging. Their results show that the battery properties strongly influence the cost-competitiveness of BETs and that battery life may be more important than the specific battery price.

Mauler et al. [11] compared the life cycle costs of a BET with lithium iron phosphate (LFP) cells, a BET with high-nickel cells and a hydrogen truck in the US, taking into account the profits foregone due to charging times and lower cargo capacity. Their results

* Corresponding author.

E-mail address: olaf.teichert@tum.de (O. Teichert).

Nomenclature

Vehicle simulation

a	Applied acceleration in m s^{-2}
a_{acc}	Acceleration limit in m s^{-2}
a_{dec}	Deceleration limit in m s^{-2}
a_{mot}	Max. acceleration achievable by motor in m s^{-2}
a_{target}	Target acceleration in m s^{-2}
b	Energy consumption in kWh km^{-1}
c_A	Drag area in m^2
c_{rr}	Coefficient of rolling resistance
$f_b(m)$	Interpolant: energy consumption vs. vehicle mass
$f_v(m)$	Interpolant: avg. speed vs. vehicle mass
F_{drag}	Drag resistance in N
F_{incl}	Inclination resistance in N
F_{res}	Total driving resistance in N
F_{roll}	Rolling resistance in N
g	Gravitational acceleration in m s^{-2}
j	Simulation step index
k	Driving cycle step index
k_{dec}	Index where a target speed reduction occurs
m	Vehicle mass in kg
P	Applied motor power in W
P_{aux}	Auxiliary power consumption in W
P_{bat}	Battery power in W
P_{mot}	Rated motor power in W
s	Distance along the route in m
t	Time in s
t_{stop}	Stop duration in s
v	Vehicle speed in m s^{-1}
v_{cycle}	Target speed defined by driving cycle in m s^{-1}
v_{target}	Target speed incl. deceleration phases in m s^{-1}
α	Slope in radians
Δs	Distance step length in m
η	Powertrain efficiency
ρ	Air density in kg m^{-3}

Battery sizing

b_{BET}	Typical BET energy consumption in kWh km^{-1}
E_{bat}	Required battery size in kWh
$E_{\text{crate-lim}}$	Required battery size for cell charging rate in kWh
E_{Plim}	Required battery size for charging power in kWh
E_{max}	Energy demand without fast charging in kWh
m_{bat}	Battery mass in kg

m_{gvw}	Gross vehicle weight in t
$m_{\text{payload,max}}$	Maximum payload in kg
m_{spec}	Cell specific energy in Wh kg^{-1}
$m_{\text{veh,nobat}}$	Vehicle mass without battery in t
n_{cycle}	Cell cycle life
s_{life}	Battery life in km
V_{bat}	Battery volume in L
z_{fc}	Share of fast chargeable energy
z_{EOL}	Share of energy at battery replacement
$z_{\text{m,c2s}}$	Gravimetric packaging efficiency
$z_{\text{v,c2s}}$	Volumetric packaging efficiency
ρ_{cell}	Cell energy density in Wh L^{-1}

Cost model

b_{DT}	Typical DT energy consumption in L km^{-1}
C_{bat}	Battery cost in €
$C_{\text{bat,inv}}$	Battery investment in €
$C_{\text{bat,scrap}}$	Battery scrappage value in €
$C_{\text{bat,res}}$	Battery residual value in €
$C_{\text{bat,imp}}$	Battery imputed interest in €
c_{diesel}	Diesel cost in € L^{-1}
c_{ene}	Specific energy cost in € km^{-1}
C_{ene}	Energy costs in €
c_{fc}	Cost of fast charging in € kWh^{-1}
c_{maint}	Specific maintenance cost in € km^{-1}
C_{maint}	Maintenance costs in €
C_{pt}	Powertrain cost in €
$C_{\text{pt,inv}}$	Powertrain investment in €
$C_{\text{pt,res}}$	Powertrain residual value in €
$C_{\text{pt,imp}}$	Powertrain imputed interest in €
c_{sc}	Cost of slow charging in € kWh^{-1}
c_{spec}	Cell specific cost in € kWh^{-1}
c_{tax}	Annual motor vehicle tax in € years^{-1}
C_{taxes}	Taxes in €
c_{toll}	Toll cost in € km^{-1}
C_{tolls}	Tolls in €
n_{repl}	Number of battery replacements
r	Discount rate
s_{annual}	Annual vehicle mileage in km
t_{own}	Ownership duration in years
$z_{\text{c,c2s}}$	Ratio between cell and system costs
$z_{\text{ene,fc}}$	Share of fast charged energy
z_{scr}	Ratio between investment and scrappage value
z_{SOH}	Share of remaining battery life
z_{toll}	Share of kilometers driven on toll roads

show that LFP batteries excel in volume-constrained transport on short routes, whereas high-nickel batteries have the advantage in weight-constrained transportation. Hydrogen trucks only become cost-competitive on routes that are long and weight-constrained.

Although these studies recognize the impact of the battery cell properties, a method for selecting the optimal cell is still missing. Other studies have developed methods for cell selection in general.

The most well-known decision aid for energy storage device selection is the Ragone plot presented by David Ragone in 1968 [12]. The Ragone plot maps energy density and power density to automotive driving requirements, such as top speed and range, enabling the selection of a suitable energy storage device. Since its introduction, the Ragone plot has been extended to include a wider variety of energy storage

technologies, such as supercapacitors or lithium-ion batteries, and has been applied in a wider range of applications [13].

More recently, Catenaro et al. [14] developed an enhanced Ragone plot that takes the operating temperature of the cell into account. Dechent et al. [15] proposed a further extension of the Ragone plot, called ENPOLITE, which visualizes the energy, power, lifetime and temperature of energy storage technologies in a single figure.

Although these cell selection methods visualize the characteristics of a wide range of energy storage technologies, they do not quantify the impact of the cell selection on the system costs. On the other hand, life cycle cost studies only compare a small number of cell technologies and do not provide a tool for selecting the best cell from a database.

To bridge this gap, we have developed the techno-economic cell selection method for BETs to support selecting the optimal individual cell. The method uses the characteristics specified in a cell's datasheet to determine the price per kWh required to reach cost-parity with a DT, in the following referred to as the cost-parity price. We demonstrate the method by selecting the optimal cell from a database containing 160 cells for a long-haul BET operating with a single driver in Germany.

The contributions of this study can be summarized as follows:

- a novel cell selection method that incorporates the trade-off between cell cost and performance;
- results showing the cost-competitiveness of different cell chemistries and cell formats for a BET application;
- a parameter sensitivity analysis quantifies the impact of cell, pack, and system characteristics.

The method serves as a decision making aid for battery designers at truck manufacturing companies. Furthermore, the method can be used by cell manufacturers to optimize their cell design. The method and the developed cell database are available open source and can be accessed at the following repository: <https://github.com/TUMFTM/TechnoEconomicCellSelection>.

2. Method

To determine the cost-parity price for a single cell, we combine a vehicle simulation with a battery sizing algorithm and a cost model, as illustrated in Fig. 1. First, the vehicle simulation determines the energy consumption and average speed for a range of vehicle masses, based on the vehicle parameters and a driving cycle. The results are used to create interpolation functions between vehicle mass on the one hand, and energy consumption and average speed on the other. Second, the battery sizing algorithm determines the required battery size subject to the results from the vehicle simulation, cell properties and mobility requirements. The volume, weight, maximum payload, typical energy consumption and battery life are calculated for the determined battery size. Third, based on the results from the battery sizing algorithm and cost & operating conditions, the cost model determines the cost-parity price, using bisection to minimize the cost difference between a BET and a DT.

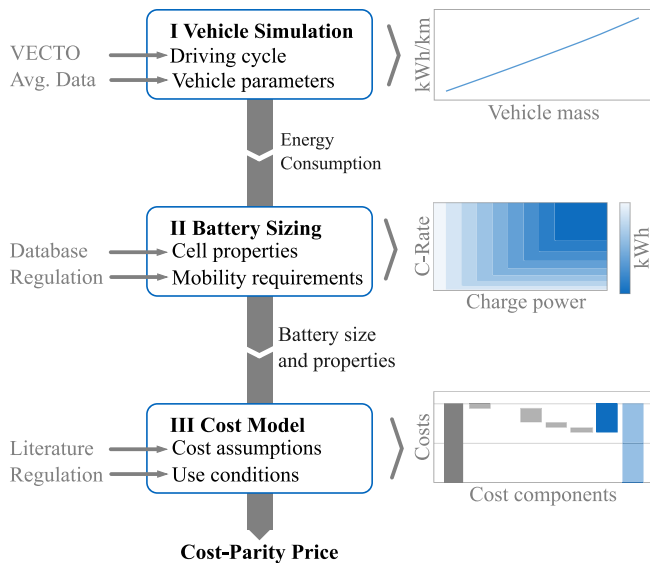


Fig. 1. Schematic representation of the techno-economic cell selection for BET, which combines a vehicle simulation with a battery sizing algorithm and a cost model.

2.1. Vehicle simulation

The vehicle model simulates a vehicle's speed and energy consumption using a quasi-static distance-based longitudinal-dynamics model, based on the vehicle characteristics and the VECTO long-haul driving cycle [16]. The driving cycle defines the target speed, road gradient and duration of stops along a route, as shown in Fig. 2.

The driving cycle does not prescribe braking or acceleration behavior because these are strongly influenced by the vehicle characteristics. The acceleration and braking behavior are therefore determined by the simulation. We simulate braking behavior by adding constant deceleration phases in front of distance steps at which a reduction of the target speed occurs, in accordance with Eq. (1), where $v_{target,k}$ denotes the modified target speed at a distance step with index k , v_{cycle} is the driving cycle target speed, k_{dec} is the distance step index at which the target speed reduction occurs, a_{dec} is the deceleration, and s_k is the distance along the route. Fig. 3 illustrates the addition of a deceleration phase.

$$v_{target,k} = \sqrt{v_{cycle,k=k_{dec}}^2 + 2 a_{dec} (s_{k=k_{dec}} - s_k)} \quad (1)$$

The acceleration behavior and energy consumption of the truck are then simulated in a forward simulation. The simulation uses a different step index, denoted j , because two time-values occur for a single distance-value during a stop. The start conditions are given by Eq. (2), where t denotes the time and v the vehicle speed.

$$\begin{aligned} s_{j=1} &= 0 \\ t_{j=1} &= 0 \\ v_{j=1} &= 0 \end{aligned} \quad (2)$$

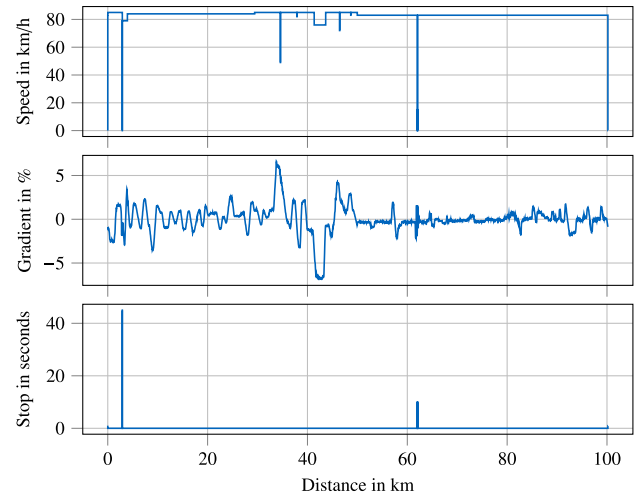


Fig. 2. The VECTO long-haul driving cycle is one of a range of driving cycles that was developed by the European commission to determine the CO₂ emissions from heavy-duty vehicles and represents the typical operation of a long-haul truck [16].

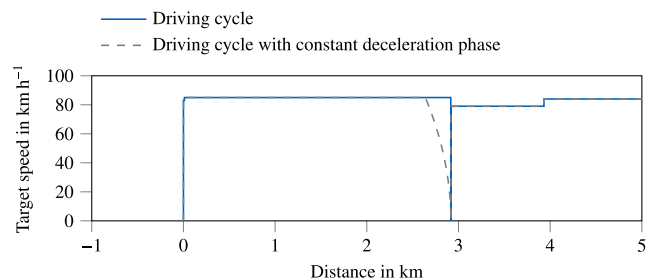


Fig. 3. Illustration of an added constant deceleration phase.

For every distance step, we first check if the vehicle is stopped. If it is, an additional data point is added according to Eq. (3), where t_{stop} denotes the stop duration and P the applied motor power.

$$\left. \begin{array}{l} s_{j+1} = s_j \\ t_{j+1} = t_j + t_{\text{stop},k} \\ v_{j+1} = 0 \\ P_j = 0 \\ j = j + 1 \end{array} \right\} \text{if } t_{\text{stop},k} > 0 \quad (3)$$

Subsequently, the driving resistances are calculated using Eqs. (4)–(6), where m denotes the vehicle mass, g the gravitational acceleration, c_{rr} the rolling resistance coefficient, α the slope, ρ the density of air, and c_A the drag area.

$$F_{\text{roll},j} = m g c_{\text{rr}} \cos(\alpha_k) \quad (4)$$

$$F_{\text{drag},j} = 0.5 \rho c_A v_j^2 \quad (5)$$

$$F_{\text{incl},j} = m g \sin(\alpha_k) \quad (6)$$

Then we calculate the acceleration required to reach the target speed, a_{target} , and the maximum acceleration that can be achieved by the motor, a_{mot} , using Eqs. (7) and (8), respectively, where Δs denotes the distance step length, P_{mot} the rated motor power, and η the overall powertrain efficiency,

$$a_{\text{target},j} = \frac{v_{\text{target},k+1}^2 - v_j^2}{2 \Delta s} \quad (7)$$

$$a_{\text{mot},j} = \frac{1}{m} \left(\frac{P_{\text{mot}} \eta}{v_j} - F_{\text{roll},j} - F_{\text{incl},j} - F_{\text{drag},j} \right) \quad (8)$$

The applied acceleration is the minimum of the target acceleration, motor-limited acceleration and an absolute acceleration limit, $a_{\text{acc,max}}$, as shown in Eq. (9).

$$a_j = \min(a_{\text{target},j}, a_{\text{mot},j}, a_{\text{acc,max}}) \quad (9)$$

Based on the applied acceleration, the new vehicle speed, time, and applied power are calculated using Eq. (10)–(14).

$$v_{j+1} = \sqrt{v_j^2 + 2 a_j \Delta s} \quad (10)$$

$$t_{j+1} = t_j + \frac{2 \Delta s}{v_j + v_{j+1}} \quad (11)$$

$$s_{j+1} = s_j + \Delta s \quad (12)$$

$$F_{\text{res},j} = m a_j + F_{\text{roll},j} + F_{\text{drag},j} + F_{\text{incl},j} \quad (13)$$

$$P_j = F_{\text{res},j} v_j \eta^{-\text{sgn}(F_{\text{res},j})} \quad (14)$$

Finally, we calculate the power drawn from or supplied to the battery using Eq. (15), where we assume that negative powers up to the rated motor power are recuperated and the remaining power is converted into heat by the mechanical brakes.

$$P_{\text{bat},j} = \max(P_j, -P_{\text{mot}}) \quad (15)$$

Eq. (3) to (15) are repeated for every distance step in the driving cycle. The energy consumption per kilometer can then be calculated using Eq. (16), where P_{aux} denotes the energy consumption of auxiliary loads and n is the number of simulation steps. The constant corresponds to the conversion from kJ km^{-1} to kWh km^{-1} .

$$b = \frac{1}{3600 s_{j=n}} \left(P_{\text{aux}} t_{j=n} + \sum_{j=1}^{j=n-1} P_{\text{bat},j} (t_{j+1} - t_j) \right) \quad (16)$$

The average vehicle speed v_{avg} is calculated using Eq. (17), where the constant corresponds to the conversion from m s^{-1} to km h^{-1} .

$$v_{\text{avg}} = 3.6 \frac{s_{j=n}}{t_{j=n}} \quad (17)$$

The vehicle simulation is executed for a range of vehicle weights to generate the linear interpolation functions $f_b(m)$ and $f_v(m)$ for energy consumption and average speed, respectively.

2.2. Battery sizing model

The battery sizing algorithm determines the required battery size subject to the results from the vehicle simulation, cell properties and mobility requirements. The BET mimics the operation of a DT without any additional time loss.

In Europe, truck drivers are prohibited to drive for more than 4.5 h at a time and are then required to take a 45 minute break before continuing [17]. The 45 minute break may be replaced by a break of at least 15 minutes followed by a break of at least 30 min, which would result in the same rest duration after 4.5 h of driving. We assume that these rest periods can be used to recharge the BET. The daily driving time is limited to 10 h [17]. For a 10-hour drive, the battery can be recharged before the last hour of driving, which makes a 9-hour drive with a 45 minute break the most demanding single-driver scenario in Europe.

The maximum energy demand for driving nine hours, E_{max} is given by Eq. (18), where m_{gvw} is the gross vehicle weight, i.e. the maximum combined operating weight of the truck, trailer and payload.

$$E_{\text{max}} = 9 f_b(m_{\text{gvw}}) f_v(m_{\text{gvw}}) \quad (18)$$

The battery size that is required to complete a day of driving depends on the amount of energy that can be recharged during the rest period, as illustrated in Appendix A. The amount of energy that can be recharged during the rest period may be limited by the installed charging power, given by Eq. (19), or the cell's charging rate, given by Eq. (20). P_{fc} denotes the installed charging power, t_{fc} the time available for charging, z_{EOL} the share of remaining energy at battery replacement, z_{usable} the share of usable energy, C_{cell} the cell's charging rate, and z_{fc} the share of the battery that can be recharged using fast charging. The required battery size is simply the maximum of both constraints, Eq. (21). Note that the resulting battery can power a fully loaded vehicle for the maximal legal driving duration during its entire operating life.

$$E_{\text{p-lim}} = E_{\text{max}} - P_{\text{fc}} t_{\text{fc}} \quad (19)$$

$$E_{\text{crate-lim}} = \frac{E_{\text{max}}}{1 + \min\left(\frac{C_{\text{cell}} t_{\text{fc}}}{z_{\text{EOL}} z_{\text{usable}}}, z_{\text{fc}}\right)} \quad (20)$$

$$E_{\text{bat}} = \frac{\max(E_{\text{crate-lim}}, E_{\text{p-lim}})}{z_{\text{EOL}} z_{\text{usable}}} \quad (21)$$

Based on the determined battery size, the battery volume, V_{bat} , battery weight, m_{bat} , and the resulting maximum payload, $m_{\text{payload,max}}$, can be calculated using Eq. (22)–(24), where ρ_{cell} and m_{spec} denote a cell's energy density and specific energy, $z_{\text{m,c2s}}$ and $z_{\text{v,c2s}}$ the gravimetric and volumetric packaging efficiency, and $m_{\text{veh,nobat}}$ the weight of the vehicle without the battery.

$$V_{\text{bat}} = \frac{E_{\text{bat}}}{\rho_{\text{cell}} z_{\text{v,c2s}}} \quad (22)$$

$$m_{\text{bat}} = \frac{E_{\text{bat}}}{m_{\text{spec}} z_{\text{m,c2s}}} \quad (23)$$

$$m_{\text{payload,max}} = m_{\text{gvw}} - m_{\text{veh,nobat}} - m_{\text{bat}} \quad (24)$$

Eq. (25) then calculates the typical energy consumption, b_{BET} , under the loading conditions that are used by the European Commission to estimate the CO_2 emissions during long-haul operation of a newly registered truck. These correspond to a low load of 2.6 t over 30 % of the trip distance and a reference load of 19.3 t over the remaining 70 % [18]. A cell resulting in a maximum payload below the reference load is considered unfeasible for a long-haul BET.

$$b_{\text{BET}} = 0.3 f_{\text{con}} (m_{\text{bat}} + m_{\text{veh,nobat}} + 2600) + 0.7 f_{\text{con}} (m_{\text{bat}} + m_{\text{veh,nobat}} + 19300) \quad (25)$$

Finally, the battery life in kilometers, s_{life} , is calculated using Eq. (26), where n_{cycle} denotes the cell's cycle life.

$$s_{\text{life}} = \frac{E_{\text{bat}} n_{\text{cycle}}}{b_{\text{BET}}} \quad (26)$$

2.3. Cost model

To determine cost-parity, the cost model only needs to consider the cost components that differ between a BET and a DT. To determine these cost-components, a cost breakdown of a long-haul truck was analyzed, shown in Table 1. Converting a DT to a BET affects the cost of the powertrain (motor and transmission) and battery, but is assumed not to influence the cost of other vehicle components. Additionally, the conversion influences the maintenance costs, cost of energy, taxes and tolls. The costs for insurance and the driver are assumed to be unaffected because the vehicle operation remains unchanged. BET subsidies are not considered.

The sum of cost components that differ between a BET and a DT is referred to as the relevant cost of ownership (RCO) and is given by Eq. (27), where C_{maint} denotes the maintenance costs, C_{ene} the cost for energy consumption, C_{taxes} taxes, C_{tolls} tolls, C_{pt} the powertrain costs, and C_{bat} the battery costs. To account for both operating costs and investment costs, all costs are expressed by their net present value.

$$\text{RCO} = C_{\text{maint}} + C_{\text{ene}} + C_{\text{taxes}} + C_{\text{tolls}} + C_{\text{pt}} + C_{\text{bat}} \quad (27)$$

We assume that taxes are due annually, maintenance costs are incurred twice a year, and toll and energy are paid weekly. The corresponding net present value is then calculated using Eq. (28) to (31), where t_{own} denotes the ownership duration in years, r the discount rate, c_{tax} the annual motor vehicle tax, s_{annual} the annual vehicle mileage, c_{maint} the specific maintenance cost per kilometer, z_{toll} the share of kilometers driven on toll roads, c_{toll} the toll costs per kilometer, and c_{ene} the cost of energy per kilometer. The cost of energy for diesel trucks simply corresponds to the product of the DT consumption, b_{DT} , and the cost of diesel per liter, c_{diesel} . The cost of energy for the BET is the product of the typical BET consumption, b_{BET} , and the cost of charging, which differentiates between slow charging overnight, c_{sc} , and fast charging, c_{fc} , where $z_{\text{ene,fc}}$ denotes the share of fast charged energy. To avoid any bias from forecasts, we assume that the electricity costs and diesel costs are constant throughout the ownership duration.

$$C_{\text{taxes}} = \sum_{n=1}^{n=t_{\text{own}}} c_{\text{tax}} r^{-n} \quad (28)$$

$$C_{\text{maint}} = \sum_{n=0}^{n=2 \times t_{\text{own}} - 1} \frac{1}{2} s_{\text{annual}} c_{\text{maint}} r^{-n/2} \quad (29)$$

$$C_{\text{toll}} = \sum_{n=0}^{n=52 \times t_{\text{own}} - 1} \frac{1}{52} s_{\text{annual}} z_{\text{toll}} c_{\text{toll}} r^{-n/52} \quad (30)$$

$$C_{\text{ene}} = \sum_{n=0}^{n=52 \times t_{\text{own}} - 1} \frac{1}{52} s_{\text{annual}} c_{\text{ene}} r^{-n/52} \quad (31)$$

$$\text{where } c_{\text{ene}} = \begin{cases} b_{\text{DT}} c_{\text{diesel}} & \text{for DT} \\ b_{\text{BET}} (c_{\text{fc}} z_{\text{ene,fc}} + c_{\text{sc}} (1 - z_{\text{ene,fc}})) & \text{for BET} \end{cases}$$

The powertrain costs include the initial investment, $c_{\text{pt,inv}}$, the resale value at the end of ownership, $c_{\text{pt,res}}$, and the imputed interest, $c_{\text{pt,imp}}$,

given by (32). The resale value is calculated by Eq. (33), where the first term in the equation describes the relation between the resale value and the vehicle mileage that was determined for a semi-trailer truck by Kleiner and Friedrich [19]. The imputed interest describes the interest that could have been earned by the bound investment and is given by Eq. (34).

$$C_{\text{pt}} = C_{\text{pt,inv}} - C_{\text{pt,res}} + C_{\text{pt,imp}} \quad (32)$$

$$C_{\text{pt,res}} = (0.951 \exp(\frac{-t_{\text{own}} s_{\text{annual}}}{500000})) C_{\text{pt,inv}} r^{-t_{\text{own}}} \quad (33)$$

$$C_{\text{pt,imp}} = \frac{C_{\text{pt,inv}} + C_{\text{pt,res}}}{2} (r^{t_{\text{own}}} - 1) \quad (34)$$

The RCO of diesel trucks does not include any battery costs. For the BET, the costs for the battery consist of the sum of all investments, $C_{\text{bat,inv}}$, the scrappage value of all replaced batteries (e.g. for use in second-life applications), $C_{\text{bat,scrap}}$, the resale value at the end of ownership $C_{\text{bat,res}}$ and the imputed interest, $C_{\text{bat,imp}}$, as given in Eq. (35).

$$C_{\text{bat}} = \sum C_{\text{bat,inv},n} - \sum C_{\text{bat,scrap},n} - C_{\text{bat,res}} + C_{\text{bat,imp}} \quad (35)$$

The investment costs are given by Eq. (36), where c_{spec} denotes the specific battery costs and $z_{\text{c,c2s}}$ the ratio between costs at the cell and system level. The number of required replacements, n_{repl} , is given by Eq. (37).

$$C_{\text{bat,inv},n} = c_{\text{spec}} z_{\text{c,c2s}} E_{\text{bat}} r^{-\frac{n s_{\text{life}}}{s_{\text{annual}}}} \quad \forall n \in [0, \dots, n_{\text{repl}}] \quad (36)$$

$$n_{\text{repl}} = \lfloor t_{\text{own}} s_{\text{annual}} / s_{\text{life}} \rfloor \quad (37)$$

The value for second-use applications is calculated with Eq. (38), where z_{scr} denotes the share of remaining value at scrappage.

$$C_{\text{bat,scrap},n} = z_{\text{scr}} c_{\text{spec}} z_{\text{c,c2s}} E_{\text{bat}} r^{-\frac{n s_{\text{life}}}{s_{\text{annual}}}} \quad \forall n \in [1, \dots, n_{\text{repl}}] \quad (38)$$

The resale value of the battery at the end of ownership is assumed to be proportional to the remaining battery life as given by Eq. (39), where the remaining battery life, z_{SOH} , is calculated from Eq. (40). Finally, the imputed interest is given by Eq. (41).

$$C_{\text{bat,res}} = (z_{\text{scr}} + (1 - z_{\text{scr}}) z_{\text{SOH}}) c_{\text{spec}} z_{\text{c,c2s}} E_{\text{bat}} r^{-t_{\text{own}}} \quad (39)$$

$$z_{\text{SOH}} = n_{\text{repl}} + 1 - t_{\text{own}} s_{\text{annual}} / s_{\text{life}} \quad (40)$$

$$C_{\text{bat,imp}} = \sum_{n=0}^{n=n_{\text{repl}}-1} \frac{C_{\text{bat,inv},n} + C_{\text{bat,scrap},n}}{2} (r^{s_{\text{life}}/s_{\text{annual}}} - 1) + \frac{C_{\text{bat,inv},n_{\text{repl}}} + C_{\text{bat,res}}}{2} (r^{(t_{\text{own}} - \frac{n_{\text{repl}} s_{\text{life}}}{s_{\text{annual}}})} - 1) \quad (41)$$

The cost-parity price is found by using bisection to minimize the difference between the RCO of a DT and a BET.

3. Implementation

The method is demonstrated by selecting the optimal cell for a BET out of a database containing 160 unique cells. To highlight the impact of the available installed charging power, we evaluated two scenarios. In the first scenario, trucks are charged during the rest period using a 350 kW charger, which corresponds to the maximum currently available charging power under the CCS-standard [32]. In the second scenario, the trucks are charged using a 1 MW charger, which would be possible under the MCS-standard that is currently being developed for commercial vehicles and expected to be available within the next years [33]. In the following, we first present the parameters that define the use case and subsequently show the characteristics of the cells in our database.

Table 1
Analysis of cost components that differ between a BET and a DT.

Cost component	Differs between BET & DT
Powertrain	Yes
Battery	Yes
Vehicle w/o powertrain	No
Maintenance	Yes
Energy (electricity/fuel)	Yes
Taxes	Yes
Tolls	Yes
Insurance	No
Driver	No

Table 2
Use case parameters for a BET operating in Germany.

Model	Parameter	Symbol	Value	Comments & sources	
Vehicle simulation	Drag area	c_A	5.68 m ²	DT Average, see Appendix B	
	Rolling resistance coefficient	c_{rr}	5.48 ‰	DT Average, see Appendix B	
	Engine motor power	P_{mot}	352.4 kW	DT Average, see Appendix B	
	Auxiliary power consumption	P_{aux}	2.3 kW	[20] Standard trailer w/o additional auxiliaries	
	Powertrain efficiency	η	85 %	[21]	
	Maximum acceleration	a_{max}	1 m s ⁻²	[16]	
	Deceleration	a_{dec}	1 m s ⁻²	[16]	
	Gravitational acceleration	g	9.81 m s ⁻²	[16]	
	Air density	ρ	1.188 kg m ⁻³	[16]	
	Sizing algorithm	Charging time	t_{fc}	40 min	Mandatory break period minus 5 min [17]
Share of usable energy		z_{usable}	93 %	[22]	
Share of fast chargeable energy		z_{fc}	80 %	[10]	
Gross vehicle weight		m_{gvw}	42 t	[23]	
Vehicle weight without battery		$m_{veh,nobat}$	13.8 t	See Appendix C	
Volumetric packaging efficiency		$z_{v,c2s}$	Cylindrical	29.5 %	Electric vehicle average [24]
			Pouch/Prismatic	35.3 %	Electric vehicle average [24]
Gravimetric packaging efficiency		$z_{m,c2s}$	Cylindrical	55.2 %	Electric vehicle average [24]
	Pouch/Prismatic		57.5 %	Electric vehicle average [24]	
Cost model	Service life	t_{own}	5 years	[2]	
	Annual mileage	s_{annual}	116 000 km	[18]	
	Discount rate	r	1.095	[2]	
	Diesel fuel cost	c_{diesel}	€1.36 L ⁻¹	Average in Germany on the 1st of Jan 2022, excluding VAT	
	DT consumption	b_{DT}	0.301 L km ⁻¹	DT average, see Appendix B	
	Battery scrappage	z_{scr}	15 %	[25]	
	Cost scaling cell to system	$z_{c,c2s}$	2.07	Electric vehicle average [26]	
	Share of toll kilometers	z_{toll}	92 %	[27]	
	Share of fast charged energy	$z_{ene,fc}$	20 %	[2]	
	Slow charging cost	c_{sc}	350 kW	€0.25 kWh ⁻¹	See Appendix C
			1 MW	€0.29 kWh ⁻¹	For a 350 kW charger in Germany on the 1st of Jan 2022, excluding VAT [28]
	Fast charging cost	c_{fc}	1 MW	€0.37 kWh ⁻¹	Limit announced by the German government [29], excluding VAT
			DT	€0.147 km ⁻¹	[19]
	Maintenance costs	c_{maint}	BET	€0.098 km ⁻¹	[19]
			DT	€0.182 km ⁻¹	[30]
	Toll costs	c_{toll}	BET	€0 km ⁻¹	[30]
			DT	€556 years ⁻¹	[31]
	Taxes	c_{tax}	BET	€278 years ⁻¹	[31]
			DT	€48 712	See Appendix C
	Powertrain costs	c_{pt}	BET	€34 232.51	See Appendix C

3.1. Use case

The parameters that define the use case are summarized in [Table 2](#). To realistically model the vehicle characteristics, we used data reported for newly registered heavy-duty vehicles between the 1st of January 2019 and the 30th June 2020. The analysis of the reported data and deduction of average values for a DT can be found in [Appendix B](#). The BET was assumed to have the average drag area, tire rolling coefficient and rated engine power of the registered DTs. For the volumetric and gravimetric packaging efficiency we differentiated between cylindrical and pouch/prismatic cells. The time available for charging was assumed to be 5 min shorter than the legally required break period to account for the time it takes to connect to and disconnect from the charger. The DT fuel consumption corresponds to the reported fuel consumption at the same payload split used to determine the typical BET energy consumption. The costs for charging at 350 kW correspond to the cheapest rate in Germany [28] excl. VAT. The cost for charging at 1 MW is the upper limit for the charging cost announced by the German government [29], excl. VAT. The detailed calculations of the vehicle weight excluding the battery, the cost of slow charging and the powertrain component costs can be found in [Appendix C](#).

3.2. Cell database

To calculate the cost-parity price, the following cell properties need to be known: energy density, specific energy, charging rate, cycle life

and corresponding EOL condition. We collected these properties from publicly available cell data sheets resulting in a database containing 160 unique cells.

Since the charging rate has a large impact on the cycle life and our use case requires frequent fast charging, we used the cell charging rate at which the cycle life was specified. If the cycle life at multiple EOL conditions or charging rates was specified, we determined the cost-parity price for each configuration. Additionally, we characterized the cells according to their format and chemistry. Since the cell chemistry was mostly not specified on the data sheet, we differentiated only based on the nominal voltage: below 3 V as lithium-titanium-oxide (LTO) cells, between 3 V and 3.4 V as LFP cells, and above 3.4 V as other cell chemistries.

[Fig. 4](#) shows the characteristics of the 160 cells in our database. The LTO cells have the lowest specific energy and energy density, followed by the LFP cells. The highest specific energy and energy densities are reached by pouch cells with a nominal voltage above 3.4 V, corresponding to 393 Wh kg⁻¹ and 1047 Wh L⁻¹. The majority of cell datasheets limit charging to 1 h⁻¹ or lower. The highest charging rate is provided by an LTO cell, that allows charging at 4 h⁻¹. The longest cycle life is achieved by LTO cells, followed by the LFP cells. The cylindrical cells have a shorter cycle life on average.

4. Results

The cells in our database that reach the highest cost-parity price, meaning they can be purchased at the highest price to reach cost-parity,

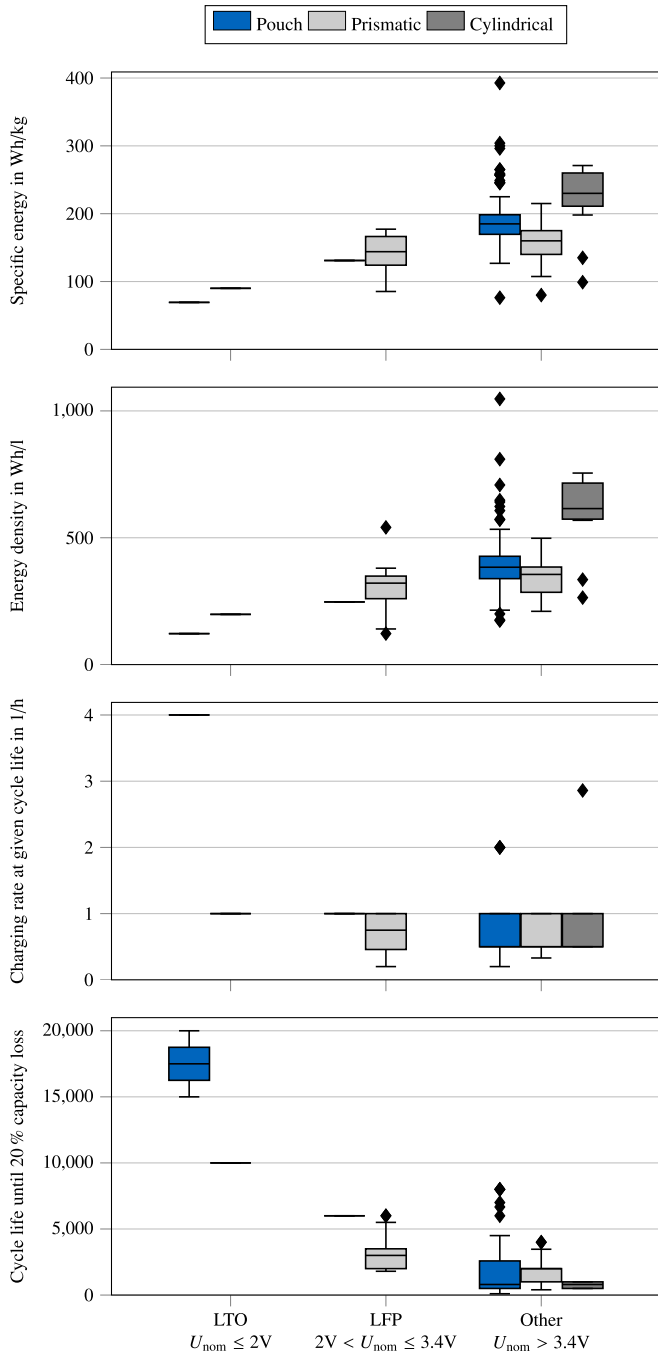


Fig. 4. Specific energy, energy density, charging rate and cycle life of the cells in our database. For the visualization, cycle life specified to different end-of-life conditions was converted to 80% of initial capacity using cross-multiplication. In all further calculations, the specified cycle life and end-of-life condition are used.

are the LG E78 in the 350kW scenario and the Leclanché GL65 in the 1 MW scenario. In the following we will refer to these cells as reference cell 1 and 2. The reference cell properties and results from the method are summarized in Table 3.

In the following, we first illustrate the implementation of the vehicle simulation, sizing algorithm and cost model for reference cell 2 in the 1 MW charging scenario. Subsequently, the cost-parity price of all cells in our database is shown for both charging scenarios. Finally a parameter sensitivity analysis shows the impact of cell, pack, and system parameters.

Table 3

Reference cell properties and results for both charging scenarios.

Scenario	350 kW charging	1 MW charging
Capacity	78 Ah	65 Ah
Nominal voltage	3.6 V	3.72 V
Format	Pouch	Pouch
Specific energy	265 Wh kg ⁻¹	216 Wh kg ⁻¹
Energy density	623 Wh L ⁻¹	395 Wh L ⁻¹
Cycle life	1500	7000
EOL	0.8	0.8
Charging rate	0.33 h ⁻¹	1 h ⁻¹
Battery size	1111 kWh	792 kWh
Battery volume	5051 L	5681 L
Battery mass	7293 kg	6377 kg
Max. Payload	20.9 t	21.9 t
Typical energy consumption	1.34 kWh km ⁻¹	1.32 kWh km ⁻¹
Battery life	1.2 × 10 ⁶ km	4.2 × 10 ⁶ km
Cost-parity price	€63.12 kWh ⁻¹	€96.57 kWh ⁻¹

4.1. Method implementation for a single cell

Fig. 5(a) shows the result of the vehicle simulation, which is independent of the cell selection. The BET energy consumption was simulated for a range of vehicle masses, ranging from the mass of an empty vehicle excluding the battery weight up to the gross vehicle weight. Energy consumption increases with vehicle weight. The energy consumption of a fully loaded vehicle of 1.49 kWh km⁻¹ matches the results from previous studies well [2,3,21,34].

Fig. 5(b) shows the battery sizing for different installed charging powers and cell charging rates. Increasing the charging rate or installed charging power reduces the required battery size because more energy can be recharged during the driver rest period. Installed charging powers above 707 kW or charging rates above 0.9 h⁻¹ do not result in a further decrease of the required battery size because the battery size is limited by the energy consumption during a single leg of the trip and the share of fast-chargeable energy. The required battery size for reference cell 2 in the 1 MW charging scenario is 792 kWh.

The cost model components for the DT and BET and their differences are shown in Fig. 5(c). To reach cost-parity, the battery costs can be compensated by the lower costs of the BET in the other cost components. The costs of the powertrain, taxes, toll and maintenance are independent of the cell properties. The BET energy consumption costs depend on the battery sizing and the cell's specific mass. The battery costs are influenced by the battery sizing, cell cycle life and the cell specific cost. The cell specific cost at which cost-parity is reached, i.e. the cost-parity price, is determined using bisection. A BET using reference cell 2 in the 1 MW charging scenario would reach cost-parity with a DT if the cell can be purchased at €96.57 kWh⁻¹.

4.2. Comparison of the cells in our database

Fig. 6 shows the cost-parity price for all cells in our database versus the maximum payload and battery volume in both scenarios. The cell chemistry and format are indicated by the marker color and shape respectively. Additionally, for each scenario the reference cell is highlighted, and the reference load, maximum payload of a DT and powertrain volume of a DT are indicated.

The cost parity-price could be determined for more cells in the 1 MW charging scenario because the higher available charging power means the operating requirements can be fulfilled with a smaller battery, allowing cells with a lower specific energy to transport the reference load without exceeding the maximum payload. For the same reason, the use of reference cell 2 and LFP cells is infeasible in the 350 kW charging scenario and LTO cells cannot be used in either scenario. The smaller battery size in the 1 MW charging scenario also results in a higher cost-parity price.

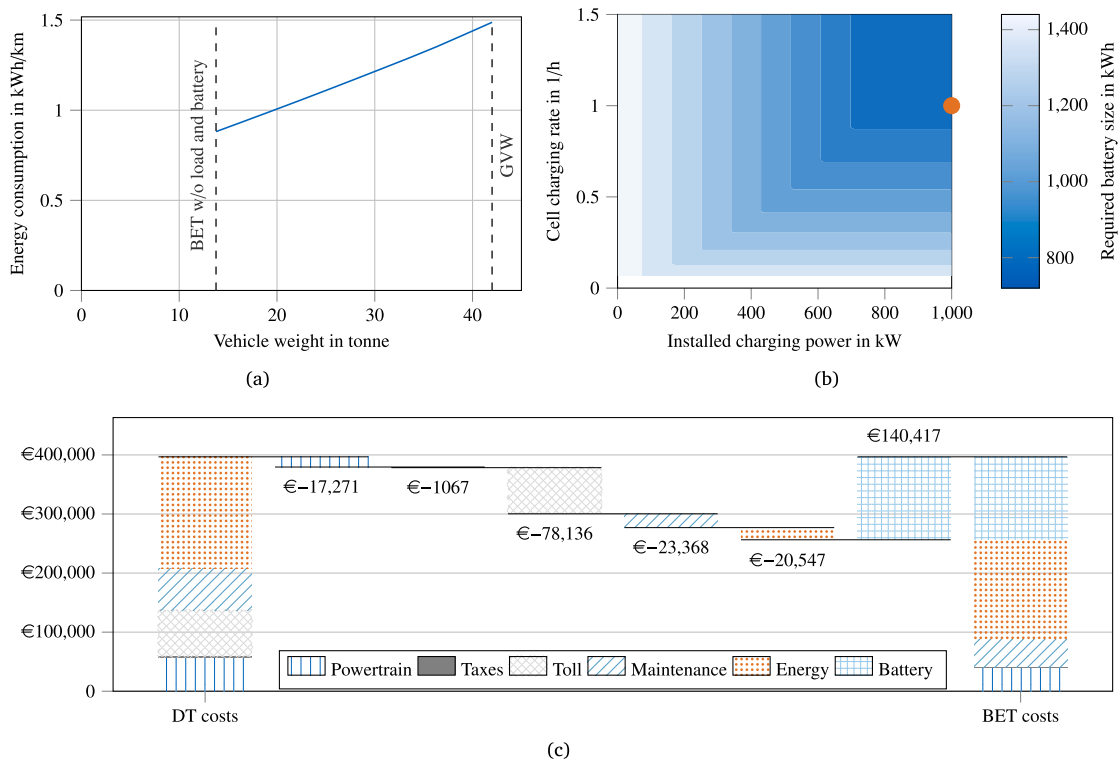


Fig. 5. Illustration of the method steps for the reference cell in the 1 MW charging scenario: (a) Vehicle energy consumption for a range of vehicle masses determined by the vehicle simulation; (b) Impact of the charging rate and installed charging power on the required battery size (● marks the required battery size for reference cell 2); (c) Comparison between the DT cost components and the BET costs at a specific cell cost of €96.57 kWh⁻¹.

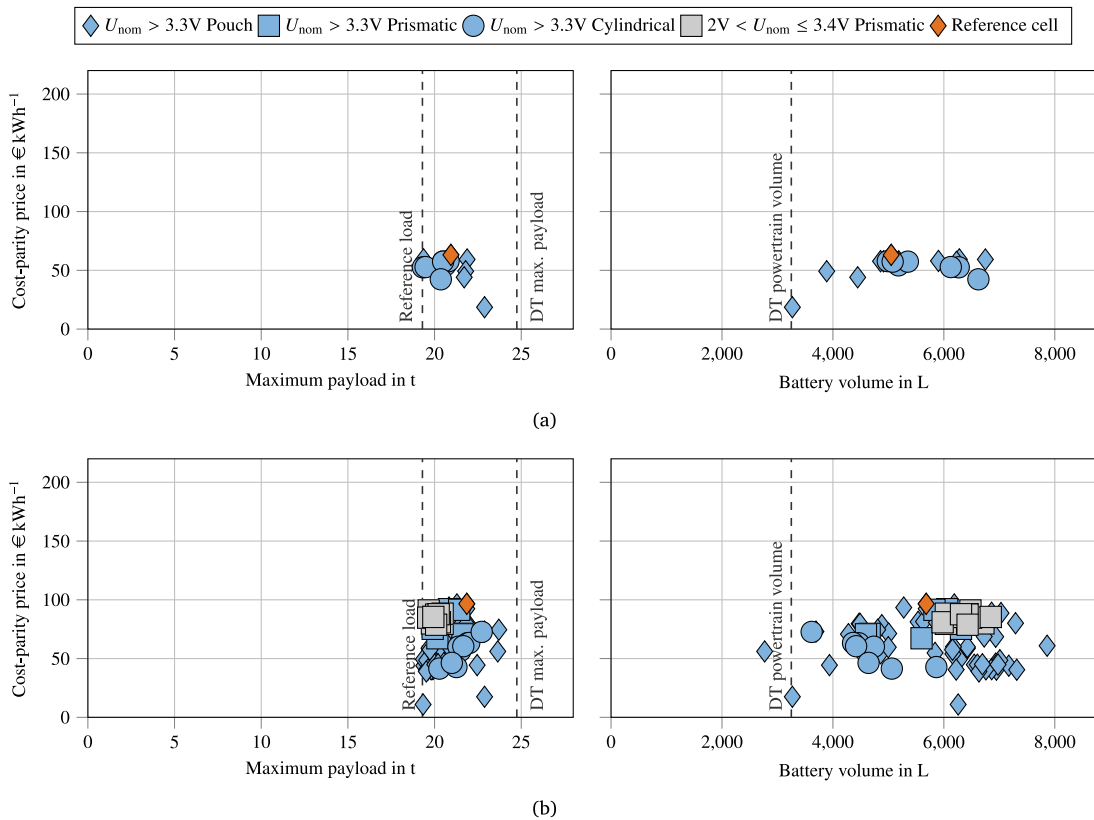


Fig. 6. Cost-parity price of all cells in the database vs. the maximum payload and required battery volume for the (a) 350 kW scenario and (b) 1 MW scenario.

The maximum payload of a DT is higher than the payload that can be realized by any cell in both scenarios. The battery volume exceeds the volume of the DT powertrain for all cells in the 350 kW scenario, whereas one cell results in a smaller battery volume in the 1 MW scenario. Vehicle manufacturers may select cells that results in a higher payload or a smaller volume than the reference cells, but would have to purchase these at a lower price to reach cost-parity with a DT, because of the lower cycle life of these cells.

4.3. Parameter sensitivity analysis

We conducted a parameter sensitivity analysis to quantify the impact of cell, pack, and system parameters on the cost-parity price, maximum payload and battery volume for reference cell 1 in the 350 kW scenario and reference cell 2 in the 1 MW scenario.

Fig. 7 shows the impact of the cell properties: cycle life, specific energy, energy density and charging rate. Each property was varied between the minimum and maximum value of all cells in our database.

The minimum and maximum cycle life of the cells in our database corresponds to 100 cycles and 20000 cycles until 80% of the initial capacity. Changing the cycle life does not affect the payload or required volume, but has the largest impact on the cost-parity price among the cell properties. In both charging scenarios, improving the cell's cycle life leads to a small increase in the cost-parity price, whereas reducing the cell's cycle life leads to a large reduction.

The cell's specific energy was varied between the minimum value that was able to transport the reference load, corresponding to 216 Wh kg⁻¹ and 154 Wh kg⁻¹ in the 350 kW and 1 MW charging scenarios, and the highest specific energy of a cell in our database, corresponding to 393 Wh kg⁻¹. Improving the cell's specific energy results in an increase in the cost-parity price, because the typical energy

consumption is reduced. Additionally, an increase in specific energy enables a higher maximum payload. Increasing the specific energy of the reference cells to the best-in-class specific energy would enable transporting the same payload as a DT in the 1 MW charging scenario.

The cell energy density is varied between the minimum and maximum value of the cells in our database, corresponding to 122 Wh L⁻¹ and 1047 Wh L⁻¹. The cell energy density only affects the battery volume and is therefore only shown in the right panes of Fig. 7. The lower energy density limit results in a battery volume exceeding the figure bounds and is therefore indicated by an arrow. The best-in-class energy density would result in a smaller battery volume than the volume that would become available if the DT powertrain is removed.

Finally, the impact of the cell's charging rate is shown. Increasing the charging rate beyond 0.3 h⁻¹ in the 350 kW charging scenario and 0.9 h⁻¹ in the 1 MW charging scenario does not reduce the required battery size, as was shown in Fig. 5(b). In the 1 MW charging scenario, the lower limit is the minimum value that enables transporting the reference load. Increasing the charging rate leads to an increase in cost-parity-price and maximum payload, and a decrease of the battery volume, because the required battery size is decreased.

Fig. 8 shows the impact of the pack parameters: the cell-to-pack cost ratio, gravimetric packaging efficiency and volumetric packaging efficiency. The cell-to-pack cost ratio was varied between the minimum and maximum values reported for battery-electric vehicles in the year 2020 by König et al. [26], corresponding to 1.94 and 2.21. Reducing the cell-to-pack cost ratio results in a higher cost-parity price, while it does not affect the maximum payload or battery volume.

The gravimetric packaging efficiency was varied between the minimum and maximum value for pouch cells in commercial battery-electric vehicles [24], corresponding to 49.5% and 74.2%. Increasing the gravimetric packaging efficiency results in a higher cost-parity

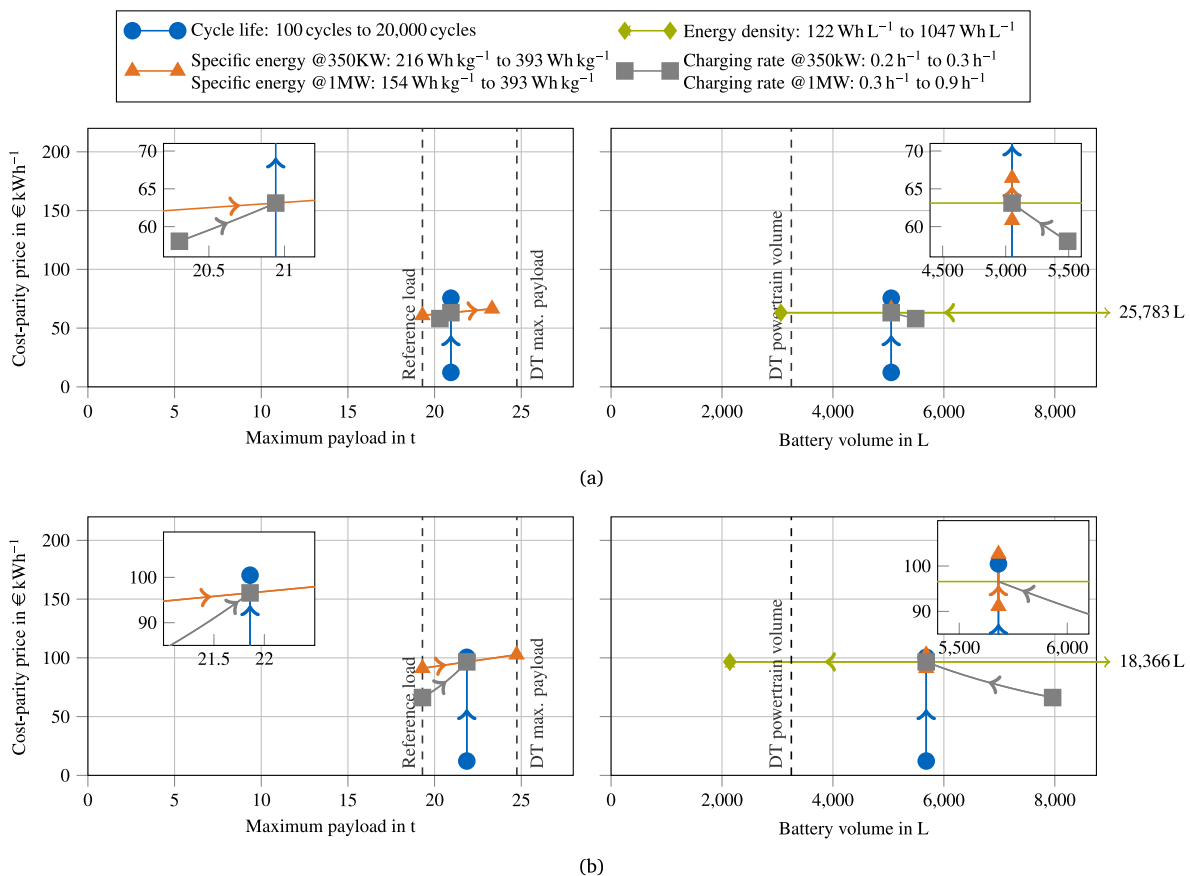


Fig. 7. Impact of cell properties on the cost-parity price, maximum payload and battery volume for (a) the 350kW scenario and (b) the 1 MW scenario. The insets show a close-up of the area around the reference cell characteristics. The arrow indicates the direction of the parameter variation.

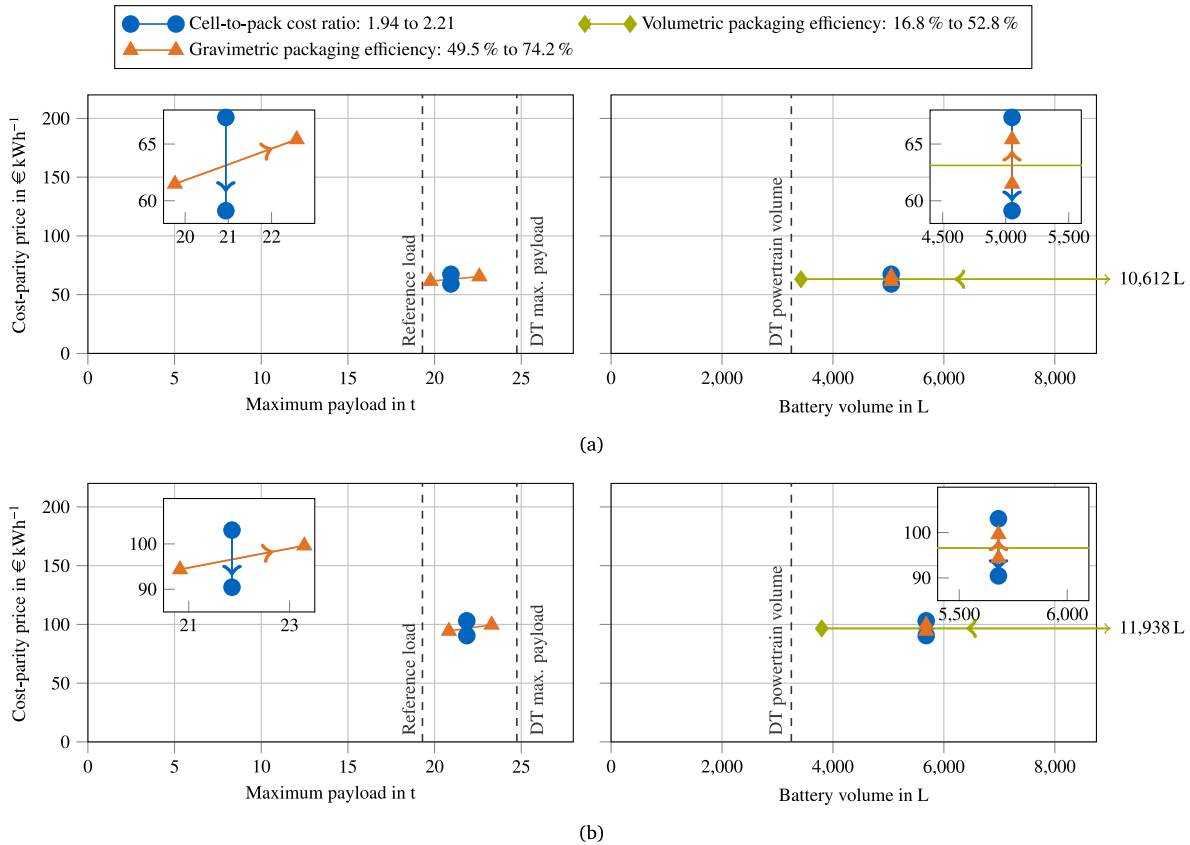


Fig. 8. Impact of pack properties on the cost-parity price, maximum payload and battery volume for (a) the 350kW scenario and (b) the 1MW scenario. The insets show a close-up of the area around the reference cell characteristics. The arrow indicates the direction of the parameter variation.

price, since the typical energy consumption is decreased. Additionally, the maximum payload is increased. However, even at the best-in-class gravimetric packaging efficiency, the reference cells do not achieve the same payload as a DT in either scenario.

The volumetric packaging efficiency was varied between 16.8% and 52.8%, corresponding to the minimum and maximum values for pouch cells used in commercial battery-electric vehicles [24]. The volumetric packaging efficiency only affects the battery volume and is therefore only shown in the right panes of Fig. 8. The lower limit requires a volume exceeding the figure bounds and is therefore indicated by an arrow. Increasing the volumetric packaging efficiency results in a smaller battery volume, but even the best-in-class packaging efficiency results in a battery with more volume than the DT powertrain.

Fig. 9 shows the impact of the system parameters: annual mileage, service life, diesel cost, cost of charging, and vehicle energy consumption. Apart from the vehicle energy consumption, the system parameters only influence the cost-parity price and not the payload or battery volume.

For the annual mileage, the lower limit corresponds to the average annual mileage of all semi-trailer trucks in Germany, including drayage trucks [35]. The upper limit is the annual mileage resulting from driving 9 h a day on 250 days a year. On the one hand, increasing the annual mileage reduces the battery residual value at the end of the service life. On the other hand, BETs benefit from a lower cost per kilometer than DTs for toll, maintenance and energy costs. Overall, the latter effect is more significant, which results in an increased cost-parity price as the annual mileage increases.

For the BET energy consumption, the lower limit corresponds to the typical and maximum energy consumption simulated for a truck with the lowest reported rolling friction coefficient and drag area of all trucks registered between the 1st January 2019 and the 30th June 2020. The upper limit corresponds to the values that were used in the case

study, as defined in Table 2. Reducing the energy consumption results in an increase in the cost-parity price, since the required battery size is reduced and the typical energy consumption is decreased. Additionally, reducing energy consumption results in a higher maximum payload and smaller battery volume.

For the service life, the lower limit corresponds to the payback period considered by large fleets [36] and the upper limit is the average service life of a truck in Germany [5]. The cost-parity price decreases as the service life is increased, because a longer service life results in a longer bound investment and a smaller net present value of the residual battery value.

The cost of charging is varied between the cost that might be realized if truck companies can participate in the electricity wholesale market [34] and the current upper limit for the charging cost stipulated by the German government, excluding VAT. [29]. Increasing the cost of charging results in a decrease in the cost-parity price.

Finally, the diesel cost is varied between the lowest and highest diesel cost in Germany excluding VAT between Jan 2021 and March 2022 [37]. An increase in the diesel cost results in an increase in the cost-parity price.

Comparing the impact of cell-, pack, and system parameters shows that improving the cell specific energy and energy density has the biggest impact on matching the payload and volume of a DT powertrain. This can be supported by improving the volumetric and gravimetric packaging efficiencies. The impact of improving the cycle life beyond the cycle life of the reference cells is relatively small, but reducing the cycle life leads to a strong decline in the cost-parity price. The biggest potential to increase the cost-parity price is providing 1 MW charging, reducing the cost of charging and reducing the vehicle energy consumption.

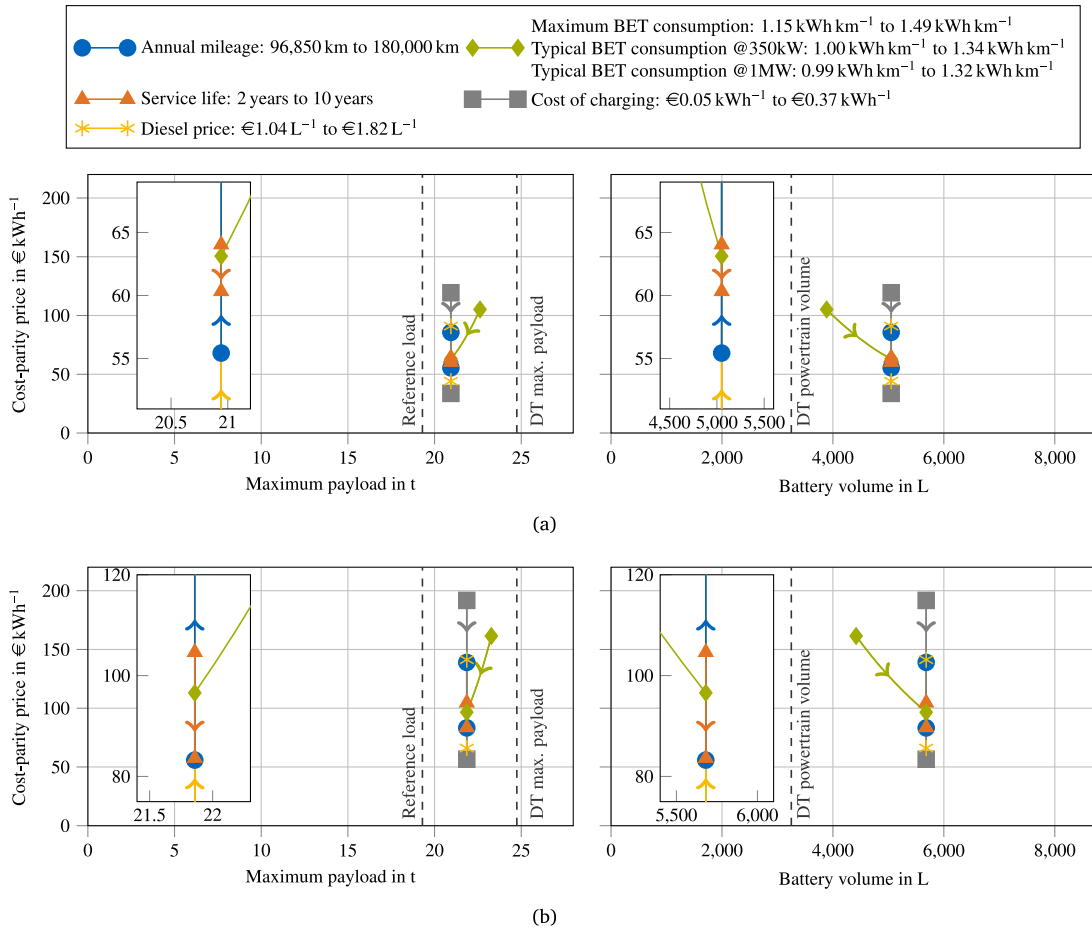


Fig. 9. Impact of system properties on the cost-parity price, maximum payload and battery volume for (a) the 350kW scenario and (b) the 1 MW scenario. The insets show a close-up of the area around the reference cell characteristics. The arrow indicates the direction of the parameter variation.

5. Discussion

Techno-economic cell-selection extends traditional cell selection methods, such as the Ragone plot, by quantifying the impact of individual cell characteristics on the system cost. The visualization in Fig. 6 allows truck manufacturers to compare the cost-parity price of different cells with properties that do not influence the system cost directly, such as the maximum payload and battery volume. Based on this visualization, a truck manufacturer can exclude cells that do not meet the payload and volume requirements for a given vehicle concept. Additionally, cells that are not available in the required quantities or that do not meet safety standards can be excluded. Other constraints, such as the preferred cell format, or a minimum cell capacity for handling during production may be considered. By obtaining quotes for the remaining cells, and comparing these to the cost-parity price for each cell, the optimal cell can be selected. Additionally, the parameter sensitivity analysis of the pack and system parameters, and the comparison of different scenarios show how system performance can be improved independent from the cell selection.

Techno-economic cell selection can not only help truck manufacturers select the optimal cell, but also provides cell manufacturers with insights. First, the cost-parity price quantifies at which price point a cell becomes cost-competitive. Second, the parameter sensitivity analysis, illustrated in Fig. 7, shows which price increases are justified if individual cell properties are improved. Finally, the sensitivity analysis of use case parameters and the comparison of different scenarios can support the anticipation of future business opportunities for cell technologies.

Techno-economic cell selection relies solely on values provided in cell data sheets. This enables the comparison of a wide range of

different cells during the early-stage design phase before conducting resource-intensive parametrization studies. However, this approach also leads to simplifications. Most notably, the data provided on the cell's aging behavior is limited. Only cyclic battery aging can be considered, since data sheets do not provide information on the storage life of a cell. Furthermore, due to the limited information available in cell datasheets, the impact of the depth of discharge, C-rate, and temperature on the battery life cannot be quantified. Therefore, after using the method to shortlist one or multiple cells, a detailed characterization of the electric, thermal and aging behavior of the cell is required to estimate the battery life for the given usage condition and optimize further design parameters such as the battery size or the battery thermal management system.

We demonstrated techno-economic cell-selection by selecting a cell from a database containing 160 unique cells for a long-haul truck operating with a single driver in Germany. The results show that for BETs charged at 350 kW, the cell price needs to drop to ca. €60 kWh⁻¹ to reach cost-parity with a DT. When 1 MW charging power is available, cost-parity can be reached at a cell price around €100 kWh⁻¹, which is within reach of optimistic cost estimates [26]. The maximum payload of a BET charged with 1 MW using reference cell 2 would be 2.9t less than a DT, which may be acceptable because trucks are mostly volume-constrained instead of payload-constrained [8]. The required volume, however, would be almost double the volume of the DT powertrain, which may be challenging to realize. Other cells provide a higher maximum payload and require less volume, but need to be purchased at a lower price to reach cost-parity, due to their lower cycle life. The parameter sensitivity analysis showed that improving packaging efficiency and vehicle energy consumption can support matching the

payload and powertrain volume of a diesel truck, while the cost of charging and vehicle energy consumption provide the biggest opportunity for increasing the cost-parity price. These results indicate that it will remain challenging, but possible, to make BETs cost-competitive with DT.

For our use case, we sized the battery based on the single-driver daily driving-time limit of 10 h and an average speed of 80 km h^{-1} , which results in a maximum daily driving distance of 800 km. This approach covers a large share of truck driving patterns: Basma et al. [2] and Tol et al. [38] show that 98% of truck daily distances in Europe are shorter than 800 km, where the remaining 2% are likely operated by multiple drivers. That said, trip distances and durations vary widely. Link et al. [39] recorded over one million vehicle kilometers from a German truck fleet revealing high variance in durations and distances of single trips, daily mileage, number of trips per day, and different shift schedules (i.e., single shift or multi-shift operations). Similarly, Tol et al. [38] find a standard deviation of up to 40% for day-to-day distances for current DT. This indicates the potential of an individual battery sizing and highlights the importance of future research in truck travel patterns.

Furthermore, we assumed that a charger is available after 4.5 h of driving, resulting in a maximum distance between two chargers of 360 km. This is in-line with the targets of the European Commission for electric recharging infrastructure dedicated to heavy-duty vehicles [40]: By the end of 2025 a 350 kW charger shall be available every 60 km along the TEN-T-core network and every 100 km along the TEN-T-comprehensive network. However, the MCS-Standard that will enable 1 MW charging will only be available from the mid-2020s, and in addition to charging infrastructure at public rest areas, semi-public charging infrastructure needs to be available to enable trucks to charge while loading and unloading cargo [39]. The presented results are therefore only valid, if the available charging infrastructure is increased and future research in charging infrastructure optimization is required.

Finally, although we took great care in using realistic design criteria and use case parameters for the BET application, the following limitations should be taken into account. First, our cell database contains information from data sheets that were available to researchers, which might not reflect the status quo of cells used in the automotive industry [41]. Second, operation with multiple drivers, or with cooled trailers would influence the battery sizing. Third, the cost function assumes a linear depreciation of the battery value with the vehicle mileage, favoring cells with a high cycle life. However, it might not be in the interest of vehicle manufacturers to provide a battery life that exceeds the warranty conditions. Fourth, the impact of axle load limitations on the battery sizing should be considered before selecting a cell. Finally, the results are specific to a truck operating in Germany today. Policy measures, such as toll and tax exemptions, the cost of charging and diesel cost vary widely in different countries and have a large impact on the cost-competitiveness of BET [2,6]. By publishing the source code of our method, we hope to enable other researchers to extend the cell database, sizing model and cost model, and implement the techno-economic cell selection in further scenarios.

6. Conclusion

Techno-economic cell selection is a novel cell selection method that takes the trade-off between cost and performance into consideration. Additionally, the method enables quantifying the impact of improving cell, pack, and system properties. We demonstrated the method by selecting a cell from a database containing 160 unique cells for a long-haul truck operating with a single driver in Germany. Our results show that, when 1 MW charging is available, the best performing cell becomes cost-competitive around $\text{€}100\text{ kWh}^{-1}$, which is within reach of price estimates for lithium-ion cells today. However, the achievable payload and required volume on board the vehicle still pose challenges for battery technology.

In future work, we plan to implement techno-economic cell selection in further automotive and non-automotive applications to show the general applicability and compare cost-parity prices across applications.

CRedit authorship contribution statement

Olaf Teichert: Conceptualization, Methodology, Software, Writing – original draft. **Steffen Link:** Methodology, Investigation, Data curation, Writing – original draft. **Jakob Schneider:** Investigation, Writing – review & editing. **Sebastian Wolff:** Validation, Writing – review & editing. **Markus Lienkamp:** Resources, Supervision, Writing – review & editing, Funding acquisition.

Declaration of competing interest

The authors declare that they have no known competing financial interests or personal relationships that could have appeared to influence the work reported in this paper.

Data availability

Data will be made available on request.

Acknowledgments

The work of O.T. and S.L. was sponsored by the Federal Ministry of Education and Research Germany with the project “BetterBat” under grant number 03XP0362C. The work of J.S. was sponsored by the Federal Ministry for Economic Affairs and Energy Germany within the project “NEFTON” under grant number 01MV21004A. The work of S.W. was funded by general research funds of the Technical University of Munich, Germany. We would like to thank M.(anuel) Bstieler for preparing the visualization of a DT during his student thesis.

Appendix A. Battery energy throughput for different charging scenarios

Fig. A.1 illustrates the cumulative energy throughput of a truck battery for two scenarios: with a 350 kW and with a 1 MW charger available during the rest period. In both scenarios the truck consumes 530 kWh of energy during the driving phase, but due to the different charging powers, the cumulative energy throughput after the second driving event is larger for the 350 kW charging scenario. Further reductions in the amount of recharged energy may be caused by the cell’s maximum charging rate. Note that the amount of fast chargeable energy during the rest period is limited to 80% of the usable energy at the end of life of the battery. As a result, in the 1 MW scenario the battery is fully recharged before the end of the rest period, which shows that a lower charging power would have been sufficient. The required battery size is determined by dividing the cumulative energy throughput after the second driving event by the EOL condition and the share of usable energy. If the amount of rechargeable energy is not limited by the cell’s charging rate, the required battery size for the 350 kW and 1 MW charging scenario are 792 kWh and 1111 kWh respectively.

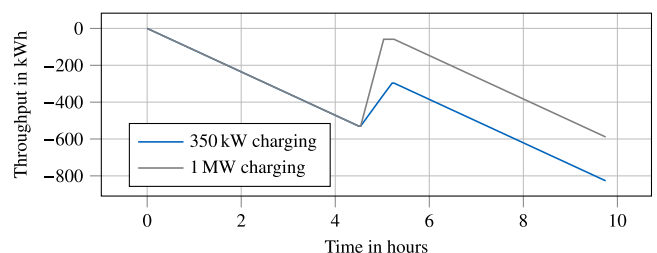


Fig. A.1. Energy throughput of a battery charged with 350 kW and 1 MW during the charging break.

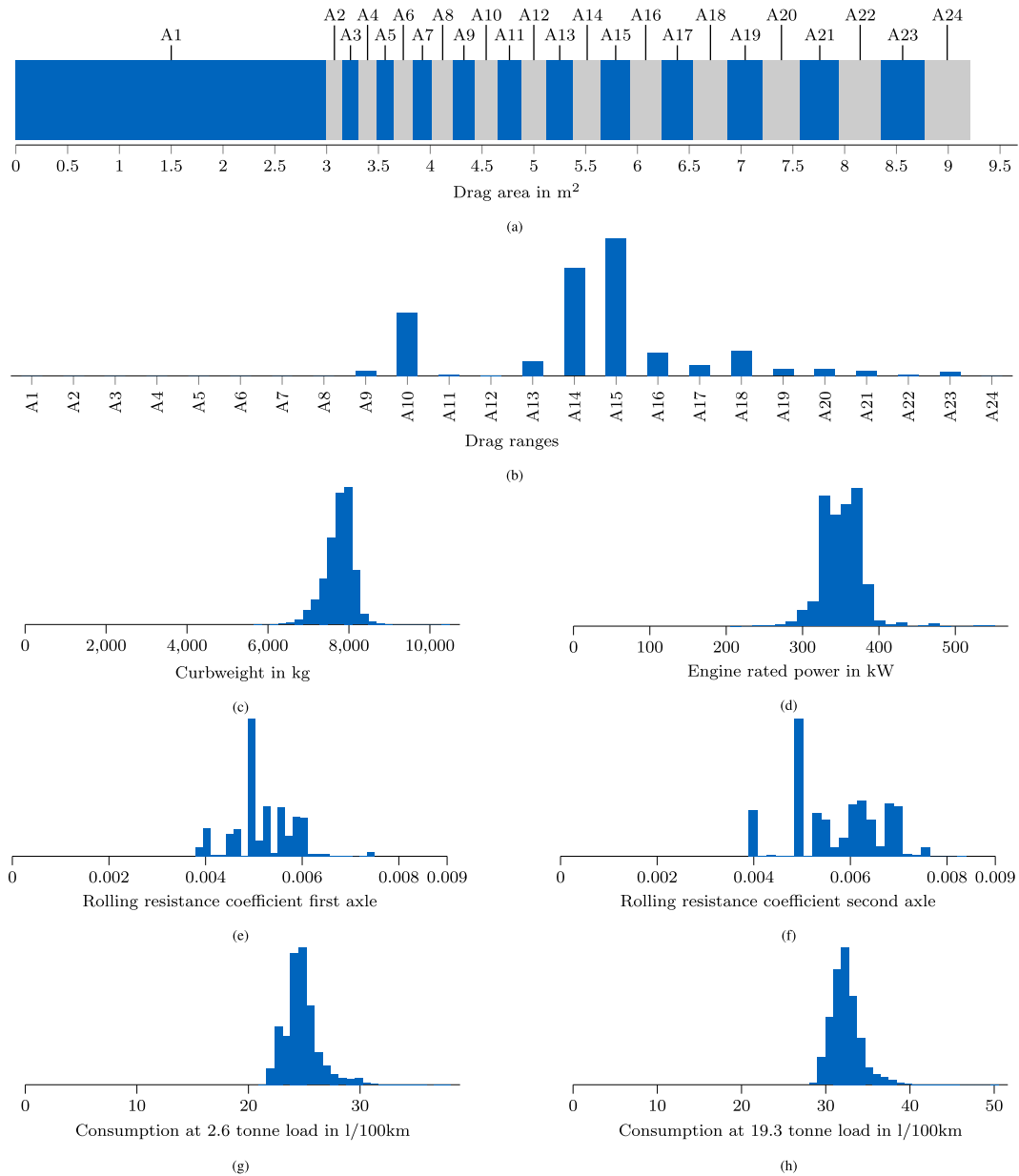


Fig. B.1. (a) Drag ranges defined by the European Parliament and the council [42]; (b-h) reported vehicle characteristics of 161 129 trucks in the vehicle sub-group “LH-5” that were registered between the 1st January 2019 and the 30 June 2020.

Appendix B. Analysis of reported long-haul truck data

To realistically model the vehicle characteristics, we use data that heavy-duty vehicle manufacturers are required to report in accordance with EU Regulation 2018/956. We limit the data to vehicle sub-group “LH-5”, which comprises tractors that have a 4 × 2 axle configuration, a sleeper cab, and a technically permissible maximum laden mass over 16 tonnes [18]. This vehicle sub-group makes up 62% of new regulated truck sales [43]. The parameters of interest for the vehicle simulation are the engine rated power, drag area, and tire rolling resistance coefficient. Additionally, the chassis curb mass is required to determine the vehicle mass for the sizing algorithm, and the consumption of a diesel truck is needed for the cost model.

The reported data directly includes the chassis curb mass and the engine rated power. The rolling resistance coefficient is given for the first and second axle, the fuel consumption is specified for a 2.6t and 19.3t load and the drag area is specified according to the drag ranges defined by the European Commission, shown in Fig. B.1(a). The

distribution of these parameters for 161 129 trucks registered between the 1st of January 2019 and the 30th June 2020 is shown in Fig. B.1(b) to B.1(h).

The average values are summarized in Table B.1. For the rolling resistance coefficient this is the average of the front and rear axle. The drag area is calculated by assuming that the center of each drag range is representative for the drag areas in that range. The average diesel truck fuel consumption is determined based on the loading conditions defined by the European Commission, which correspond to 2.6t over 30% of the trip distance and 19.3 t over the remaining 70%.

Appendix C. Vehicle weight without battery, cost of slow charging and powertrain component costs

The vehicle weight without the battery is the sum of the average DT chassis curb mass (7753 kg, Table B.1), minus the weight of the DT powertrain (25% [44]), plus the weight of the e-axle (450 kg [8]), plus the weight of the trailer (7500 kg [45]), resulting in 13.8t.

Table B.1

Average vehicle parameters of 161,129 trucks in the vehicle sub-group “LH-5” that were registered between the 1st January 2019 and the 30 June 2020.

Parameter	Average
Engine rated power	352.4 kW
Rolling resistance coefficient	0.00548
Drag area	5.68 m ²
Chassis curb mass	7753 kg
DT fuel consumption	0.301 L km ⁻¹

The costs of slow charging corresponds to the sum of the average industrial electricity price in 2021 of €0.2138 kWh⁻¹ [46] and an overhead costs for the overnight charging infrastructure of €0.0377 kWh⁻¹ [2]. The resulting cost of slow charging is €0.2515 kWh⁻¹.

We model the powertrain costs based on the specific direct manufacturing costs for major powertrain components in the reference year 2020 published by Speth et al. [47]. For DT, these are the internal combustion engine plus gearbox (€72 kW⁻¹), fuel tank (€2 L⁻¹, 800 L tank volume), and the emission after-treatment system (€19.8 kW⁻¹). For BETs, these are electric motors (€32 kW⁻¹) and power electronics plus HV system components (€35 kW⁻¹). Additionally, we use a markup factor of 1.45 to account for indirect manufacturing costs such as overhead, warranty and margins [2]. The resulting powertrain costs for the DT and BET are €49 223.64 and €34 232.51 respectively.

Appendix D. DT powertrain volume

The powertrain volume of a DT is determined using a package model of a diesel 4 × 2 semi-tractor with a wheelbase of 3600 mm, as shown in Fig. D.1(a). When converting the DT to a BET, the cab, frame, wheelbase, and axles remain unchanged [48]. By removing all ICEV-specific components (engine, tank, transmission, cardan shaft, exhaust), large areas outside the ladder frame (between the axles) and in the engine compartment are freed up, as illustrated in Fig. D.1(b). The total volume that becomes available is 3250 L. Smaller, irregular areas and the inside of the ladder frame at the rear axle, which is reserved for the axle suspension and the electric motor [49] are not included.

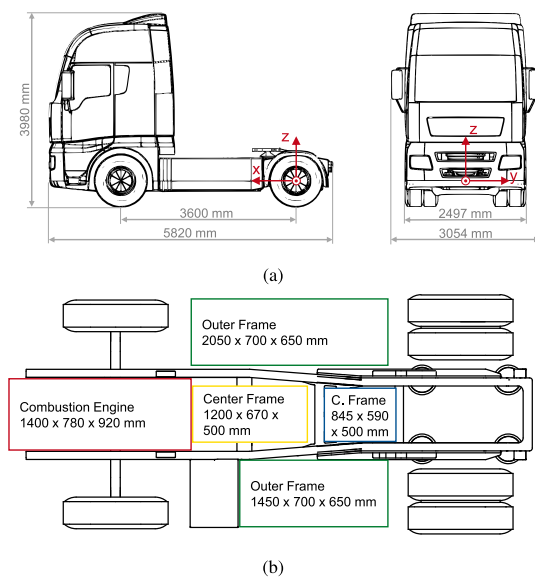


Fig. D.1. Visualization of (a) the DT measurements, and (b) the volume that becomes available when the DT powertrain components are removed.

References

- [1] Meszler D, Delgado O, Rodríguez F, Muncrief R. European heavy-duty vehicles: Cost-effectiveness of fuel-efficiency technologies for long-haul tractor-trailers in the 2025–2030 timeframe. International Council on Clean Transportation; 2018, www.theicct.org/publications/cost-effectiveness-of-fuel-efficiency-tech-tractor-trailers.
- [2] Basma H, Saboori A, Rodríguez F. Total cost of ownership for tractor-trailers in Europe: Battery electric versus diesel. International Council on Clean Transportation; 2021, <https://theicct.org/sites/default/files/publications/TCO-BETs-Europe-white-paper-v4-nov21.pdf>.
- [3] Sripad S, Viswanathan V. Quantifying the economic case for electric semi-trucks. ACS Energy Lett 2018;4(1):149–55. <http://dx.doi.org/10.1021/acsenergylett.8b02146>.
- [4] Forrest K, Mac Kinnon M, Tarroja B, Samuelsen S. Estimating the technical feasibility of fuel cell and battery electric vehicles for the medium and heavy duty sectors in California. Appl Energy 2020;276:115439. <http://dx.doi.org/10.1016/j.apenergy.2020.115439>.
- [5] Wolff S, Lienkamp M, Schaller K-V. Status nutzfahrzeuge 2020: Alles auf eine Karte? Researchgate; 2021.
- [6] Noll B, del Val S, Schmidt TS, Steffen B. Analyzing the competitiveness of low-carbon drive-technologies in road-freight: A total cost of ownership analysis in Europe. Appl Energy 2022;306:118079. <http://dx.doi.org/10.1016/j.apenergy.2021.118079>.
- [7] Sripad S, Viswanathan V. Performance metrics required of next-generation batteries to make a practical electric semi truck. ACS Energy Lett 2017;2(7):1669–73. <http://dx.doi.org/10.1021/acsenergylett.7b00432>.
- [8] Mareev I, Becker J, Sauer DU. Battery dimensioning and life cycle costs analysis for a heavy-duty truck considering the requirements of long-haul transportation. Energies 2018;11(1):55. <http://dx.doi.org/10.3390/en11010055>.
- [9] Çabukoglu E, Georges G, Küng L, Pareschi G, Boulouchos K. Battery electric propulsion: An option for heavy-duty vehicles? Results from a Swiss case-study. Transp Res C 2018;88:107–23. <http://dx.doi.org/10.1016/j.trc.2018.01.013>.
- [10] Nykvist B, Olsson O. The feasibility of heavy battery electric trucks. Joule 2021;5(4):901–13. <http://dx.doi.org/10.1016/j.joule.2021.03.007>.
- [11] Mauler L, Dahrendorf L, Duffner F, Winter M, Leker J. Cost-effective technology choice in a decarbonized and diversified long-haul truck transportation sector: A US case study. J Energy Storage 2022;46:103891. <http://dx.doi.org/10.1016/j.est.2021.103891>.
- [12] Ragone DV. Review of battery systems for electrically powered vehicles. In: Proceedings of the Society of Automotive Engineers Mid-Year Meeting, Detroit, Michigan, May 20–24. 1968, <http://dx.doi.org/10.4271/680453>.
- [13] Christen T, Carlen MW. Theory of Ragone plots. J Power Sources 2000;91(2):210–6. [http://dx.doi.org/10.1016/S0378-7753\(00\)00474-2](http://dx.doi.org/10.1016/S0378-7753(00)00474-2).
- [14] Catenaro E, Rizzo DM, Onori S. Experimental analysis and analytical modeling of enhanced-Ragone plot. Appl Energy 2021;291:116473. <http://dx.doi.org/10.1016/j.apenergy.2021.116473>.
- [15] Dechent P, Epp A, Jöst D, Preger Y, Attia PM, Li W, et al. ENPOLITE: Comparing lithium-ion cells across energy, power, lifetime, and temperature. ACS Energy Lett 2021;6:2351–5. <http://dx.doi.org/10.1021/acsenergylett.1c00743>.
- [16] European Commission. User Manual: Vehicle energy consumption calculation tool. 2023.
- [17] The European parliament and the council. The harmonisation of certain social legislation relating to road transport and amending council regulations (EEC) No 3821/85 and (EC) No 2135/98 and repealing council regulation (EEC) No 3820/85. 2006, <https://eur-lex.europa.eu/eli/reg/2006/561/oj>.
- [18] The European Parliament and The Council. Regulation (EU) 2019/1242: Setting CO2 emission performance standards for new heavy-duty vehicles and amending regulations (EC) No 595/2009 and (EU) 2018/956 of the European Parliament and of the Council and Council Directive 96/53/EC. 2019, <https://eur-lex.europa.eu/eli/reg/2019/1242/oj>.
- [19] Kleiner F, Friedrich HE. Maintenance & repair cost calculation and assessment of resale value for different alternative commercial vehicle powertrain technologies. In: Proceedings of the 30th Electric Vehicle Symposium. 2017, <https://elib.dlr.de/114666/>.
- [20] Zhao H, Burke A, Miller M. Analysis of class 8 truck technologies for their fuel savings and economics. Transp Res Part D: Transp Environ 2013;23:55–63. <http://dx.doi.org/10.1016/j.trd.2013.04.004>.
- [21] Earl T, Mathieu L, Cornelis S, Kenny S, Ambel CC, Nix J. Analysis of long haul battery electric trucks in EU. Transport & Environment; 2018, <https://www.transportenvironment.org/discover/analysis-long-haul-battery-electric-trucks-eu/>.
- [22] Wassiliadis N, Steinsträter M, Schreiber M, Rosner P, Nicoletti L, Schmid F, et al. Quantifying the state of the art of electric powertrains in battery electric vehicles: Range, efficiency, and lifetime from component to system level of the Volkswagen ID. 3. ETransportation 2022;12:100167. <http://dx.doi.org/10.1016/j.etrans.2022.100167>.
- [23] Bundesministerium der Justiz. Straßenverkehrs-zulassungs-ordnung §34. 2002, http://www.gesetze-im-internet.de/stvzo_2012/_34.html.

- [24] Löbbberding H, Wessel S, Offermanns C, Kehrner M, Rother J, Heimes H, et al. From cell to battery system in BEVs: Analysis of system packing efficiency and cell types. *World Electr Veh J* 2020;11(4):77. <http://dx.doi.org/10.3390/wevj11040077>.
- [25] Burke A, Fulton L. Analysis of advanced battery-electric long haul trucks: Batteries, performance, and economics. UC Davis Institute of Transportation Studies; 2019. <https://ucdavis.app.box.com/s/cfpoywahc2so21hogykiga6h8r9ppxe>.
- [26] König A, Nicoletti L, Schröder D, Wolff S, Waclaw A, Lienkamp M. An overview of parameter and cost for battery electric vehicles. *World Electr Veh J* 2021;12(1):21. <http://dx.doi.org/10.3390/wevj12010021>.
- [27] Hülsmann F, Mottschall M, Hacker F, Kasten P. Konventionelle und alternative fahrzeugtechnologien bei pkw und schweren nutzfahrzeugen - potenziale zur minderung des energieverbrauchs bis 2050. Öko-Institut; 2014. <https://digital.zlb.de/viewer/metadata/15823045/1/>.
- [28] Ionity. Access and payment, ionity-passport. 2022. <https://ionity.eu/en/access-and-payment.html>, [Accessed 14 February 2022].
- [29] NOW-GmbH. Deutschlandnetz: Bundesverkehrsminister scheuer stellt 1.000 standorte für schnellladesäulen und preismodell vor. 2021, <https://www.now-gmbh.de/aktuelles/pressemitteilungen/deutschlandnetz-bundesverkehrsminister-scheuer-stellt-1-000-standorte-fuer-schnellladesaeulen-und-preismodell-vor/>. [Accessed 09 February 2022].
- [30] Bundesministerium der Justiz. Gesetz über die erhebung von streckenbezogenen gebühren für die benutzung von bundesautobahnen und bundesstraßen §1. 2011, https://www.gesetze-im-internet.de/bfstrmg/_1.html.
- [31] Bundesministerium der Justiz. Kraftfahrzeugsteuergesetz §9. 2002, https://www.gesetze-im-internet.de/kraftstg/_9.html.
- [32] Coordination Office Charging Interface. Combined Charging system 1.0 specification - CCS 1.0. Version 1.2.1.
- [33] CHARIN. Megawatt charging system (MCS). 2022, <https://www.charin.global/technology/mcs/>. [Accessed on 28 April 2022].
- [34] Phadke A, McCall M, Rajagopal D. Reforming electricity rates to enable economically competitive electric trucking. *Environ Res Lett* 2019;14(12):124047. <http://dx.doi.org/10.1088/1748-9326/ab560d>.
- [35] Kraftfahrtbundesamt. Verkehr in kilometern 1.25 sattelzugmaschinen nach fahrzeugalter seit 2014. 2020, https://www.kba.de/DE/Statistik/Produktkatalog/produkte/Kraftverkehr/vk_uebersicht.html.
- [36] The future of trucks - implications for energy and the environment. International Energy Agency; 2017, <http://dx.doi.org/10.1787/9789264279452-en>.
- [37] ADAC. Kraftstoffpreisentwicklung. 2022, <https://www.adac.de/verkehr/tanken-kraftstoff-antrieb/deutschland/kraftstoffpreisentwicklung/>. [Accessed 19 April 2022].
- [38] Toi D, Frateur T, Verbeek M, Riemersma I, Mulder H. Techno-economic uptake potential of zero-emission trucks in Europe. TNO; 2022.
- [39] Link S, Plötz P, Griener J, Moll C. Lieferverkehr mit batterie-lkw: Machbarkeit 2021. Fraunhofer-Institut für System- und Innovationsforschung ISI; 2021, <http://dx.doi.org/10.24406/publica-fhg-301266>.
- [40] The European parliament and the council. Proposal for a regulation on the deployment of alternative fuels infrastructure, and repealing directive 2014/94/EU of the European Parliament and of the Council. 2021, <https://eur-lex.europa.eu/legal-content/en/TXT/?uri=CELEX:52021PC0559>.
- [41] Teichert O, Grube Doiz N, Schreiber M, Lin X, Lienkamp M. Substandard? Lithium-ion cells available on online marketplaces. In: *Advanced battery power*. 2022, <http://dx.doi.org/10.13140/RG.2.2.19218.12480>.
- [42] The European Parliament and The Council. Regulation (EU) 2018/956: On the monitoring and reporting of CO2 emissions from and fuel consumption of new heavy-duty vehicles. 2018, <https://eur-lex.europa.eu/legal-content/EN/TXT/?uri=celex:32018R0956>.
- [43] Ragon P-L, Rodríguez F. CO2 emissions from trucks in the EU: An analysis of the heavy-duty CO2 standards baseline data. The International Council on Clean Transportation; 2021, <https://theicct.org/publication/co2-emissions-from-trucks-in-the-eu-an-analysis-of-the-heavy-duty-co2-standards-baseline-data/>.
- [44] Phadke A, Khandekar A, Abhyankar N, Wooley D, Rajagopal D. Why regional and Long-Haul trucks are primed for electrification now. Lawrence Berkeley National Laboratory; 2021, <https://escholarship.org/uc/item/3kj8s12f>.
- [45] Norris J, Escher G. Heavy duty vehicles technology potential and cost study. The International Council on Clean Transportation; 2017, <https://theicct.org/publication/heavy-duty-vehicles-technology-potential-and-cost-study/>.
- [46] BDEW. Strompreisanalyse Juni 2021. 2021, <https://www.bdew.de/service/daten-und-grafiken/bdew-strompreisanalyse/>. [Accessed 27 April 2022].
- [47] Speth D, Kappler L, Link S, Keller M. Attractiveness of alternative fuel trucks with regard to current tax and incentive schemes in Germany: A total cost of ownership analysis. In: *Proceedings of the 35th Electric Vehicle Symposium*. 2022, <http://dx.doi.org/10.24406/publica-228>.
- [48] Wolff S, Seidenfus M, Gordon K, Álvarez S, Kalt S, Lienkamp M. Scalable life-cycle inventory for heavy-duty vehicle production. *Sustainability* 2020;12(13):5396. <http://dx.doi.org/10.3390/su12135396>.
- [49] Wolff S, Kalt S, Bstieler M, Lienkamp M. Influence of powertrain topology and electric machine design on efficiency of battery electric trucks—A simulative case-study. *Energies* 2021;14(2):328. <http://dx.doi.org/10.3390/en14020328>.

3.1.3 Changes to the published method

The results from the previous publication and other studies [36, 38] agree that high charging powers are required to make long-haul truck electrification feasible and cost-competitive. Therefore, in the following, I will limit the results to the scenario where 1 MW charging power is available during the rest period, matching the charging capability of BET announced by truck manufacturers [105].

Additionally, I decided to update the following model components based on numerous feedback I have received since the publication: the battery life estimation, energy consumption, packaging efficiency, and cell-to-pack cost ratio.

Battery life

In the previous publication the battery life was determined solely based on the cycle life given in the cell's datasheet, ignoring any calendar aging. This assumption was made because of the short service-life of long-haul trucks and the lack of information on a cell's calendar life in the datasheet. To improve the battery life estimation, I here include calendar life estimates for different cell chemistries from literature as follows.

As described in Subsubsection 2.2.2, semi-empirical aging models typically superimpose cyclic and calendar aging to determine a cell's capacity loss [79, 106], resulting in a formula similar to Equation (3.1).

$$Q_{\text{loss}} = \alpha_{Q,\text{cal}} t^{z_{Q,\text{cal}}} + \alpha_{Q,\text{cyc}} n^{z_{Q,\text{cyc}}} \quad (3.1)$$

The exponents $z_{Q,\text{cal}}$, and $z_{Q,\text{cyc}}$ depend on the aging mechanism and the cell chemistry. In Section 3.2 an aging model will be introduced that takes these details into account, but here I assume that both calendar and cyclic aging are linear.

The coefficients $\alpha_{Q,\text{cal}}$ and $\alpha_{Q,\text{cyc}}$ depend on aging stress factors, such as temperature, SOC, DOD and the charging rate. To quantify the impact of these individual stress factors for a given cell, extensive aging studies are required. To estimate the battery life without extensive testing, I make the following simplifications.

A cell's calendar life, t_{cal} , describes the time until the EOL capacity loss criterion, $Q_{\text{loss,end}}$ is reached in the absence of any cycling. Therefore, Equation (3.1) can be rewritten to calculate coefficient $\alpha_{Q,\text{cal}}$.

$$\alpha_{Q,\text{cal}} = \frac{Q_{\text{loss,end}}}{t_{\text{cal}}} \quad (3.2)$$

A cell's cycle life, n_{cyc} , describes the number of FEC that can be completed before the EOL capacity loss criterion is reached. By neglecting the calendar aging that occurs during the relatively short duration of cyclic aging tests, Equation (3.1) can be rewritten to determine coefficient $\alpha_{Q,\text{cyc}}$.

$$\alpha_{Q,cyc} = \frac{Q_{loss,end}}{n_{cyc}} \quad (3.3)$$

By combining Equation (3.2) and (3.3), the battery life until the EOL condition is reached can be calculated for a given calendar and cycle life using Equation (3.4), where n_{annual} denotes the number of FEC per year. Because the calendar life is not specified in the cell's datasheet, I use literature estimates differentiating between cells with an NMC and LFP cathode: 13 years for NMC and 15 years for LFP [107]. The cycle life corresponds to the cycle life specified in a cell's datasheet. Equation (3.4) replaces Equation (26) in the sizing model of the previous publication.

$$t_{bat} = \frac{1}{\frac{1}{t_{cal}} + \frac{n_{annual}}{n_{cycle}}} \quad (3.4)$$

Energy consumption

In the previous publication, the vehicle simulation used the average rolling friction coefficient and drag area of all DT registered between the 1st January 2019 and the 30 June 2020, resulting in an energy consumption of 1.49 kWh km^{-1} for a 42 t BET. This matches results from previous literature studies well [26, 33, 35, 108].

However, the drag area and rolling friction coefficient of BET will likely be optimized for energy consumption and therefore have a smaller the drag area and rolling friction coefficient than status-quo DT. Results from prototype tests show an energy consumption of 1.1 kWh km^{-1} for a 40 t BET [109], which is 26 % lower than the energy consumption used in the previous publication. To align my simulation results with these prototype tests, I here use the lowest drag area and rolling friction coefficient of all trucks registered between the 1st January 2019 and the 30 June 2020, resulting in a simulated energy consumption of 1.11 kWh km^{-1} for a 40 t BET.

Packaging efficiency

In the previous publication, I used the average volumetric and gravimetric packaging efficiencies reported for passenger cars released between 2010 and 2019: for cylindrical cells 29.5 % and 55.2 %, and for pouch or prismatic cells 35.3 % and 57.5 % respectively [110]. However, newer vehicle models reach higher packaging efficiencies: the VW ID.3 achieves a volumetric packaging efficiency of 41.5 % and a gravimetric efficiency of 63.4 % [74], while the Tesla Model 3 with an LFP battery achieves a volumetric and gravimetric packaging efficiency of 55.3 % and 71.6 % respectively [111].

To match the packaging efficiency of status quo BEV and differentiate between the achievable packaging efficiencies for different cell chemistries, I use the packaging efficiencies reported for the VW ID.3 and Tesla Model 3 for pouch and prismatic cells, and scale the packaging efficiencies of cylindrical cells accordingly. Using the same packaging efficiencies for BEV and BET matches the EUCAR targets [112], which do not differentiate between passenger cars and commercial heavy-duty vehicles.

Cell-to-pack cost ratio

The previous publication used a conservative estimate for the ratio between costs at the cell and system level of 2.07. More recent publications show that this ratio has come down significantly: Bloomberg reports an average cell-to-pack cost ratio of 1.2 for the year 2022 [22], while the EUCAR consortium considers a ratio of 1.3 the state-of-the-art in 2019 [112]. To take these advances into account, while still taking a conservative approach, I will use the value of 1.3 reported by the EUCAR consortium in the following.

3.1.4 Updated results

The results for all cells in the database are shown in Figure 3.3. The vertical axis shows the cost-parity price, while the horizontal axis in the left pane shows the maximum payload and in the right pane the battery volume. Additionally, the reference load used for homologation in the EU, the maximum payload of a DT, the volume of a DT powertrain and the 2022 average cell price [22] are indicated. Cells that result in a vehicle that cannot transport the EU reference load are not considered. Cells in the green area can transport a higher payload or require less volume than a DT and can be more expensive than the 2022 average cell price to reach cost-parity. Finally, different cell formats, cell chemistries and the selected cell are indicated by marker shapes and colors.

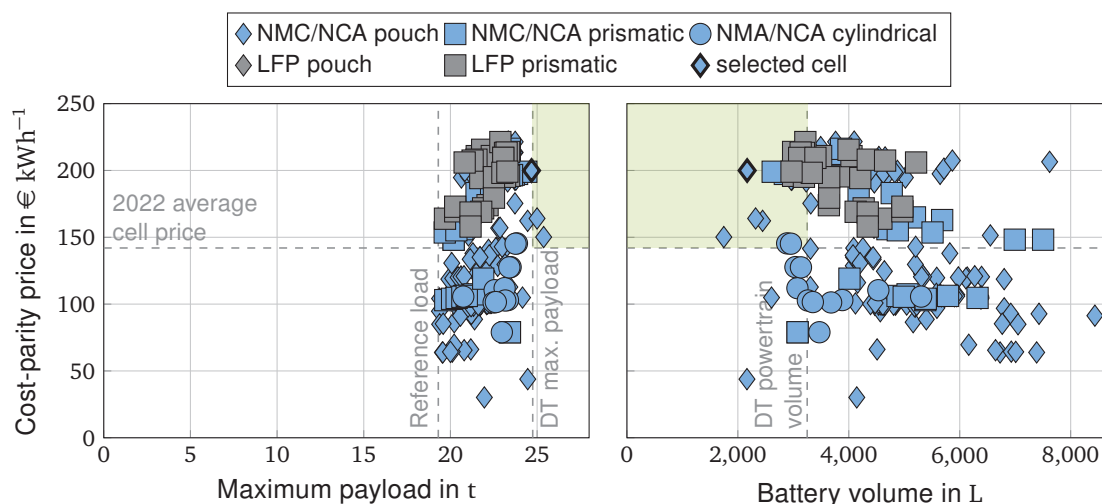


Figure 3.3: Comparison of all cells in the cell database.

The results show that only few cells in the database reach payload parity with a DT. However, a small decrease in payload capability may be acceptable because long-haul trucks are mostly volume constrained instead of payload constrained [37]. Several cells achieve the same or less volume onboard the vehicle than the current DT powertrain. LFP cells can transport less payload and require more volume than NMC cells, due to their lower energy density. Additionally, a trade-off between cost and performance can be seen. Some cells reach cost parity at $\text{€ } 222 \text{ kWh}^{-1}$, but would require more volume onboard the vehicle and enable less payload than a DT powertrain. Cells that result in a better match with payload and volume of status quo DT, would need to be bought at a lower price to reach cost parity.

A truck manufacturer may use this visualization to exclude cells that do not meet the payload or volume requirement for a given vehicle concept. Additionally, cells that do not meet safety standards or are not available in the required quantities might be excluded. Further constraints

regarding the cell size or format for handling during production may be enforced. By obtaining quotes for the remaining cells, a cell can be selected. Cells that have a higher cost-parity price than the quoted price would result in a cost-competitive vehicle.

Because I am not in a position to obtain quotations for large-volume cell purchases, I select the cell with the highest cost-parity price that results in less than 1 t payload loss compared to a DT. The resulting cell is produced by LG Chem and used in the VW ID.3 battery pack. The cell characteristics and resulting battery properties are shown in Table 3.1. The resulting battery size, battery mass and vehicle energy consumption match announcements from truck manufacturers well [31].

Table 3.1: Properties of the selected cell, obtained from the cell database, and results from the cell selection method.

Cell characteristics from database	Capacity	78 Ah [74]
	Nominal voltage	3.7 V [74]
	Format	Pouch [74]
	Specific energy	273 Wh kg ⁻¹ [74]
	Energy density	685 Wh L ⁻¹ [74]
	Cycle life	2000 FEC [74]
	EOL	0.8 [74]
	Charging rate	1 h ⁻¹ [74]
Results from cell selection method	Battery size	616 kWh
	Battery volume	2168 L
	Battery mass	3559 kg
	Max. Payload	24.7 t
	Typical energy consumption	0.97 kWh km ⁻¹
	Battery life	5.9 years
	Cost-parity price	€ 200 kWh ⁻¹

3.2 Step 2: battery model parametrization

To obtain a better estimate of the battery life for the selected cell under typical truck operating conditions, the cell is characterized to parametrize a battery model. I published the implemented battery model as a first author in a previous study [113]. The initial published model has been adapted for the selected cell. In the following, I will summarize the previous publication, specify my contribution, and provide the published manuscript and supplement. Subsequently, changes to the model are explained and the parametrization for the electric and thermal model is presented. Finally, the validation of these models, and the parametrization and validation of the aging model are shown.

3.2.1 Summary of the published battery model

The previous publication investigated the cost-effectiveness of different BTMS designs in different climates using a combined electric-thermal-aging model. The battery model consists of 5 submodels, shown in Figure 3.4, that are executed at every time step in a transient simulation.

First, the cell power limits are calculated, based on the cell's SOC, temperature and aging condition. Subsequently, based on the power profile, power limits and battery temperature, the control algorithm determines the power drawn from or supplied to the battery, and the applied cooling & heating power. The electric model then calculates the ohmic losses and updates the SOC, based on the battery power, cell temperature, SOC and aging status. The thermal model

updates the battery temperature based on the ohmic losses, applied cooling & heating power and the ambient temperature. Finally, the aging model updates the capacity loss and internal resistance increase of the cell, based on the cell temperature, SOC and depth of discharge.

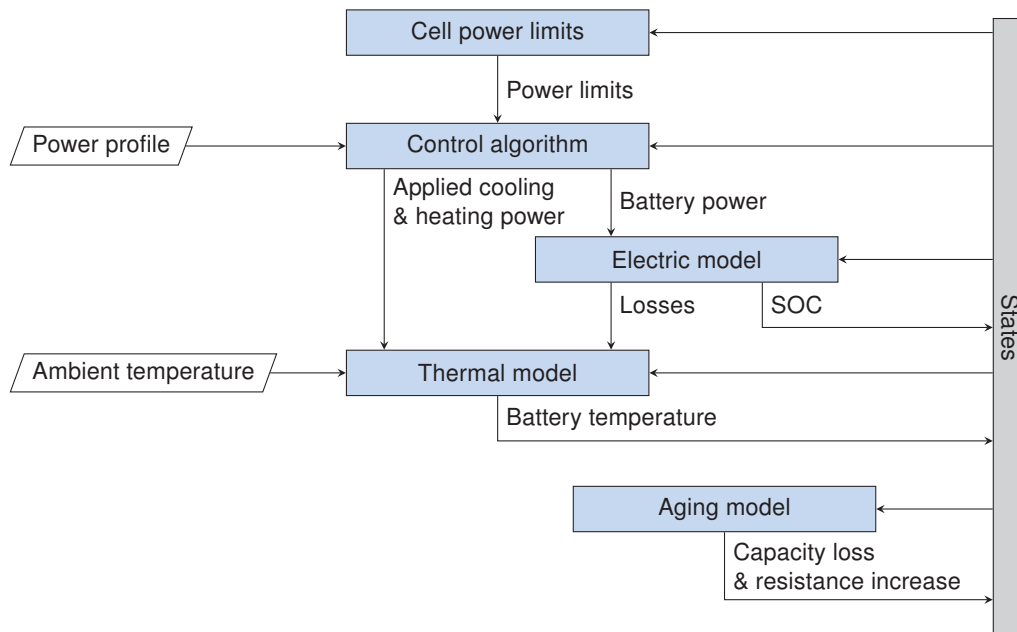


Figure 3.4: Schematic of implemented battery model, adapted from [113].

The model was applied to a stationary energy storage system supporting a fast charging station. The results showed that the cost-effectiveness of different BTMS designs depends on the climate in which the battery is operated. In Munich, passive cooling results in the lowest costs, whereas in Singapore, enhancing the heat transfer to ambient air with cooling fins proved to be the most cost-effective.

3.2.2 Contributions

I initiated the idea of the paper, implemented the battery model, wrote the first draft and implemented all revisions. Florian Müller helped reduce the computation time of the model significantly during his master thesis. Florian Müller and Markus Lienkamp provided valuable feedback during the many iterations following the first draft.



Contents lists available at ScienceDirect

Journal of Energy Storage

journal homepage: www.elsevier.com/locate/est

Research papers

Techno-economic design of battery thermal management systems in different climates

Olaf Teichert^{a,b,*}, Florian Müller^b, Markus Lienkamp^{a,b}^a TUMCREATE Ltd., 1 #10-02 Create Way, CREATE Tower, 138602, Singapore^b Technical University of Munich (TUM), School of Engineering & Design, Department of Mobility Systems Engineering, Institute of Automotive Technology, 85748 Garching, Germany

ARTICLE INFO

Keywords:

Battery thermal management system
 Techno-economic design
 Lithium-ion
 Climate
 Stationary energy storage

ABSTRACT

The battery thermal management system (BTMS) of a lithium-ion battery aims to prevent accelerated battery aging at elevated temperatures and reduced operability at low temperatures. Cooling or heating the battery prevents it from being operated outside the preferred temperature window but increases energy consumption, increases maintenance costs and requires an additional investment. Therefore, for a given use case, battery designers need to decide whether installing a heating system is required, if it is cost effective to install a cooling system, and how the battery should be thermally connected to the ambient air. This study presents a method for the techno-economic assessment of different BTMS. The method is applied to stationary energy storage (SES) supporting a fast charging station. This use case was chosen because these batteries are located outdoors and their heat transfer to the surrounding air can be increased or reduced without being limited by packaging constraints. The method is demonstrated by evaluating the cost of five different BTMS in the tropical climate of Singapore and the continental climate of Munich, Germany. The results show that the cost-effectiveness of different BTMS depends on the climate in which the battery is operated. For the Munich climate, the passively cooled baseline design results in the lowest cost, whereas in the Singapore climate the lowest cost is achieved by equipping the SES with cooling fins. Installing active cooling is not cost-effective in both climates for the given use case, but might be considered for ecological considerations, warranty requirements, or to allow safe operation in unexpected extreme conditions. The method enables thermal system designers to evaluate the cost effectiveness of different BTMS in different climate conditions during the early-stage design phase.

1. Introduction

Lithium-ion batteries play a central role in the reduction of global carbon emissions: they enable mobility without local emissions, and support the integration of renewable energy sources into the electric grid. Lithium-ion batteries are used for this wide range of applications due to their high energy density, high efficiency, low self discharge, and long cycle life [1]. However, lithium-ion cells are sensitive to the temperature at which they are stored and operated [2].

Temperatures above 25 °C cause accelerated capacity loss and internal resistance increase of a cell, thereby shortening the cell's operating life [3]. Temperatures above 60 °C can lead to safety critical conditions, that might result in a thermal runaway, and should thus be avoided at all times [3,4]. Operating a cell at temperatures below 15 °C decreases the available discharging power and can result in rapid capacity loss

caused by lithium plating, especially at high charging rates [5].

To prevent the negative effects of operating lithium-ion cells outside of their preferred temperature window, a wide range of battery thermal management systems (BTMS) is used to heat or cool the cells. The review papers by Xia et al. [6] and Jaguemont et al. [7] give a detailed overview of state-of-the-art BTMS and their advantages and disadvantages.

Low temperatures can be avoided by equipping a battery with insulation, electric heating mats, or a heat pump. Adding insulation requires a relatively small investment and does not generate energy consumption or maintenance costs, but can lead to undesired high battery temperatures at high ambient temperatures. Heating mats and heat pumps do not cause undesired high temperatures, since they are only activated when needed, but have higher investment and operating

* Corresponding author at: Technical University of Munich (TUM), School of Engineering & Design, Department of Mobility Systems Engineering, Institute of Automotive Technology, 85748 Garching, Germany.

E-mail address: olaf.teichert@tum.de (O. Teichert).

<https://doi.org/10.1016/j.est.2021.103832>

Received 28 April 2021; Received in revised form 12 December 2021; Accepted 13 December 2021
 2352-152X/© 2022 Elsevier Ltd. All rights reserved.

Nomenclature

$A_{sides,conv}$	SES effective side surface area for convection in m^2	\bar{P}_{dem}	Charging demand power profile in W
$A_{sides,rad}$	SES effective side surface area for radiation in m^2	P_{grid}	Power drawn from the grid in W
A_{top}	SES top surface area in m^2	P_{heat}	Applied heating power in W
c_{bat}	Specific battery cost in €Wh^{-1}	P_{heater}	Installed heating power in W
c_{cell}	Cell heat capacity in JK^{-1}	P_{ch}	Cell maximum charging power in W
c_{ene}	Energy cost in €kWh^{-1}	P_{dch}	Cell maximum discharging power in W
c_h	Battery housing heat capacity in JK^{-1}	P_{th}	Peak shaving threshold in W
C_{bat}	Annual discounted battery depreciation in €year^{-1}	P_{top}	SES top surface perimeter in m
C_{BTMS}	Annual BTMS costs in €year^{-1}	Q	Cell capacity in Ah
C_{cool}	Average annual cooling system energy consumption cost in €year^{-1}	Q_{loss}	Aging-induced capacity loss
C_{heat}	Average annual heating system energy consumption cost in €year^{-1}	$Q_{loss,EOL}$	End of life capacity loss criterion
C_{inv}	BTMS investment cost in €	Q_{nom}	Cell nominal capacity in Ah
C_{loss}	Average annual energy consumption cost due to parasitic losses in €year^{-1}	$R_{conv,top}$	Thermal resistance of convective heat transfer at the top of the housing in KW^{-1}
C_{maint}	BTMS annual maintenance costs in €year^{-1}	$R_{conv,sides}$	Thermal resistance of convective heat transfer at the sides of the housing in KW^{-1}
C_{rate}	Cell C-rate in h^{-1}	R_i	Cell internal resistance in Ω
C_{tot}	Sum of all considered cost components in €year^{-1}	R_{in}	Thermal resistance between cell and battery housing in KW^{-1}
COP_{cool}	Cooling system coefficient of performance	R_{inc}	Aging-induced internal resistance increase
COP_{heat}	Heating system coefficient of performance	R_{ins}	Thermal resistance of insulation material in KW^{-1}
CRF_{bat}	Capital recovery factor for battery investment	$R_{i,d}$	Cell discharging resistance in Ω
CRF_{BTMS}	Capital recovery factor for BTMS investment	$R_{i,c}$	Cell charging resistance in Ω
E_{bat}	Battery size in Wh	R_{out}	Thermal resistance between SES housing and ambient temperature in KW^{-1}
$E_{ene,cool}$	Average annual cooling system energy consumption in kWh	R_{rad}	Thermal resistance of radiative heat transfer in KW^{-1}
$E_{ene,heat}$	Average annual heating system energy consumption in kWh	s_{fins}	Cooling fin spacing in m
$E_{ene,p}$	Average annual energy consumed by parasitic losses in kWh	SOC	Cell state of charge (SOC)
h	SES height in m	SOC_{max}	Upper SOC limit
i	Interest rate	SOC_{min}	Lower SOC limit
I_{ch}	Cell instantaneous charging current limit in A	$t_{eol,bat}$	Battery life in s
$I_{ch,cont}$	Cell continuous charging current limit A	$t_{eol,BTMS}$	BTMS investment duration in s
I_{dch}	Cell instantaneous discharging current limit in A	t_{ins}	Insulation thickness in m
$I_{dch,cont}$	Cell continuous discharging current limit in A	$\bar{T}_{ambient}$	Ambient temperature profile in K
I_{cell}	Cell applied current in A	T_c	Cell temperature in K
j	Subscript denoting aging time step	T_{cool}	Cooling threshold in K
k	Subscript denoting simulation time step	T_h	Battery housing temperature in K
k_{air}	Thermal conductivity of air in $\text{W m}^{-1} \text{K}^{-1}$	T_{heat}	Heating threshold in K
k_{ins}	Thermal conductivity of insulation in $\text{W m}^{-1} \text{K}^{-1}$	T_{limit}	Safety critical temperature limit in K
l	SES length in m	U_{max}	Cell maximum voltage in V
l_{fins}	Cooling fin length in m	U_{min}	Cell minimum voltage in V
n_{cells}	Number of cells in the battery	U_{nom}	Cell nominal voltage in V
n_{fins}	Number of cooling fins	U_{OCV}	Cell open circuit voltage in V
Nu_{sides}	Nusselt number for convection at the side surfaces	w	SES width in m
Nu_{top}	Nusselt number for convection at the top surface	$z_{cell2pack}$	Ratio between the mass on cell level and pack level
P_{avail}	Power available for cooling or heating in W	Δt_j	Aging timestep in s
P_{bat}	Power drawn from or supplied to the battery in W	Δt_k	Simulation timestep in s
P_{cell}	Cell power in W	ϵ	Emittance
P_{cool}	Applied cooling power in W	σ	Stefan-Boltzmann constant
P_{cooler}	Installed cooling power in W		

costs. Heat pumps are more efficient than heating mats and may be used for cooling as well, but require a larger investment.

High temperatures can be avoided by increasing the heat transfer to ambient air, installing air cooling, or installing a refrigerant cooling

system [8]. Increasing the heat transfer to ambient air, also referred to as passive cooling, can be achieved with relatively small investment costs and without energy consumption or maintenance costs, but can lead to undesired low battery temperatures at low ambient

temperatures. Air cooling and a refrigerant cooling system do not cause undesired low temperatures, since they are only activated when needed, but have higher investment and operating costs. In contrast to the air cooling system, a refrigerant cooling system can cool the battery to temperatures below the ambient temperature, but requires larger investment and maintenance costs.

The majority of studies investigating BTMS evaluate the thermal system's performance by assessing the increase in cell temperature for a single load cycle or charging cycle, representing a typical or worst-case scenario. Few studies analyzed the performance of the BTMS for longer time periods under varying ambient conditions.

Neubauer et al. [9] assessed the operability of a passively cooled stationary energy storage (SES) coupled with a photovoltaic system providing peak shaving services at three different levels of shading in the climates of Phoenix, Arizona, Los Angeles, California, and Minneapolis, Minnesota. The thermal response of the cells and corresponding degradation was simulated over 10 years, where the peak shaving target was adjusted according to the degradation status. The results show that in all investigated climates the original peak shaving target of the SES could be maintained the longest in the fully shaded scenario.

In a later study, Neubauer et al. [10] investigated the impact of battery cooling and heating on the annual-miles-traveled of a battery electric vehicle in different climates, assuming that drivers will resort to different modes of transportation if the energy in the battery is insufficient to complete a given trip. The thresholds at which cooling and heating are activated were set to 30 °C and 10 °C, respectively. The results show that battery wear can be reduced by actively cooling the battery, especially in hot climates. In cold climates, the improvement in vehicle utilization achieved by heating is offset by the increase in energy consumption.

Yuksel et al. [11] simulated the lifetime of batteries in plug-in hybrid-electric vehicles, comparing an air-cooled battery to a passively cooled battery in different climates and for different driving cycles. Air cooling is activated when the battery temperature exceeds a fixed cooling threshold of 35 °C. The results show that air cooling can more than double the battery life in hot climates or under high-acceleration driving cycles.

Keyser et al. [12] investigated the effects of three BTMS for fast charging vehicles in Seattle and Phoenix: passive cooling, active cooling during driving, and active cooling during driving and standby. The cooling thresholds are not specified. The authors conclude that the choice of thermal system has little impact on the 10-year capacity loss in moderate climates such as Seattle, but can have a large impact in hot climates such as Phoenix.

Although previous studies investigated the impact of the BTMS choice on the battery life and the resulting operability in different climates, no conclusions with respect to the cost effectiveness were made. Furthermore, the impact of the selected cooling and heating threshold was not investigated. Finally, none of the previous studies investigated the impact of enhancing or reducing the heat transfer to ambient air.

In this study we present a holistic method for evaluating the cost effectiveness of different BTMS. The method is applied to an SES that supports a fast charging station by reducing the power drawn from the grid, thereby reducing peak demand charges and grid reinforcement costs. This application was selected because SES supporting fast-charging stations present a unique use case for the thermal system design: different from SES coupled with photovoltaic systems, they are located outdoors and are therefore directly affected by climate conditions; different from vehicle batteries, the packaging constraints for SES supporting fast charging stations are less strict, which makes it possible to enhance or reduce the heat transfer to the ambient air through cooling fins or insulation [13].

The method combines a cost model with an operability constraint, a safety constraint and a battery simulation that quantifies the battery

life, cooling system energy consumption, heating system energy consumption, and parasitic losses. For each BTMS, the minimum heating threshold that prevents the operability constraint from being violated is found. Furthermore, for the active-cooled BTMS the cost-optimal cooling threshold is determined. BTMS configurations that violate the safety constraint are not considered. A case study investigates the cost effectiveness of installing active cooling, installing cooling fins, or insulating the SES, for two different climates: the tropical climate of Singapore and the continental climate of Munich, Germany. The method serves as a decision-making aid for BTMS designers during the early-stage design phase.

The contributions of this study can be summarized as follows:

- A techno-economic assessment of BTMS configurations in different climates
- Evaluation of the optimal cooling threshold and required heating threshold for different BTMS
- Quantification of the impact of thermal design measures that enhance or reduce the heat transfer to the ambient heat sink

The presented method and simulation are available open source and can be accessed at the following repository: <https://github.com/TUMFTM/BTMS-Design>. The method was implemented in the Julia programming language to accommodate the computational intensity of the simulations [14].

2. Method

To quantify the cost effectiveness of different BTMS, a cost model is combined with a battery simulation. Furthermore, an operability constraint ensure that the SES can effectively reduce the power drawn from the grid throughout its entire operating life, and a safety constraint warrants that the maximum temperature never exceeds the safety critical temperature limit. An overview of all the variables introduced in the following can be found in the nomenclature.

2.1. Cost model

The cost model only considers cost components that are influenced by the BTMS configuration. To allow comparing investment costs and operational costs, investments are expressed by their annual discounted depreciation, while operational costs are expressed by the average annual operating costs. The total costs are given by Eq. (1), where C_{bat} is the annual discounted battery depreciation, C_{BTMS} denotes the annual depreciation and maintenance cost of the BTMS, C_{cool} and C_{heat} are the average annual energy cost for operating the cooling and heating system, respectively, and C_{loss} is the average annual energy cost due to parasitic losses in the battery.

$$C_{\text{tot}} = C_{\text{bat}} + C_{\text{BTMS}} + C_{\text{cool}} + C_{\text{heat}} + C_{\text{loss}} \quad (1)$$

The annual discounted battery depreciation is calculated by Eq. (2), where E_{bat} denotes the battery size and c_{bat} is the specific battery cost. The capital recovery factor of the battery investment, denoted by CRF_{bat} , is used to convert the investment cost into the annual discounted depreciation and is given by Eq. (3), where i denotes the discount factor and $t_{\text{eol, bat}}$ is the time until the end of life (EOL) of the battery is reached in years.

$$C_{\text{bat}} = E_{\text{bat}} c_{\text{bat}} CRF_{\text{bat}} \quad (2)$$

$$CRF_{\text{bat}} = \frac{i(1+i)^{t_{\text{eol, bat}}}}{(1+i)^{t_{\text{eol, bat}}} - 1} \quad (3)$$

The depreciation and maintenance costs of the BTMS are calculated using Eq. (4), where C_{maint} denotes the annual maintenance costs and C_{inv} denotes the BTMS investment costs. The capital recovery factor, CRF_{BTMS} is used to calculate the annual discounted depreciation of

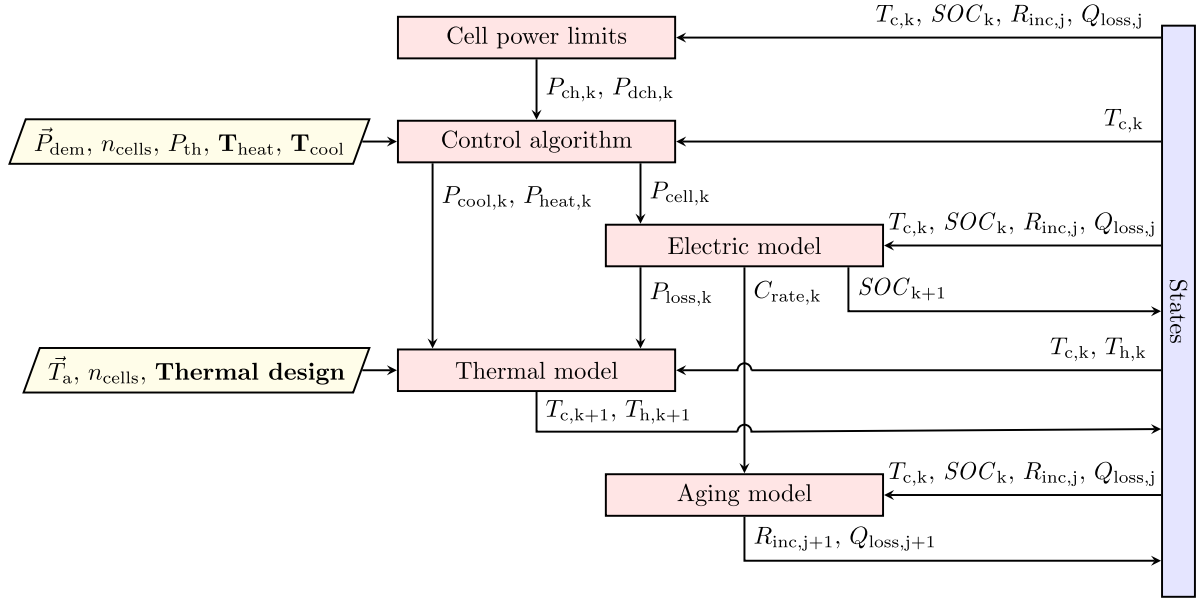


Fig. 1. Overview of the battery simulation framework. Inputs are represented by yellow parallelograms, functions by red horizontal rectangles and the logged system states are denoted by a blue vertical rectangle. The variables that define the BTMS configuration are emphasized in bold, whereas input vectors are marked by an arrow superscript.

the investment, analogous to the battery investment costs, following Eq. (5).

$$C_{BTMS} = C_{maint} + C_{inv} CRF_{BTMS} \quad (4)$$

$$CRF_{BTMS} = \frac{i(1+i)^{t_{eol,BTMS}}}{(1+i)^{t_{eol,BTMS}} - 1} \quad (5)$$

The average annual energy consumption costs resulting from operating the cooling system, operating the heating system, and parasitic losses are calculated by Eqs. (6)–(8), where c_{ene} is the specific energy cost and $E_{ene,cool}$, $E_{ene,heat}$ and $E_{ene,loss}$ denote the average annual energy consumption of the cooling system, the heating system, and parasitic losses, respectively.

$$C_{cool} = E_{ene,cool} c_{ene} \quad (6)$$

$$C_{heat} = E_{ene,heat} c_{ene} \quad (7)$$

$$C_{loss} = E_{ene,loss} c_{ene} \quad (8)$$

To determine the battery life and the energy consumed by cooling, heating, and parasitic losses, the battery operation is simulated.

2.2. Battery simulation

The battery simulation models the operation of the battery for a given BTMS configuration, using the cell's power limits, a control algorithm, an electric model, a thermal model, and an aging model. The simulation framework is shown in Fig. 1. The variables that define the BTMS configuration are emphasized in bold and correspond to the heating threshold, denoted by T_{heat} , the cooling threshold, denoted by T_{cool} and the thermal design, which determines the addition of cooling fins or insulation. In the following, first an overview of the simulation framework is given and then the calculations are described in detail.

It is assumed that all cells in the battery pack start with equal parameters and have the same temperature throughout the simulation, which enables reducing the model to a single cell. The number of cells in the pack are calculated using Eq. (9), where U_{nom} and Q_{nom} correspond to the nominal voltage and capacity of the cell, respectively.

$$n_{cells} = \frac{E_{bat}}{U_{nom} Q_{nom}} \quad (9)$$

The simulation uses two time steps: a short time step, denoted by the subscript k , to update the cells state of charge (SOC), SOC_k , cell temperature, $T_{c,k}$, and housing temperature, $T_{h,k}$; and a larger time step, denoted by the subscript j , at which the aging-induced capacity loss, $Q_{loss,j}$ and internal resistance increase $R_{inc,j}$ are updated.

For every short time step, first the maximum charging and discharging power of a single cell, denoted by $P_{ch,k}$ and $P_{dch,k}$, are calculated, subject to the cell temperature, SOC and aging status of the cell. Subsequently, a control algorithm determines the power drawn from or supplied to a cell, $P_{cell,k}$, the applied cooling power, $P_{cool,k}$, and the applied heating power, $P_{heat,k}$, based on the power demand, $\vec{P}_{dem,k}$, the number of cells, the peak shaving threshold, P_{th} , the heating and cooling thresholds, and the cell temperature. The electric model then computes the C-rate, $C_{rate,k}$, the ohmic losses, $P_{loss,k}$, and the new SOC, based on the cell temperature, SOC, and aging state. Based on the ohmic losses, the thermal model calculates the new cell temperature and housing temperature taking into account the ambient temperature, \vec{T}_a,k , the number of cells and the thermal design. At the larger time step, the aging states are updated, based on the battery temperatures, SOC, and C-rates over that interval.

The simulation steps are repeated until the capacity loss exceeds a predefined end of life condition, $Q_{loss,eol}$. Finally, the inputs required for the cost model can be calculated, using Eqs. (10)–(13), where Δt_k denotes the short simulation time step duration and Δt_j denotes the duration at which the aging status is updated. The constant in Eq. (10) converts the battery life from seconds to years, while the constants in Eq. (11)–(13) correspond to the conversion from Joule to kilowatt-hours.

$$t_{eol,bat} = \frac{1}{3600 \times 24 \times 365} \sum_{j=1}^{Q_{loss,j} > Q_{loss,eol}} \Delta t_j \quad (10)$$

$$E_{ene,cool} = \frac{1}{1000 \times 3600} \frac{1}{t_{eol,bat}} \sum P_{cool,k} \Delta t_k \quad (11)$$

$$E_{ene,heat} = \frac{1}{1000 \times 3600} \frac{1}{t_{eol,bat}} \sum P_{heat,k} \Delta t_k \quad (12)$$

$$E_{ene,loss} = \frac{1}{1000 \times 3600} \frac{1}{t_{eol,bat}} \sum P_{loss,k} \Delta t_k \quad (13)$$

2.2.1. Cell power limits

To determine the power limits of the cells, first the maximum charging and discharging currents, denoted by I_{ch} and I_{dch} , are calculated

according to the method proposed by Plett [15] and given in (14) and Eq. (15). Negative powers and currents correspond to discharging the cell, while positive powers and currents correspond to charging. The first term prevents exceeding the continuous charging and discharging current limits, $I_{ch,cont}$ and $I_{dch,cont}$, the second term prevents exceeding the voltage limits, U_{min} and U_{max} , and the third term prevents exceeding the state of charge limits, SOC_{min} and SOC_{max} . The constant converts the cell capacity from ampere-hours to coulomb. The cell open circuit voltage, U_{OCV} , remaining capacity, Q , charging resistance, $R_{i,c}$, and discharging resistance, $R_{i,d}$, are updated at each time step according to the cell temperature, SOC, and aging status. To prevent lithium plating, the charging rate is reduced at low temperatures by the factor k_{der} , following the relationship between the maximum non-harming charging rate and cell temperature derived by Remmlinger et al. [5]. Subsequently, the maximum charging and discharging power are calculated using Eqs. (16) and (17).

$$I_{ch} = \min \left(k_{der} I_{ch,cont}, \frac{U_{max} - U_{OCV}}{R_{i,c}}, \frac{3600 Q (SOC_{max} - SOC_k)}{\Delta t_k} \right) \quad (14)$$

$$I_{dch} = \max \left(-I_{dch,cont}, \frac{U_{min} - U_{OCV}}{R_{i,d}}, \frac{3600 Q (SOC_{min} - SOC_k)}{\Delta t_k} \right) \quad (15)$$

$$P_{ch,k} = I_{ch}(U_{OCV} + R_{i,c} I_{ch}) \quad (16)$$

$$P_{dch,k} = I_{dch}(U_{OCV} + R_{i,d} I_{dch}) \quad (17)$$

$$\text{where } \begin{cases} U_{OCV} &= f(SOC_k) \\ R_{i,d} &= f(SOC_k, T_{c,k}) (1 + R_{inc,j}) \\ R_{i,c} &= f(SOC_k, T_{c,k}) (1 + R_{inc,j}) \\ Q &= Q_{nom} - Q_{loss,j} \\ k_{der} &= f(T_{c,k}) \end{cases}$$

2.2.2. Control algorithm

The control algorithm ensures that the power drawn from the grid does not exceed the peak shaving threshold by discharging the battery when the power demand exceeds this threshold. The remaining available power, denoted by P_{avail} , and calculated by Eq. (18), is then used to power the heating and cooling system if the cell temperature falls below the heating threshold or exceeds the cooling threshold, following Eqs. (19) and (20), where P_{heater} and P_{cooler} denote the installed heating and cooling power. If the power demand drops below the peak shaving threshold, the battery is recharged, subject to the maximum charging power. The power drawn from or supplied to the battery, the power on cell level, and the power drawn from the grid are then calculated using Eqs. (21)–(23).

$$P_{avail} = \max(P_{th} - \bar{P}_{dem,k} - n_{cells} P_{dch,k}, 0) \quad (18)$$

$$P_{heat,k} = \begin{cases} \min(P_{heater}, P_{avail}) & \text{if } T_{c,k} \leq T_{heat} \\ 0 & \text{if } T_{c,k} > T_{heat} \end{cases} \quad (19)$$

$$P_{cool,k} = \begin{cases} 0 & \text{if } T_{c,k} < T_{cool} \\ \min(P_{cooler}, P_{avail}) & \text{if } T_{c,k} \geq T_{cool} \end{cases} \quad (20)$$

$$P_{bat} = \min(P_{th} - \bar{P}_{dem,k} - P_{heat,k} - P_{cool,k}, n_{cells} P_{ch,k}) \quad (21)$$

$$P_{grid} = \bar{P}_{dem,k} + P_{bat} \quad (22)$$

$$P_{cell,k} = P_{bat} / n_{cells} \quad (23)$$

2.2.3. Electric model

The electric behavior of the battery is modeled by the equivalent circuit model shown in Fig. 2(a). The cell current, I_{cell} , is calculated by Eq. (24), where the internal resistance, R_i , corresponds to the charging

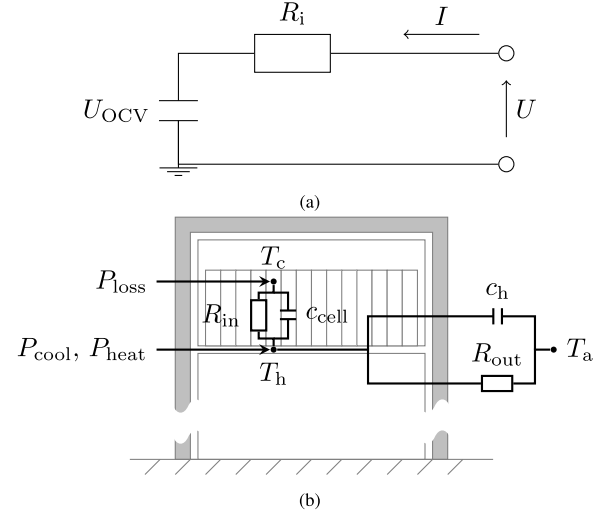


Fig. 2. Model representation of the SES: (a) Equivalent circuit model of a single cell, (b) Thermal Model of the SES, shown here with insulation material.

resistance for positive cell powers and to the discharging resistance for negative cell powers. Subsequently, the C-rate, the state of charge at the end of the time step and the ohmic losses are calculated using Eqs. (25)–(27), respectively.

$$I_{cell} = \frac{-U_{OCV} + \sqrt{U_{OCV}^2 + 4 R_i P_{cell,k}}}{2 R_i} \quad (24)$$

$$C_{rate,k} = \frac{I_{cell}}{Q} \quad (25)$$

$$SOC_{k+1} = SOC_k + \frac{C_{rate,k} \Delta t_k}{3600} \quad (26)$$

$$P_{loss,k} = R_i I_{cell}^2 \quad (27)$$

$$\text{where } \begin{cases} U_{OCV} &= f(SOC_k) \\ R_{i,d} &= f(SOC_k, T_{c,k}) (1 + R_{inc,j}) \\ R_{i,c} &= f(SOC_k, T_{c,k}) (1 + R_{inc,j}) \\ R_i &= \begin{cases} R_{i,c} & \text{if } P_{cell,k} > 0 \\ R_{i,d} & \text{if } P_{cell,k} \leq 0 \end{cases} \\ Q &= Q_{nom} - Q_{loss,j} \end{cases}$$

2.2.4. Thermal model

The thermal model assumes that the SES consists of a cuboid housing with internal shelves on which the battery modules are placed, as shown in Fig. 2(b). The battery temperature is modeled by a lumped capacitance model with two thermal masses, corresponding to a single cell and the battery housing, similar to [10,11]. The thermal model therefore assumes that all cells within the battery pack have the same temperature and that the housing temperature is uniform. As Neubauer et al. [9] showed that it is beneficial to provide full shading for the SES, it is assumed that the SES is unaffected by solar irradiation, wind, or precipitation. Furthermore, the heat exchange with the ground is assumed to be negligible and it is assumed that there is no heat exchange between the battery and the power electronic components of the charging station. Heat flow entering the thermal masses is defined as positive.

The temperature of the battery cells at the end of the time-step is calculated using Eq. (28), where c_{cell} denotes the cell's heat capacity and R_{in} is the thermal resistance between the cell internals and the housing.

$$T_{c,k+1} = T_{c,k} + \frac{\Delta t_k}{c_{cell}} \left(P_{loss,k} + \frac{T_{h,k} - T_{c,k}}{R_{in}} \right) \quad (28)$$

The updated housing temperature is calculated using Eq. (29), where c_h denotes the housing heat capacity, COP_{heat} and COP_{cool} are the coefficients of performance of the heating and cooling systems respectively and R_{out} is the thermal resistance between the battery housing and the ambient air. The cooling and heating systems are assumed to act directly on the housing, which approximates the behavior of integrated cooling channels or a heating mat.

$$T_{h,k+1} = T_{h,k} + \frac{\Delta t_k}{c_h} \left(P_{heat,k} COP_{heat} + P_{cool,k} COP_{cool} + \frac{n_{cells} (T_{c,k} - T_{h,k})}{R_{in}} + \frac{T_{a,k} - T_{h,k}}{R_{out}} \right) \quad (29)$$

The housing heat capacity is estimated by assuming that the housing's specific heat capacity matches the specific heat capacity of aluminum. The heat capacity can then be calculated using Eq. (30), where m_{cell} is the cell mass, $z_{cell2pack}$ is the ratio between the mass on cell and on pack level, and $c_{p,alu}$ is the specific heat capacity of aluminum.

$$c_h = n_{cells} m_{cell} (z_{cell2pack} - 1) c_{p,alu} \quad (30)$$

The thermal resistance between the battery housing and the ambient air, R_{out} , takes into account insulation, natural convection at the top and sides of the battery, and radiation, according to Eq. (31), where R_{ins} is the thermal resistance of any installed insulation material, $R_{conv,top}$ and $R_{conv,sides}$ are the thermal resistances of convection at the top and sides of the housing, and R_{rad} is the thermal resistance of radiation.

$$R_{out} = R_{ins} + \left(\frac{1}{R_{conv,top}} + \frac{1}{R_{conv,sides}} + \frac{1}{R_{rad}} \right)^{-1} \quad (31)$$

To determine the thermal resistances, first the surface areas of the SES are calculated using Eqs. (32)–(36), where l , w , and h are the length, width, and height of the SES respectively, t_{ins} is the thickness of the insulation material, s_{fins} is the spacing between cooling fins, l_{fins} is the cooling fin length, A_{top} denotes the top surface area, P_{top} is the top surface perimeter, and n_{fins} is the number of installed cooling fins. We differentiate between the effective side surface areas for natural convection, $A_{side,conv}$, and for radiation, $A_{side,rad}$, where the latter does not include the surface area of cooling fins facing each other. The impact of the cooling fin efficiency on the effective surface area for convection is neglected, as the fin efficiency approaches unity for low heat transfer coefficients such as those resulting from natural convection [16].

$$A_{top} = (l + 2 t_{ins}) (w + 2 t_{ins}) \quad (32)$$

$$P_{top} = 2 l + 2 w + 8 t_{ins} \quad (33)$$

$$n_{fins} = P_{top} / s_{fins} + 4 \quad (34)$$

$$A_{sides,conv} = h (P_{top} + 2 l_{fins} n_{fins}) \quad (35)$$

$$A_{sides,rad} = h (P_{top} + 8 l_{fins}) \quad (36)$$

Finally, the individual thermal resistances are calculated using Eqs. (37)–(40), where k_{ins} is the thermal conductivity of the insulation material, Nu_{top} and Nu_{sides} are the Nusselt numbers for natural convection on the top and side surfaces, k_{air} is the thermal conductivity of air, ϵ is the emittance, and σ the Stefan–Boltzmann constant. The Nusselt numbers are calculated using empirical correlations for natural convection over vertical [17] and horizontal [18] isothermal plates.

$$R_{ins} = \frac{t_{ins}}{k_{ins}(A_{top} + A_{sides,rad})} \quad (37)$$

$$R_{conv,top} = \frac{1}{Nu_{top} k_{air} P_{top}} \quad (38)$$

$$R_{conv,sides} = \frac{h}{Nu_{sides} k_{air} A_{sides,conv}} \quad (39)$$

$$R_{rad} = \frac{1}{\epsilon \sigma (T_{s,k}^2 + T_{a,k}^2) (T_{s,k} + T_{a,k}) (A_{top} + A_{sides,rad})} \quad (40)$$

2.2.5. Aging model

The aging model calculates the decrease in capacity and the increase in internal resistance due to battery aging using the semi-empirical aging model developed by Naumann et al. [3,19]. The aging model superimposes calendaric aging and cyclic aging, where calendaric aging is a function of the cell temperature and SOC, and cyclic aging is a function of the depth of discharge (DOD) and C-rate. To determine the DOD of the charge–discharge cycles in the interval over which aging is evaluated, the rainflow counting algorithm described by Downing et al. is used [20]. Two minor adjustments to the aging model were made.

First, the aging tests performed by Naumann et al. at temperatures below 25 °C showed ambiguous results and were therefore excluded during the parametrization of the aging model, limiting its validity to temperatures above this point. To model the full range of occurring temperatures, it is assumed that the aging rate does not decrease further for temperatures below 25 °C. This is implemented by using the temperature-dependent aging factor at 25 °C for all temperatures below this point. Cell aging at low temperatures due to lithium plating is assumed to be fully prevented by reducing the charging current in the power limit estimation in Eq. (14).

Second, Naumann et al. investigated the impact of the C-rate on battery aging for C-rates up to 1 C, finding a negative correlation between the magnitude of the C-rate and the aging-induced increase in internal resistance. However, using the linear curve fit they applied results in a reduction of the internal resistance at large C-rates. Therefore, the C-rate-dependent aging factor for the internal resistance increase at 1 C is used for all larger C-rates. Note that this adjustment does not apply to the capacity loss, that it results in a larger internal resistance increase compared to the unaltered aging model, and that it only applies to discharging, as the non-harming charging rate defined by Remmlinger et al. is limited to 1 C.

2.3. Constraints

At the end of the battery simulation, it is evaluated whether the operability constraint and the safety constraint are met. BTMS configurations that do not meet either of the constraints are not considered.

The operability constraint guarantees that the power drawn from the grid never exceeds the peak shaving threshold, by ensuring that the discharging power limit of the SES is sufficient throughout the operating life of the SES, as given in Eq. (41).

$$n_{cells} P_{dch,k} \leq (P_{th} - \max(\vec{P}_{dem})) \quad \forall k \in [1..t_{eol,bat}/\Delta t_k] \quad (41)$$

The safety constraint guarantees that the maximum cell temperature never exceeds the safety critical temperature limit, denoted by T_{limit} , as given in Eq. (42).

$$T_{c,k} < T_{limit} \quad \forall k \in [1..t_{eol,bat}/\Delta t_k] \quad (42)$$

3. Case study

In the following, first the design of experiment is described to give an overview of the simulations that were conducted. Subsequently, the details of the considered use case are presented.

3.1. Design of experiment

The case study investigates the cost of five BTMS: a baseline design, a design with cooling fins, the baseline design with active cooling, a design with cooling fins and active cooling, and a design with insulation and active cooling. An uncooled design with insulation is not considered, as it would result in cells exceeding the safety-critical temperature limit. The absence of active cooling is modeled by setting the cooling threshold to infinity. The costs of BTMS with active cooling are calculated for cooling thresholds between 25 °C and 60 °C to determine the cost-optimal threshold. Additionally, to ensure functionality at low

Table 1

Investigated BTMS and the investment costs, operating life and maintenance costs of their components.

BTMS	BTMS Components	C_{inv}	$t_{eol,BTMS}$	C_{maint}
I	–	€0	–	€0 year ⁻¹
II	Cooling fins [22]	€810	30 years	€0 year ⁻¹
III	Active cooling [21]	€13,000	20 years	€135 year ⁻¹
IV	Active cooling [21] Cooling fins [22]	€13,000 €810	20 years 30 years	€135 year ⁻¹ €0 year ⁻¹
V	Active cooling [21] Insulation [23]	€13,000 €10	20 years 30 years	€135 year ⁻¹ €0 year ⁻¹

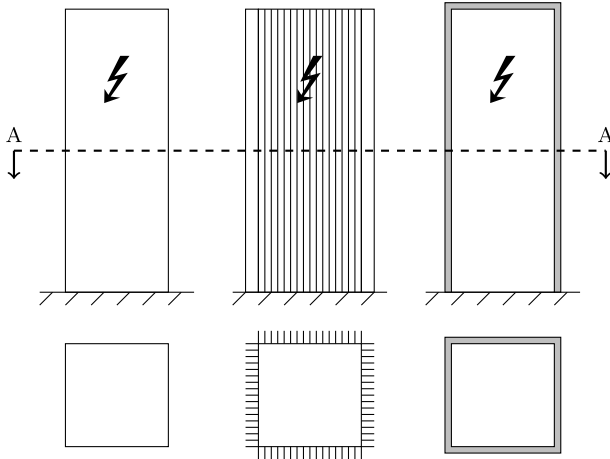


Fig. 3. Thermal designs from left to right: baseline, baseline with cooling fins, and insulated baseline design.

ambient temperatures, for each combination of cooling threshold and thermal design, the heating threshold is increased iteratively from 10 °C to 20 °C until the operability constraint is met. The BTMS including the investment costs, operating life and annual maintenance costs of their components are shown in Table 1. On top of the listed components, a heater with an investment cost of €8000, operating life of 30 years and maintenance cost of €810 year⁻¹ is added if using the heater was required to fulfill the operability constraint in the simulation, i.e. $E_{ene,heat} > 0$ [21].

A schematic representation of the baseline design, the design with cooling fins, and the insulated design is shown in Fig. 3. For the baseline design, the insulation thickness and fin length are both set to 0 m. The design with cooling fins adds cooling fins with a length, l_{fins} , of 0.1 m and spacing, s_{fins} , of 0.05 m along the battery housing perimeter, whereas the insulated design adds expanded polystyrene padding with a thickness, t_{ins} , of 0.02 m to the side and top surfaces of the battery housing.

The cost effectiveness is investigated for the tropical climate of Singapore and the continental climate of Munich, Germany. Both climates are modeled using hourly ambient temperature data, \bar{T}_a , that was recorded for the year 2015 in each location [24] and is shown in Fig. S1. In the simulation, the hourly temperature data is interpolated to match the small simulation time-step and is repeated until the end of life condition is reached.

3.2. Use case

The power demand, \bar{P}_{dem} , corresponds to the demand of a bus charging station and was derived in previous work by using an agent-based city-scale simulation to simulate the operation of all buses in Singapore [25]. The power demand is shown in Fig. S2 and has a maximum demand of 705 kW. The same power demand profile is used

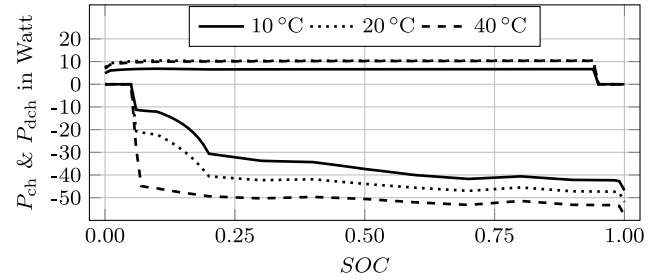


Fig. 4. Power limits of the considered cell with SOC limits at 0.05 and 0.95.

for both climates. In the simulation, the power profile is repeated until the end of life condition is reached.

The peak shaving threshold is set to 300 kW to reduce the maximum power drawn from the grid, thereby reducing peak demand charges and reducing the required power rating of the grid transformer. The battery size is set to 98 kWh, which was iteratively determined to be the smallest battery size that does not violate the operability constraint of a well-heated and well-cooled battery in the Munich climate. The resulting maximum discharging C-rate of the battery equals 4.13 C.

The calculations of the cell power limits and electric model are parametrized with data corresponding to the Sony US26650FTC1 LiFePO₄/graphite cell, which was also used to parametrize the implemented aging model. A curve fit is used to determine the open circuit voltage for different SOC values, whereas the charging and discharging resistance for different SOC and temperatures are determined by linear interpolation and extrapolation [26]. The resulting power limits for an unaged cell, calculated with Eqs. (16)–(17), are shown in Fig. 4.

An overview of all constant parameters used to parametrize the model is given in Table 2. The small simulation time-step was set to 10 s to match the timestep of the used charging demand profile, whereas the aging state is updated at the end of each day. The end of life criterion was defined as 30% capacity loss. The width, length, and height of the SES are based on a similarly sized SES, which supports fast charging buses [27]. The COP of the heating system matches an ideal heating mat, the emittance corresponds to a painted surface, and the thermal conductivity of the insulation material corresponds to expanded polystyrene.

4. Results

In the following, first the battery operation is illustrated for a single BTMS configuration. Subsequently, the required heating threshold and optimal cooling threshold for all BTMS is presented. Finally, a comparison between the total cost of all BTMS is made.

4.1. BTMS operation

The SES operation is illustrated at the example of a BTMS with the baseline thermal design and a cooling threshold of 35 °C in the Singapore climate, as shown in Fig. 5. BTMS operation in the climate of Munich and operation over a longer period are shown in Fig. S3 and S4. The first pane shows how the grid power is effectively reduced to the selected peak shaving threshold by discharging the battery during the high power demand phase that occurs after the buses return from the Singapore morning rush hour around 9 AM.

As a result, the battery is discharged to 48.8% SOC, as shown in the second pane. Lower SOC values are reached when the battery capacity and efficiency reduce through aging or when the battery charge rate is limited at lower cell temperatures. However, the minimum SOC is never reached, as the reduced discharging power at low SOC requires over-sizing the SES.

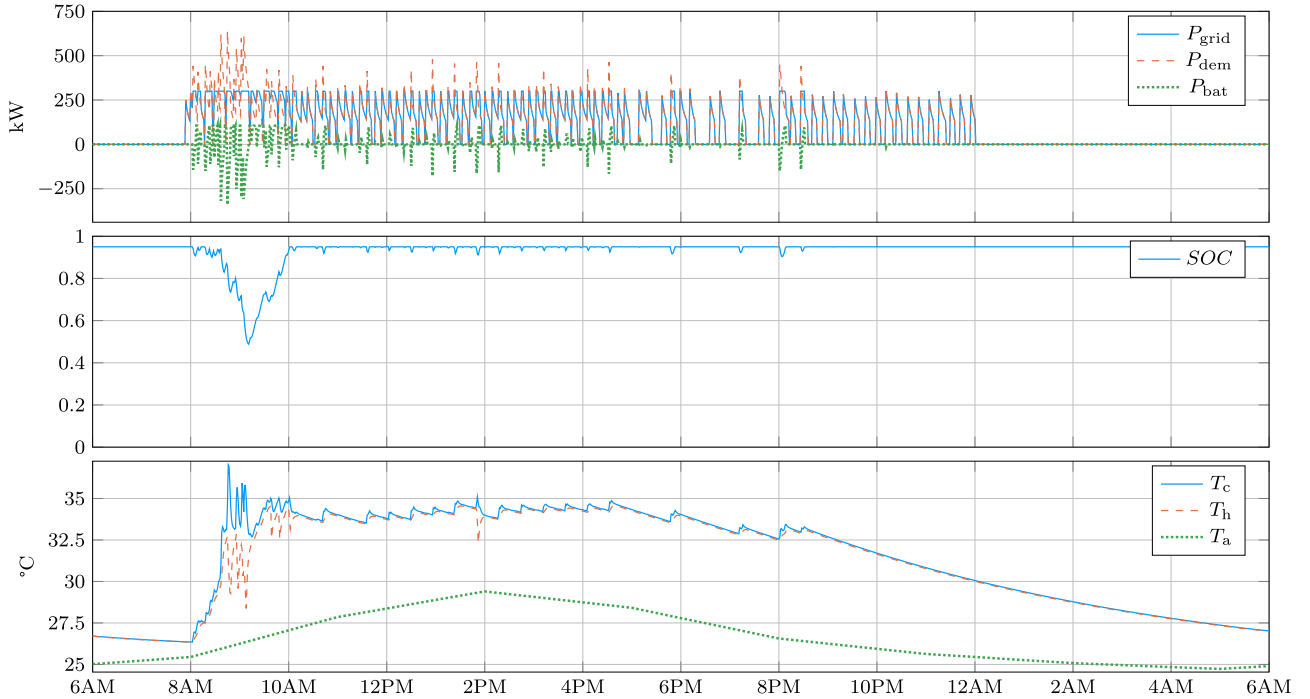


Fig. 5. Single day of operation for a 98 kWh SES with the baseline thermal design and a cooling threshold of 35 °C limiting the power drawn from the grid by a bus charging station to 300 kW in the Singapore climate.

Table 2
Constant parameters used in the case study.

Parameter	Symbol	Value
Discount factor	i	0.05 [25]
Specific battery cost	c_{bat}	€0.420 Wh ⁻¹ [28]
Specific energy cost	c_{ene}	€0.1909 kW ⁻¹ h [29]
Simulation timestep	Δt_k	10 s
Aging timestep	Δt_j	86,400 s
EOL capacity loss	$Q_{loss,EOL}$	0.3
Cell nominal capacity	Q_{nom}	3.0 Ah [3]
Cell nominal voltage	U_{nom}	3.2 V [3]
Cell min. voltage	U_{min}	2.0 V [3]
Cell max. voltage	U_{max}	3.6 V [3]
Cell min. SOC	SOC_{min}	0.05 [30]
Cell max. SOC	SOC_{max}	0.95 [30]
Cell max. discharge current	$I_{min,cont}$	20 A [3]
Cell max. charge current	$I_{max,cont}$	3 A [3]
Cell heat capacity	c_{cell}	76.27 J K ⁻¹ [31]
Cell thermal resistance	R_{in}	3.3 KW ⁻¹ [31]
Cooling power	P_{cool}	10 kW [32]
Heating power	P_{heat}	11.2 kW [32]
Cooling COP	COP_{cool}	-3 [32]
Heating COP	COP_{heat}	1
Cell mass	m_{cell}	0.0845 kg [3]
Cell-to-pack mass ratio	$z_{cell2pack}$	1.8 [33]
Aluminum spec. heat capacity	$c_{p,alu}$	896 J kg ⁻¹ K ⁻¹ [34]
SES height	h	2.2 m [27]
SES width	w	0.8 m [27]
SES length	l	0.8 m [27]
Insulation thermal conductivity	k_{ins}	0.035 W m ⁻¹ K ⁻¹ [34]
Air thermal conductivity	k_{air}	0.0264 W m ⁻¹ K ⁻¹ [34]
Emittance	ϵ	0.92 [34]
Stefan-Boltzmann constant	σ	5.67e-8 [34]
Safety critical temperature limit	T_{limit}	60 °C [3]

The resulting cell and housing temperatures are shown in the third pane, together with the ambient temperature. During the high power demand phase, the cell temperature and subsequently the housing temperature increase. Once the cell temperature exceeds the cooling threshold of 35 °C, the cooling system is activated, which directly lowers the housing temperature. Due to the thermal inertia of the

battery cells and the thermal resistance between the cells and the housing, the cell briefly exceeds the cooling threshold before the cells cool down. After the morning peak in power demand, the battery is recharged and used sporadically throughout the rest of the day, not discharging below 90 % SOC. The short discharge events result in minor temperature rises that require the cooling system to be briefly activated again once around 2pm. Finally, during the night, the battery cools down towards the ambient temperature.

4.2. Required heating thresholds

For each combination of cooling threshold and thermal design, the required heating threshold was determined by iteratively increasing the heating threshold from 10 °C to 20 °C until the operability constraint was met. Increasing the heating threshold prevents the operability constraint from being violated in two ways. First, a higher heating threshold prevents the cells from reaching low temperatures at which the internal resistance is higher and therefore the discharging power is limited. Second, by preventing low temperatures, the cells are able to recharge faster, which prevents them from reaching low SOC at which the discharging power is limited as well.

For the Singapore climate, no heating is required, since the battery never reaches temperatures at which the charging power is reduced. The required heating thresholds for the Munich climate are shown in Fig. 6. The required heating thresholds for the baseline design and the design with cooling fins increase with the cooling threshold. At higher cooling thresholds, the battery is operated at higher average temperatures, which results in a larger increase of the internal resistance at the end of life of the battery, as shown in Fig. S5, and therefore reduces the maximum discharging power. The heating threshold is slightly higher for the design with cooling fins as more heat is dissipated to the ambient air due to the enhanced thermal connectivity. The insulated design does not require any heating. Due to the safety constraint, only insulated BTMS with cooling thresholds below 53 °C are considered, since higher cooling thresholds would result in cell temperatures exceeding the safety critical temperature.

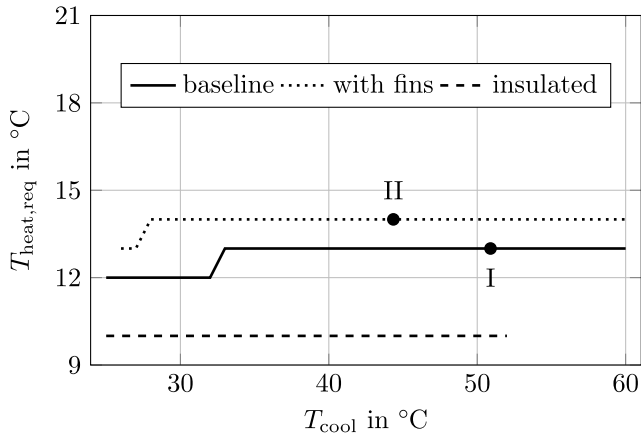


Fig. 6. Required heating thresholds to fulfill the operability constraint for a 98 kWh SES limiting the power drawn from the grid by a bus charging station to 300 kW in the Munich climate for different thermal designs and cooling thresholds. The annotations refer to the passively cooled BTMS defined in Table 1 and are placed at the cooling threshold at which no cooling energy is consumed.

4.3. Optimal cooling threshold

The individual cost components for the range of cooling threshold are shown for all BTMS in Fig. 7 for the Munich and Singapore climates. The impact of the cooling threshold on the BTMS investment and maintenance costs is not shown, since these costs are independent from the cooling threshold. The impact of the cooling threshold on the battery life, internal resistance increase, minimum temperature, average temperature and maximum temperature is shown in Fig. S5.

The top panes in Fig. 7 show the annual battery depreciation for the Munich and Singapore climates. For both climates and for all thermal designs, the annual battery depreciation increases with higher cooling thresholds. SES with higher cooling thresholds are, on average, operated at higher temperatures, which results in a shorter battery life and therefore higher battery depreciation costs. For both climates, the increase in battery costs at higher cooling thresholds is largest for the insulated design and smallest for the design with cooling fins. This is due to the higher passive dissipation of heat for the designs with a better thermal connectivity to the ambient heat sink, resulting in a lower average temperature and longer battery life. Since the ambient temperatures in the Munich climate are, on average, lower than those in Singapore, this effect is more pronounced for the Munich climate. Finally, for both climates, the battery depreciation converges for all thermal designs as the cooling threshold approaches 25 °C, since battery aging was assumed not to decrease further for temperatures below 25 °C.

The second row of panes in Fig. 7 shows the average annual cooling system energy consumption costs for the Munich and Singapore climates. In both climates and for all thermal designs, the cooling system energy consumption costs decline with higher cooling thresholds. For higher cooling thresholds, a larger amount of heat is dissipated to the ambient air before the cooling system is activated, thereby reducing the energy consumption. In the Munich climate and in the Singapore climate for cooling thresholds above 28 °C, the cooling system energy consumption is lower for the designs with a higher thermal connectivity to the ambient air. For cooling thresholds below 28 °C in the Singapore climate, the order is reversed and cooling system energy consumption is lower for the thermal designs with a reduced thermal connectivity to the ambient air. 28 °C is close to the average ambient temperature in Singapore and therefore cooling thresholds below this point benefit from insulation, as less heat is entering the SES from the surrounding air.

The third row of panes in Fig. 7 shows the average annual heating system energy consumption costs for the Munich and Singapore climates. For the insulated design in the Munich climate and for all thermal designs in the Singapore climate, no heating is required and therefore no heating energy consumption costs occur. In the Munich climate, the heating energy consumption costs of the design with cooling fins are higher than those of the baseline design, since the design with cooling fins dissipates more heat to the surroundings. Additionally, the heating energy consumption is higher for the configurations that require a higher heating threshold.

The fourth row of panes in Fig. 7 shows the average annual energy consumption costs due to parasitic losses for the Munich and Singapore climates. Since the internal resistance decreases at higher temperatures, the parasitic losses decrease for higher cooling threshold in both climates. For the Munich climate, parasitic losses are largest for the design with cooling fins, followed by the baseline design. The thermal designs with an increased dissipation of heat to the ambient air are, on average, operated at lower temperatures at which the internal resistance of the cells is higher, thereby increasing parasitic losses. For the Singapore climate, the impact of the thermal design on the parasitic losses is negligible, as the cells are not operated at low temperatures in this climate. A slight increase in the parasitic losses at high cooling thresholds can be seen for the insulated design in both climates, which is caused by the larger aging-induced increase in internal resistance, as shown in Fig. S5.

The bottom row of panes in Fig. 7 shows the total annual costs for the Munich and Singapore climates. The optimal cooling thresholds of the actively cooled designs balance the trade-off between increased battery depreciation costs and increased costs for cooling and parasitic losses. Additionally, the optimal cooling threshold is influenced by the discontinuous increase in the required heating threshold.

4.4. Comparison of BTMS costs

Finally, the total cost of all BTMS is shown in Fig. 8. The percentages in the figure refer to the relative change in total cost compared to the baseline design without active cooling, following $(C_{\text{tot},i} - C_{\text{tot},I})/C_{\text{tot},I} \quad \forall i \in \{II,III,IV,V\}$. Table 3 gives an overview of the key parameters of each BTMS for both climates.

For the Munich climate, the baseline BTMS without active cooling results in the lowest costs. Although the battery depreciation cost can be reduced by the other BTMS, this does not compensate the higher costs for the BTMS investment. The total costs are highest for the designs with cooling fins, due to the high energy consumption of the required heating system. The insulated design does not require a heating system, avoiding the heating energy consumption and heating system costs, but has higher energy consumption costs for cooling.

For the Singapore climate, installing cooling fins can reduce the sum of the considered cost components by 8.7 %, due to the large reduction in battery depreciation costs.

5. Discussion

The presented method investigates the cost effectiveness of different BTMS configurations by simulating the battery operation until the EOL criterion is reached. This enables modeling the impact of seasonal variations in ambient temperature, aging-induced capacity loss, and aging-induced internal resistance increase, on the battery temperature and operability. However, simulating battery operation with a timestep of 10 s over a period of multiple years for a large number of BTMS configurations results in a large computational load. By implementing the simulation in a compiled programming language such as Julia, the computation time of the simulations was drastically reduced compared to a simulation written in an interpreted language, thereby enabling the comparison of a large number of BTMS configurations as presented in this work.

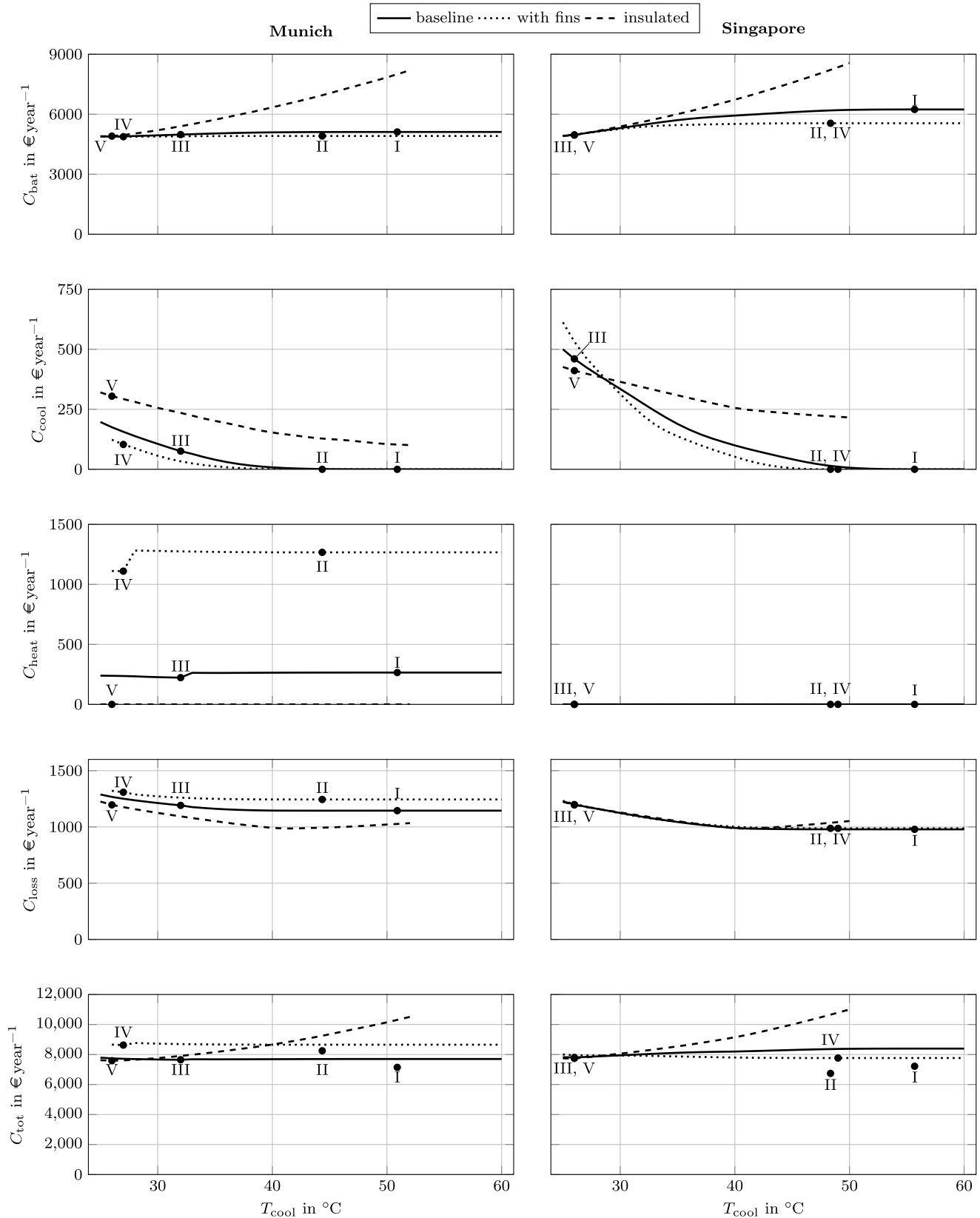


Fig. 7. Cost components for a 98 kWh SES limiting the power drawn from the grid by a bus charging station to 300 kW for the baseline design, the design with cooling fins, and the insulated design in the climates of Munich, Germany, and Singapore. The annotations refer to the BTMS defined in Table 1, where the annotations of the passively cooled systems are placed at the cooling threshold at which no cooling energy is consumed, and the annotations of the actively cooled systems are placed at the optimal cooling threshold.

The results show that the cost effectiveness of different BTMS depends on the considered climate and use case and therefore needs to

be evaluated on a case-by-case basis. For the given use case, installing active cooling was not cost-effective in both the climate of Munich and

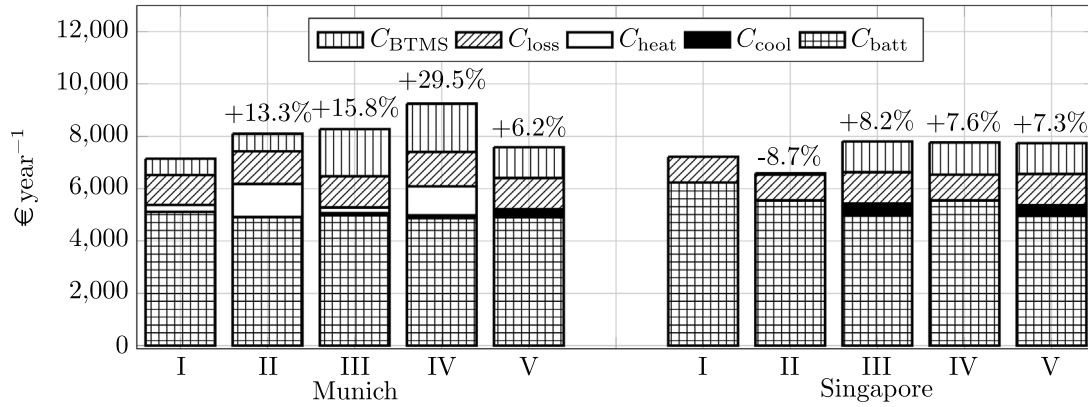


Fig. 8. Costs of the different BTMS for a 98 kWh SES limiting the power drawn from the grid by a bus charging station to 300 kW in the climates of Singapore and Munich, Germany. The numbers refer to the BTMS defined in Table 1. The percentages in the figure correspond to the relative change in total cost compared to the baseline design without active cooling, following $(C_{tot,i} - C_{tot,I})/C_{tot,I}$ $\forall i \in \{II,III,IV,V\}$.

Table 3

Parameters of the different BTMS for the a 98 kWh SES limiting the power drawn from the grid by a bus charging station to 300 kW in the climates of Munich, Germany, and Singapore.

Parameter	Unit	Munich					Singapore				
		I	II	III	IV	V	I	II	III	IV	V
T_{heat}	°C	13	14	12	13	–	–	–	–	–	–
T_{cool}	°C	–	–	32	27	26	–	–	26	49	26
C_{tot}	€ year ⁻¹	7,143	8,096	8,271	9,249	7,585	7,218	6,588	7,805	7,766	7,740
C_{inv}	€ year ⁻¹	620	673	1,799	1,851	1,179	0	53	1,178	1,231	1,179
C_{bat}	€ year ⁻¹	5,113	4,912	4,982	4,876	4,906	6,238	5,548	4,968	5,548	4,954
C_{BTMS}	€ year ⁻¹	620	825	1,178	1,231	1,179	0	205	1,178	1,231	1,179
C_{cool}	€ year ⁻¹	0	0	76	103	305	0	0	460	0	411
C_{heat}	€ year ⁻¹	265	1,267	223	1,110	0	0	0	0	0	0
C_{loss}	€ year ⁻¹	1,145	1,244	1,192	1,308	1,196	979	988	1,199	988	1,196
t_{eol}	years	10.6	11.1	10.9	11.2	11.1	8.2	9.5	11.0	9.5	11.0
$R_{inc,eol}$	Ω	0.166	0.145	0.147	0.136	0.136	0.270	0.203	0.138	0.203	0.137
$\min(T_c)$	°C	13.0	13.8	12.0	12.9	14.8	24.7	23.9	23.3	23.9	23.2
$\text{mean}(T_c)$	°C	22.5	18.6	20.9	17.3	23.9	35.7	31.2	25.5	31.2	25.4
$\max(T_c)$	°C	50.9	44.3	37.8	34.6	33.8	55.7	48.3	33.9	48.3	33.8

the climate of Singapore. However, ecological considerations, warranty requirements, or being able to safely operate in worst-case scenarios might justify installing an active cooling system.

The method can be used to evaluate the impact of further thermal design parameters such as the installed heating power, installed cooling power, or heating and cooling systems with different COP. The performance of different cells can be evaluated by adjusting the parametrization of the cell power limits calculation, the electric model, and the aging model. Furthermore, the method can be extended to evaluate other applications, such as electric trucks, by adjusting the control algorithm, the thermal model and the operability constraint. On top of that, for mobile applications the cost function should be adjusted to reflect the impact of the thermal system weight and packaging requirements on the overall system costs.

The method can be adapted to specific use case conditions. First, the manufacturer might not benefit from increasing the battery life beyond a set warranty condition, which can be included in the cost function. Second, the presented implementation uses an operability constraint that leads to the requirement of heating the battery for BTMS without insulation in the Munich climate. Alternatively, if reduced performance is acceptable to the operator, the operability could be included in the cost function, where limited performance of the SES would result in an increase of the peak demand charges during the months with low ambient temperatures. The selected implementation should reflect the requirements of the specific use case and operator.

Although the presented method supports decisions in the early-stage design phase, additional factors should be taken into account during the detailed design. First, a more detailed thermal model is required that takes into account temperature differences within the battery pack, the

cell configuration, the coolant flow, heat emitted from power electronic components, solar irradiation when shading is not possible, and the impact of wind, rain, or snow. The BTMS needs to ensure a homogeneous temperature distribution within the battery pack, because the operability and lifetime of a battery are determined by the cell with the lowest power limits or highest degradation, respectively. Locally increased temperatures can therefore reduce the lifetime of the SES, whereas the coldest battery cell determines the SES power limits. An active cooling system could reduce the thermal inhomogeneities in the system. Further research is required to quantify the resulting impact on system costs.

Second, the results strongly depend on the aging behavior of the cell and the modeling thereof. The aging model used in this study parametrized the impact of the cell temperature on battery aging based on measurements at three different temperatures, corresponding to 25 °C, 40 °C, and 60 °C. As a result, the validity of the aging model is limited to this temperature range and the accuracy for small temperature changes is unknown. Therefore, a carefully parametrized aging model of the considered battery cell over a wide temperature range is required for the detailed BTMS design.

Finally, although we took great care in using appropriate validated data to parametrize all subcomponents of our model, the combined model was not validated and the results can therefore not be interpreted as proof of superiority of a certain BTMS for this use case. The results rather illustrate the implementation of the method and the trade-offs involved in designing a BTMS. By publishing the source code of the simulation framework, we hope to enable others to compare the cost-effectiveness of their fully validated BTMS models.

6. Conclusion

To support battery designers in designing their battery thermal management system, we presented a method to determine the cost effectiveness of different BTMS in different climates. For each configuration, we iteratively determined the heating threshold that is required to maintain operability, whereas for each actively cooled configuration the cost-optimal cooling threshold was found.

The results showed that the cost effectiveness of different BTMS depends on the climate. For the considered use case in the Munich climate the lowest total cost was achieved by the baseline design without active cooling. In the Singapore climate, the design with cooling fins resulted in the lowest total cost. The longer battery life achieved by installing an active cooling system could not justify the additional investment and energy consumption costs, but ecological considerations, warranty requirements, or the ability to safely operate in worst-case scenarios might justify installing an active cooling system nonetheless.

In future work, we plan to extend the presented method to evaluate the cost effectiveness of additional BTMS, such as non-refrigerant-based cooling systems, or phase change materials. Furthermore, we plan to apply the method to other use cases such as electric trucks.

CRedit authorship contribution statement

Olaf Teichert: Conceptualization, Methodology, Software, Formal analysis, Investigation, Writing – original draft, Writing – review & editing, Visualization. **Florian Müller:** Software, Writing – review & editing. **Markus Lienkamp:** Resources, Supervision, Writing – review & editing, Funding acquisition.

Declaration of competing interest

The authors declare that they have no known competing financial interests or personal relationships that could have appeared to influence the work reported in this paper.

Acknowledgments

This work was financially supported by the Singapore National Research Foundation under its Campus for Research Excellence And Technological Enterprise (CREATE) programme, and the German Federal Ministry of Education and Research (BMBF) within the project “BetterBat” under grant number 03XP0362C. The funding parties were not involved in the design, execution, or writing of this study and did not affect the decision to submit to this journal.

Appendix A. Supplementary data

Supplementary material related to this article can be found online at <https://doi.org/10.1016/j.est.2021.103832>.

References

- [1] H.C. Hesse, M. Schimpe, D. Kucevic, A. Jossen, Lithium-ion battery storage for the grid—A review of stationary battery storage system design tailored for applications in modern power grids, *Energies* 10 (12) (2017) 2107, <http://dx.doi.org/10.3390/en10122107>.
- [2] T.M. Bandhauer, S. Garimella, T.F. Fuller, A critical review of thermal issues in lithium-ion batteries, *J. Electrochem. Soc.* 158 (3) (2011) R1, <http://dx.doi.org/10.1149/1.3515880>.
- [3] M. Naumann, M. Schimpe, P. Keil, H.C. Hesse, A. Jossen, Analysis and modeling of calendar aging of a commercial LiFePO₄/graphite cell, *J. Energy Storage* 17 (2018) 153–169, <http://dx.doi.org/10.1016/j.est.2018.01.019>.
- [4] A.M. Divakaran, M. Minakshi, P.A. Bahri, S. Paul, P. Kumari, A.M. Divakaran, K.N. Manjunatha, Rational design on materials for developing next generation lithium-ion secondary battery, *Prog. Solid State Chem.* 62 (2021) 100298, <http://dx.doi.org/10.1016/j.progsolidstchem.2020.100298>.
- [5] J. Remmlinger, S. Tippmann, M. Buchholz, K. Dietmayer, Low-temperature charging of lithium-ion cells part II: Model reduction and application, *J. Power Sources* 254 (2014) 268–276, <http://dx.doi.org/10.1016/j.jpowsour.2013.12.101>.
- [6] G. Xia, L. Cao, G. Bi, A review on battery thermal management in electric vehicle application, *J. Power Sources* 367 (2017) 90–105, <http://dx.doi.org/10.1016/j.jpowsour.2017.09.046>.
- [7] J. Jaguemont, J. Van Mierlo, A comprehensive review of future thermal management systems for battery-electrified vehicles, *J. Energy Storage* 31 (2020) 101551, <http://dx.doi.org/10.1016/j.est.2020.101551>.
- [8] A.M. Divakaran, D. Hamilton, K.N. Manjunatha, M. Minakshi, Design, development and thermal analysis of reusable Li-ion battery module for future mobile and stationary applications, *Energies* 13 (6) (2020) 1477.
- [9] J. Neubauer, A. Pesaran, D. Coleman, D. Chen, Analyzing the effects of climate and thermal configuration on community energy storage systems (presentation), presented at Electrical Energy Storage Applications and Technologies (EESAT) Conference, 2013.
- [10] J. Neubauer, E. Wood, Thru-life impacts of driver aggression, climate, cabin thermal management, and battery thermal management on battery electric vehicle utility, *J. Power Sources* 259 (2014) 262–275, <http://dx.doi.org/10.1016/j.jpowsour.2014.02.083>.
- [11] T. Yuksel, S. Litster, V. Viswanathan, J.J. Michalek, Plug-in hybrid electric vehicle LiFePO₄ battery life implications of thermal management, driving conditions, and regional climate, *J. Power Sources* 338 (2017) 49–64, <http://dx.doi.org/10.1016/j.jpowsour.2016.10.104>.
- [12] M. Keyser, A. Pesaran, Q. Li, S. Santhanagopalan, K. Smith, E. Wood, S. Ahmed, I. Bloom, E. Dufek, M. Shirk, A. Meintz, C. Kreuzer, C. Michelbacher, A. Burnham, T. Stephens, J. Francfort, B. Carlson, J. Zhang, R. Vijayagopal, K. Hardy, F. Dias, M. Mohanpurkar, D. Scofield, A.N. Jansen, T. Tanim, A. Markel, Enabling fast charging—battery thermal considerations, *J. Power Sources* 367 (2017) 228–236, <http://dx.doi.org/10.1016/j.jpowsour.2017.07.009>.
- [13] M. Henke, G. Hailu, Thermal management of stationary battery systems: A literature review, *Energies* 13 (16) (2020) 4194, <http://dx.doi.org/10.3390/en13164194>.
- [14] J. Bezanson, A. Edelman, S. Karpinski, V.B. Shah, Julia: A fresh approach to numerical computing, *SIAM Rev.* 59 (1) (2017) 65–98, <http://dx.doi.org/10.1137/141000671>.
- [15] G.L. Plett, High-performance battery-pack power estimation using a dynamic cell model, *IEEE Trans. Veh. Technol.* 53 (5) (2004) 1586–1593, <http://dx.doi.org/10.1109/TVT.2004.832408>.
- [16] R. Harper, W.B. Brown, *Mathematical Equations for Heat Conduction in the Fins of Air-Cooled Engines*, Tech. Rep. NACA-TR-158, NASA, 1923.
- [17] S.W. Churchill, H.H. Chu, Correlating equations for laminar and turbulent free convection from a vertical plate, *Int. J. Heat Mass Transfer* 18 (11) (1975) 1323–1329, [http://dx.doi.org/10.1016/0017-9310\(75\)90243-4](http://dx.doi.org/10.1016/0017-9310(75)90243-4).
- [18] H.D. Baehr, K. Stephan, *Wärme- und Stoffübertragung*, Vol. 7, Springer, 1994, <http://dx.doi.org/10.1007/978-3-540-87689-2>.
- [19] M. Naumann, F.B. Spingler, A. Jossen, Analysis and modeling of cycle aging of a commercial LiFePO₄/graphite cell, *J. Power Sources* 451 (2020) 227666, <http://dx.doi.org/10.1016/j.jpowsour.2019.227666>.
- [20] S.D. Downing, D. Socie, Simple rainflow counting algorithms, *Int. J. Fatigue* 4 (1) (1982) 31–40, [http://dx.doi.org/10.1016/0142-1123\(82\)90018-4](http://dx.doi.org/10.1016/0142-1123(82)90018-4).
- [21] Danish Energy Agency, *Technology data for energy plants. Individual heating plants and energy transport*, 2012.
- [22] H. Peng, X. Ling, Optimal design approach for the plate-fin heat exchangers using neural networks cooperated with genetic algorithms, *Appl. Therm. Eng.* 28 (5–6) (2008) 642–650, <http://dx.doi.org/10.1016/j.applthermaleng.2007.03.032>.
- [23] M.F. Alsayed, R.A. Tayeh, Life cycle cost analysis for determining optimal insulation thickness in palestinian buildings, *J. Build. Eng.* 22 (2019) 101–112, <http://dx.doi.org/10.1016/j.jobe.2018.11.018>.
- [24] T. Huld, R. Müller, A. Gambardella, A new solar radiation database for estimating PV performance in Europe and Africa, *Sol. Energy* 86 (6) (2012) 1803–1815, <http://dx.doi.org/10.1016/j.solener.2012.03.006>.
- [25] F. Trocker, O. Teichert, M. Gallet, A. Ongel, M. Lienkamp, City-scale assessment of stationary energy storage supporting end-station fast charging for different bus-fleet electrification levels, *J. Energy Storage* 32 (2020) 101794, <http://dx.doi.org/10.1016/j.est.2020.101794>.
- [26] M. Naumann, C.N. Truong, M. Schimpe, D. Kucevic, A. Jossen, H.C. Hesse, Simses: Software for techno-economic simulation of stationary energy storage systems, in: *International ETG Congress 2017, VDE*, 2017, pp. 1–6.
- [27] H.A. B.V., Sprintcharge leaflet: Battery buffered opportunity charging, 2021, https://global-uploads.webflow.com/60bd9cb47fc056344d74ebde/60d1d1b01a91b07de6d163f6.Whitepaper_SprintCharge.pdf. (Accessed 11 February 2021).
- [28] Verband der Elektrotechnik, *Batteriespeicher in der nieder- und mittel spannungsebene*, 2015.
- [29] BDEW, *Strompreisanalyse Juni 2021*, 2021, <https://www.bdew.de/service/daten-und-grafiken/bdew-strompreisanalyse/>.
- [30] R. Martins, H.C. Hesse, J. Jungbauer, T. Vorbuchner, P. Musilek, Optimal component sizing for peak shaving in battery energy storage system for industrial applications, *Energies* 11 (8) (2018) 2048, <http://dx.doi.org/10.3390/en11082048>.

- [31] C. Forgez, D.V. Do, G. Friedrich, M. Morcrette, C. Delacourt, Thermal modeling of a cylindrical LiFePO₄/graphite lithium-ion battery, *J. Power Sources* 195 (9) (2010) 2961–2968, <http://dx.doi.org/10.1016/j.jpowsour.2009.10.105>.
- [32] M. Schimpe, M. Naumann, N. Truong, H.C. Hesse, S. Santhanagopalan, A. Saxon, A. Jossen, Energy efficiency evaluation of a stationary lithium-ion battery container storage system via electro-thermal modeling and detailed component analysis, *Appl. Energy* 210 (2018) 211–229, <http://dx.doi.org/10.1016/j.apenergy.2017.10.129>.
- [33] H. L bberding, S. Wessel, C. Offermanns, M. Kehrer, J. Rother, H. Heimes, A. Kampker, From cell to battery system in BEVs: analysis of system packing efficiency and cell types, *World Electr. Veh. J.* 11 (4) (2020) 77, <http://dx.doi.org/10.3390/wevj11040077>.
- [34] J.H. Lienhard, J.H. Lienhard, *A Heat Transfer Textbook, fifth ed.*, Dover Publications, Mineola, NY, 2019.

Supplementary material to:
Techno-Economic Design of Battery Thermal Management Systems in
Different Climates

Olaf Teichert^{a,b,*}, Florian Müller^b, Markus Lienkamp^{a,b}

^a*TUMCREATE Ltd., 1 #10-02 Create Way, CREATE Tower, 138602 Singapore.*

^b*Technical University of Munich (TUM), School of Engineering & Design, Department of Mobility Systems Engineering,
Institute of Automotive Technology, 85748 Garching, Germany*

*Corresponding author: olaf.teichert@tum.de

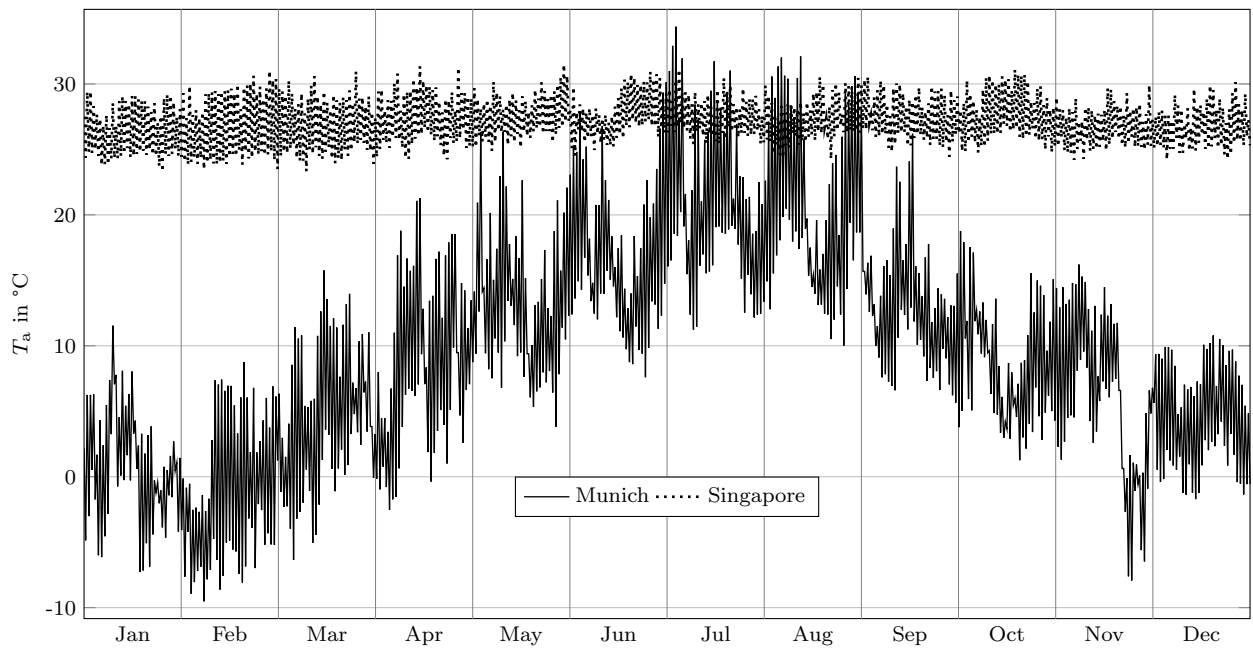


Figure S1: Hourly ambient temperature profiles from Munich and Singapore for the year 2015¹

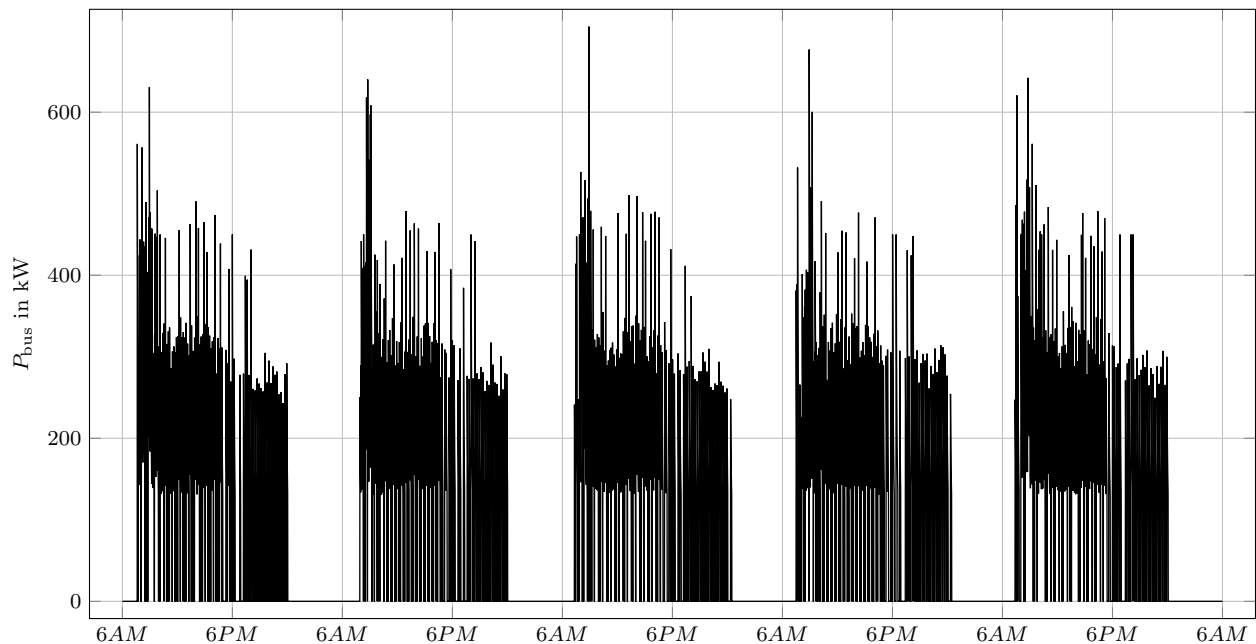


Figure S2: Power demand from buses charging at the Kent Ridge bus terminal in Singapore. The charging power supplied to the buses is derived from previous work where an agent-based city-scale simulation was used to simulate the operation of all buses in Singapore². The considered bus terminal serves one electrified bus route that operates all day, and two peak hour lines, which corresponds to a scenario where 50% of all bus lines in Singapore are electrified. The charging station consists of two chargers that charge buses with a constant power of 450 kW, which is gradually reduced as the SOC of the buses exceeds 80%. The day-to-day differences are caused by the stochasticity of the traffic simulation that causes slight variations in the bus arrival times.

¹T. Huld, R. Müller, A. Gambardella, A new solar radiation database for estimating pv performance in europe and africa, *Solar Energy* 86 (6) (2012) 1803–1815. doi:10.1016/j.solener.2012.03.006

²F. Trocker, O. Teichert, M. Gallet, A. Ongel, M. Lienkamp, City-scale assessment of stationary energy storage supporting end-station fast charging for different bus-fleet electrification levels, *Journal of Energy Storage* 32 (2020) 101794. doi:10.1016/j.est.2020.101794

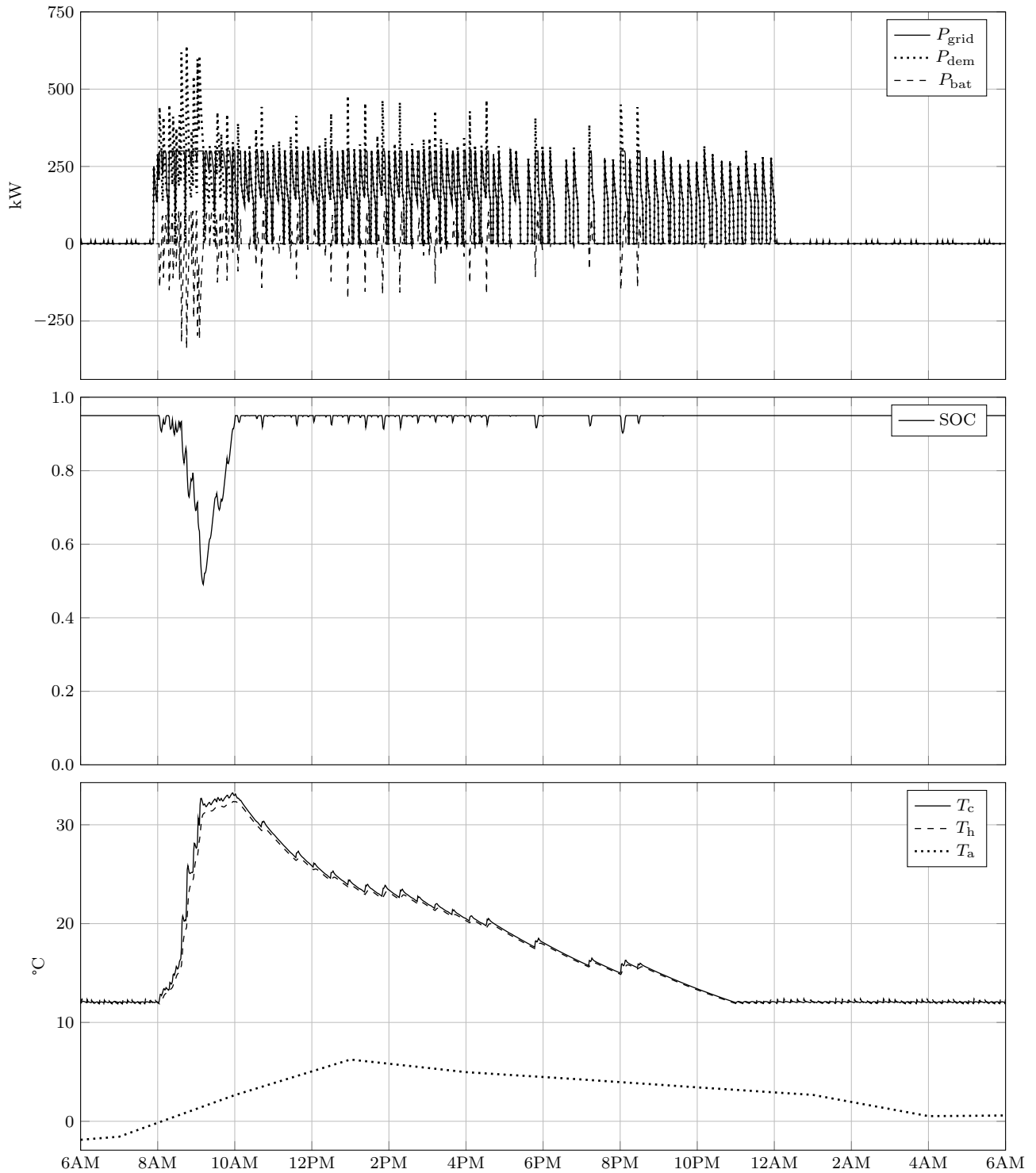


Figure S3: Single day of operation for a 98 kWh SES with the passively cooled baseline thermal design and a heating threshold of 13°C in the Munich climate. The top pane shows how the SES effectively reduces the power drawn from the grid to the peak shaving threshold. Additionally, the power drawn from the grid to power the heating system during the night can be seen. The middle pane shows the resulting SOC of the battery throughout the day. During the morning rush hour, the batteries are discharged the most to support the charging station with charging incoming buses. During the rest of the day, the battery is discharged occasionally to reduce smaller peak powers, but the SOC never drops below 90%. The lower pane shows the battery temperature, the housing temperature and the ambient temperature. During the high demand phase in the morning, the cell temperature increases to 32.6°C, closely followed by the housing temperature. Afterwards the cell temperature decreases, except from minor increases due to battery operation, until the heating threshold is reached around 11pm and the cell temperature is maintained by the heating system afterwards.

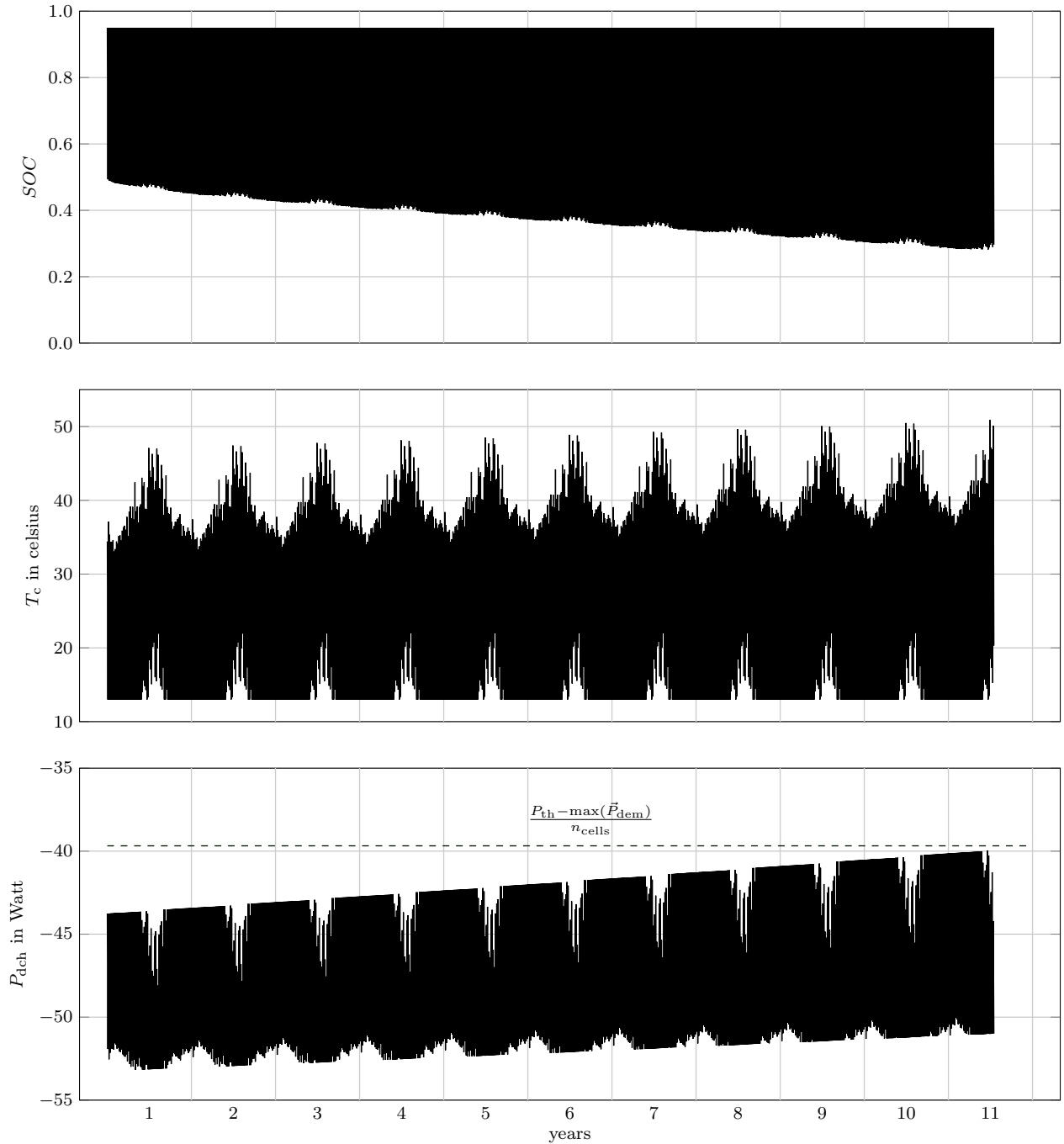


Figure S4: Long term operation of a 98 kWh SES with the passively cooled baseline thermal design and a heating threshold of 13 °C in the Munich climate. The top pane shows that battery reaches lower SOC over the course of operation, since the battery capacity declines due to aging. Additionally, the battery is discharged slightly deeper in winter due to the higher internal resistance and the reduced charging power. The second pane shows the cell temperature throughout the battery life, where seasonal changes are clearly visible. In winter the minimum battery temperature is kept constant by activating the heating at the heating threshold. The peak temperature reached in summer increases over the years as a result of the aging-induced internal resistance increase. The lowest pane shows the maximum discharging power of a single cell, combined with the operability constraint. The gap between the discharge power limit and the operability constraint reduces as the battery ages, due to the increased internal resistance and the lower SOC reached. Adapting the heating strategy to the batteries aging state could reduce the heating energy consumption during the early battery life.

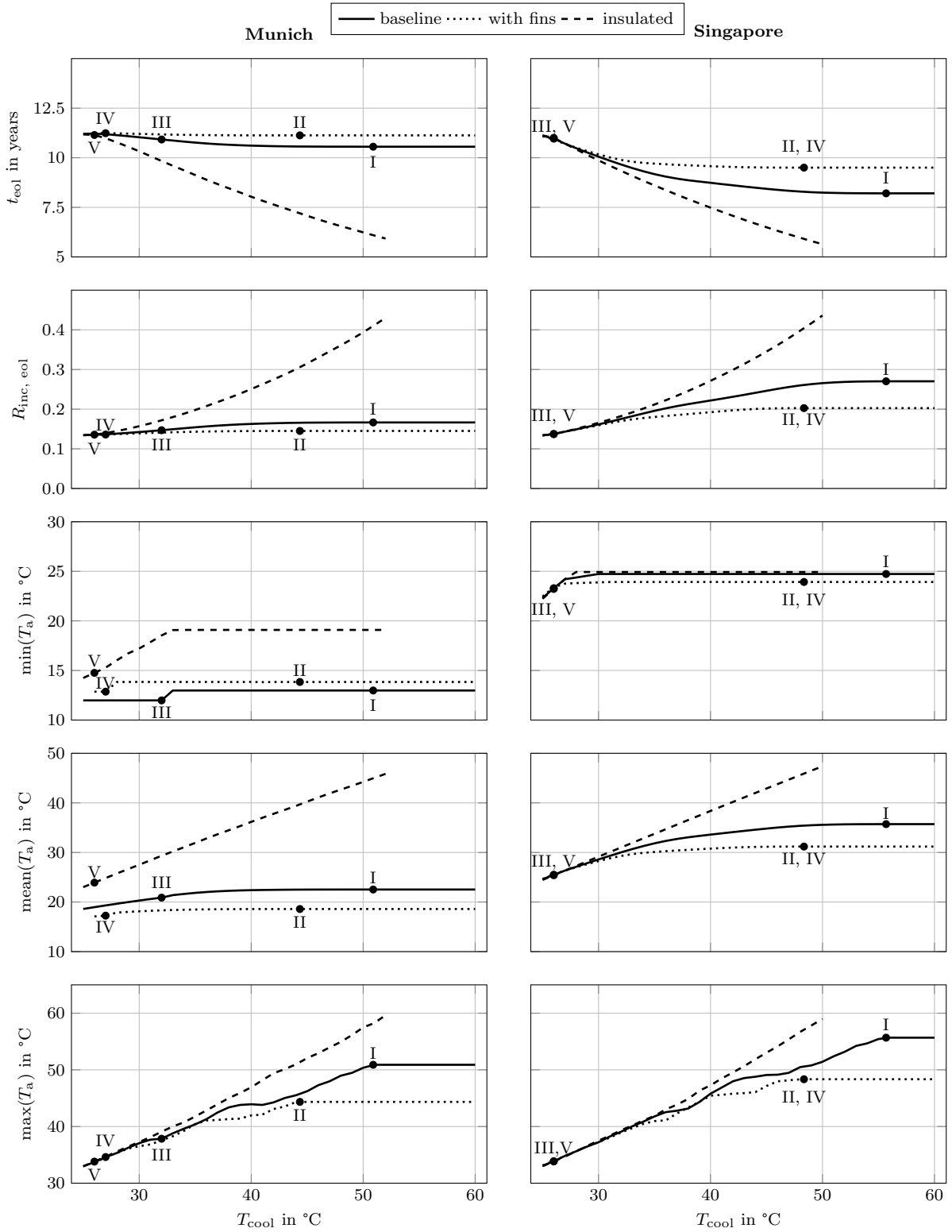


Figure S5: Battery characteristics for a 98 kWh SES limiting the power drawn from the grid by a bus charging station to 300 kW for the baseline design, the design with cooling fins, and the insulated design in the climates of Munich, Germany, and Singapore. The annotations refer to the BTMS defined in Table 1 of the paper, where the annotations of the passively cooled systems are placed at the cooling threshold at which no cooling energy is consumed, and the annotations of the actively cooled systems are placed at the optimal cooling threshold. The top panes show the battery life in years, which decreases at higher cooling thresholds for all thermal designs and in both climates. At higher cooling thresholds, the battery is operated at higher temperatures on average, resulting in a shorter battery lifetime. This effect is more pronounced for the thermal designs with a lower thermal conductivity to the ambient air and for the hotter Singapore climate. The second row of panes shows the aging-induced internal resistance increase at the EOL of the battery. Although the battery is replaced at the same capacity loss for all BTMS configurations, the final internal resistance increase is higher for batteries that are operated at higher temperatures. The bottom three row of panes shows the minimum, average and maximum temperatures of the batteries throughout their operating life, underlining the impact of the thermal connectivity to the ambient air.

3.2.3 Changes to the published battery model

To model the selected cell in an automotive application, the electric model, thermal model and control algorithm of the battery model are changed.

Electric model

The ECM used in the previous publication did not take the dependence of the cell's internal resistance on the pulse duration into account, because measurement data to parametrize this behavior was not available. For the cell selected in Section 3.1, however, this data is available and will be included to improve the model's accuracy.

To model the transient response of the cell to a current pulse, I use an ECM with a single RC-element, as was introduced in Fig. 2.2. The addition of the RC-elements changes the calculation of battery current, ohmic losses, and power limits.

To account for the voltage drop over the RC element, an extra term is added to the calculation of the cell current (Equation (3.5)), where j denotes the time step and P_{cell} is the power drawn from or supplied to the cell. The voltage drop is also taken into account in calculating the ohmic losses P_{loss} in Equation (3.6) and the voltage across the cell terminal in Equation (3.7), and is updated for the next time step using Equation (3.8).

$$I_{\text{cell}} = \frac{-U_{\text{OCV}} - U_{1,j} + \sqrt{(U_{\text{OCV}} + U_{1,j})^2 + 4 R_0 P_{\text{cell}}}}{2R_0} \quad (3.5)$$

$$P_{\text{loss}} = I_{\text{cell}}(U_{1,j} + I_{\text{cell}}R_0) \quad (3.6)$$

$$U_k = U_{\text{OCV}} + (U_{1,j} + I_{\text{cell}}R_0) \quad (3.7)$$

$$U_{1,j+1} = U_{1,j} + \left(\frac{I_{\text{cell}}}{C_1} - \frac{U_{1,j}}{R_1 C_1} \right) \Delta t \quad (3.8)$$

The addition of the RC-element also needs to be considered in the calculation of the power limits. The voltage drop over the RC-element adds an extra term to the calculation of the current and power limits in charging and discharging direction, as shown in Equation (3.9) - (3.12). $I_{\text{ch,cont}}$ and $I_{\text{dch,cont}}$ denote the maximum continuous charging and discharging current, U_{min} and U_{max} the voltage limits, SOC_{min} and SOC_{max} the SOC limits, $R_{0,c}$ and $R_{0,d}$ the series resistance for charging and discharging, Q the cell's capacity and Δt the time step duration.

$$I_{\text{ch,lim}} = \min \left(I_{\text{ch,cont}}, \frac{U_{\text{max}} - U_{\text{OCV}} - U_{1,j}}{R_{0,c}}, \frac{Q (\text{SOC}_{\text{max}} - \text{SOC}_j)}{\Delta t} \right) \quad (3.9)$$

$$I_{\text{dch,lim}} = \max \left(I_{\text{dch,cont}}, \frac{U_{\text{min}} - U_{\text{OCV}} - U_{1,j}}{R_{0,d}}, \frac{Q (\text{SOC}_{\text{min}} - \text{SOC}_j)}{\Delta t} \right) \quad (3.10)$$

$$P_{\text{ch}} = I_{\text{ch,lim}}(U_{\text{OCV}} + U_{1,j} + R_{0,c} I_{\text{ch,lim}}) \quad (3.11)$$

$$P_{\text{dch}} = I_{\text{dch,lim}}(U_{\text{OCV}} + U_{1,j} + R_{0,d} I_{\text{dch,lim}}) \quad (3.12)$$

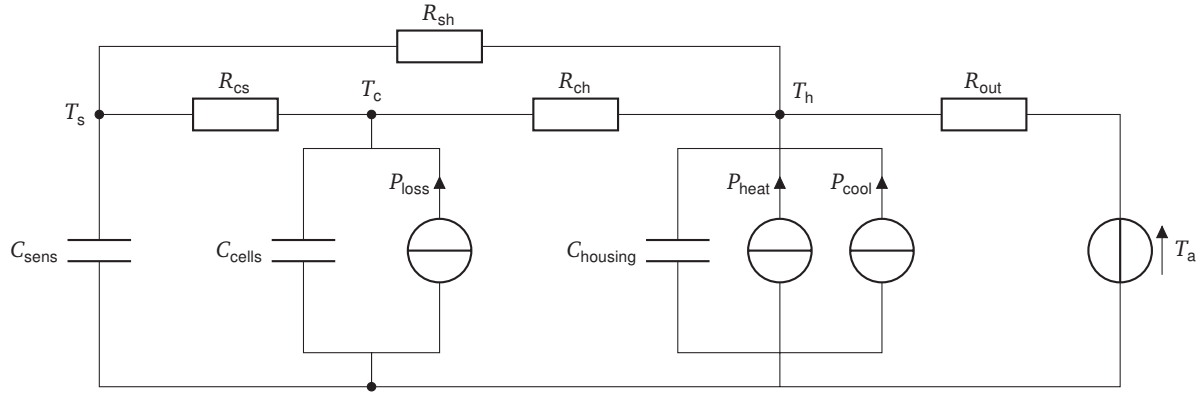


Figure 3.5: Lumped thermal capacitance model

Thermal model

The thermal model in the previous publication used two thermal masses to simulate the cell and housing temperature. To allow validating the model, I add an additional thermal mass for the temperature at the position of the temperature sensor.

The updated lumped thermal capacitance model is shown in Figure 3.5. T_c , T_s , and T_h denote the temperatures of the cell, sensor and housing respectively. Identical to the previous publication, Ohmic losses act directly on the cell, whereas the applied heating and cooling power act on the housing, approximating the behavior of integrated cooling and heating channels. Heat transfer between the cell core, the temperature sensor, the housing, and ambient air, is modeled by the thermal resistances R_{cs} , R_{ch} , R_{sh} , and R_{out} . The cell, sensor and housing temperature at the next time step are calculated using Equation (3.13) - (3.15), where c_{cell} , c_s and c_h denote the thermal capacity of the cells, sensors and housing respectively, and COP_{heat} and COP_{cool} are the coefficients of performance of the heating and cooling system. Note that although not every cell in the vehicle has a temperature sensor, the temperature at the top of the cell, where the temperature sensor would be, is modeled for all cells to avoid the need to model cells with and without temperature sensors individually.

$$T_{c,j+1} = T_{c,j} + \frac{\Delta t}{c_c} \left(P_{loss} + \frac{T_{s,j} - T_{c,j}}{R_{cs}} + \frac{T_{h,j} - T_{c,j}}{R_{ch}} \right) \quad (3.13)$$

$$T_{s,j+1} = T_{s,j} + \frac{\Delta t}{c_s} \left(\frac{T_{c,j} - T_{s,j}}{R_{cs}} + \frac{T_{h,j} - T_{s,j}}{R_{hs}} \right) \quad (3.14)$$

$$T_{h,j+1} = T_{h,j} + \frac{\Delta t}{c_h} \left(P_{heat} COP_{heat} + P_{cool} COP_{cool} + \frac{n_{cells} (T_{c,j} - T_{h,j})}{R_{ch}} + \frac{n_{cells} (T_{s,j} - T_{h,j})}{R_{sh}} + \frac{T_a - T_{h,j}}{R_{out}} \right) \quad (3.15)$$

Control algorithm

In the previous publication, the control algorithm prioritized discharging the battery over heating and cooling, because a lack of discharging power might violate the peak-shaving threshold and therefore incur additional costs. For an automotive application, derating the discharging power in

extreme operating conditions is acceptable and discharging will therefore not be prioritized over heating or cooling.

Additionally, where in the previous publication heating and cooling could be activated any time, because stationary storage systems are typically active continuously, for the automotive application heating and cooling are only activated when the vehicle is driving or charging.

3.2.4 Electric model parametrization

Parametrizing the electric model requires constant parameters, the OCV-curve and the dependency of the series resistance and RC-element on the SOC and temperature. The constant parameters needed to model the electric behavior of the cell are listed in Table 3.2. The open-circuit voltage curve was parametrized using a pOCV-measurement [74] and is shown in Figure 2.3.

Table 3.2: Constant parameters of ECM

Parameter	Symbol	Value	Source
Nominal Capacity	Q_{nom}	78 Ah	[74]
Upper voltage limit	U_{max}	4.2 V	[74]
Lower voltage limit	U_{min}	2.5 V	[74]
Minimum SOC	SOC_{min}	4.1 %	[74]
Maximum SOC	SOC_{max}	97 %	[74]
Maximum charging current	I_{max}	125 A	[74]
Maximum discharging current	I_{min}	250 A	[74]

The series resistance and the RC-element of the ECM are parametrized using HPPC measurements at different SOC and temperatures. The dynamic response of the cell differs for different SOC and temperatures. R_0 , R_1 and C_1 were fitted for 1/2C charge and 1/2C discharge pulses, at 0 °C, 20 °C and 40 °C, and between 10 % and 90 % SOC in increments of 10 %. These charging and discharging rates were chosen, because they match those occurring during BET driving the closest. A dependency on the charging rate was not included, as Wassiliadis et al. [74] show that the impact of the charging rate on the cell's internal resistance is small compared to the impact of SOC or temperature. The coefficient of determination for all fits, the series resistance R_0 , the asymptotic resistance R_{tot} and the RC times t_{RC} are shown in Figure 3.6.

For all curve fits, a coefficient of determination above 93 % could be realized. The quality of the fit is better at high temperatures than at low temperatures. The series resistance and asymptotic resistance both increase as the temperature and SOC decrease. A dependency of the RC time on the SOC or temperature cannot be seen.

For a tight link between the ECM properties and physical processes in the cell, the series resistance should model the ohmic resistance, while the dependency of diffusion processes on temperature and SOC should be modeled by the RC element. However, because I only use a single RC element, the dependency of the initial diffusion processes is also included in the parametrization of the series resistance. Using two RC elements would enable decoupling the series resistance from transient processes and result in a curve fit quality above 99.3 % for all SOC and temperatures, as shown in Appendix A. However, this would result in an RC time of less than 0.01 s for one of the RC elements, which would require a small time step in the simulation. Because I will simulate the battery operation over the entire lifetime to estimate the battery life in Section 3.4, the large increase in computational load caused by using 2 RC-elements cannot be justified by the improved curve fit quality.

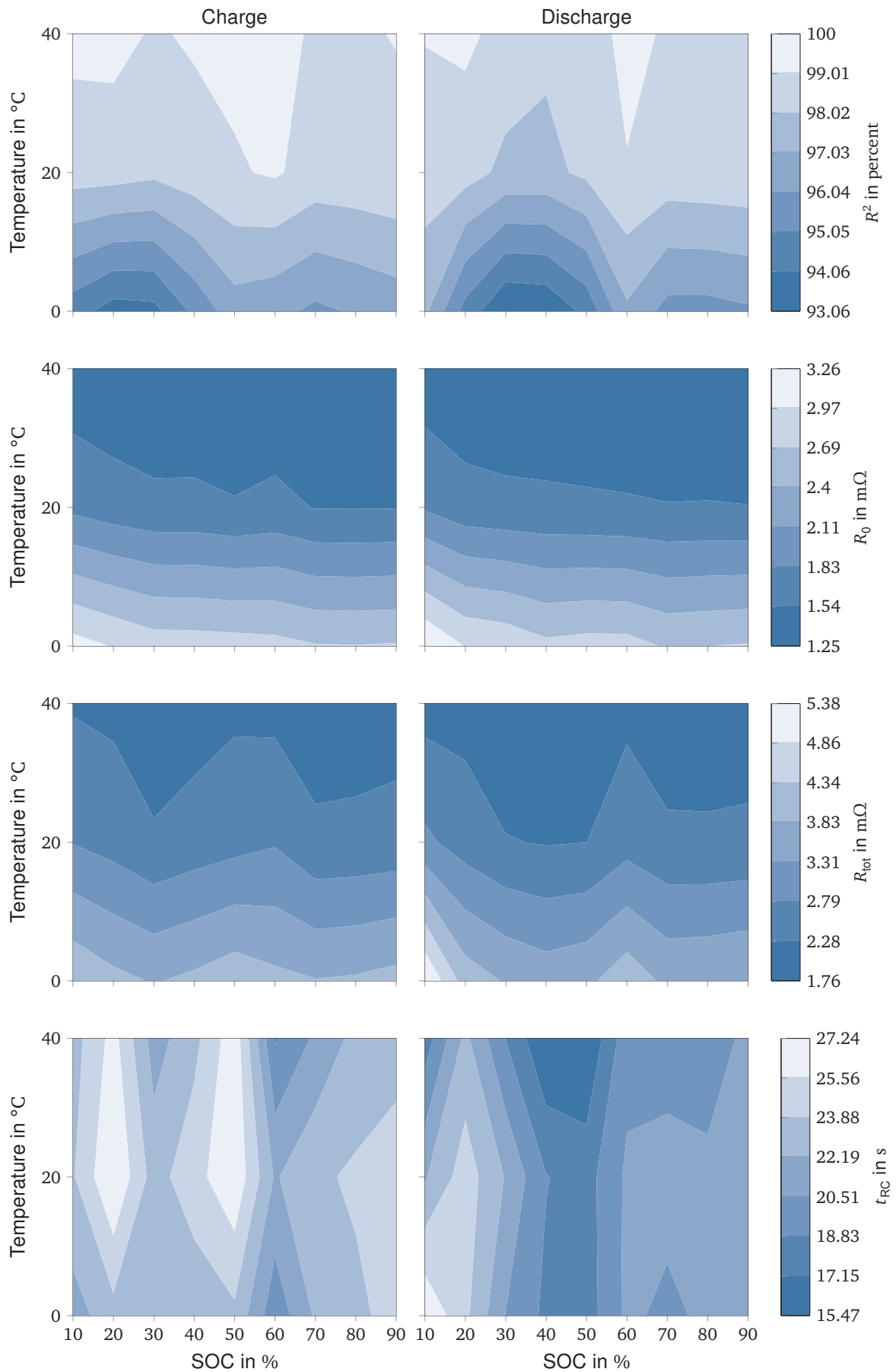


Figure 3.6: Quality and found parameters of the ECM parametrization

3.2.5 Thermal model parametrization

The thermal model parameters are listed in Table 3.3. The cell's thermal capacity is estimated by multiplying the cell mass of 1.101 kg [74], with an assumed specific heat capacity of $1045 \text{ J kg}^{-1} \text{ K}^{-1}$. This specific heat capacity corresponds to the average of six measured specific heat capacities of lithium-ion cells [114] with the same format and chemistry as the selected cell.

Table 3.3: Constant parameters of the thermal model

Parameter	Symbol	Value	Comments & source
Thermal resistance between cell and sensor	R_{cs}	0.578 KW^{-1}	[115]
Thermal resistance between cell and housing	R_{ch}	0.899 KW^{-1}	[115]
Thermal resistance between sensor and housing	R_{sh}	2.151 KW^{-1}	[115]
Cooling coefficient of performance	COP_{cool}	-3	[81]
Heating coefficient of performance	COP_{heat}	4	[81]
Cell thermal capacity	c_c	1150 JK^{-1}	Calculated
Housing thermal capacity	c_h	112 kJK^{-1}	Calculated
Thermal resistance between housing and ambient	R_{out}	10.9 WK^{-1}	Based on curve fit

The thermal capacity of the housing is estimated based on the housing components mass of 125 kg, and the assumption that the specific heat capacity of all housing components matches that of aluminum ($896 \text{ J kg}^{-1} \text{ K}^{-1}$) [116].

To determine the heat transfer coefficient between the VW ID.3 and ambient air, I conducted an experiment on vehicle level: First, the vehicle battery was heated up on the chassis dynamometer. Once the battery temperature reached $32 \text{ }^\circ\text{C}$, the vehicle was stopped and the cool down was logged using the onboard temperature sensors of the battery modules. The ambient temperature was recorded using a Lascar Electronics EL-USB-1 temperature logger. To log the battery temperature, the low-voltage electronics of the car needed to be active. To avoid any resulting current flow from the traction battery, the low-voltage battery was connected to an external power supply.

The recorded ambient temperature, minimum and maximum battery temperature and the curve fit are shown in Fig. 3.7. Over time, the battery temperature approaches the ambient temperature. Because the ambient temperature was not constant, the curve fit uses a transient simulation taking the variable ambient temperature signal as an input. The curve fit has a coefficient of determination of 91.2% for an effective heat transfer coefficient of 10.9 WK^{-1} .

3.2.6 Electric & thermal model validation

To validate the electric & thermal models, I use measurements on vehicle level that were recorded by Wassiliadis et al. [74] during driving and charging a Volkswagen ID.3 Pro Performance, which uses the selected cell.

The driving and charging sequences are shown in Figure 3.8. The driving data was generated on a chassis dynamometer for three different speed profiles, corresponding to typical operation in an urban, interurban and highway driving scenario. The shown velocity profiles were repeated until the vehicle could no longer follow the target velocity. All driving measurements were conducted at two different ambient temperatures: approximately $15 \text{ }^\circ\text{C}$ and $30 \text{ }^\circ\text{C}$. The recorded charging sequences correspond to charging at a mode 3 Alternating Current (AC) Wallbox charger and at a mode 4 Direct Current (DC) fast charger. The charging power during the AC-charging event is relatively constant at 11 kW, while the charging power at the DC fast charger is reduced by the vehicle at higher SOC to avoid damaging the battery. For both the

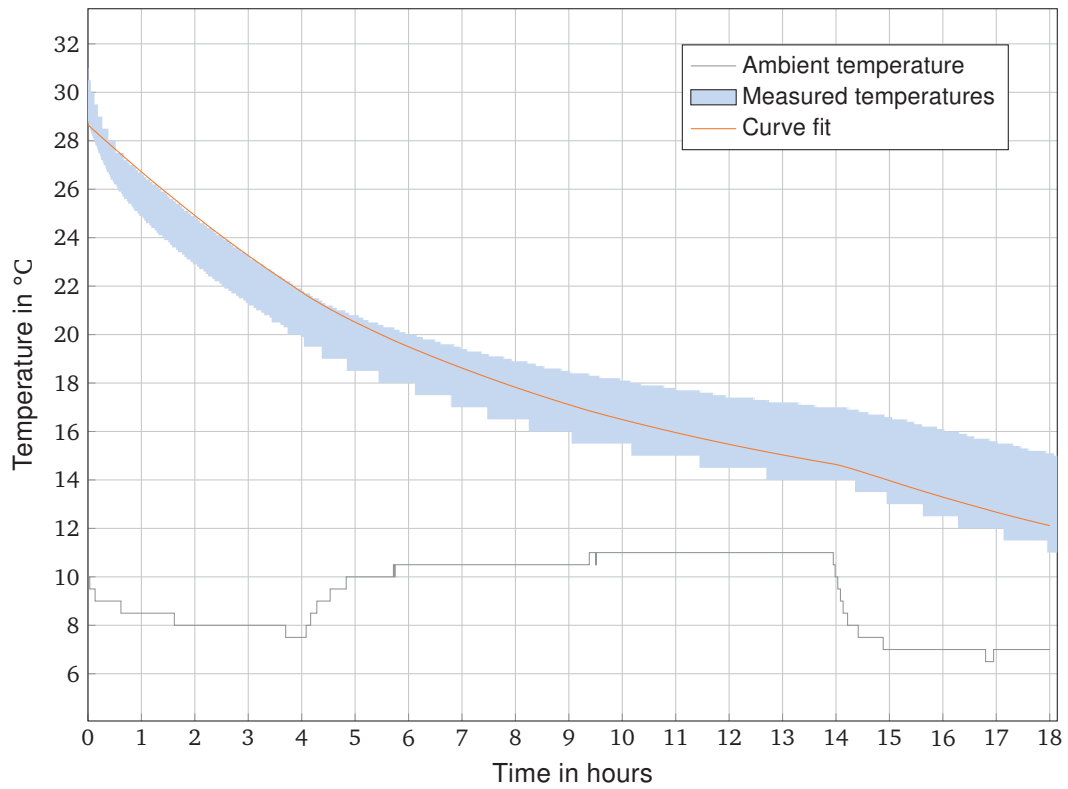


Figure 3.7: Measurement of passive heat transfer between the battery and ambient air. The blue band corresponds to the area between the minimum and maximum measured temperature.

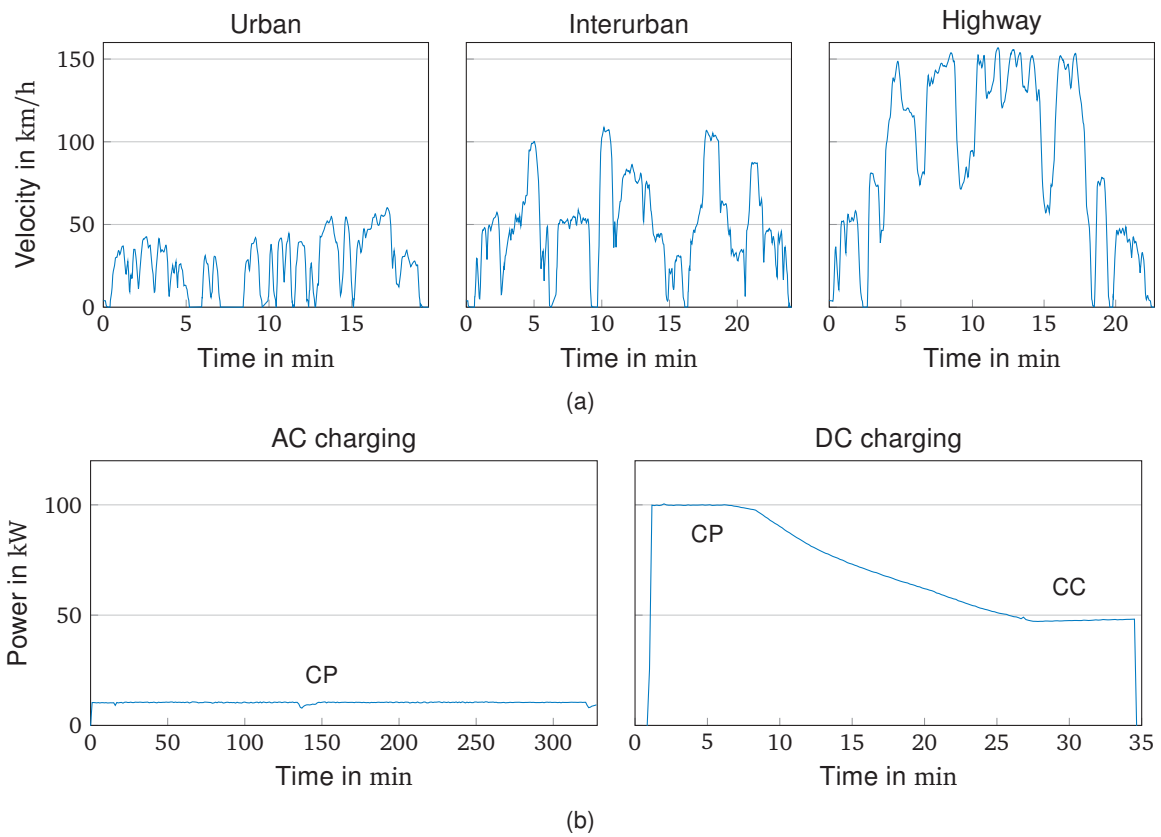


Figure 3.8: Data used to validate the electric and thermal model: a) driving at different speed profiles b) charging at different charging powers.

driving and charging sequences, the battery voltage, current and temperature were recorded, resulting in over 100 hours of validation data on vehicle level.

To validate the electric and thermal model I calculate the voltage and temperature error. The voltage error is the difference between the average measured voltage and simulated terminal voltage. The temperature error is the difference between the average measured temperature and the simulated sensor temperature. Figure 3.9 summarizes the validation results for all driving and charging profiles.

The voltage error of all driving profiles is concentrated around zero, while the maximum errors increase with the average velocity of the driving profile. At higher velocities, the current drawn from the battery increases, resulting in a larger error if the simulated resistance does not match the measurement. For the charging profiles, a systematic offset can be seen. The errors in the thermal model show a larger variation among the different driving and charging cycles, but no systematic offset.

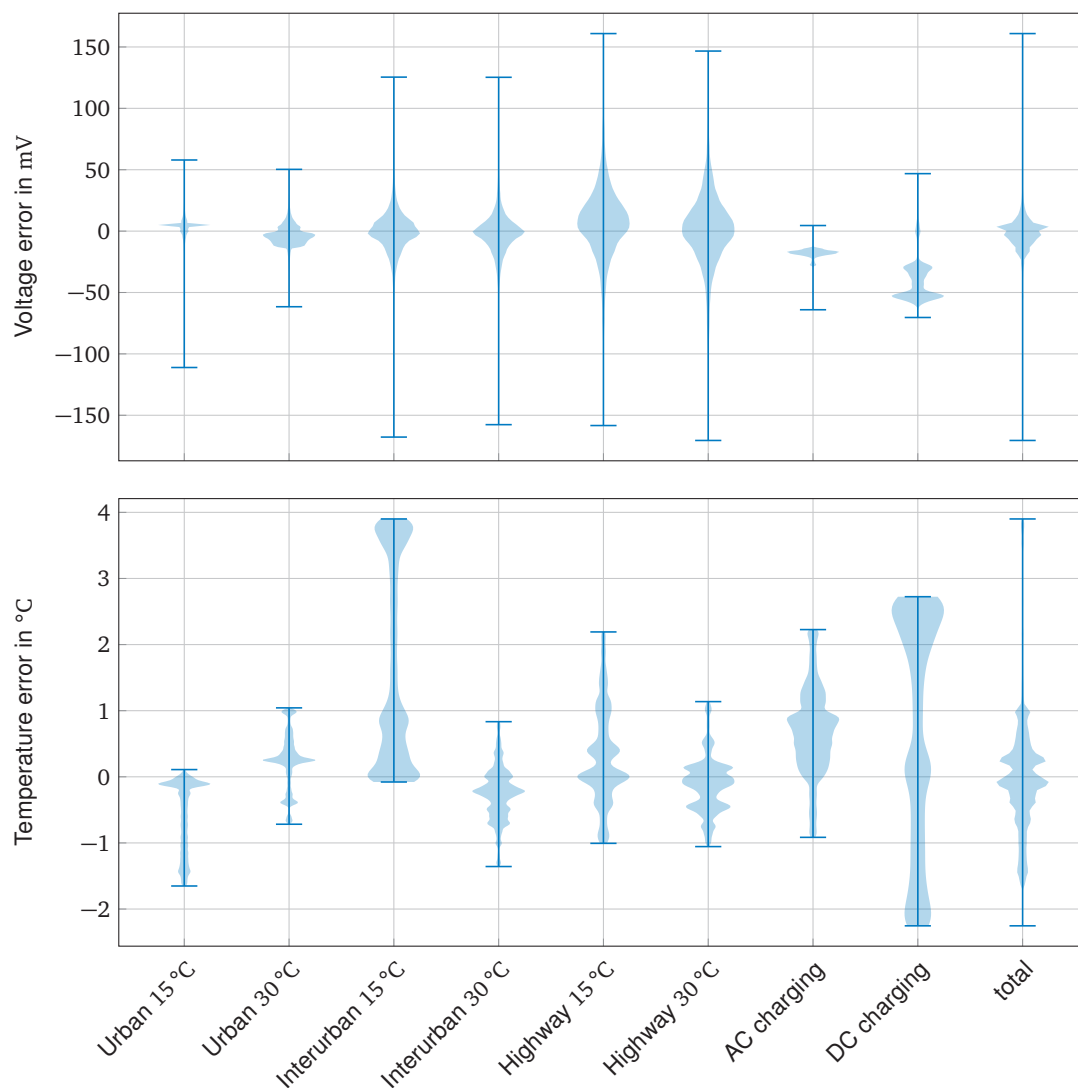


Figure 3.9: Voltage and temperature distributions for all validation profiles.

To elucidate the cause of the model errors, I will discuss the validation cycles with the highest errors in detail: the interurban cycle at 15 °C, the highway cycle at 15 °C, and both charging cycles. A discussion of the remaining validation cycles is included in Appendix B.

Figure 3.10 shows the results of the validation based on the interurban cycle at 15 °C. Using the interurban driving cycle, the battery was depleted in 9.3 hours. The top pane shows the measured and simulated voltage. The voltage decreases as the battery is discharged, due to the SOC dependency of the OCV. The spikes in the measured voltage correspond to acceleration and deceleration events in the driving cycle, that require higher currents and therefore cause an increased voltage drop over the cell's internal resistance.

The third pane shows the measured and simulated temperatures. The blue band is defined by the minimum and maximum temperature in the entire pack. The simulated temperature matches the measurement well in the first half of the driving cycle, but strongly overestimates the temperature rise during the second half, even though the applied power profile remained the same. This may be caused by entropy effects: Jalkanen et al. [117] showed that entropy effects can lead to temperature reductions during discharging, especially at low SOC. Due to the lack of entropy effects in the model, the temperature increase in the battery is overestimated and the cooling system is activated in the simulation, even though it was not during the measurement.

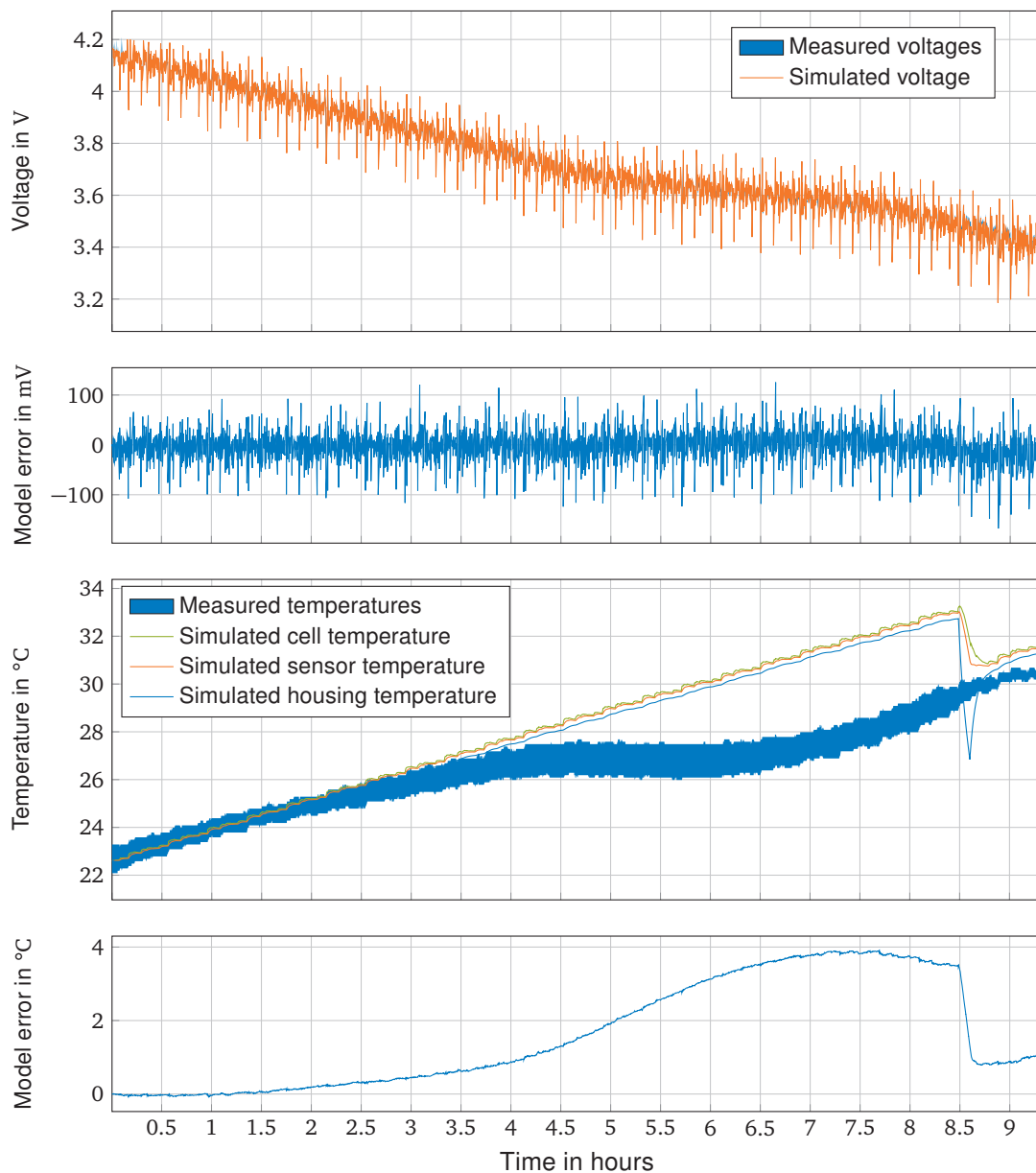


Figure 3.10: Interurban cycle at 15 °C ambient temperature

Figure 3.11 shows the validation results for the highway driving profile at an ambient temperature of 15 °C. The highway driving cycle has the highest energy consumption among all recorded driving cycles and depletes the battery within 3 hours. As a result of the higher energy consumption, the currents in the battery are higher, resulting in a larger absolute voltage error.

The measurement shows that it takes 1.8 hours for the battery temperature to increase from 24 °C to 32 °C. The battery heats up at different rates, caused by differences in driving intensity in the speed profile. The recurrence is caused by repetitions of the 20 minute long speed profile. The simulated temperature matches the measured temperature well during the first hour, but then starts to overestimate it. Because the battery reaches a different SOC here, it may again be due to entropy effects that are not considered in the model. In the second half of the measurement, the cooling system is activated and deactivated when the measured temperature exceeds 32.5 °C, or drops below 30.5 °C. The simulation matches this behavior well, but due to a phase shift an additional model error is incurred.

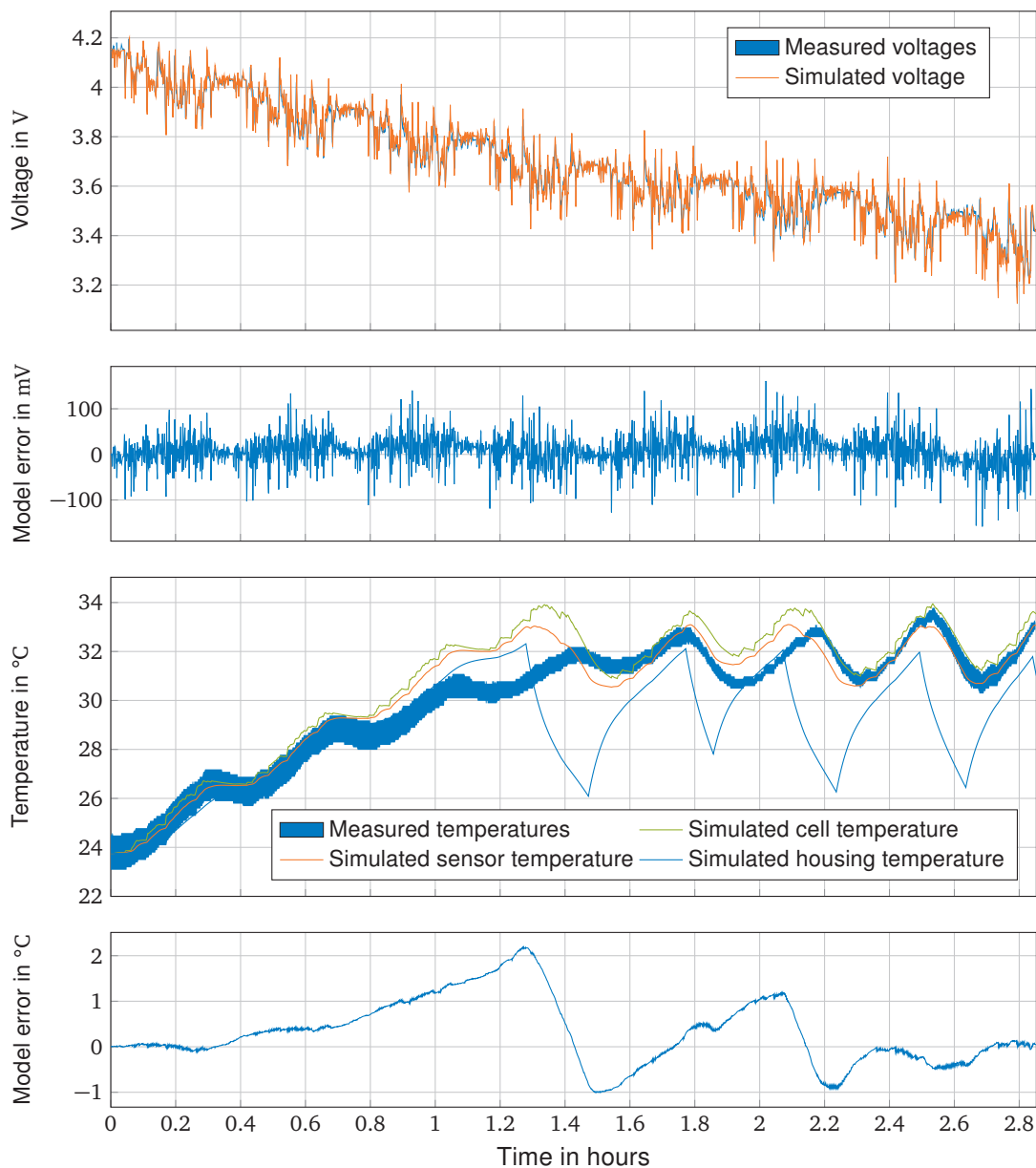


Figure 3.11: Highway cycle at 15 °C ambient temperature

Figure 3.12 shows the validation results for the Wallbox charging measurement. The voltage increases over time, due to the SOC dependency of the OCV. At the end of the measurement, some cells briefly exceed the voltage limit of 4.2 V. The simulated voltage underestimates the measured voltage, except during the first minutes of the measurement. This is likely caused by the fact that the electric model was parametrized using pulse tests of 30 s. This approach captures voltage loss caused by charge transfer well, but does not account for the voltage loss caused by diffusion, which happens on a longer timescale [50]. The internal resistance for the charging event, which is a much longer pulse, is therefore underestimated. At the end of the measurement, the model error increases, due to the upper SOC limit implemented in the simulation.

The temperature measurement shows an increase in the battery temperature, that resulted in the activation of the cooling system. The simulation underestimates this temperature increase, which is likely due to the underestimation of the cell's internal resistance at long pulse durations that is also responsible for the voltage error.

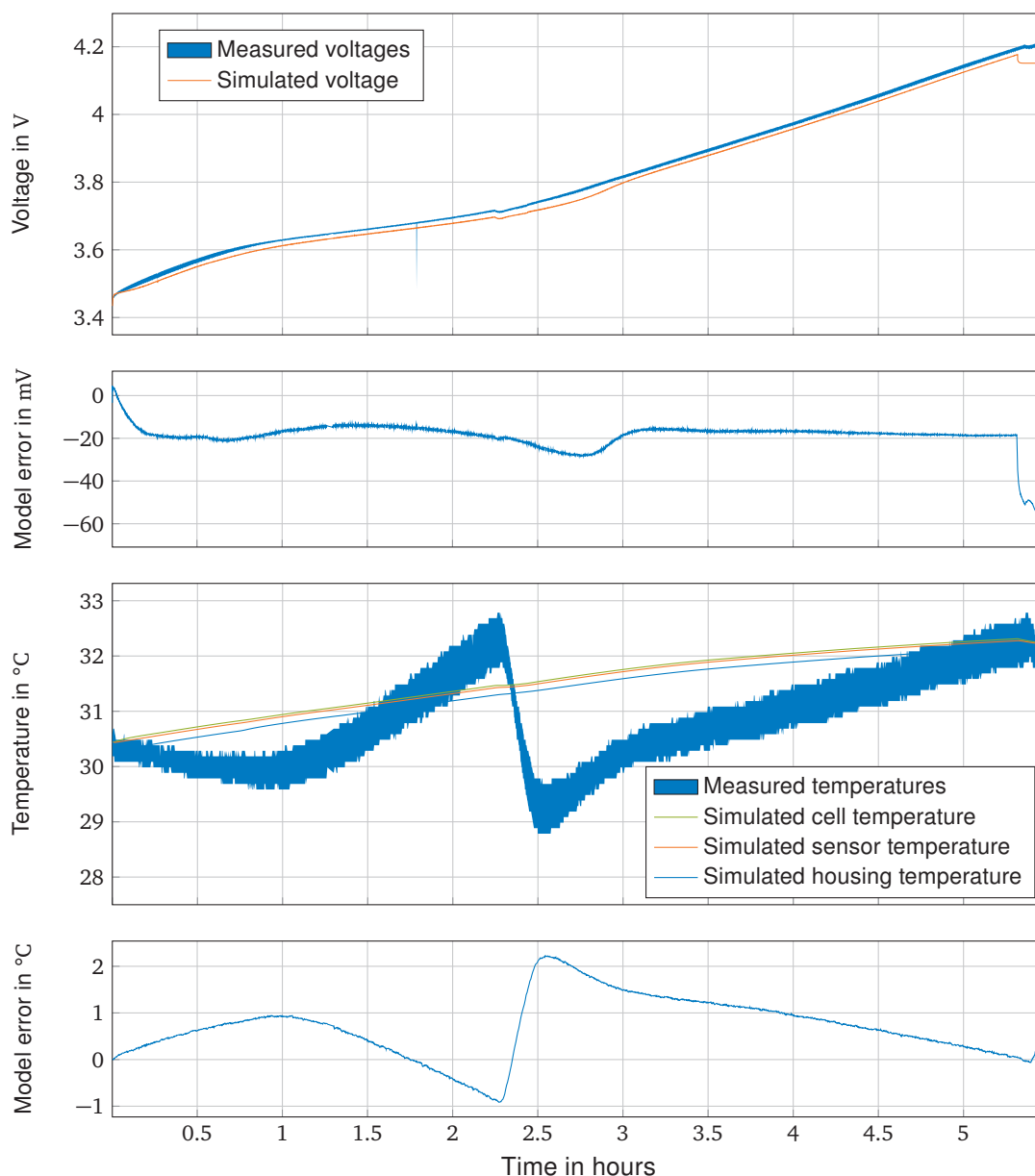


Figure 3.12: Wallbox charging cycle

Finally, Figure 3.13 shows the validation results for fast charging. The vehicle is charged from 5.2% SOC to 97% SOC in just over one hour. Similar to the Wallbox charging event, the simulation underestimates the voltage drop. The error is larger for fast charging due to the higher charging current.

The temperature measurement shows that the battery reaches a maximum temperature of 45 °C, despite activation of the cooling system. This may be caused by insufficient cooling power, or may be part of the vehicle's charging strategy. A vehicle's charging strategy may target increased battery temperatures to reduce the internal resistance of the cells, which could help avoid lithium plating [74]. Among all validation cycles, the difference between the simulated temperature in the cell and the housing, i.e. the temperature gradient across the cell, is the largest for the fast charging event.

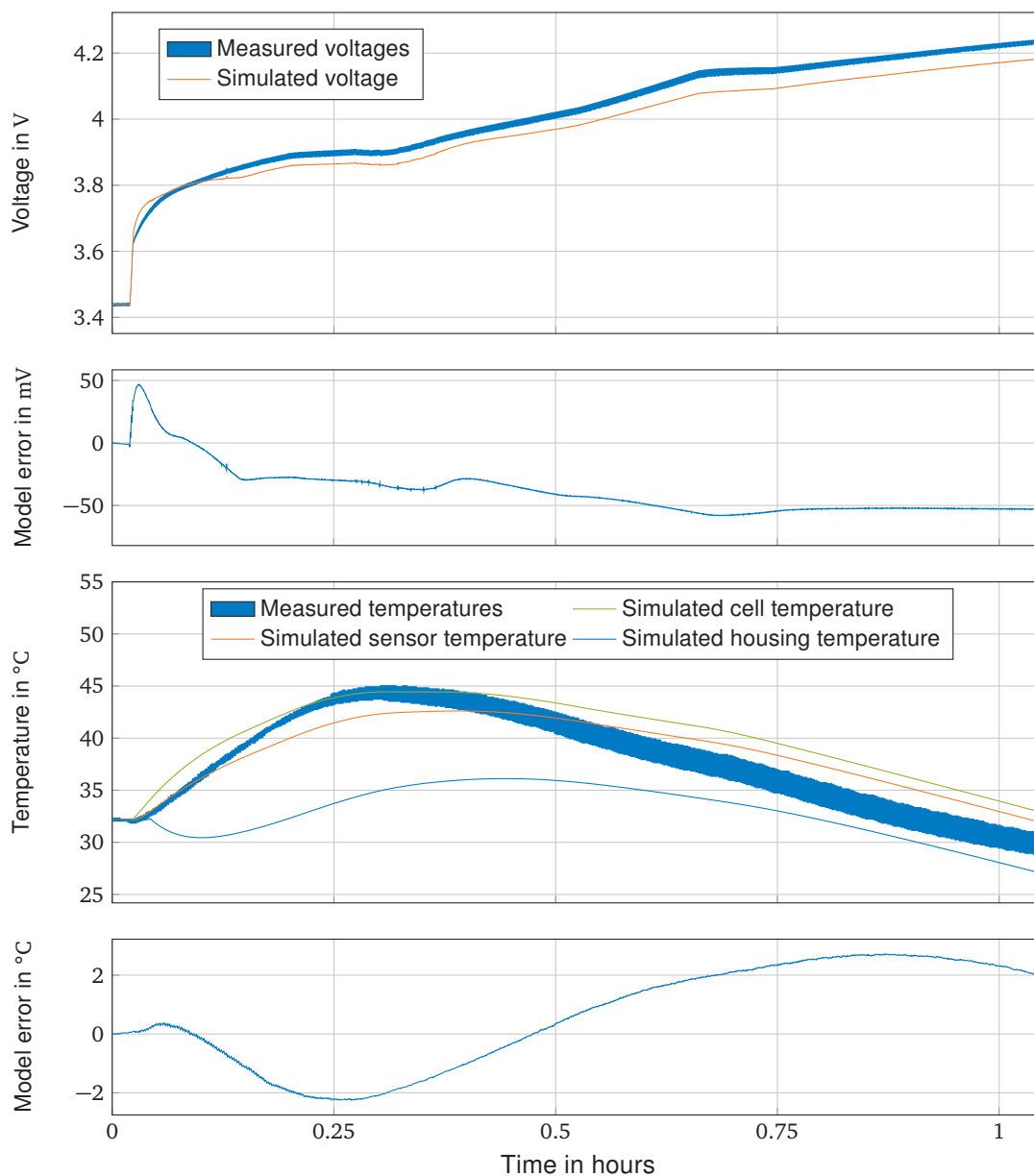


Figure 3.13: Fast charging cycle

The major causes of error are the underestimation of the internal resistance for long pulse durations and the missing impact of entropy coefficients. Further errors may be caused by differences in the aging state of the cell that was used for parametrization and the vehicle battery

that was used for validation, inhomogeneities between the battery cells, and heat generated by other electric components in the pack.

Therefore, a simulation error can be expected. Nonetheless, the model accurately covers a wide range of operating conditions with an average temperature error below 1 °C. The model will be used to estimate the battery life, which is affected by the simulated SOC and temperature. For this purpose, I consider the simulation errors to be reasonable, and will use the presented electric and thermal model in the following chapters.

3.2.7 Aging model parametrization & validation

Parametrizing a semi-empirical aging model requires conducting extensive aging tests with different combinations of aging stress factors, such as temperature, charging rate, DOD and SOC. Unfortunately, results from such tests or the resources to conduct them were not available for the selected cell. However, Schreiber [118] provided measurement data on the degradation of the selected cell at three different aging conditions: 1C/1C charging and discharging cycles at 100 % DOD, a commuter trip power profile, and a long distance trip power profile. By using one of these measurements to scale an existing fully-parametrized semi-empirical aging model for a cell with a similar chemistry, an approximation of the cell aging behavior can be achieved.

The fully parametrized semi-empirical aging model that will be scaled was published by Schmalstieg et al. [79] and describes capacity loss and internal resistance increase of the 2.05 Ah Sanyo UR18650E cell. The parametrized cell uses NMC for the positive electrode and graphite for the negative electrode, which matches the material composition of the selected cell [119]. The model considers the impact of the OCV, temperature, DOD, and voltage around which the battery is cycled. The impact of the charging rate was not included in the parametrization by Schmalstieg et al.

To implement the model in my simulation, a linear scaling factor for both capacity loss and internal resistance increase is implemented to match the degradation measurements of the selected cell. Because the charging rates of the long distance trip power profile are closest to those occurring during truck operations, these measurements are used to find the scaling factor. For this purpose, I use the generalized reduced gradient solver provided by Microsoft Excel. The two other measurements are used for validation.

The measured cell degradation and the results from the scaled aging model are shown in Figure 3.14. The capacity loss of the aging model is scaled by a factor 0.43 to match the measured degradation of the selected cell for the long-distance profile, obtaining a coefficient of determination of 91 %. For the 1C/1C profile and the commuter profile, coefficients of determination of 99 % and 73 % are achieved. I thus consider the scaled aging model to capture capacity loss at different operating conditions reasonably well.

The internal resistance increase is scaled by a factor 0.12 to match the measured internal resistance increase for the long-distance profile, obtaining a coefficient of determination of 53 %. The low quality of the curve fit is caused by irregularities in the measurements during the first 500 cycles, as shown in the inset of the graph. The measurement shows a steep initial increase of the internal resistance, which may be caused by initial SEI growth [118]. Subsequently, the internal resistance decreases, which is likely caused by irregularities in the test plan that resulted in longer rest durations between checkups. The same irregularities also caused an increase in the measured cell capacity. After the first 500 cycles, the internal resistance increases continuously on a linear slope.

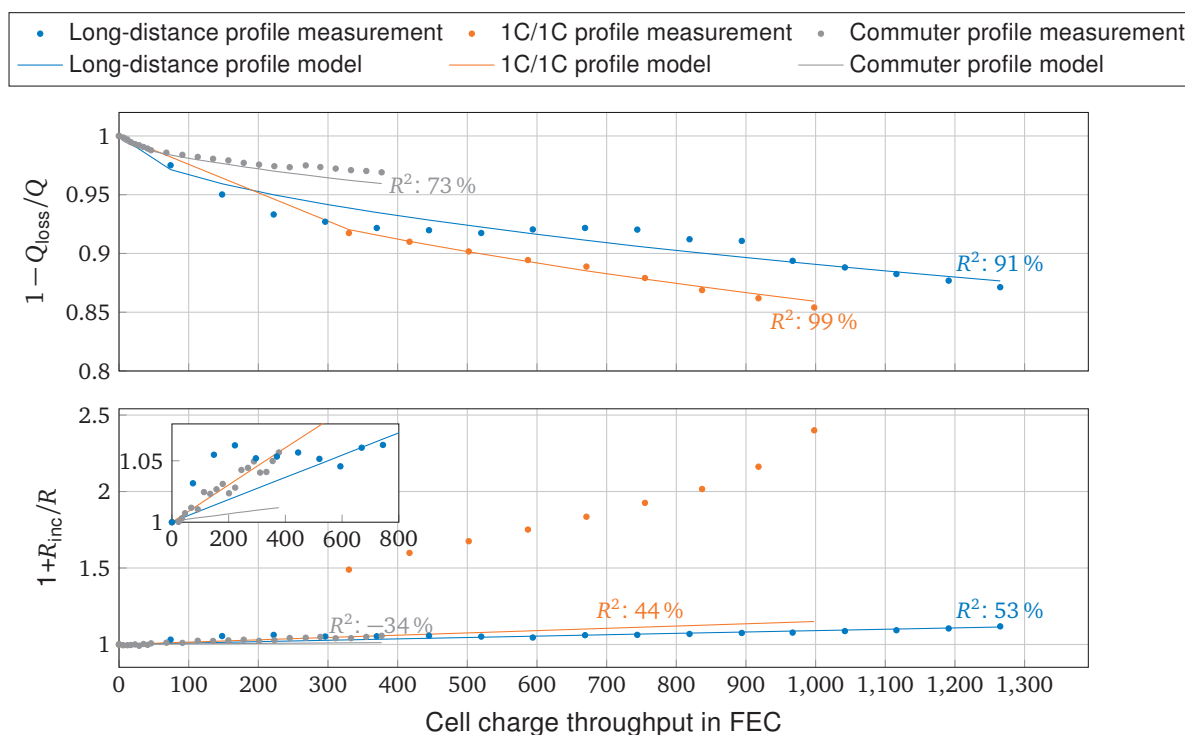


Figure 3.14: Curve fit of scaled aging model for three different aging conditions [118]. The degradation was not recorded during the first 300 cycles of the 1C/1C profile due to a faulty measurement setup.

The scaled model underestimates the internal resistance increase seen in the 1C/1C and commuter measurements, obtaining coefficients of determination of 44 % and -34 %. Note that a negative coefficient of determination means that the curve fit is worse than a straight line through the average value. The scaled model is therefore not well equipped to predict the internal resistance increase of the selected cell for different aging conditions. Because the model will be used to estimate when the battery has reached 80 % of its initial capacity, I consider this error to be acceptable. Nonetheless, conclusions regarding maximum cell temperatures should be treated with caution, because the heat generation within the cells directly depends on the internal resistance.

3.3 Step 3: power profile generation

In addition to the validated battery model, a power profile corresponding to typical truck operation is required to estimate the battery life for the selected cell. The power profile should represent the typical power demand (driving) and supply (charging and regeneration) for BET. In the following, I will present my method and conclude with the results.

3.3.1 Method

The method consists of three steps, as shown in Fig. 3.15. First, a vehicle mobility algorithm generates a trip schedule by sampling the number of trips per day, departure time of the first trip, distance & duration of each trip, and the stop durations, while taking EU driving time regulations into account. Second, the energy consumption simulation samples the payload for each trip,

selects a driving cycle based on the average trip speed and simulates the energy consumption. Finally, the charger assignment algorithm samples the available charging power at the depot and rest areas to generate a power profile that does not violate the SOC limits. The algorithm is limited to single-driver operation, where the truck always returns to the depot within the daily driving time limit of 10 hours. The maximum daily driving distance is thus 800 km, which covers 98% of daily truck driving distances [33, 120].

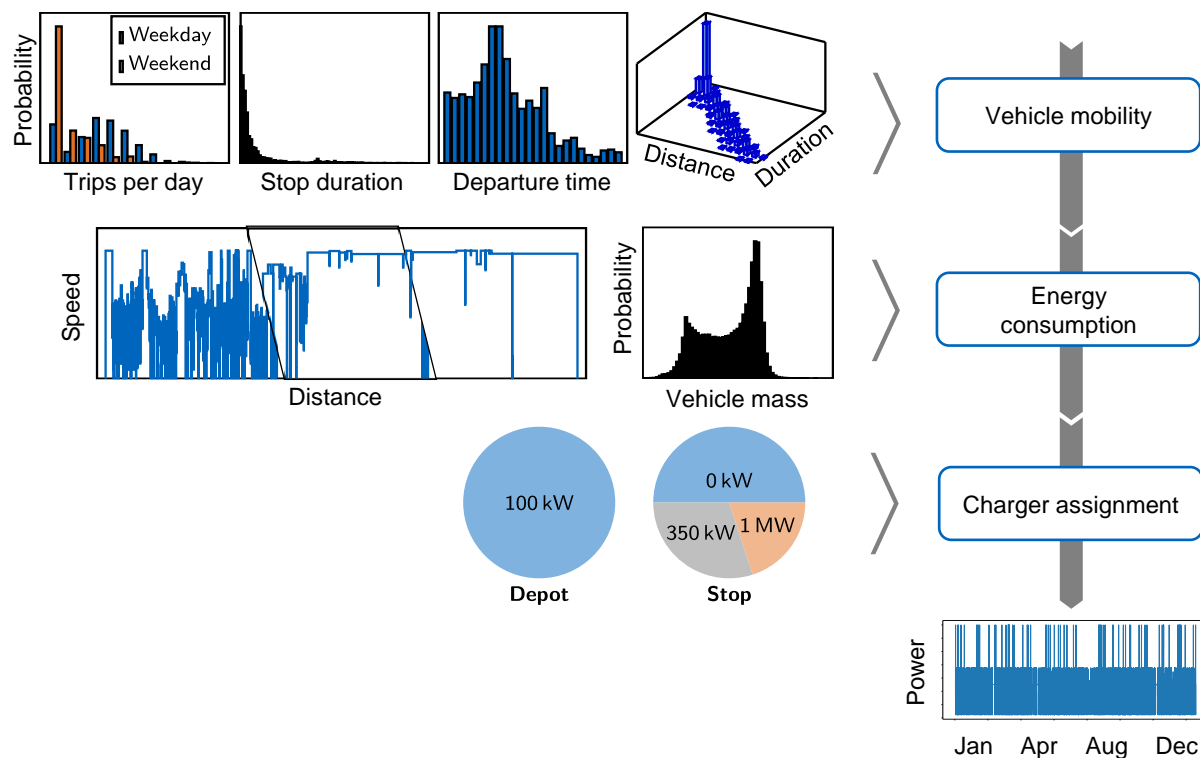


Figure 3.15: Schematic overview of the method that generates a power profile for BET.

The method is available open source within the *emobpy* framework developed by Gaete et al. and can be accessed at the following repository: <https://gitlab.com/diw-evu/emobpy/emobpy>

Vehicle mobility

The vehicle mobility algorithm generates a mobility profile that fulfills EU driving time regulations, based on distributions of the number of trips per day, stop duration, initial departure time and the distance & duration of each trip. All input data was derived from recorded measurements of a truck fleet published by Balke et al. [121]. The investigated truck fleet consisted of 18 vehicles that traveled $91\,950\text{ km year}^{-1}$ on average. The generated power profile is therefore specific to the operating pattern of this operator and might differ largely for different truck operators.

The distribution of the number of trips per day is shown in Figure 3.16. I differentiate between the number of trips on weekdays and the weekend. To ensure that the truck is returned to the depot, the probability of a single trip per day was removed during post processing. The trucks in the dataset complete up to 11 trips per day and are most likely to make 3 trips on weekdays. On weekends the trucks are most likely to make no trips at all.

The distribution of the first departure time of the day is shown in Figure 3.17, where the recorded departure times have been discretized in one-hour time steps. The trucks are most likely to

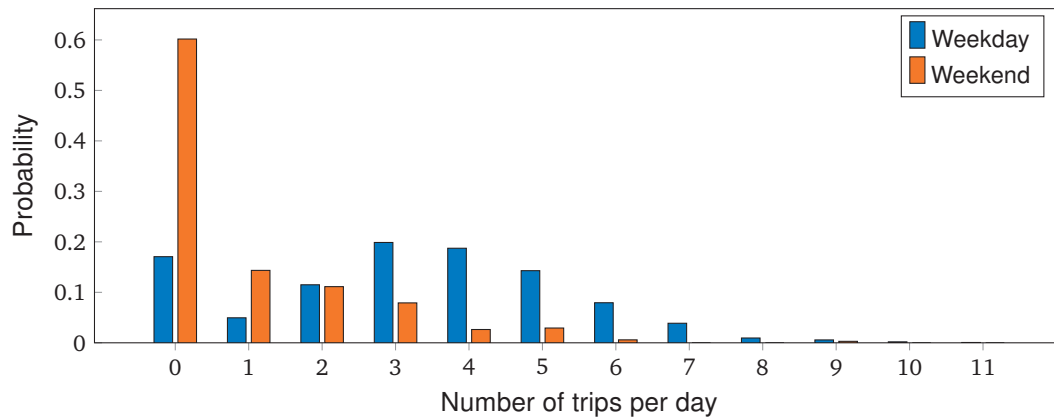


Figure 3.16: Distribution of number of trips per day

depart on their first trip at 6 a.m. or 7 a.m. The lowest probability of departing on a trip is at 8 p.m..

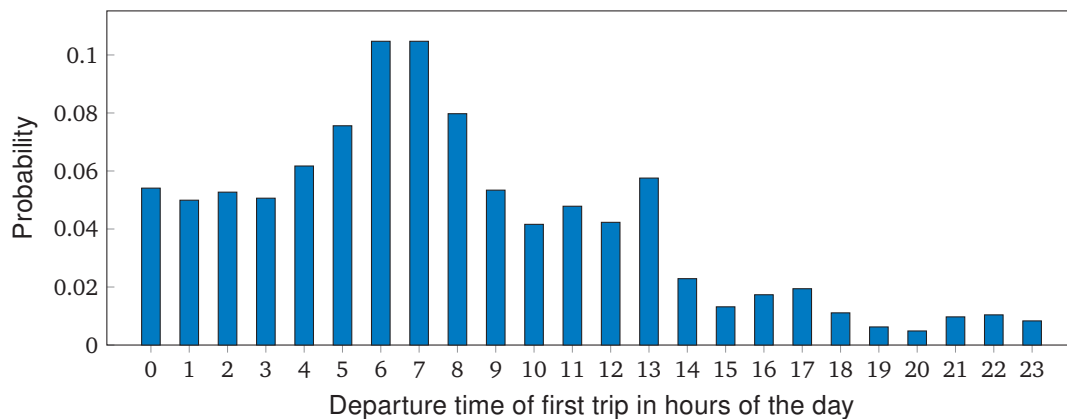


Figure 3.17: Distribution of first departure time

The distance-duration distribution is shown in Figure 3.18. The trip distance and duration are linked by the average trip velocity, resulting in the diagonal distribution. The most frequent trip was short in terms of both distance and duration. Furthermore, a decline in probability can be seen for combinations of distance and duration that deviate from the typical average velocity.

The final input for the mobility algorithm, the distribution of stop durations, is shown in Figure 3.19, where the mandatory break duration after 4.5 h is indicated by a dashed line. Shorter stops are more frequent than long stops. A small increase in probability can be seen around a stop duration of 9 h, which corresponds to the minimum daily rest duration.

A pseudocode representation of the algorithm is shown in Algorithm 3.1. For each day in the desired mobility profile length, the algorithm first samples the number of trips on that day, differentiating between weekdays and the weekend. If the number of trips is larger than zero, the departure time of the first trip is sampled. Subsequently, the distance & duration of each trip is sampled, while checking that the maximum driving duration does not exceed the daily driving time limit of 10 hours [104]. Similarly, the stop durations between the trips are sampled until a sequence is found that does not violate the EU regulation requiring drivers to take a 45 minute break after 4.5 hours of driving. The 45 minute break may be replaced by a break of at least 15 minutes followed by a break of at least 30 minutes. The trips and stops of each day are concatenated to generate a mobility profile.

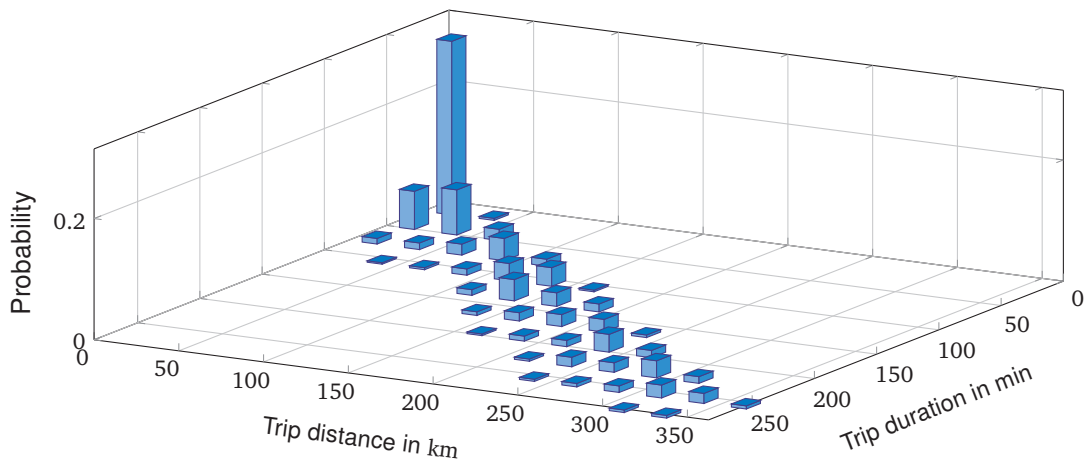


Figure 3.18: Distribution of trip distance and duration

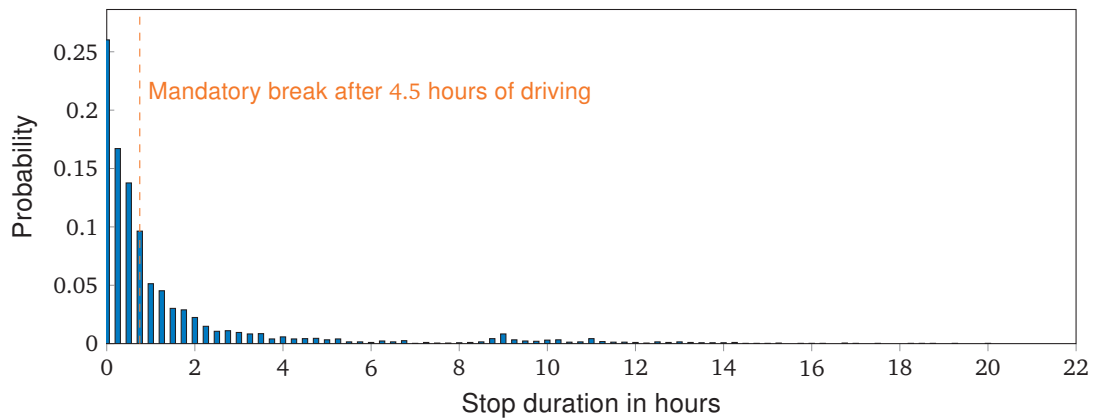


Figure 3.19: Distribution of stop duration

Data: profile length, trips per day distribution, departure time distribution, distance-duration distribution, rest-time distribution, EU regulations

Result: mobility profile

```

for Days in profile length do
  Sample number of trips;
  if Number of trips > 0 then
    Sample departure time of first trip;
    while EU regulations on max. driving time per day not met do
      | Sample distance-duration of trips
    end
    while EU regulations on max. rest time per day not met do
      | Sample rest times between trips
    end
  end
  Add trips and stops to mobility profile;
end
  
```

Algorithm 3.1: Pseudocode of vehicle mobility algorithm.

Energy consumption

The energy consumption simulation uses the generated mobility profile, combined with standardized driving cycles and a payload distribution, to simulate the truck energy consumption.

Depending on the average speed of the trip, I differentiate between the three VECTO driving cycles shown in Figure 3.20: long haul, regional delivery, and urban delivery. The VECTO driving cycles have been developed by the European Union to determine a truck's energy consumption and the resulting carbon dioxide emissions [103]. The driving cycles define a target speed, gradient and stop duration over a distance of 100 km. The long-haul profile has the highest average speed and the fewest stops. The regional-delivery profile has more frequent stops and does not reach the truck's top speed at the start and end of the cycle. The urban-delivery profile has the lowest average speed, with frequent, sometimes long, stops and only few sections where the maximum vehicle speed is reached. Additionally, the urban-delivery profile encounters the steepest road gradient.

The vehicle mass distribution corresponds to axle-load measurements for semi-trailer trucks with three-axle trailers from 41 measuring stations in Germany in January 2022 [122]. The resulting distribution is shown in Figure 3.21. Most trucks are fully loaded and operating with the maximum vehicle mass in Germany of 40 t [123, p. 30]. Trucks that were operated with a higher vehicle mass are removed during post processing, since they were either overweight or engaging in intermodal transport, i.e. transporting one or more containers on the initial or final leg of a journey while the remaining journey is covered by rail, maritime services or inland waterways. An increased probability occurs at a vehicle mass of 15 t, which roughly corresponds to the mass of an empty semi-trailer truck. Lower masses correspond to a tractor without a trailer or measurement errors. Vehicle masses below the 7.8 t average mass of a diesel tractor [102] were removed during post processing, because I assume they are measurement errors.

A pseudocode representation of the energy consumption simulation is shown in algorithm 3.2. The energy consumption simulation first calculates the share of payloads that cannot be transported due to the reduced payload capability caused by the mass of the battery. The distribution of DT payloads is calculated by subtracting the average diesel tractor mass from the curve in Figure 3.21. The selected cell can transport 70 kg less than a DT that adheres to the Gross Vehicle Weight (GVW) limit. I consider this payload loss to be negligible and therefore do not adjust the payload distribution here.

Subsequently, for each trip in the mobility profile, the energy consumption is simulated. First, a payload from the payload distribution is sampled. Then, a driving cycle is selected and modified to match the trip distance and duration in the mobility profile. To obtain the trip distance, the selected driving cycle is simply repeated and then cropped at the end. Matching the trip duration, however, is less straightforward.

The trip duration and distance determine the average speed. The average speed that a vehicle can achieve for a given driving cycle depends on the payload and on the distance at which the driving cycle was cropped. For the standard driving cycle length of 100 km and a vehicle at full payload, i.e. 42 t vehicle mass, the long-haul, regional and urban driving cycles have an average speed of 79.4 km h^{-1} , 60.8 km h^{-1} , and 25.9 km h^{-1} respectively.

To match the trip duration defined in the mobility profile, I first select the most suited driving cycle: for trips with an average speed above 70 km h^{-1} I use the long-haul driving cycle, between 40 km h^{-1} and 70 km h^{-1} the regional-driving cycle, and below 40 km h^{-1} the urban-driving cycle. These thresholds were chosen to obtain a rounded equidistant split between the average speed

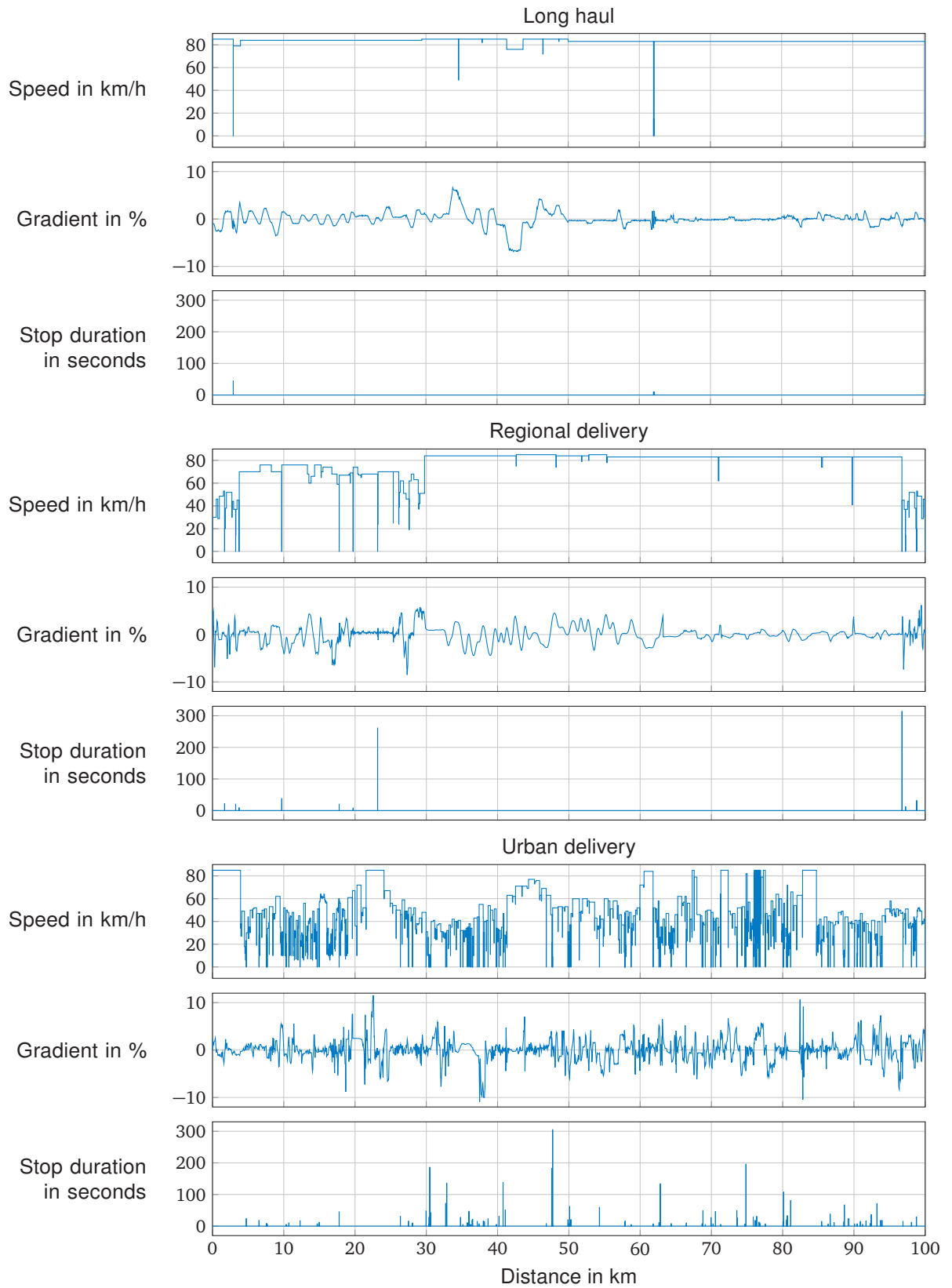


Figure 3.20: VECTO driving cycles [103]

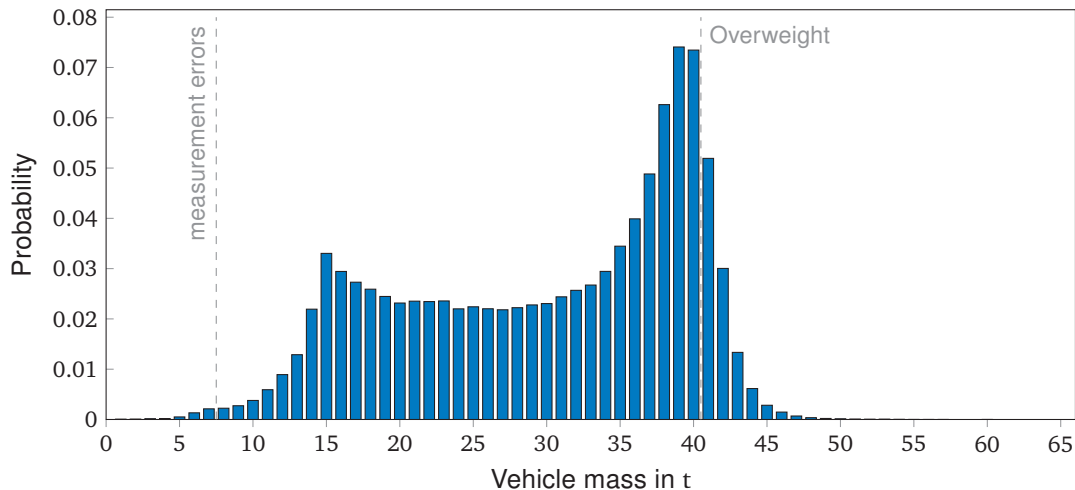


Figure 3.21: Vehicle mass distribution. Values below 7.8 t are assumed to be measurement errors and are not included. Vehicle masses above 40 t are outside of the legal operating limits or non-intermodal transport and are therefore not included.

of the driving cycles at full length and payload. To match the exact trip duration, I scale the selected speed profile with a constant factor, that I find using bisection.

Finally, the energy consumption is simulated for the cropped and scaled driving cycle using the longitudinal vehicle simulation from my previous publication included in Section 3.1. The energy consumption profile of each trip is added to the mobility profile to generate the mobility consumption profile.

Data: mobility profile, payload distribution, driving cycles, battery mass

Result: mobility & consumption profile

Calculate share of payloads that cannot be transported without violating the GVW;

Drop unfeasible payloads from payload distribution;

for *Trips in mobility profile* **do**

 Sample payload;

if *Average trip speed* > 70 km h⁻¹ **then**

 | Use VECTO long-haul driving cycle

end

else if *Average trip speed* > 40 km h⁻¹ **then**

 | Use VECTO regional driving cycle

end

else

 | Use VECTO urban driving cycle

end

 Crop driving cycle to trip distance;

 Scale the speed profile to match the trip duration;

 Simulate energy consumption ;

 Add trip energy consumption profile to mobility & consumption profile ;

end

Algorithm 3.2: Pseudocode of energy consumption simulation.

Charger assignment

In the last step, the charger assignment algorithm assigns chargers to the vehicle at rest stops. As an input, the algorithm uses a probability distribution of the availability of charging powers, where a charging power of 0 kW corresponds to a stop with no charger available. Since the Megawatt Charging System (MCS) standard is not available yet, an artificial scenario is created, where I assume that the trucks always have access to 100 kW chargers at the depot, and that the probability distribution of charging powers at the rest stops is as follows: 50 % chance that no charger is available, 30 % chance that a truck can be charged with 350 kW, which is the maximum available charging power under the Combined Charging System (CCS) standard [124], and a 20 % chance that the truck can be charged with 1 MW, which will be possible under the new MCS standard.

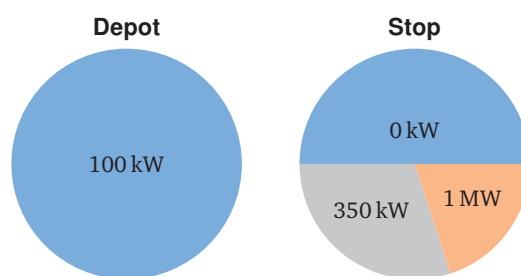


Figure 3.22: Charger availability

A pseudocode representation of the charger assignment is shown in algorithm 3.3. The algorithm first splits the mobility & consumption profile into tours, where one tour includes all trips and stops between starting and leaving the depot. For each tour, chargers are assigned until a solution is found that does not violate the SOC limit, taking the EOL condition of the battery into account. The feasibility check of the SOC limit does not use the detailed model presented in Section 3.2, but uses a simple energy balance based on the battery size that was determined for the selected cell by the sizing algorithm in Section 3.1. A charging strategy is implemented, where the truck is only charged at stops if the SOC drops below 80 %. The resulting charging powers are combined with the simulated energy consumption during driving to create the power profile.

3.3.2 Results

The first week of the generated power profile and resulting SOC are shown in Figure 3.23a. The vehicle is not moved on the first day. On the second day, the vehicle embarks on a tour with six trips with a long rest duration between the last three trips. The minimum and maximum power during driving correspond to the maximum truck motor power of 352 kW. Because the vehicle SOC during the stops is higher than the charging threshold, the battery is not recharged. When the vehicle returns to the depot it has access to a 100 kW charger, although it does not need the full time at the depot to recharge. On the eve of the third day, the vehicle embarks on a longer trip, discharging the battery to 62 % SOC. During the subsequent stop, the vehicle has access to a 350 kW charger to recharge the battery, but does not need the full stop duration to recharge. The rest of the week, the vehicle completes multiple trips, charging at both the depot and during the stops.

Figure 3.23b shows the power profile for the full length of one year. In the weeks following the first week, charging events of up to 1 MW can be seen. The SOC also reaches lower levels than

Data: mobility & consumption profile, charger availability distribution, charging threshold

Result: power profile

```

for Tours in mobility & consumption profile do
  while SOC limit breached do
    for Stops in tour do
      if SOC < charging threshold or stop at depot then
        | Sample charger power
      end
      else
        | Charger power = 0
      end
      Calculate SOC after stop;
    end
    Add charging power to mobility & consumption profile
  end
end

```

Generate power profile from charging power and power consumption during driving;

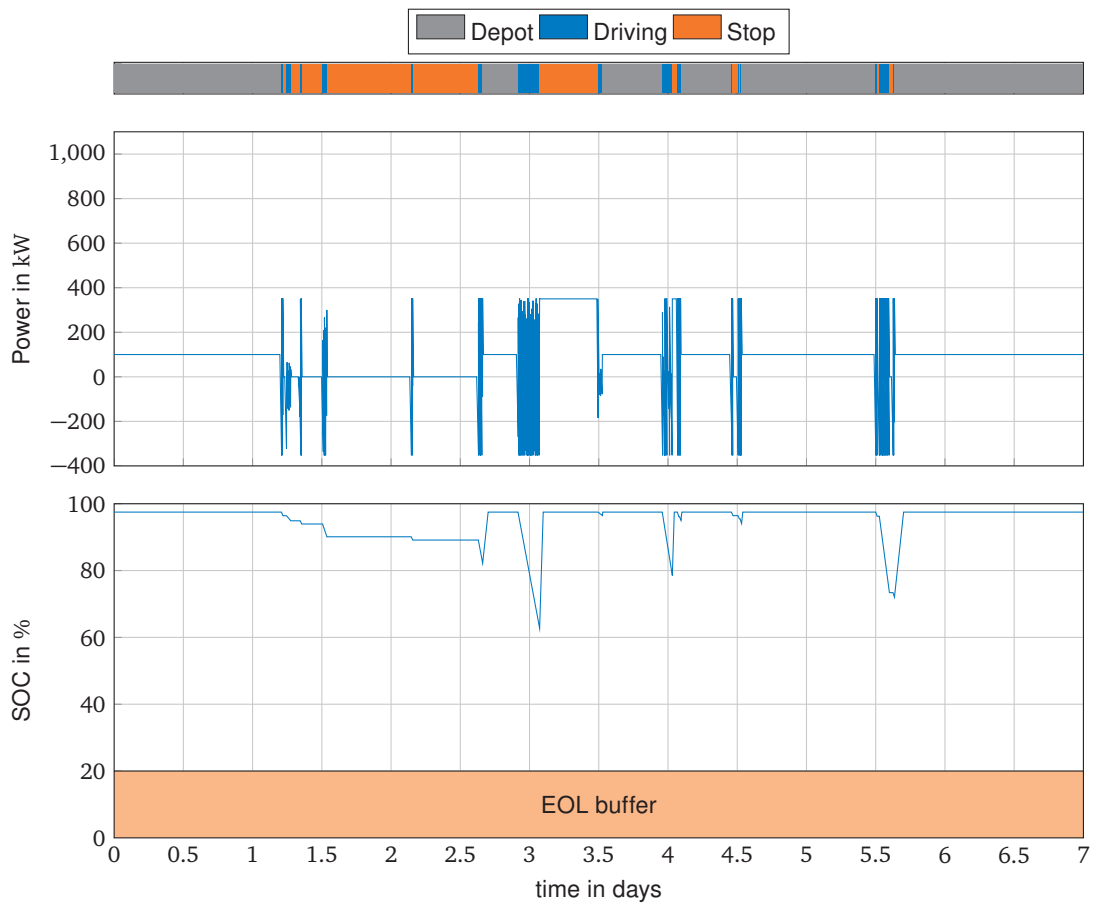
Algorithm 3.3: Pseudocode of charger assignment algorithm.

during the first week, getting close to the buffer reserved for battery aging, although this only happens a few times per month.

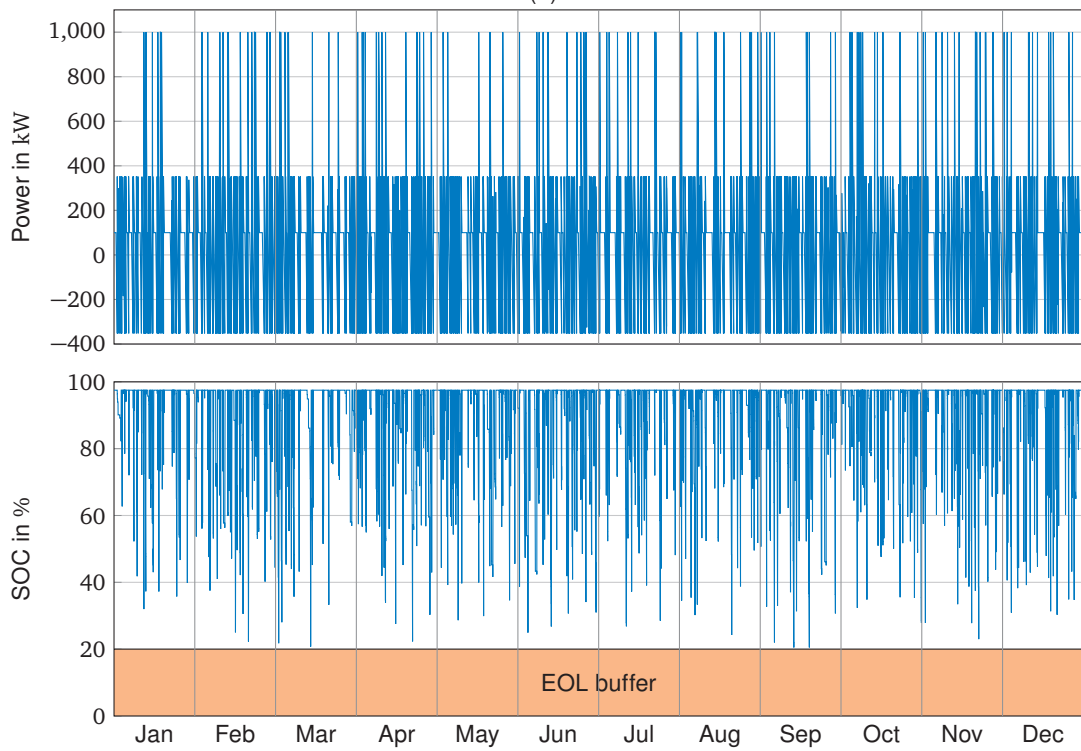
The driven distance of the generated power profile is 101 788 km annually. Note that I generated multiple power profiles and selected the profile with the highest annual mileage, to approach the annual driving distance used for homologation in the EU. The furthest trip without a stop is 362.5 km with a duration of 4.5 hours. The truck spends 18 % of the year driving, 20 % stopped away from the depot, and the remaining time in the depot. This matches the data recorded by Balke et al. [121] well, where vehicles were driving 17 % of the investigated period. The truck is charged away from the depot 248 times a year. The available charging power is 0 kW at 71 % of the stops, 350 kW at 15 % of the stops, and 1 MW at 14 % of the stops. The share of stops without a charger is higher than the charger availability distribution, due to the applied charging strategy that only charges the truck when the SOC drops below 80 %. The split between 350 kW and 1 MW chargers has shifted towards 1 MW chargers, because these are the only feasible option in some cases, but the shift is relatively small.

The presented method enables generating an annual power profile based on probability distributions of truck mobility data and charger availability. Due to the stochastic nature of the method, every power profile will be different and variations in operating behavior can be investigated. Additionally, the tool may be used to investigate the impact of different charging station availability.

Although the tool uses real-world mobility data, the following limitations should be taken into account. Due to the limited data availability, the mobility data and payload data were not determined for the same vehicles. Additionally, the available data could only take the covariance between the trip distance and duration into account, and not between the other parameters. For example, there might be a correlation between payload and trip distance, which could not be considered here. Finally, the trial and error approach for assigning trip durations and chargers may result in an overrepresentation of short trips and high power chargers.



(a)



(b)

Figure 3.23: Power profile and resulting SOC of the truck battery (a) for the first week, and (b) for the full power profile length of one year.

3.4 Step 4: battery lifetime simulation

Based on the validated battery model of the selected cell and the generated power profile that reflects typical truck operating conditions, the lifetime of the truck battery can be simulated.

The battery model that was parametrized in Section 3.2 is scaled to the BET battery size of 616 kWh determined in Section 3.1. The number of cells is scaled linearly to obtain the required battery capacity. Similarly, the mass of the pack components and the installed cooling power are scaled linearly. The effective heat transfer coefficient to ambient air is assumed to scale with the surface area, i.e. with an exponent of $2/3$. The cooling and heating thresholds were assumed to be the same as for the passenger car.

The battery operation is simulated over the entire battery lifetime with a time step of 10 s, where the annual power profile and ambient temperature are repeated until the EOL criterion of 20 % capacity loss is reached. The ambient temperature data corresponds to temperature measurements in Munich, Germany in 2017 [125], which was the most up-to-date dataset at the time of writing.

The resulting capacity loss, internal resistance increase, SOC and temperature are shown in Figure 3.24. The EOL criterion is reached after 9.5 years of operation. The majority of the capacity loss is caused by cyclic aging. The internal resistance at EOL has increased by 17 %, where cyclic aging was the dominating aging mechanism as well. As a result of the capacity decrease and internal resistance increase, the battery reaches lower SOC at the EOL compared to the beginning of life. Similarly, the highest battery temperature of 55 °C is reached near the EOL, which is still within the safe operating range of the cell.

The battery temperature over the course of the first year of operation is shown in Figure 3.25. The battery temperature is strongly affected by seasonal temperature changes, because of the long duration the vehicle is parked. As a result, high temperatures that lead to accelerated aging are more frequent in summer. High battery temperatures coincide with high temperature gradients, given by the difference between the cell and the housing temperature. Due to the implemented heating strategy, the battery temperature rarely drops below 15 °C.

A close up of the battery temperature on the day that the hottest temperature was reached within the first year is shown in Figure 3.26. The top pane shows the power profile and the battery power. The battery closely follows the power profile, but stops charging when the maximum SOC is reached. The power profile shows three trips, with no option to charge between the first two trips and the option to charge with a 1 MW charger between the last two trips. After the last trip the battery is recharged with 100 kW in the depot.

During the first two driving events, the battery is discharged down to 29 % SOC. The fast charging event recharges the battery to 83 % SOC. Subsequently, the battery is discharged during the last short trip and then recharged fully at the depot.

The battery temperature increases during driving, followed by a sharp increase in the battery temperature during the charging event. The highest battery temperature of 49.5 °C is reached at the end of the charging event. During the short trip after the charging event and the charging event in the depot, the battery temperature decreases and converges towards the ambient temperature.

The simulated battery life of 9.5 years is 61 % higher than the battery life that was estimated based on the assumed calendar life and the cycle life that was specified in the cell's datasheet. This is caused by the lower stress factors that occur in real-life operation compared to the aging

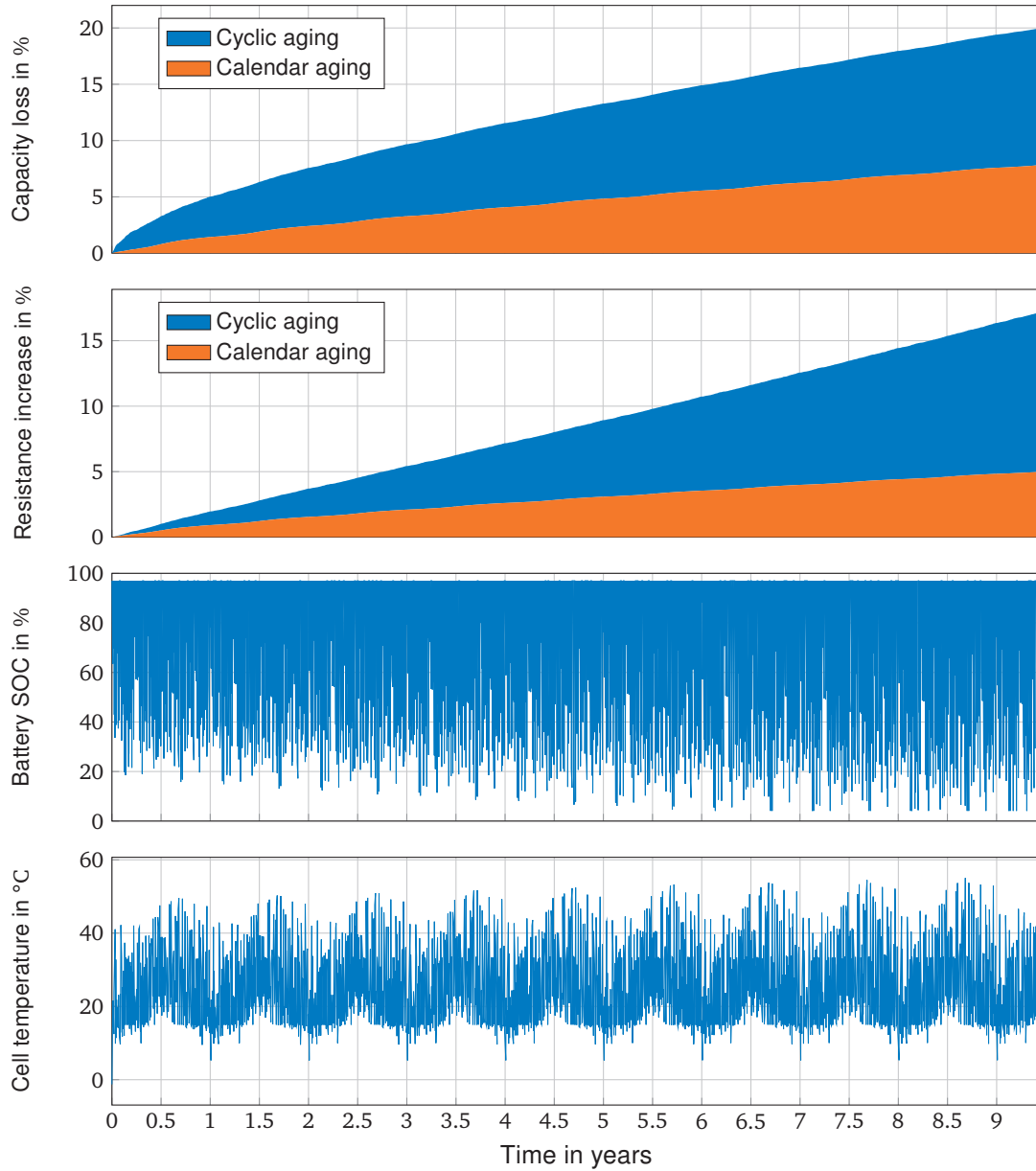


Figure 3.24: Battery capacity loss, resistance increase, SOC and cell temperature for the full battery life.

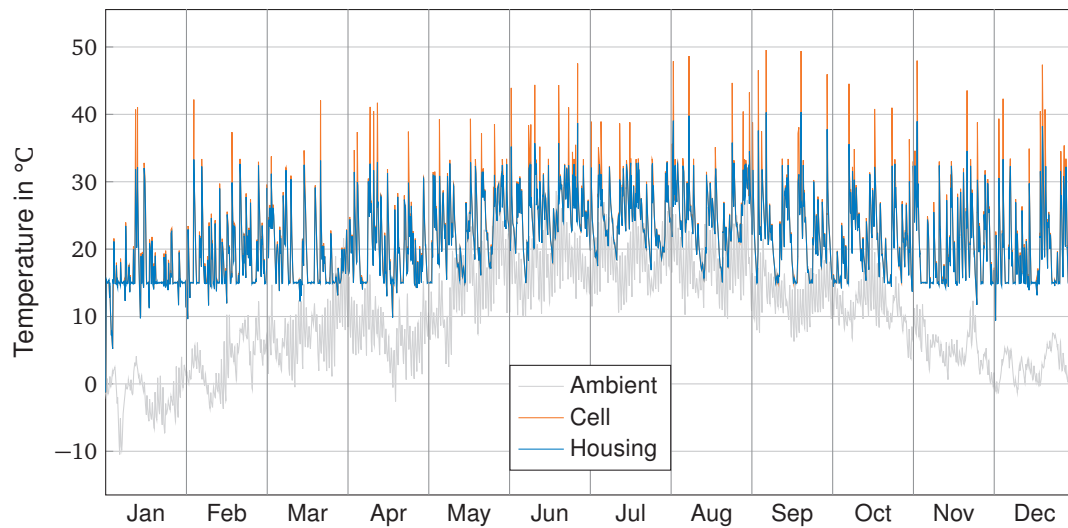


Figure 3.25: Battery temperature during the first year of operation.

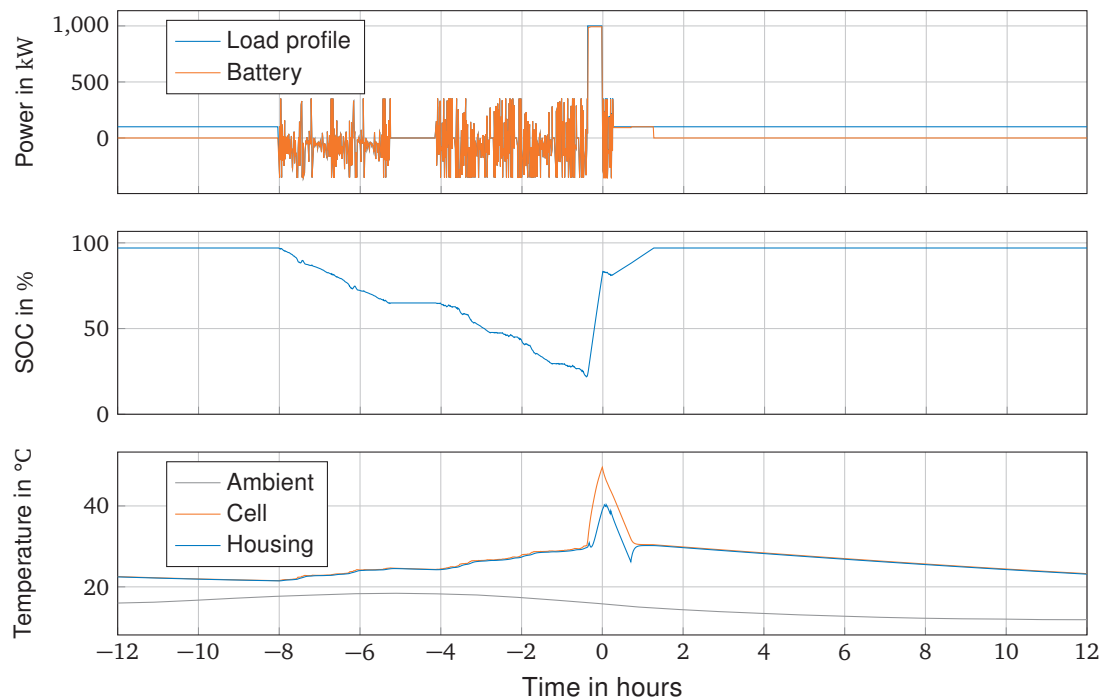


Figure 3.26: Close up of battery temperature on the day where the hottest temperature was reached in the first year, where the origin is placed at the time step in which the hottest cell temperature was reached.

conditions at which the cell's cycle life was specified in the datasheet: 1C/1C at 100% DOD. This emphasizes the need to perform a detailed simulation of the battery life, which requires a detailed cell characterization. Based on the lifetime obtained by the detailed simulation, a BET using the selected cell would reach cost-parity with a DT if the cell can be purchased at 223€ kWh^{-1} .

3.5 Step 5: battery thermal management system design

In the last step of the battery design method, the impact of the BTMS on the battery life and battery safety is investigated. I published this analysis for a different cell as a first author in a previous study [126].

To model the impact of the BTMS design on the battery life, I use the simulation that was presented in Section 3.4. To investigate the impact of the installed cooling power and cooling threshold, I conduct full factorial simulations for both parameters. The results are shown in Figure 3.27, where the BTMS configuration corresponding to the results in Section 3.4 is highlighted by the VW-marker.

The top-left pane shows the impact of the installed cooling power and the cooling threshold on the maximum cell temperature. The highest cell temperature of 65°C is reached at a cooling power of 0 kW , corresponding to a battery without an active cooling system. This temperature exceeds the typical safe operating window of lithium-ion cells [98], suggesting that an active cooling system is necessary to allow charging the battery with 1 MW during the entire operating life. The lowest maximum temperature of 41.3°C is achieved by high installed cooling powers

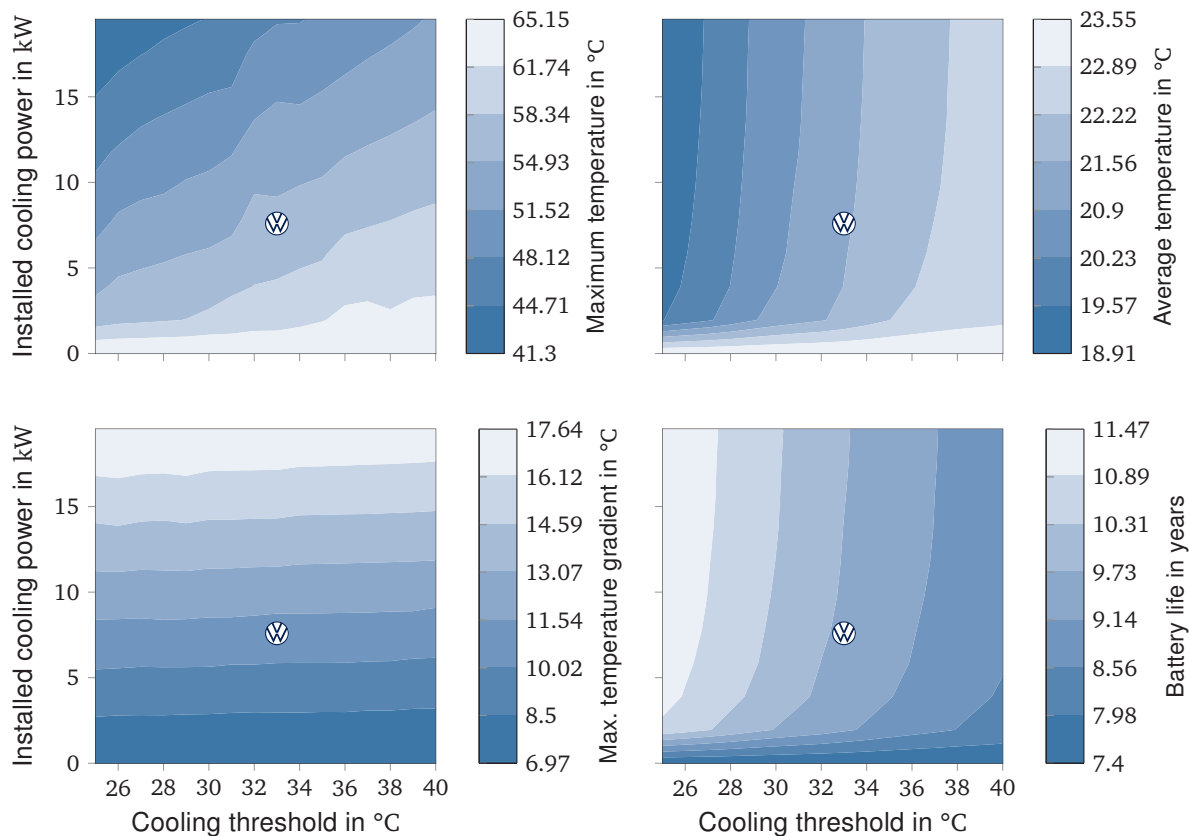



Figure 3.27: Impact of the installed cooling power and selected cooling threshold on the truck's battery life. The scaled configuration of the VW ID.3 cooling system is denoted by 

and a low cooling threshold. The irregularities in the top-left pane are caused by simulating the battery until the EOL is reached. This causes some simulations end on a day with a fast-charging event in summer, whereas others end before, resulting in variations of the maximum temperature.

The top-right pane shows the impact on the average temperature. A similar trend as for the maximum temperature can be seen, but the impact of the installed cooling power is relatively smaller than the impact of the cooling threshold.

The lower-left pane shows the impact on the temperature gradient within the cell. Although temperature gradients are not considered in the implemented aging model, Offer et al. [127] showed that they cause accelerated aging behavior. The temperature gradients in the cell increase with an increase in installed cooling power. Additionally, a slight increase in the temperature gradient can be seen at lower cooling thresholds.

Finally, the impact on the battery life is shown in the bottom-right pane. The impact of the installed cooling power and cooling threshold on the battery life closely matches the impact on the average cell temperature: the battery life can be extended from 9.5 years, achieved by the scaled VW ID.3 BTMS configuration, to 11.5 years, achievable with an installed cooling power of 18 kW and a cooling threshold of 25 °C. However, the impact of the installed cooling power on the battery life is small. A reduction of the installed cooling power by a factor of five leads to a reduction of the battery life of only 4.4%. The cooling threshold, however, has a larger impact, where a reduction in cooling threshold to 25 °C results in a lifetime increase of 15%.

Whether the reduced battery life resulting from a decrease in the installed cooling power is justified is highly dependent on the cost, volume reduction and impact on noise pollution.

Similarly, whether the increased battery life achieved by a lower cooling threshold is justified strongly depends on the additional energy consumption and resulting range reduction. Because I do not have sufficient data to quantify these impacts, the result does not provide an optimal solution, but rather a sensitivity analysis of these BTMS parameters that highlight the impact of the BTMS design.

The following limitations should be taken into account. First, the impact of battery temperature in the aging model was solely parametrized based on calendar aging tests. Therefore, the model only applies accelerated aging during the duration that the battery has a high temperature. Because high battery temperatures only occur during a small fraction of the vehicle life, the impact is relatively small. However, other aging stress factors might not be captured by the aging model that cause accelerated aging during short periods of high temperatures.

Second, in some cases high battery temperatures are beneficial in terms of efficiency and power capability. In particular during charging, higher battery temperatures are desirable to avoid lithium plating. This aspect is not considered by the implemented aging model and should be included in future work on BTMS design.

Finally, in addition to typical operating conditions, worst case operation in strenuous terrain or ambient conditions must be taken into account during the BTMS design.

4 Discussion & Conclusion

The top-level battery-design resulting from the five-step method is summarized below.

- The battery uses the LG Chem ID.3 cell and requires a 616 kWh battery to mimic DT operation at the maximum vehicle weight over the entire operating life.
- BET using this cell would become cost-competitive if the cell can be bought for less than €225 kWh⁻¹. Note that the cost-parity price found in Section 3.1 was updated based on the simulated lifetime in Section 3.4. The current average cell price for automotive applications is €142 kWh⁻¹ [22], meaning that cost-parity with DT can be achieved today.
- The battery would require a volume of 2168 L onboard the vehicle, which is 33 % less than the volume of the current DT powertrain.
- The BET with this battery could transport a payload of 24.7 t, which is only 70 kg, or 0.3 % lower than state-of-the-art DT.
- Using a scaled-up version of the VW ID.3 cooling system, would result in a battery life of 9.5 years (967 thousands kilometers) under typical truck operating conditions and avoid safety critical cell temperatures throughout the entire operating life.
- Increasing the installed cooling power and lowering the cooling threshold could extend the battery life to 11.5 years, corresponding to 1.2 million kilometers.

The results show, that BET are not only our best bet for reaching the goals of the Green Deal, but also feasible and cost-competitive. Using a status-quo lithium-ion cell, BET can mimic DT operation in a cost-competitive manner, with negligible payload losses and no volume constraints onboard the vehicle, provided that 1 MW charging is available during the mandatory driver rest period. The found battery size and resulting vehicle range and mass match announcements from truck manufacturers well (Table 2.1). The remaining results can not be verified, due to the lack of commercially available BET and their properties.

The presented method supports vehicle designers with the top-level battery design of a BET. In addition to the overall novelty of the design method, novel contributions are achieved by the individual method steps.

The cell selection method extends traditional cell selection methods, such as the Ragone plot, by quantifying the impact of individual cell characteristics on the system cost. The challenging requirements for BET batteries make it difficult to find one cell that meet all aspects. Trade-offs must therefore be managed effectively. Figure 3.3 serves truck manufacturers as a tool to compare the cost-effectiveness of different cells with properties that do not directly influence system costs, such as the achievable payload or required volume onboard the vehicle. Additionally, the parameter sensitivity analysis allows cell manufacturers to quantify the impact of improving individual cell properties in different scenarios.

The battery model was parametrized for a status-quo automotive-grade lithium-ion cell and validated based on over 100 hours of measurements on vehicle level. To the best of my knowledge, a validation on this scale for a commercially-available vehicle has not been presented in literature before. Additionally, the implementation of the battery model in a compiled programming language allows taking seasonal temperature and load variations into account within reasonable computation times. As a result, the simulation is well equipped to do detailed parameter sensitivity studies.

Finally, the power profile generation method combines truck mobility data and a longitudinal vehicle simulation to generate detailed power profiles that cover driving, charging and idling phases of a vehicle. In contrast to previous BET load profile generation methods, the power profiles can be used to simulate battery operation in a wide variety of scenarios.

Although previous studies presented battery design methods, none covered the entire process from cell selection to BTMS design in this level of detail. The method can be easily adapted to design batteries for other applications. I developed the cell selection method for the BetterBat project, where it will be extended to cover further applications. If a different cell is selected, a new parametrization of the battery model needs to be conducted. The battery model remains unchanged, except for the thermal model, which is application specific. The presented load profile generation is specific to BET. For some other applications load profiles are available in literature, e.g. for home storage [128] or peak shaving [129], others may require new methods and measurements. Finally, the last two steps of the method that assess the battery life, safety and impact of the cooling system can be used unchanged.

That said, the following limitations need to be taken into account. First and foremost, the designed battery will only be able to mimic DT operation if 1 MW charging is available during the rest duration. Although Charin, a global association with over 300 members, is actively developing a standard to make this possible, 1 MW charging infrastructure does not exist yet. Future research is required to support the cost-effective implementation of high power charging infrastructure.

Second, the presented battery model uses the simplest possible models that reproduce the observable behavior. Nonetheless, the analysis of the model errors identified opportunities for future research for each sub-model. The electric model underestimates the cell's internal resistance for long pulse durations, typically occurring during charging, because the diffusion behavior of the internal resistance could not be captured in the 30 s HPPC pulses. The thermal model does not consider entropy effects, which may explain deviations from the measurements. And finally, the aging model could not describe the resistance increase well under different operating conditions. Additionally, the model was only parametrized for three different temperatures and did not take the impact of temperature gradients on battery aging into account.

Third, the considered load profile only covers the average operation of a German truck operator. BET should be designed to cover a wide range of use cases, including worst-case operation. Additionally, designing batteries for different use case, e.g. weight and volume-constrained, could prove to be economical.

By making all measurement data and code available open-source, I hope to enable other researchers to improve upon the current limitations of the method and investigate new scenarios.

List of Figures

Figure 1.1:	Share of heavy-duty truck emissions in the transport sector [2, p. 18].	2
Figure 1.2:	Thesis structure	3
Figure 2.1:	The original Ragone diagram [61]. Lithium-ion batteries and other energy storage devices were only included in later versions.	10
Figure 2.2:	An ECM with a single RC-element.	11
Figure 2.3:	pOCV measurement and OCV-curve of the VW ID.3 cell [74]	12
Figure 2.4:	Voltage response to a 1/2C 30 s current pulse for the VW ID.3 cell at 50 % SOC and 20 °C [74]	12
Figure 2.5:	Exemplary curve fit for the VW ID.3 cell at 50 % SOC and 20 °C. The curve fit achieves a coefficient of determination of 98.2 %, where the biggest deviation occurs at the beginning of the pulse.	13
Figure 2.6:	Rainflow counting algorithm	16
Figure 2.7:	Research gap	20
Figure 3.1:	Overview of the battery design method. The results from the first step are used as an input to the second and third step, which then feed in to the fourth step. Finally, the fifth step uses the model from the fourth step to generate a top-level battery-design.	21
Figure 3.2:	Schematic of the cell selection method [102]	23
Figure 3.3:	Comparison of all cells in the cell database.	42
Figure 3.4:	Schematic of implemented battery model, adapted from [113].	44
Figure 3.5:	Lumped thermal capacitance model	64
Figure 3.6:	Quality and found parameters of the ECM parametrization	66
Figure 3.7:	Measurement of passive heat transfer between the battery and ambient air. The blue band corresponds to the area between the minimum and maximum measured temperature.	68
Figure 3.8:	Data used to validate the electric and thermal model: a) driving at different speed profiles b) charging at different charging powers.	68
Figure 3.9:	Voltage and temperature distributions for all validation profiles	69
Figure 3.10:	Interurban cycle at 15 °C ambient temperature	70
Figure 3.11:	Highway cycle at 15 °C ambient temperature	71
Figure 3.12:	Wallbox charging cycle	72
Figure 3.13:	Fast charging cycle	73
Figure 3.14:	Curve fit of scaled aging model for three different aging conditions [118]. The degradation was not recorded during the first 300 cycles of the 1C/1C profile due to a faulty measurement setup.	75
Figure 3.15:	Schematic overview of the method that generates a power profile for BET.	76
Figure 3.16:	Distribution of number of trips per day	77
Figure 3.17:	Distribution of first departure time	77
Figure 3.18:	Distribution of trip distance and duration	78
Figure 3.19:	Distribution of stop duration	78

Figure 3.20:	VECTO driving cycles [103]	80
Figure 3.21:	Vehicle mass distribution. Values below 7.8 t are assumed to be measurement errors and are not included. Vehicle masses above 40 t are outside of the legal operating limits or non-intermodal transport and are therefore not included.	81
Figure 3.22:	Charger availability	82
Figure 3.23:	Power profile and resulting SOC of the truck battery (a) for the first week, and (b) for the full power profile length of one year.	84
Figure 3.24:	Battery capacity loss, resistance increase, SOC and cell temperature for the full battery life.	86
Figure 3.25:	Battery temperature during the first year of operation.	86
Figure 3.26:	Close up of battery temperature on the day where the hottest temperature was reached in the first year, where the origin is placed at the time step in which the hottest cell temperature was reached.	87
Figure 3.27:	Impact of the installed cooling power and selected cooling threshold on the truck's battery life.	88
Figure A.1:	ECM with two RC-elements.	xxi
Figure A.2:	Quality and found parameters of the ECM parametrization.....	xxii
Figure B.1:	Urban cycle at 15 °C ambient temperature	xxiii
Figure B.2:	Urban cycle at 30 °C ambient temperature	xxv
Figure B.3:	Interurban cycle at 30 °C ambient temperature	xxvi
Figure B.4:	Interurban cycle at 30 °C ambient temperature	xxvii

List of Tables

Table 2.1:	Characteristics and SOP of announced long-haul trucks [31]	6
Table 3.1:	Properties of the selected cell, obtained from the cell database, and results from the cell selection method.....	43
Table 3.2:	Constant parameters of ECM	65
Table 3.3:	Constant parameters of the thermal model.....	67

Bibliography

- [1] „The European Green Deal,“ European Commission, Brussels rep. COM(2019) 640 final, 11/12/2019.
- [2] „Transport and environment report 2021: Decarbonising road transport — the role of vehicles, fuels and transport demand,“ European Environment Agency, 02/2022, DOI: 10.2800/68902.
- [3] „Global EV Outlook 2022: Securing supplies for an electric future,“ International Energy Agency, 2022. Available: <https://www.iea.org/reports/global-ev-outlook-2022> [visited on 03/06/2023].
- [4] N. Hill et al., „Reduction and Testing of Greenhouse Gas (GHG) Emissions from Heavy Duty Vehicles – Lot 1: Strategy,“ Ricardo Energy & Environment, 22/02/2011. Available: https://climate.ec.europa.eu/system/files/2016-11/ec_hdv_ghg_strategy_en.pdf [visited on 03/06/2022].
- [5] S. Hänggi et al., „A review of synthetic fuels for passenger vehicles,“ *Energy Reports*, vol. 5, pp. 555–569, 2019, DOI: 10.1016/j.egyr.2019.04.007.
- [6] Agora Verkehrswende, Agora Energiewende and Frontier Economics, „Die zukünftigen Kosten strombasierter synthetischer Brennstoffe,“ 2018. Available: https://www.agora-energiewende.de/fileadmin/Projekte/2017/SynKost_2050/Agora_SynCost-Studie_WEB.pdf [visited on 03/06/2023].
- [7] S. Altenburg et al., „Nullemissionsnutzfahrzeuge: vom ökologischen Hoffnungsträger zur ökonomischen Alternative,“ e-mobil BW GmbH, 2017. Available: <https://www.e-mobilbw.de/service/presse/pressemitteilungen/pressemitteilungen-detail/neue-studie-zu-nullemissions-nutzfahrzeugen> [visited on 03/06/2023].
- [8] N. Wassiliadis et al., „Review of fast charging strategies for lithium-ion battery systems and their applicability for battery electric vehicles,“ *Journal of Energy Storage*, vol. 44, p. 103306, 2021, DOI: 10.1016/j.est.2021.103306.
- [9] P. Plötz, „Hydrogen technology is unlikely to play a major role in sustainable road transport,“ *Nature Electronics*, vol. 5, no. 1, pp. 8–10, 2022, DOI: 10.1038/s41928-021-00706-6.
- [10] T. Earl, „Roadmap to decarbonizing European cars,“ Transport & Environment, 11/2018. Available: https://www.transportenvironment.org/wp-content/uploads/2021/07/2050_strategy_cars_FINAL.pdf [visited on 03/06/2023].
- [11] S. Verhelst, „Recent progress in the use of hydrogen as a fuel for internal combustion engines,“ *international journal of hydrogen energy*, vol. 39, no. 2, pp. 1071–1085, 2014, DOI: 10.1016/j.ijhydene.2013.10.102.
- [12] S. Wolff, „Eco-Efficiency Assessment of Zero-Emission Heavy-Duty Vehicle Concepts,“ Dissertation, Institute of Automotive Technology, Technical University of Munich, Munich, 2023.

- [13] S. Wolff, M. Fries and M. Lienkamp, „Technoecological analysis of energy carriers for long-haul transportation,” *Journal of Industrial Ecology*, vol. 24, no. 1, pp. 165–177, 2020, DOI: 10.1111/jiec.12937.
- [14] S. Sripad and V. Viswanathan, „Performance metrics required of next-generation batteries to make a practical electric semi truck,” *ACS Energy Letters*, vol. 2, no. 7, pp. 1669–1673, 2017, DOI: 10.1021/acseenergylett.7b00432.
- [15] J. Teter, P. Cazzalo and G. Timur, „The future of Trucks – Implications for Energy and the Environment. Second edition,” International Energy Agency, 2017. Available: <https://iea.blob.core.windows.net/assets/a4710daf-9cd2-4bdc-b5cf-5141bf9020d1/TheFutureofTrucksImplicationsforEnergyandtheEnvironment.pdf> [visited on 03/06/2023].
- [16] J. Deng et al., „Electric vehicles batteries: requirements and challenges,” *Joule*, vol. 4, no. 3, pp. 511–515, 2020, DOI: 10.1016/j.joule.2020.01.013.
- [17] M. S. Ziegler and J. E. Trancik, „Re-examining rates of lithium-ion battery technology improvement and cost decline,” *Energy & Environmental Science*, vol. 14, no. 4, pp. 1635–1651, 2021, DOI: 10.1039/D0EE02681F.
- [18] E. Den Boer et al., „Zero emissions trucks. An overview of state-of-the-art technologies and their potential,” CE Delft, 2013. Available: https://ce.nl/wp-content/uploads/2021/03/CE_Delft_4841_Zero_emissions_trucks_Def_1374483553.pdf [visited on 03/06/2023].
- [19] B. Lenz et al., „Shell Nutzfahrzeug-Studie Diesel oder Alternative Antriebe-Womit Fahren Lkw und Bus Morgen,” Shell Deutschland Oil GmbH, 30/06/2016. Available: <https://elib.dlr.de/108867/> [visited on 03/06/2023].
- [20] T. Placke et al., „Lithium ion, lithium metal, and alternative rechargeable battery technologies: the odyssey for high energy density,” *Journal of Solid State Electrochemistry*, vol. 21, pp. 1939–1964, 2017, DOI: 10.1007/s10008-017-3610-7.
- [21] J. T. Frith, M. J. Lacey and U. Ulissi, „A non-academic perspective on the future of lithium-based batteries,” *Nature Communications*, vol. 14, no. 1, p. 420, 2023, DOI: 10.1038/s41467-023-35933-2.
- [22] V. Henze, „Lithium-ion Battery Pack Prices Rise for First Time to an Average of \$151/kWh,” BloombergNEF, 2022. Available: <https://about.bnef.com/blog/lithium-ion-battery-pack-prices-rise-for-first-time-to-an-average-of-151-kwh/> [visited on 02/07/2023].
- [23] C. Calvo Ambel, „Roadmap to climate-friendly land freight and buses in Europe,” Transport & Environment, 2017. Available: <https://www.transportenvironment.org/discover/roadmap-climate-friendly-land-freight-and-buses-europe/> [visited on 03/06/2023].
- [24] C. Calvo Ambel, „Electric trucks’ contribution to freight decarbonisation,” Transport & Environment, 09/2017. Available: https://www.transportenvironment.org/wp-content/uploads/2021/07/2017_09_Update_Norway_study_final.pdf [visited on 03/06/2023].
- [25] S. Suzah and L. Mathieu, „Unlocking Electric Trucking in the EU: recharging along highways,” 2021. Available: https://www.transportenvironment.org/wp-content/uploads/2021/07/202102_pathways_report_final.pdf [visited on 03/06/2023].
- [26] S. Sripad and V. Viswanathan, „Quantifying the economic case for electric semi-trucks,” *ACS Energy Letters*, vol. 4, no. 1, pp. 149–155, 2018, DOI: 10.1021/acsenergylett.8b02146.
- [27] A. Phadke et al., „Why regional and long-haul trucks are primed for electrification now,” Lawrence Berkeley National Lab.(LBNL), Berkeley, CA (United States), 2021, DOI: 10.2172/1834571.

- [28] MAN. „Executive Board and General Works Council agree on Key Issues Paper to realign the Company,“ 2021. Available: <https://press.mantruckandbus.com/corporate/executive-board-and-general-works-council-agree-on-key-issues-paper-to-realign-the-company/> [visited on 02/11/2023].
- [29] SCANIA. „Scania’s commitment to battery electric vehicles,“ 2021. Available: <https://www.scania.com/group/en/home/newsroom/news/2021/Scanias-commitment-to-battery-electric-vehicles.html> [visited on 02/11/2023].
- [30] ACEA. „All new trucks sold must be fossil free by 2040, agree truck makers and climate researchers,“ 2020. Available: <https://www.acea.auto/press-release/all-new-trucks-sold-must-be-fossil-free-by-2040-agree-truck-makers-and-climate-researchers/> [visited on 02/11/2023].
- [31] MAN. „BEV overview Tractors 4x2,“ Internal MAN Benchmark IAA Transportation Hannover. 2022.
- [32] S. Wolff, M. Lienkamp and K.-V. Schaller, *STATUS NUTZFAHRZEUGE 2020: ALLES AUF EINE KARTE?*, Researchgate, 2021.
- [33] H. Basma, A. Saboori and F. Rodríguez, „Total cost of ownership for tractor-trailers in Europe: Battery electric versus diesel,“ International Council on Clean Transportation, 11/2021. Available: <https://theicct.org/sites/default/files/publications/TCO-BETs-Europe-white-paper-v4-nov21.pdf> [visited on 03/06/2023].
- [34] B. Noll et al., „Analyzing the competitiveness of low-carbon drive-technologies in road-freight: A total cost of ownership analysis in Europe,“ *Applied Energy*, vol. 306, p. 118079, 2022, DOI: 10.1016/j.apenergy.2021.118079.
- [35] T. Earl et al., „Analysis of long haul battery electric trucks in EU,“ in *Commercial Vehicle Workshop, Graz*, 2018. Available: https://www.transportenvironment.org/wp-content/uploads/2021/07/20180725_T&E_Battery_Electric_Trucks_EU_FINAL.pdf [visited on 03/06/2023].
- [36] K. Forrest et al., „Estimating the technical feasibility of fuel cell and battery electric vehicles for the medium and heavy duty sectors in California,“ *Applied Energy*, vol. 276, p. 115439, 2020, DOI: 10.1016/j.apenergy.2020.115439.
- [37] I. Mareev, J. Becker and D. U. Sauer, „Battery dimensioning and life cycle costs analysis for a heavy-duty truck considering the requirements of long-haul transportation,“ *Energies*, vol. 11, no. 1, p. 55, 2018, DOI: 10.3390/en11010055.
- [38] B. Nykvist and O. Olsson, „The feasibility of heavy battery electric trucks,“ *Joule*, vol. 5, no. 4, pp. 901–913, 2021, DOI: 10.1016/j.joule.2021.03.007.
- [39] L. Mauler et al., „Cost-effective technology choice in a decarbonized and diversified long-haul truck transportation sector: A US case study,“ *Journal of Energy Storage*, vol. 46, p. 103891, 2022, DOI: 10.1016/j.est.2021.103891.
- [40] J. Ma et al., „The 2021 battery technology roadmap,“ *Journal of Physics D: Applied Physics*, vol. 54, no. 18, p. 183001, 2021, DOI: 10.1088/1361-6463/abd353.
- [41] P. Burda, „Verfahren zur Entwicklung und Auslegung von Energiespeichersystemen für Elektrokraftfahrzeuge,“ Dissertation, Technische Universität München, 2014.
- [42] H. C. Hesse et al., „Lithium-ion battery storage for the grid—A review of stationary battery storage system design tailored for applications in modern power grids,“ *Energies*, vol. 10, no. 12, p. 2107, 2017, DOI: 10.3390/en10122107.

- [43] M. Naumann, „Techno-economic evaluation of stationary battery energy storage systems with special consideration of aging,“ Dissertation, Technische Universität München, 2018. Available: <https://nbn-resolving.de/urn/resolver.pl?urn:nbn:de:bvb:91-diss-20180822-1434981-1-9> [visited on 03/06/2023].
- [44] S. Rothgang et al., „Battery design for successful electrification in public transport,“ *Energies*, vol. 8, no. 7, pp. 6715–6737, 2015, DOI: 10.3390/en8076715.
- [45] C. Reiter, „Thermische Vorauslegung hochbelasteter Batteriesysteme für Elektrofahrzeuge in der Konzeptphase,“ Dissertation, Institute of Automotive Technology, Technical University of Munich, 2020. Available: <https://nbn-resolving.de/urn/resolver.pl?urn:nbn:de:bvb:91-diss-20201105-1548444-1-1> [visited on 03/06/2023].
- [46] A. Epp et al., „Holistic battery system design optimization for electric vehicles using a multiphysically coupled lithium-ion battery design tool,“ *Journal of Energy Storage*, vol. 52, p. 104854, 2022, DOI: 10.1016/j.est.2022.104854.
- [47] O. Teichert et al., „Joint optimization of vehicle battery pack capacity and charging infrastructure for electrified public bus systems,“ *IEEE Transactions on Transportation Electrification*, vol. 5, no. 3, pp. 672–682, 2019.
- [48] C. Pillot, „Battery market for Hybrid, Plug in & electric Vehicles,“ Avicenne Energy, 2020.
- [49] Y. Miao et al., „Current Li-ion battery technologies in electric vehicles and opportunities for advancements,“ *Energies*, vol. 12, no. 6, p. 1074, 2019, DOI: 10.3390/en12061074.
- [50] T. B. Reddy, *Linden’s handbook of batteries*, McGraw-Hill Education, 2011.
- [51] E. J. Berg et al., „Rechargeable batteries: grasping for the limits of chemistry,“ *Journal of The Electrochemical Society*, vol. 162, no. 14, A2468, 2015, DOI: 10.1149/2.0081514jes.
- [52] G. E. Blomgren, „The development and future of lithium ion batteries,“ *Journal of The Electrochemical Society*, vol. 164, no. 1, A5019, 2016, DOI: 10.1149/2.0251701jes.
- [53] D. Andre et al., „Future generations of cathode materials: an automotive industry perspective,“ *Journal of Materials Chemistry A*, vol. 3, no. 13, pp. 6709–6732, 2015, DOI: 10.1039/C5TA00361J.
- [54] N. Nitta et al., „Li-ion battery materials: present and future,“ *Materials today*, vol. 18, no. 5, pp. 252–264, 2015, DOI: 10.1016/j.mattod.2014.10.040.
- [55] B. Scrosati and J. Garche, „Lithium batteries: Status, prospects and future,“ *Journal of power sources*, vol. 195, no. 9, pp. 2419–2430, 2010, DOI: 10.1016/j.jpowsour.2009.11.048.
- [56] D. Deng, „Li-ion batteries: basics, progress, and challenges,“ *Energy Science & Engineering*, vol. 3, no. 5, pp. 385–418, 2015, DOI: 10.1002/ese3.95.
- [57] N. Campagnol et al., „Building better batteries: Insights on chemistry and design from China,“ McKinsey & Company, 2021. Available: <https://www.mckinsey.com/industries/automotive-and-assembly/our-insights/building-better-batteries-insights-on-chemistry-and-design-from-china> [visited on 03/06/2023].
- [58] D. Andre et al., „Future high-energy density anode materials from an automotive application perspective,“ *Journal of materials chemistry A*, vol. 5, no. 33, pp. 17174–17198, 2017, DOI: 10.1039/C7TA03108D.
- [59] K. Zaghbi et al., „Safe and fast-charging Li-ion battery with long shelf life for power applications,“ *Journal of power sources*, vol. 196, no. 8, pp. 3949–3954, 2011, DOI: 10.1016/j.jpowsour.2010.11.093.

- [60] R. Schmuch et al., „Performance and cost of materials for lithium-based rechargeable automotive batteries,“ *Nature Energy*, vol. 3, no. 4, pp. 267–278, 2018, DOI: 10.1038/s41560-018-0107-2.
- [61] D. V. Ragone, „Review of battery systems for electrically powered vehicles,“ SAE Technical Paper, 1968, DOI: 10.4271/680453.
- [62] E. Catenaro, D. M. Rizzo and S. Onori, „Experimental analysis and analytical modeling of enhanced-Ragone plot,“ *Applied Energy*, vol. 291, p. 116473, 2021, DOI: 10.1016/j.apenergy.2021.116473.
- [63] P. Dechent et al., „ENPOLITE: Comparing Lithium-Ion Cells across Energy, Power, Lifetime, and Temperature,“ *ACS Energy Letters*, vol. 6, pp. 2351–2355, 2021, DOI: 10.1021/acsenenergylett.1c00743.
- [64] A. Panday and H. O. Bansal, „Multi-Objective Optimization in Battery Selection for Hybrid Electric Vehicle Applications.“ *Journal of Electrical Systems*, vol. 12, no. 2, 2016. Available: https://media.proquest.com/media/hms/PFT/1/MIvMA?_s=MKZlkyo%2BntiOGixhTfTJkjuergs%3D [visited on 03/06/2023].
- [65] M. Loganathan et al., „Multi-Criteria decision making (MCDM) for the selection of Li-Ion batteries used in electric vehicles (EVs),“ *Materials Today: Proceedings*, vol. 41, pp. 1073–1077, 2021, DOI: 10.1016/j.matpr.2020.07.179.
- [66] V. Sulzer et al., „Python battery mathematical modelling (PyBaMM),“ *Journal of Open Research Software*, vol. 9, no. 1, 2021, DOI: 10.5334/jors.309.
- [67] G. G. Botte, V. R. Subramanian and R. E. White, „Mathematical modeling of secondary lithium batteries,“ *Electrochimica Acta*, vol. 45, no. 15-16, pp. 2595–2609, 2000, DOI: 10.1016/S0013-4686(00)00340-6.
- [68] V. Boovaragavan, S. Harinipriya and V. R. Subramanian, „Towards real-time (milliseconds) parameter estimation of lithium-ion batteries using reformulated physics-based models,“ *Journal of Power Sources*, vol. 183, no. 1, pp. 361–365, 2008, DOI: 10.1016/j.jpowsour.2008.04.077.
- [69] S. Buller, „Impedance-based simulation models for energy storage devices in advanced automotive power systems,“ Dissertation, RWTH Aachen, 2003.
- [70] K. A. Smith, C. D. Rahn and C.-Y. Wang, „Control oriented 1D electrochemical model of lithium ion battery,“ *Energy Conversion and Management*, vol. 48, no. 9, pp. 2565–2578, 2007, DOI: 10.1016/j.enconman.2007.03.015.
- [71] D. Doerffel and S. A. Sharkh, „A critical review of using the Peukert equation for determining the remaining capacity of lead-acid and lithium-ion batteries,“ *Journal of power sources*, vol. 155, no. 2, pp. 395–400, 2006, DOI: 10.1016/j.jpowsour.2005.04.030.
- [72] S. R. Bhatikar et al., „Artificial neural network based energy storage system modeling for hybrid electric vehicles,“ *Society of Automotive Engineers*, vol. 192, 2000. Available: <https://citeseerx.ist.psu.edu/document?repid=rep1&type=pdf&doi=5b18720dfeedb3dfe05631dbc5828dca73c9e8a2> [visited on 03/06/2023].
- [73] P. Keil and A. Jossen, „Aufbau und parametrierung von batteriemodellen,“ in *19. DESIGN & ELEKTRONIK-Entwicklerforum Batterien & Ladekonzepte*, 2012. Available: <https://mediatum.ub.tum.de/doc/1162416/1162416.pdf> [visited on 03/06/2023].

- [74] N. Wassiliadis et al., „Quantifying the state of the art of electric powertrains in battery electric vehicles: Range, efficiency, and lifetime from component to system level of the Volkswagen ID. 3,“ *eTransportation*, vol. 12, p. 100167, 2022, DOI: 10.1016/j.etrans.2022.100167.
- [75] G. Xia, L. Cao and G. Bi, „A review on battery thermal management in electric vehicle application,“ *Journal of power sources*, vol. 367, pp. 90–105, 2017, DOI: 10.1016/j.jpowsour.2017.09.046.
- [76] W. Vermeer, G. R. C. Mouli and P. Bauer, „A comprehensive review on the characteristics and modeling of lithium-ion battery aging,“ *IEEE Transactions on Transportation Electrification*, vol. 8, no. 2, pp. 2205–2232, 2021, DOI: 10.1109/TTE.2021.3138357.
- [77] C. R. Birkl et al., „Degradation diagnostics for lithium ion cells,“ *Journal of Power Sources*, vol. 341, pp. 373–386, 2017, DOI: 10.1016/j.jpowsour.2016.12.011.
- [78] S. D. Downing and D. Socie, „Simple rainflow counting algorithms,“ *International journal of fatigue*, vol. 4, no. 1, pp. 31–40, 1982, DOI: 10.1016/0142-1123(82)90018-4.
- [79] J. Schmalstieg et al., „A holistic aging model for Li (NiMnCo) O₂ based 18650 lithium-ion batteries,“ *Journal of Power Sources*, vol. 257, pp. 325–334, 2014, DOI: 10.1016/j.jpowsour.2014.02.012.
- [80] J. Neubauer, „Battery lifetime analysis and simulation tool (BLAST) documentation,“ National Renewable Energy Lab.(NREL), Golden, CO (United States), 2014. Available: <https://www.nrel.gov/docs/fy15osti/63246.pdf> [visited on 03/06/2023].
- [81] M. Schimpe et al., „Energy efficiency evaluation of a stationary lithium-ion battery container storage system via electro-thermal modeling and detailed component analysis,“ *Applied energy*, vol. 210, pp. 211–229, 2018, DOI: /10.1016/j.apenergy.2017.10.129.
- [82] T. Yuksel et al., „Plug-in hybrid electric vehicle LiFePO₄ battery life implications of thermal management, driving conditions, and regional climate,“ *Journal of Power Sources*, vol. 338, pp. 49–64, 2017, DOI: 10.1016/j.jpowsour.2016.10.104.
- [83] D. Zhao et al., „From NEDC to WLTP for Vehicles: The Impact on Fuel Efficiency Calculation and Algorithm Optimization,“ in *2022 International Conference on Data Analytics, Computing and Artificial Intelligence (ICDACAI)*, 2022, pp. 311–315, DOI: 10.1109/ICDACAI57211.2022.00067.
- [84] N.-G. Zacharof, G. Fontaras, et al., „Report on VECTO technology simulation capabilities and future outlook,“ 2016. Available: <https://publications.jrc.ec.europa.eu/repository/handle/JRC103864?mode=full> [visited on 03/06/2023].
- [85] The European parliament and the council, „Commission regulation (EU) 2017/2400,“ *Official Journal of the European Union*, vol. L 349, 2017.
- [86] K. Walz, D. Contreras and K. Rudion, „Synthetic charging profiles development of battery–electric trucks for probabilistic grid planning,“ in *CIREN 2020 Berlin Workshop (CIREN 2020)*, 2020, pp. 124–127, DOI: 10.1049/oap-cired.2021.0259.
- [87] K. Walz, F. Otteny and K. Rudion, „A Charging Profile Modeling Approach for Battery-Electric Trucks based on Trip Chain Generation,“ in *2021 IEEE PES Innovative Smart Grid Technologies Europe (ISGT Europe)*, 2021, pp. 1–5, DOI: 10.1109/ISGTEurope52324.2021.9640136.
- [88] F. Tong et al., „Energy consumption and charging load profiles from long-haul truck electrification in the United States,“ *Environmental Research: Infrastructure and Sustainability*, vol. 1, no. 2, p. 025007, 2021, DOI: 10.1088/2634-4505/ac186a.

- [89] B. Borlaug et al., „Heavy-duty truck electrification and the impacts of depot charging on electricity distribution systems,” *Nature Energy*, vol. 6, no. 6, pp. 673–682, 2021, DOI: 10.1038/s41560-021-00855-0.
- [90] D. Wang et al., „Modeling of plug-in electric vehicle travel patterns and charging load based on trip chain generation,” *Journal of Power Sources*, vol. 359, pp. 468–479, 2017, DOI: 10.1016/j.jpowsour.2017.05.036.
- [91] J. Schäuble et al., „Generating electric vehicle load profiles from empirical data of three EV fleets in Southwest Germany,” *Journal of Cleaner Production*, vol. 150, pp. 253–266, 2017, DOI: 10.1016/j.jclepro.2017.02.150.
- [92] C. Gaete-Morales et al., „An open tool for creating battery-electric vehicle time series from empirical data, emobpy,” *Scientific data*, vol. 8, no. 1, pp. 1–18, 2021, DOI: 10.1038/s41597-021-00932-9.
- [93] C. Nobis and T. Kuhnimhof, „Mobilität in Deutschland- MiD: Ergebnisbericht,” Studie von infas, DLR, IVT und infas 360 im Auftrag des Bundesministers für Verkehr und digitale Infrastruktur (FE-Nr. 70.904/15), Bonn, Berlin, 2018. Available: https://www.mobilitaet-in-deutschland.de/pdf/MiD2017_Ergebnisbericht.pdf [visited on 03/07/2023].
- [94] T. Yuksel and J. Michalek, „Development of a Simulation Model to Analyze the Effect of Thermal Management on Battery Life,” in *SAE 2012 World Congress & Exhibition*, 2012, DOI: <https://doi.org/10.4271/2012-01-0671>.
- [95] T. Yuksel and J. J. Michalek, „Evaluation of the effects of thermal management on battery life in plug-in hybrid electric vehicles,” 2012, DOI: 10.1184/R1/6489836.v1.
- [96] J. Neubauer and E. Wood, „Thru-life impacts of driver aggression, climate, cabin thermal management, and battery thermal management on battery electric vehicle utility,” *Journal of Power Sources*, vol. 259, pp. 262–275, 2014, DOI: 10.1016/j.jpowsour.2014.02.083.
- [97] N. DiOrio et al., „Technoeconomic modeling of battery energy storage in SAM,” National Renewable Energy Lab.(NREL), Golden, CO (United States), 01/09/2015, DOI: 10.2172/1225314.
- [98] M. Naumann et al., „Analysis and modeling of calendar aging of a commercial LiFePO₄/graphite cell,” *Journal of Energy Storage*, vol. 17, pp. 153–169, 2018, DOI: 10.1016/j.est.2018.01.019.
- [99] J. Jaguemont and J. Van Mierlo, „A comprehensive review of future thermal management systems for battery-electrified vehicles,” *Journal of Energy Storage*, vol. 31, p. 101551, 2020, DOI: 10.1016/j.est.2020.101551.
- [100] Y. Xie et al., „An MPC-based control strategy for electric vehicle battery cooling considering energy saving and battery lifespan,” *IEEE Transactions on Vehicular Technology*, vol. 69, no. 12, pp. 14657–14673, 2020, DOI: 10.1109/TVT.2020.3032989.
- [101] T. Pham et al., „On-line energy and battery thermal management for hybrid electric heavy-duty truck,” in *2013 American Control Conference*, 2013, pp. 710–715, DOI: 10.1109/ACC.2013.6579919.
- [102] O. Teichert et al., „Techno-economic cell selection for battery-electric long-haul trucks,” *eTransportation*, 2023, DOI: 10.1016/j.etrans.2022.100225.
- [103] European Commission, „User Manual: Vehicle Energy Consumption Calculation tool (VECTO) 3.3,” Available: https://climate.ec.europa.eu/eu-action/transport-emissions/road-transport-reducing-co2-emissions-vehicles/vehicle-energy-consumption-calculation-tool-vecto_en#vecto-executables [visited on 03/07/2023].

- [104] The European parliament and the council of the European Union, „REGULATION (EC) No 561/2006,“ *Official journal of the European Union*, vol. L 102, 2006.
- [105] M. B. Trucks. „*Product information - eActros LongHaul*,“ Available: https://www.mercedes-benz-trucks.com/en_GB/brand/actions-and-events/iaa-2022/iaa2022-bev.html?mtm_campaign=iaa22&mtm_kwd=eActros-LongHaul [visited on 12/22/2022].
- [106] M. Naumann, F. B. Spingler and A. Jossen, „Analysis and modeling of cycle aging of a commercial LiFePO₄/graphite cell,“ *Journal of Power Sources*, vol. 451, p. 227666, 2020, DOI: 10.1016/j.jpowsour.2019.227666.
- [107] H. C. Hesse et al., „Economic optimization of component sizing for residential battery storage systems,“ *Energies*, vol. 10, no. 7, p. 835, 2017, DOI: 10.3390/en10070835.
- [108] A. Phadke, M. McCall and D. Rajagopal, „Reforming electricity rates to enable economically competitive electric trucking,“ *Environmental Research Letters*, vol. 14, no. 12, p. 124047, 2019, DOI: 10.1088/1748-9326/ab560d.
- [109] J. Burgdorf, „Supertest Volvo FH Electric,“ *Trucker supertest*, 2022. Available: <https://brochures.volvotrucks.com/de/volvo-trucks/testberichte/2022/volvo-fh-electric-testbericht-trucker-2022-01/?page=4> [visited on 10/10/2022].
- [110] H. Löbbberding et al., „From cell to battery system in BEVs: analysis of system packing efficiency and cell types,“ *World Electric Vehicle Journal*, vol. 11, no. 4, p. 77, 2020, DOI: 10.3390/wevj11040077.
- [111] N. Rosenberger et al. „*Quantifying the state of the art of electric powertrains in battery electric vehicles: comprehensive analysis of the Tesla Model 3 on vehicle level*,“ Personal communication. 2023.
- [112] „Battery requirements for future automotive applications,“ eucar, european council for automotive R&D, 07/2019. Available: <https://eucar.be/wp-content/uploads/2019/08/20190710-EG-BEV-FCEV-Battery-requirements-FINAL.pdf> [visited on 03/08/2023].
- [113] O. Teichert, F. Müller and M. Lienkamp, „Techno-economic design of battery thermal management systems in different climates,“ *Journal of Energy Storage*, vol. 48, p. 103832, 2022, DOI: 10.1016/j.est.2021.103832.
- [114] M. Steinhardt et al., „Meta-analysis of experimental results for heat capacity and thermal conductivity in lithium-ion batteries: A critical review,“ *Journal of Power Sources*, vol. 522, p. 230829, 2022, DOI: 10.1016/j.jpowsour.2021.230829.
- [115] A. Hales. „*Cell cooling coefficient of the Volkswagen ID.3 cell*,“ Personal communication. 2022.
- [116] J. H. Lienhard IV and J. H. Lienhard V, *A Heat Transfer Textbook*, 5th, Mineola, NY, Dover Publications, 2019, ISBN: 9780486837352.
- [117] K. Jalkanen, T. Aho and K. Vuorilehto, „Entropy change effects on the thermal behavior of a LiFePO₄/graphite lithium-ion cell at different states of charge,“ *Journal of Power Sources*, vol. 243, pp. 354–360, 2013, DOI: 10.1016/j.jpowsour.2013.05.199.
- [118] M. Schreiber. „*State of the art automotive battery aging: Volkswagen ID.3 Li-ion cells under realistic usage conditions*,“ Personal communication. 2022.
- [119] F. Günter and N. Wassiliadis, „State of the art of lithium-ion pouch cells in automotive applications: cell teardown and characterization,“ *Journal of The Electrochemical Society*, vol. 169, no. 3, p. 030515, 2022, DOI: 10.1149/1945-7111/ac4e11.

-
- [120] D. Tol et al., „Techno-economic uptake potential of zero-emission trucks in Europe,“ TNO, 03/10/2022. Available: <https://www.agora-verkehrswende.de/veroeffentlichungen/techno-economic-uptake-potential-of-zero-emission-trucks-in-europe/> [visited on 03/07/2023].
- [121] G. Balke and L. Adenaw, „Heavy Commercial Vehicles’ Mobility: A comprehensive real driving data set.“ *Data in Brief*, 2023.
- [122] Bundesanstalt für Straßenwesen. „Achslastmessstellen: Rohdaten 2022 Januar 2022 (zip, 49MB),“ Available: <https://www.bast.de/DE/Publikationen/Daten/Verkehrstechnik/Achslast.html> [visited on 03/07/2023].
- [123] Bundesministerium der Justiz. „Straßenverkehrs-Zulassungs-Ordnung,“ Apr. 26, 2012.
- [124] Coordination Office Charging Interface, c/o Carmeq GmbH. „Combined Charging System 1.0 Specification - CCS 1.0,“ Version 1.2.1. Available: https://tesla.o.auroraobjects.eu/Combined_Charging_System_1_0_Specification_V1_2_1.pdf [visited on 03/07/2023].
- [125] M. D. Felice and K. Kavvadias. „ERA-NUTS: time-series based on C3S ERA5 for European regions,“ version 1980-2018. Zenodo, Apr. 2019. DOI: 10.5281/zenodo.2650191.
- [126] O. Teichert, J. Schneider and M. Lienkamp, „Strategy beats power: Cooling system design for battery-electric long-haul trucks,“ Electric Vehicle Symposium, Oslo, 2022.
- [127] G. Offer et al., „Cool metric for lithium-ion batteries could spur progress,“ *Nature*, vol. 582, no. 7813, pp. 485–487, 2020, DOI: 10.1038/d41586-020-01813-8.
- [128] K.-P. Kairies et al., „Real-life load profiles of PV battery systems from field measurements,“ *Energy Procedia*, vol. 99, pp. 401–410, 2016, DOI: 10.1016/j.egypro.2016.10.130.
- [129] D. Kucevic et al., „Standard battery energy storage system profiles: Analysis of various applications for stationary energy storage systems using a holistic simulation framework,“ *Journal of Energy Storage*, vol. 28, p. 101077, 2020, DOI: 10.1016/j.est.2019.101077.

Prior Publications

During the development of this dissertation, publications and student theses were written in which partial aspects of this work were presented.

Journals; Scopus/Web of Science listed (peer-reviewed)

- [74] N. Wassiliadis et al., „Quantifying the state of the art of electric powertrains in battery electric vehicles: Range, efficiency, and lifetime from component to system level of the Volkswagen ID. 3,“ *eTransportation*, vol. 12, p. 100167, 2022, DOI: 10.1016/j.etrans.2022.100167.
- [102] O. Teichert et al., „Techno-economic cell selection for battery-electric long-haul trucks,“ *eTransportation*, 2023, DOI: 10.1016/j.etrans.2022.100225.
- [113] O. Teichert, F. Müller and M. Lienkamp, „Techno-economic design of battery thermal management systems in different climates,“ *Journal of Energy Storage*, vol. 48, p. 103832, 2022, DOI: 10.1016/j.est.2021.103832.

Journals, Conferences, Periodicals, Reports, Conference Proceedings and Poster, etc.; not Scopus/Web of Science listed

- [126] O. Teichert, J. Schneider and M. Lienkamp, „Strategy beats power: Cooling system design for battery-electric long-haul trucks,“ Electric Vehicle Symposium, Oslo, 2022.
O. Teichert et al., „Substandard? Lithium-ion cells available on online marketplaces,“ in *Advanced Battery Power*, 2022.

Non-thesis-relevant publications; Scopus/Web of Science listed (peer-reviewed)

- [47] O. Teichert et al., „Joint optimization of vehicle battery pack capacity and charging infrastructure for electrified public bus systems,“ *IEEE Transactions on Transportation Electrification*, vol. 5, no. 3, pp. 672–682, 2019.
O. Teichert, A. Koch and A. Ongel, „Comparison of Eco-Driving Strategies for Different Traffic-Management Measures,“ in *2020 IEEE 23rd International Conference on Intelligent Transportation Systems (ITSC)*, 2020, pp. 1–7.
F. Trocker et al., „City-scale assessment of stationary energy storage supporting end-station fast charging for different bus-fleet electrification levels,“ *Journal of Energy Storage*, vol. 32, p. 101794, 2020.

A. Koch et al., „Powertrain Optimization for Electric Buses under Optimal Energy-Efficient Driving,“ *Energies*, vol. 13, no. 23, p. 6451, 2020.

J. Schneider et al., „The novel Megawatt Charging System standard: Impact on battery size and cell requirements for battery-electric long-haul trucks,“ (in review process), *eTransportation*, 2023.

Thesis-relevant open-source software

O. Teichert. „Battery thermal management system design,“ 2022. [Online]. Available: <https://github.com/TUMFTM/BTMS-Design> [visited on 12/23/2022].

O. Teichert. „Techno-economic cell selection for battery-electric long-haul trucks,“ 2023. [Online]. Available: <https://github.com/TUMFTM/TechnoEconomicCellSelection> [visited on 03/07/2023].

Supervised Student's Thesis

The following student theses were written within the framework of the dissertation under the supervision of the author in terms of content, technical and scientific support as well as under relevant guidance of the author. In the following, the bachelor, semester and master theses relevant and related to this dissertation are listed. Many thanks to the authors of these theses for their extensive support within the framework of this research project.

F. Müller, „A computationally efficient model for battery sizing and thermal system optimization with special focus on aging for stationary storage peak-shaving applications,“ Master thesis, Institute of Automotive Technology, Technical University of Munich, Munich, 2020.

F. A. Farooqui, „Thermal design for heavy-duty-truck batteries,“ Master thesis, Institute of Automotive Technology, Technical University of Munich, Munich, 2021.

J. Zhang, „Thermal design for stationary energy storage systems,“ Master thesis, Institute of Automotive Technology, Technical University of Munich, Munich, 2021.

L. Bock, „Techno-ökonomische Zellauswahl von status quo Lithium-Ionen-Batterien für stationäre Speicheranwendungen,“ Semester thesis, Institute of Automotive Technology, Technical University of Munich, Munich, 2021.

C. Colás Hazeu, „Potentialanalyse elektrischer Nutzfahrzeuge,“ Semester thesis, Institute of Automotive Technology, Technical University of Munich, Munich, 2021.

J. Schumacher, „Batterieanforderungen für elektrische PKW verschiedener Fahrzeugklassen,“ Bachelor thesis, Institute of Automotive Technology, Technical University of Munich, Munich, 2022.

E. Zhang, „Development of a web-based Tool for Techno-economic Cell selection for Battery Electric Trucks,“ Semester thesis, Institute of Automotive Technology, Technical University of Munich, Munich, 2022.

J. R. Torresano Gómez, „Techno-economic cell selection for battery-electric trains,“ Bachelor thesis, Institute of Automotive Technology, Technical University of Munich, Munich, 2022.

Appendix

A	Fitting results using an ECM with 2 RC-elements	xxi
B	Additional validation results	xxiii

A Fitting results using an ECM with 2 RC-elements

In the following, I will demonstrate the impact of including a second RC-element in the ECM of the selected cell. The ECM with two RC-elements is shown in Figure A.1.

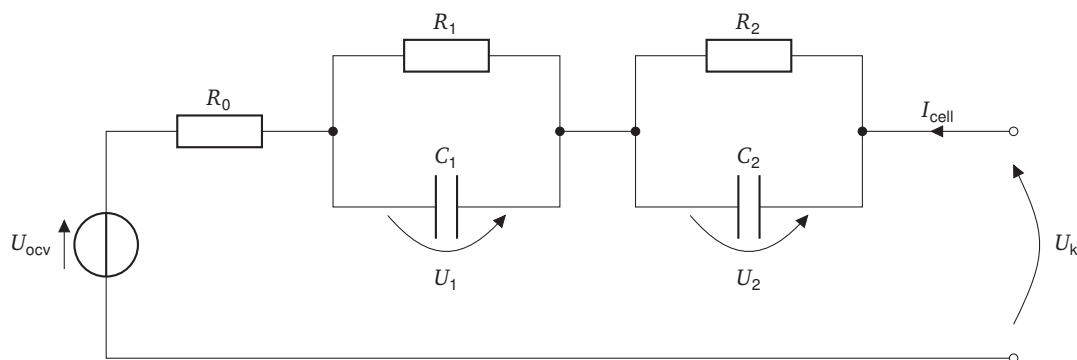


Figure A.1: ECM with two RC-elements.

Using the same pulse fitting approach as described in Figure 2.2.2 results in the parametrization shown in Figure A.2. For all SOC and temperatures, in both charging and discharging direction, a coefficient of determination above 99.3% is achieved. For the series resistance R_0 , no dependency on the SOC or temperature can be seen. The resistance of the first and second RC-element, however, decreases with an increase in cell temperature. The time constants of both RC-elements do not reveal a dependency on SOC or temperature, but differ from each other by three orders of magnitude: The time constant of the first RC-element is between 7 ms and 30 ms, while the time constant of the second RC-element is between 16 s and 30 s. They therefore model different processes in the cell: capacitive behavior and diffusion. To accurately model an ECM with two RC-elements would require a simulation time step smaller than the 7 ms, which is not feasible when simulating battery operation over the entire battery life.

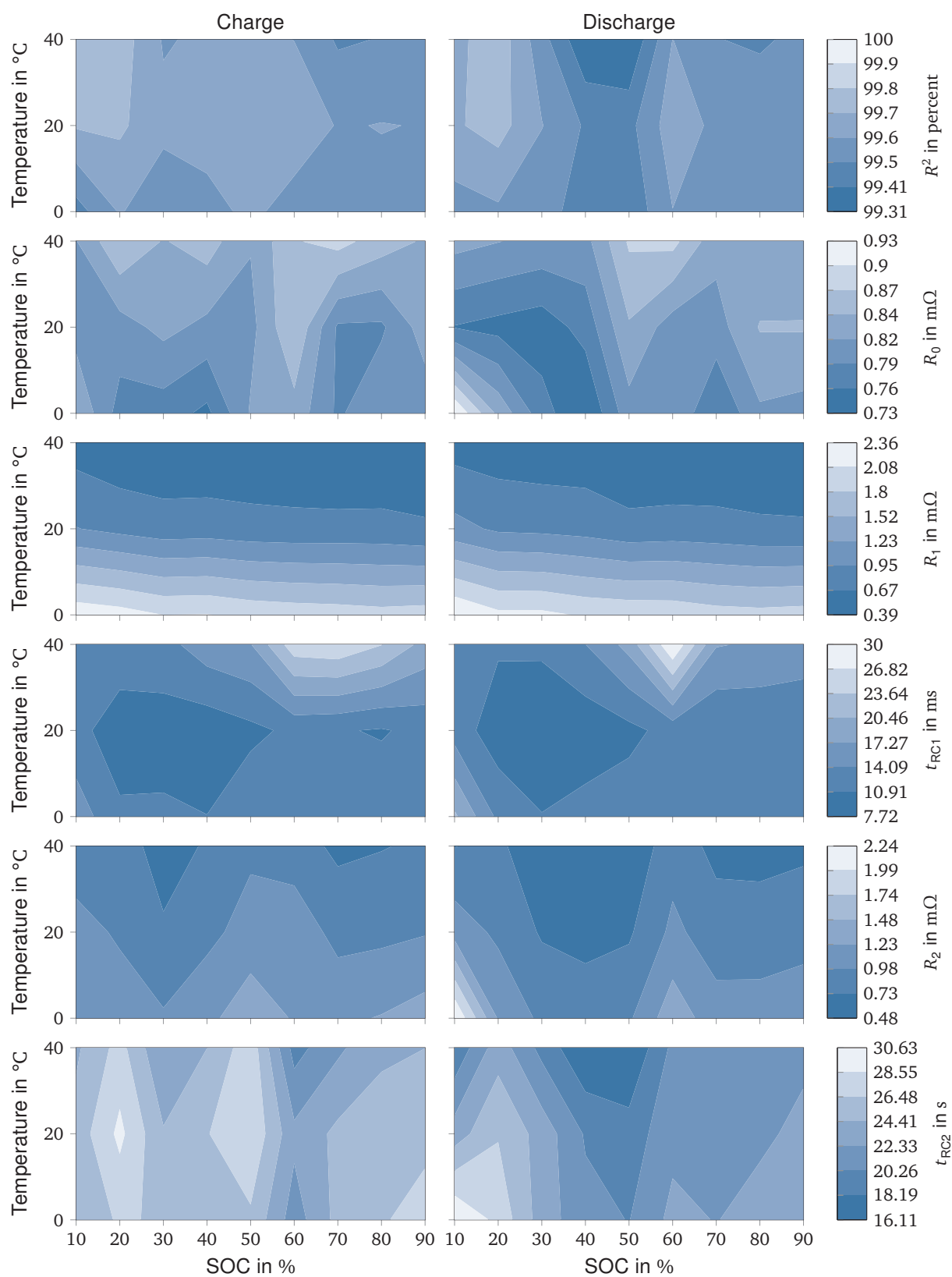


Figure A.2: Quality and found parameters of the ECM parametrization

B Additional validation results

In Subsection 3.2.6 the validation of the electric and thermal models was presented and the validation profiles with the highest errors were discussed in detail. Here, the detailed validation of the remaining profiles is shown. Figure B.1 shows the measured and simulated cell voltages and temperatures for urban driving at an ambient temperature of approximately 15 °C. Additionally, the voltage and temperature errors are shown.

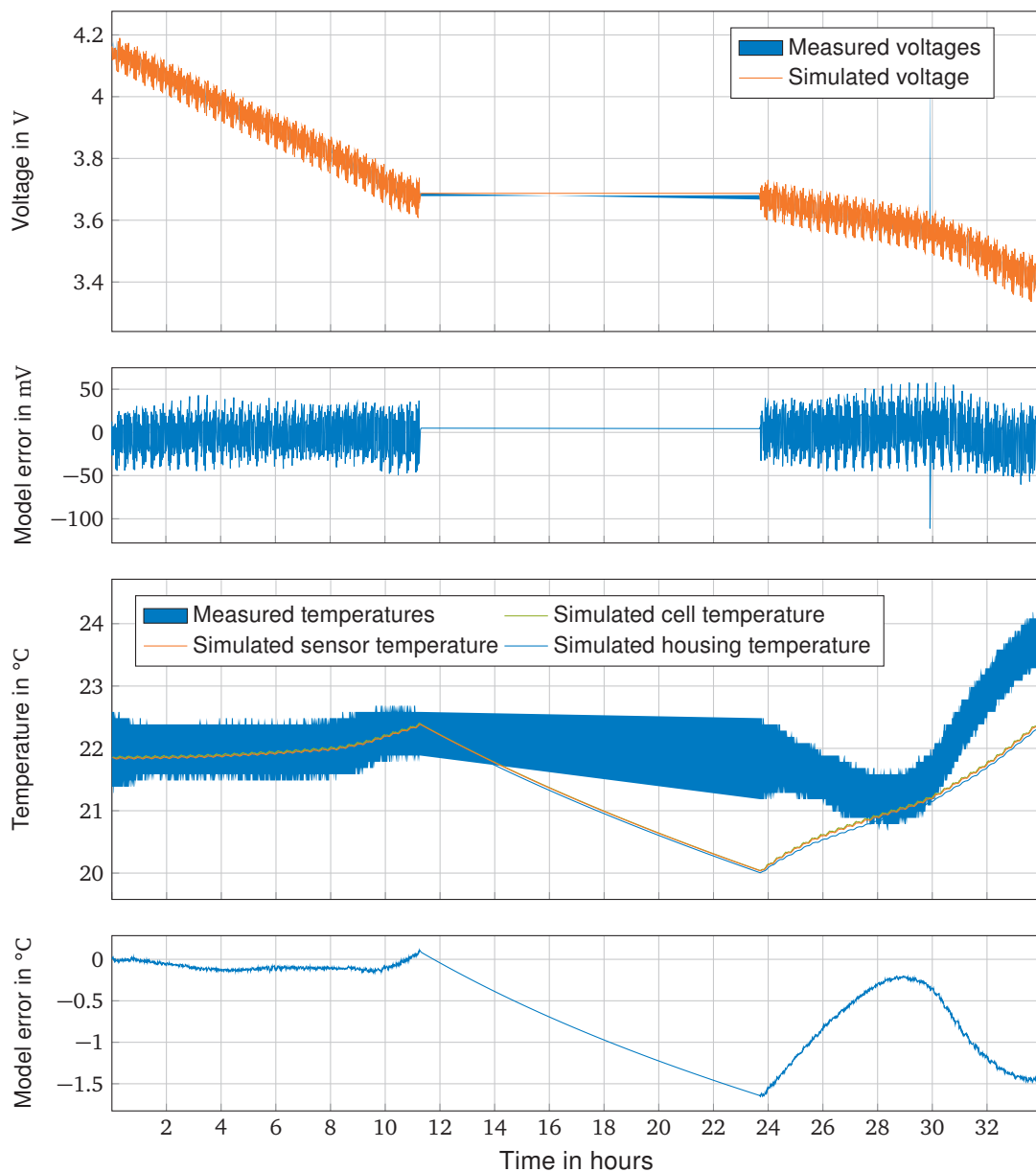


Figure B.1: Urban cycle at 15 °C ambient temperature

The measurement was spread out over two separate days, because the battery could not be discharged with the urban speed profile within 8 hours, resulting in a total duration of 34 hours. The voltage decreases as the battery is discharged, due to the SOC dependency of the open-circuit voltage.

The measured temperature remains constant during the first measurement day, showing that the ohmic losses resulting from driving with the urban speed profile are not sufficient to heat up the battery significantly. While the vehicle is parked overnight, a slight decrease in battery temperature can be seen. On the second measurement day, the battery temperature drops initially, which could be caused by entropy effects in the battery. Subsequently, the battery temperature increases, which is likely caused by the higher battery current that is required to deliver the same power at a reduced battery voltage. The simulation results show a stronger cool-down overnight, suggesting that the implemented heat transfer to ambient air might be too high. The initial dip in the battery temperature at the start of the second measurement day is not seen in the simulation, because the battery model does not include entropy effects. The simulated temperature increase at the end of the measurement matches the measurement well.

Figure B.2 shows the results of the validation for the urban driving cycle at an ambient temperature of approximately 30 °C. The measured voltage shows a relaxation overnight, which is not covered by the model. The voltage error is consistent with the measurement at 15 °C.

The battery temperature increases during the first measurement day, contrary to the measurement at an ambient temperature of 15 °C, because less heat is dissipated to the environment. During the night, the battery temperature decreases. On the second day of measurements, the battery temperature increases further and the cooling system is briefly activated, resulting in a sharp temperature drop 32.5 hours after the start of the measurement. The simulation matches the temperature on the first day and during the night well. On the second day, the simulated temperature exceeds the measured temperature, which again may be caused by entropy effects that are not included in the model.

Figure B.3 shows the validation result for the interurban driving cycle at an ambient temperature of 30 °C. The voltage error is consistent with the measurement at 15 °C shown in Subsection 3.2.6.

As a result of the higher ambient temperature, the cooling system is activated multiple times during the measurement, resulting in a saw-tooth profile. The simulation matches the measurement well, but has a phase shift during the activation and deactivation of the cooling system. In the middle of the measurement, the temperature increase of the battery is lower despite the continuous repetition of the same load-profile, which is attributed to entropy effects. The simulated temperature gradient is larger than in the urban and interurban driving cycles, due to the activation of the cooling system.

Figure B.4 shows the validation results for the highway driving cycle at an ambient temperature of 30 °C. The absolute voltage error is consistent with the measurement at 15 °C.

The measurement shows that the battery reaches 32 °C faster than during the measurement at 15 °C, because less heat is dissipated to the environment. The simulation briefly overestimates the temperature at the end of the heat-up phase, which, again, might be caused by entropy effects.

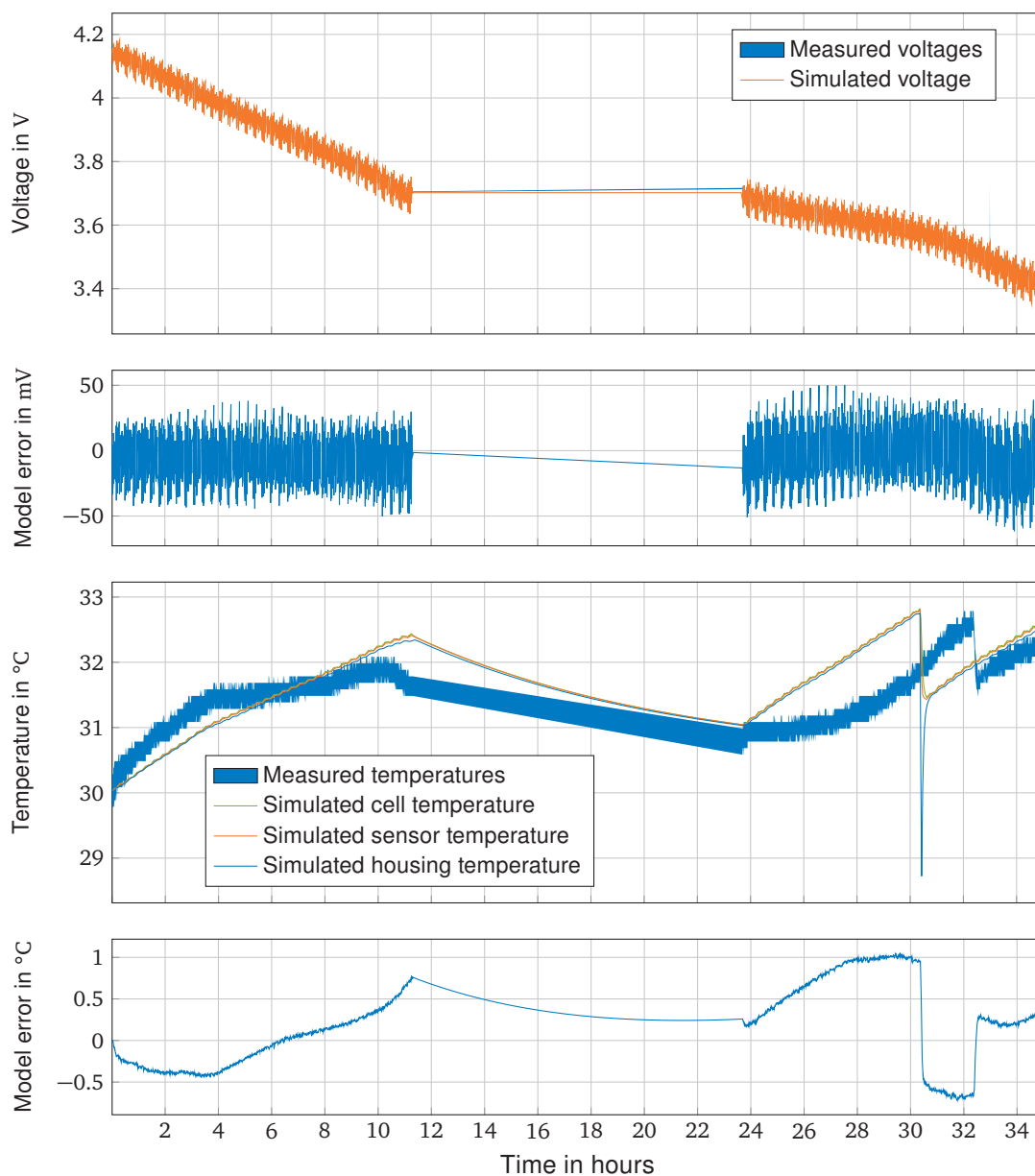


Figure B.2: Urban cycle at 30 °C ambient temperature

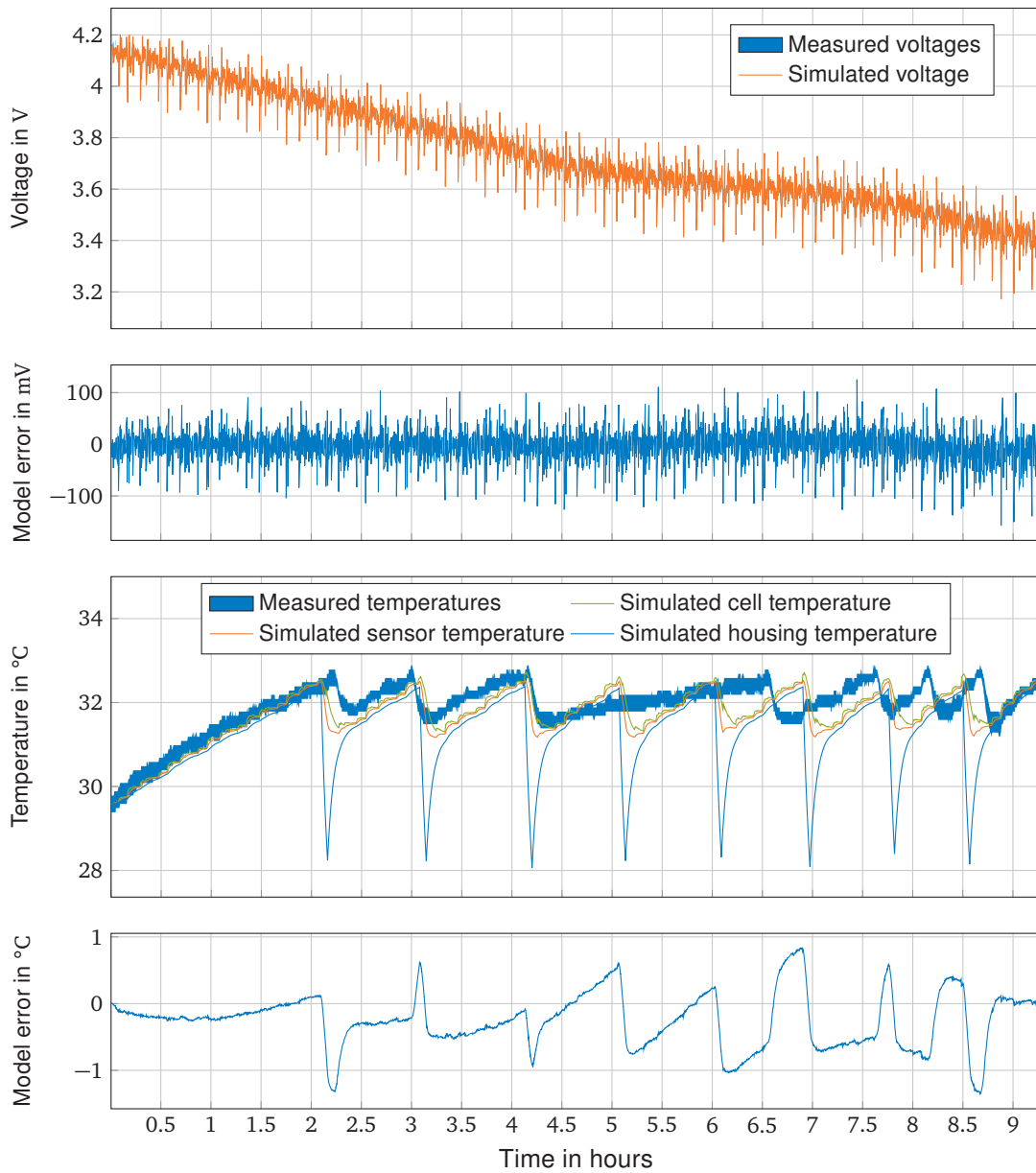


Figure B.3: Interurban cycle at 30°C ambient temperature

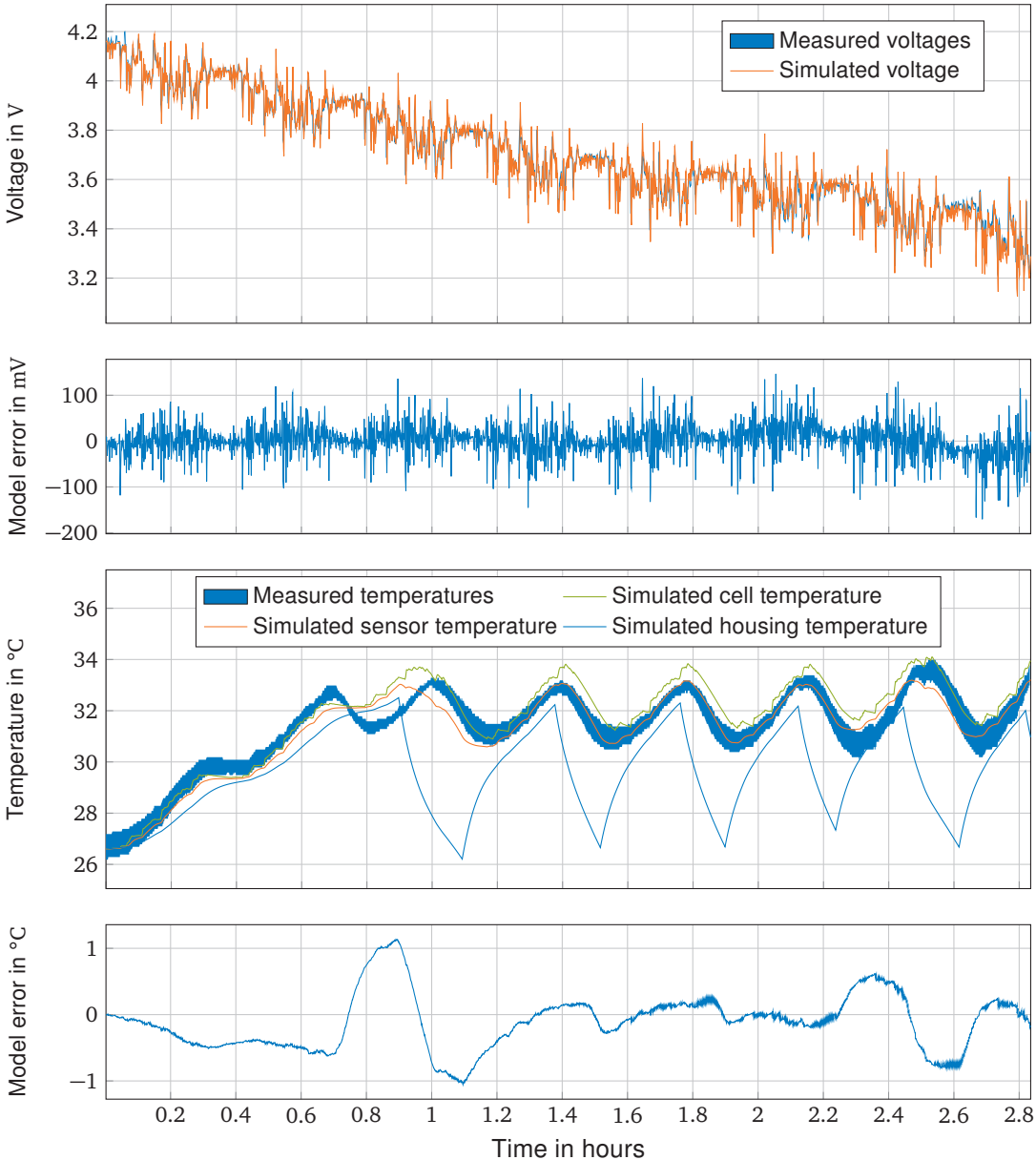


Figure B.4: Interurban cycle at 30°C ambient temperature